Universität Paderborn

Two-Photon Physics with Biexcitons in single Quantum Dots

Dem Department Physik
der Universität Paderborn
zur Erlangung des akademischen Grades

Doktor der Naturwissenschaften

vorgelegte

Dissertation

von

Björn Jonas

München, den 19. September 2022

Quantenphysik, a-hu!

Die Kassierer

Kurzfassung

Einzelne Photonen stellen eine wichtige Ressource in den Bereichen des photonischen Quantencomputings und der Quantenkommunikation dar. In dieser Arbeit wird ein theoretisch vorausgesagter Prozess, die *Nonlinear Down-Conversion*, in einem einzelnen Quantenpunkt experimentell nachgewiesen und genauer untersucht. Dieser Prozess erlaubt es, die Eigenschaften der emittierten Photonen durch ein optisches Kontrollfeld maßzuschneidern.

Um diesen Prozess beobachten zu können, mussten zunächst die notwendigen spektroskopischen Techniken entwickelt werden. Hierbei wurde ein besonderer Fokus auf die Unterdrückung zurück reflektierten Laserlichts gelegt. Das Resultat dieser Entwicklung war ein experimenteller Aufbau, der gekreuzt polarisierte Detektion mit spektraler Filterung verwendet. Weiterhin wurden *Solid Immersion Lenses* zur Erhöhung der Detektionseffizienz des von den Quantenpunkten emittierten Lichts eingesetzt. Durch Verwendung von hyperhemisphärischen Linsen aus kubischem Zirkonia konnte eine Verbesserung um den Faktor 2,9 erzielt werden.

Da der Ausgangszustand für den *Down-Conversion*-Prozess der Biexziton-Zustand ist, wurde dessen Anregung zunächst genauer untersucht. Als geeignete Methode für weitere Experimente stellte sich die phonon-assistierte Zwei-Photonen-Anregung heraus, da diese sehr robust gegenüber Verstimmungen ist.

Basierend auf diesen Vorarbeiten, konnte dann die *Nonlinear Down-Conversion* experimentell nachgewiesen werden. Im Folgenden wurde dieser Prozess dann genauer untersucht. Dabei konnte die Emission in einem Abstimmbereich von 0,5 meV um Exziton- und Biexzitonlinie beobachtet werden. Diese zeigte weiterhin ein Anti-Crossing mit diesen zwei Emissionslinien. Eine tiefergehende Analyse dieses Verhaltens zeigte die nahe Verwandtschaft zwischen der *Down-Conversion* und dem Konzept von *Dressed States*.

Weiterhin wurden polarisationsabhängige Experimente zur *Down-Conversion* durchgeführt. Hierbei konnte die theoretisch erwartete Polarisationskontrolle für lineare und zirkulare Polarisation erfolgreich demonstriert werden. Die Messdaten zeigten weiterhin eine sehr gute Übereinstimmung mit theoretischen Daten, was die Gültigkeit der Auswahlregeln auch für elliptische Polarisation nahelegt.

Abschließend wurde noch ein Spezialfall untersucht, bei dem sowohl die Biexzitonpopulation, als auch das virtuelle Niveau durch einen einzelnen Laser erzeugt werden.

Abstract

Single photons are an important resource in the growing fields of photonic quantum computation and quantum communication. This work demonstrates and takes a close look at the theoretically predicted process of nonlinear down-conversion in a single quantum dot that allows tailoring the single photon emission using an optical control field.

To be able to observe this process, the necessary spectroscopic techniques were developed, where a major emphasis was put on the suppression of backscattered laser light. The result of this development was a setup combining cross-polarized detection with spectral filtering. Furthermore, solid immersion lenses were investigated as a means to increase the collection efficiency for the light emitted by the quantum dots. By applying a super-hemispherical lens consisting of cubic zirconia, an improvement by a factor of 2.9 could be achieved.

Since the down-conversion process requires the quantum dot to be in the biexciton state, different methods of preparing this state were studied. Phonon-assisted two-photon excitation was determined as the method of choice for further experiments, as it proved to be robust against detuning.

With these building blocks in place the nonlinear down-conversion could be demonstrated and subjected to a detailed study. During these experiments a tuning range of 0.5 meV around the emission of exciton and biexciton could be achieved. Furthermore, the down-conversion showed an anti-crossing with these two lines. A closer analysis showed a close relation between nonlinear down-conversion and the concept of dressed states.

Furthermore, polarization dependent measurements of the down-conversion were conducted. Here, the theoretically expected polarization control could be experimentally demonstrated for linear and circular polarization. The results are furthermore in good agreement with a theoretical model, suggesting validity of the selection rules also for elliptical polarization.

Finally, a special case was investigated, where both the population and the virtual level are created by a single laser.

Contents

1 Introduction

In recent years the field of quantum technology has seen rapid advances. One major aspect in this regard is quantum computation, which has made the transition from purely academic research towards the development being mainly driven by privately funded companies[46, 9]. This has lead to first claims of quantum supremacy being achieved[6, 136]. In the field of communication, photonic quantum technologies are of great interest[47, 100], as photons provide stable quantum systems that can be transmitted over large distances, using optical fiber networks and satellites[27, 28].

For these applications, as well as for photonic quantum computing, high quality quantum light sources are key building blocks. Many different platforms are being investigated with regard to their quantum emission properties. Well known examples are parametric down-conversion in nonlinear crystals[90, 80, 60, 135], color-centers in diamond[69, 8], 2D materials[26, 36] or trapped atoms and ions[57, 51]. Semiconductor quantum dots (QDs) are also very interesting in this regard. Not only have they been shown to be excellent sources of single[83, 113, 124] and entangled photons[87, 110], but they can also be integrated into photonic and electronic structures using nano-fabrication techniques, well-known from semiconductor technologies[108, 75, 78, 132].

When quantum dots are used as single photon sources, nonlinearities can be exploited to enhance the performance. Well-known examples are the exploitation of Rabi oscillations, which represent a nonlinearity in the population, for deterministic single photon sources[53] or the nonlinear optical process of two-photon excitation to the biexciton state, the decay of which results in very pure single photons[111] and entangled photon pairs[93].

The properties of the photons generated by these schemes largely depend on the properties of the individual quantum dots, which show statistical variation due to the self-organized growth[84]. Examples of those parameters are the emission energy, the lifetime/linewidth and the polarization. The lifetime can be manipulated to some extend by embedding the dot into a cavity structure, to make use of the Purcell effect[72]. This has the additional benefit of increasing the brightness of the emission[116].Furthermore, electric fields[14] and strain[112] can be used to tune the emission energy of the QD, while magnetic fields have an influence on the fine-structure splitting[117].

A further mechanism for tailoring the emission is provided by exploiting a nonlinear process. Here, a strong non-resonant laser field defines the properties of the emission. Theoretical works have shown that emission energy, lifetime and polarization can be manipulated by means of a nonlinear down-conversion process from the biexciton to the ground state[55, 22, 23]. These works are supported by experimental evidence for Λ-systems in quantum dot molecules[123, 129, 103]. These systems are mathematically

equivalent to the ladder system formed by exciton and biexciton in a single quantum dot and therefore also allow the control of emission energy and lifetime[23].

On this background, this thesis is intended to study the theoretically predicted process of nonlinear down-conversion in a single quantum dot from an experimental perspective. This includes the development of the required spectroscopic techniques, the preparation of a suitable sample with sufficient brightness and a good understanding of the biexciton state before being able to study the down-conversion process itself.

Structure of this thesis

Chapter two, entitled "Fundamentals" provides a brief introduction to the underlying physics on which this thesis is based. First, some general information on quantum dots is provided, followed by a few more specialized aspects. Furthermore, the topics of single photon emission and polarization of light are discussed, as they are of particular importance for this work. The discussion of all these topics is generally done in a brief manner with a focus on the main points.

The chapter "Experimental Setup and Methods" presents the spectroscopic setup and measurement techniques used in this work. The system is broken down into basic functional units that are then discussed individually. Special attention is given to the aspect of the suppression of back-scattered laser light, which proved to be of particular importance.

This is followed by the chapter "Signal collection enhancement with solid immersion lenses". Here, the fabrication of MBE material into functional pin-diodes large enough to house a solid immersion lens and their characterization is presented. The intention behind this is to increase the collection efficiency of quantum dot emission. Therefore, the chapter includes a characterization of the achieved signal enhancement.

The fifth chapter takes a closer look at the general properties of the investigated quantum dots. It contains standard measurements that lay the foundation for further experiments and their correct interpretation.

This is followed by a thorough study of the biexciton state. Several methods for it's preparation are investigated, which provides a the starting point for the experiments on nonlinear down-conversion. In this scope several phenomena that appear during these measurements, such as saturation, dressed states and an emission from the positive trion, are studied.

These main results of this thesis are presented in the chapter entitled "Nonlinear down-conversion in a single quantum dot". This includes first a demonstration of the process by identification of the corresponding emission before a detailed study of several aspects is conducted. A point of particular importance is the polarization control of the photons emitted by this process. Finally, experiments are presented where both the biexciton population and the virtual level for the down-conversion are created by the same laser field.

The thesis is concluded with a summary of the findings presented in this work and their meaning for further research.

2 Fundamentals

This chapter aims at providing a foundation for understanding and interpreting the experimental and theoretical investigations presented in this work. Generally, this is done in a brief fashion, summarizing the key elements that are necessary to gain an overview of each subject. More in-depth information can be found in the referenced literature.

The main subject of this work are epitaxialy grown semiconductor quantum dots. Therefore, the basic properties of these nanostructures are discussed in conjunction with a few more specialized but relevant aspects. This is followed by the more general topics of single photon sources and polarized light which are important in the scope of this work.

2.1 Quantum dots - A general introduction

Quantum dots (QD) are a form of low dimensional semiconductor structure. The simplest form of these is the quantum well[41]. Here a thin layer of a semiconductor material with a smaller bandgap is embedded in a semiconductor with a larger band gap. Typically such structures are grown by molecular beam epitaxy (MBE) or metalorganic chemical vapor deposition (MOCVD) which provide the necessary layer quality. In case of a type I heterojunction, a confinement potential for both electrons and holes is formed in growth direction. If the thickness of the confinement region is in the range of the de Broglie wavelength of the confined carriers (a few nm), discrete energy levels are formed. In a quantum well, this confinement and the resulting discretization only occur in growth direction while the carriers can freely move within the layer. As a result this structure is called two-dimensional (2D) and the density of states takes a step-like shape. Restricting the carrier movement in an additional dimension results in one-dimensional (1D) quantum wires[16]. The final iteration is the quantum dot (QD) with confinement in all three spatial dimensions resulting in complete discretization of the density of states. These discrete states allow for spectrally sharp optical transitions in the quantum dot, a property usually characteristic for atoms. For this reason quantum dots are often referred to as "artificial atoms"[65].

2.1.1 Epitaxial growth of quantum dots

Quantum dots can be divided into several types. Colloidal quantum dots for example are obtained by chemical synthesis from a solution. These quantum dots can be produced in large batches making them useful for many applications[25, 71, 63]. Epitaxial quantum dots on the other hand are grown on a semiconductor substrate making it possible to integrate them into electronic or photonic structures[116, 59, 14, 132].

Within this work, only epitaxial quantum dots grown by the Stranski-Krastanov method were used. A detailed discussion of this method can be found for example in [17, 104,

115].

Here, the semiconductor material for the quantum dots is deposited on the substrate with monolayer precision by MBE or MOCVD. For this growth mode the lattice constant of the deposited material needs to be larger than the one of the substrate material. The first monolayer(s) form a strained wettinglayer on the substrate. When the critical thickness of up to several monolayers is reached, the accumulated strain causes the wettinglayer to crack and form small "islands" of several 10 nm in size. These quantum dots are then overgrown by the substrate material.

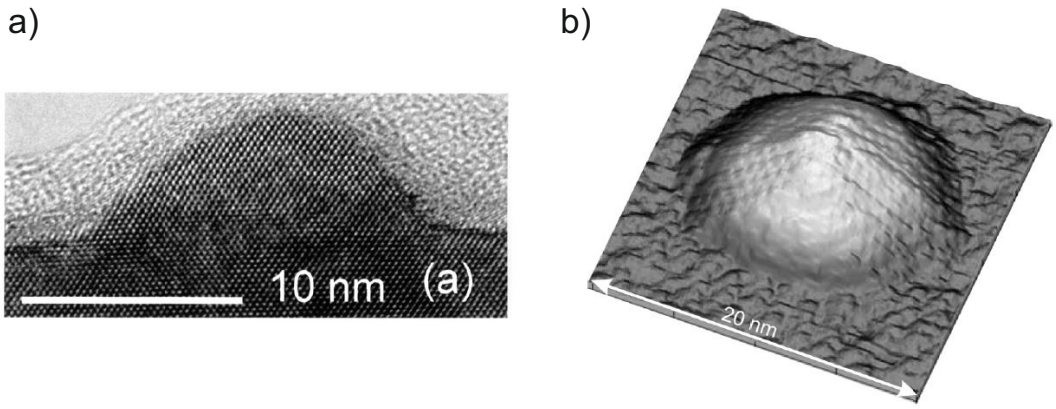

Figure 2.1: Microscopic images of quantum dots a) Image of a single QD taken with a transmission electron microscope [42]. b) Top view of a QD without capping taken with a scanning tunneling microscope [32].

This process is of statistical nature, leading to an ensemble of QDs that is heterogeneously broadened, due to variations in size, shape and composition. The area density of QDs is highly sensitive to the amount of deposited material. To fabricate samples with a low density of QDs (typically 1 QD/μm^2), often a gradient approach is applied. In an MBE, the sources for the deposited materials are usually not placed exactly perpendicular to the wafer surface, but at an angle, resulting in inhomogeneous deposition across the wafer. During the growth of homogeneous layers the wafer is rotated to compensate for this. For the growth of the quantum dots this rotations is halted. Assuming suitable growth parameters, this leads to no QDs at one side of the wafer and a high density of QDs at the other side. In between, there exists a region with the desired density that can be cleaved out and used for further experiments on single quantum dots.

Aside from the quantum dot density, the emission wavelength is an important parameter. For this work InGaAs quantum dots emitting in the range of $900 - 950$ nm were used. Here, the emission energy can be controlled by adjusting the ratio of Indium and Gallium. Another method that can be applied to obtain the same effect is the In-flush technique[38]. For other wavelength ranges different materials and/or growth methods can be used (eg. GaAs/AlAs droplet QDs for emission at $\sim$ 790 nm[31], InAs QDs on metamorphic buffer layers for emission at $\sim$ 1550 nm [102]).

2.2 Spectroscopic properties of quantum dots

This section deals with the states and optical transitions that occur in single quantum dots. The starting point is a simple model for the energy levels of single charge carriers in the confinement potential of the quantum dot. This is followed by a discussion of several multi particle configurations, the so called excitons.

2.2.1 Single particle states

Giving a precise quantum mechanical description of a quantum dot is a challenging task since the exact shape and composition of an individual quantum dot are generally not easily accessible and subject to statistical variations. In spite of this, a rather simple model can be employed to get a good qualitative system description[58].

In growth direction only the lowest level shall be considered. Since the quantum dots are rather flat structures, the energy gaps between two levels are larger in this direction than in the xy-plane. The confinement in this plane shall be described as a harmonic potential for both electrons and holes. The resulting energy levels are

$$E_{n,m} = \hbar\omega_0(n + m + 1) \tag{2.1}$$

In analogy to atomic physics, the main quantum number $N = n + m$ and the azimuthal quantum number $l = n - m$ can be defined. The azimuthal quantum number characterizes the states as s-, p-, d-,... type. For an optical transition $\Delta l = \pm 1$ must be fulfilled. Due to the p- and s-nature of the valence and the conduction band, this criteria is met for interband transitions between the energetically lowest states of electrons and holes.

Furthermore the spin configuration of the involved particles must be taken into account. Here, only the lowest level ($N = 0$, $l = 0$) will be considered, as it is the decisive for the processes investigated in this work. The electron spin of $s_e = 1/2$ results in two configurations for the electrons $j_{z,e} = l_{z,e} \pm s_{z,e} = \pm 1/2$. In case of the holes a distinction between heavy holes $j_{z,hh} = \pm 3/2$ and light holes $j_{z,lh} = \pm 1/2$ is necessary. Here, especially the heavy holes are important as they have the lower quantization energy. Based on this four configurations of $j_{z,hh} = \pm 3/2$ and $j_{z,e} = \pm 1/2$ are possible of which only the two with $j_{z,total} = j_{z,hh} + j_{z,e} = \pm 1$ are optically accessible while the other two with $j_{z,total} = \pm 2$ are dark (see figure 2.2).

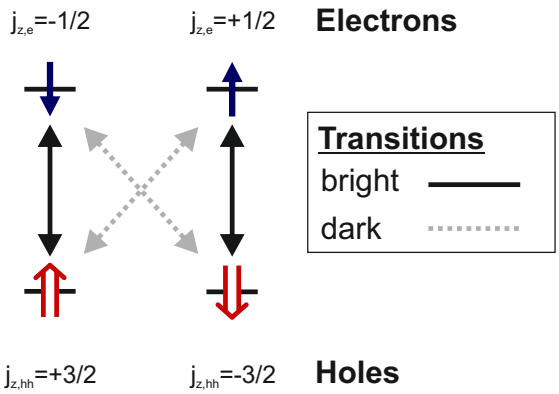

Figure 2.2: Optical transitions between electrons and holes Optical transitions are allowed if $j_{z,total} = j_{z,hh} + j_{z,e} = \pm 1$ (solid lines). The transitions with $j_{z,total} = \pm 2$ (dashed lines) are not allowed and hence called "dark".

2.2.2 The Exciton state

The previous dicussion of the energy levels in a QD does not take into account the coulomb interaction between multiple charged particles in the QD. This interaction gives rise to a renormalization of the energy levels effectively introducing a binding energy between the carriers. In principle, this binding energy can be either positive or negative depending on the charge configuration and the confinement potential of the individual QD. In analogy to bound electron-hole pairs in bulk semiconductors, the corresponding charge configurations in a QD are also called excitons.

The most basic configuration is the (neutral) exciton state consisting of one electron and one hole. Usually, it is denoted as $|X\rangle$. Due to the Coulomb interaction, its optical transition energy is different from multi-exciton states. It can therefore be selectively excited by a resonant laser field, making it a good model system to study and exploit the dynamics of a two-level system (TLS) such as coherent spectroscopy [119, 137, 120] or single-photon emission[83, 54].

By taking a closer look at this state one can identify two optically active spin configurations with anti-parallel spins of h^+ and e^- ($|\Uparrow\downarrow\rangle$ and $|\Downarrow\uparrow\rangle$), also denoted as $|\pm 1\rangle$, respectively. In a quantum dot with a perfectly rotational symmetric confinement potential these two states are energetically degenerate and couple to circularly polarized light (see figure 2.3a). In a real quantum dot however, the confinement potential is usually not perfectly rotational symmetric, due to strain or an elliptical shape of the QDs. This causes the emergence of two new eigenstates, which are a superposition of $|+1\rangle$ and $|-1\rangle$. These couple to X- and Y-oriented polarized light and are therefore usually denoted $|X\rangle$ and $|Y\rangle$.

$$|X\rangle = \frac{1}{\sqrt{2}}\left(|+1\rangle + |-1\rangle\right) \qquad |Y\rangle = \frac{1}{\sqrt{2}}\left(|+1\rangle - |-1\rangle\right) \tag{2.2}$$

These two states are not energetically degenerate, but show the so-called finestructure splitting (FSS) or anisotropic exchange splitting. The InGaAs QDs investigated in this work usually show a splitting of $10 - 20$ μeV in energy. By properly selecting the

polarization of the optical field, either one of these two states can serve as a two level system[77].

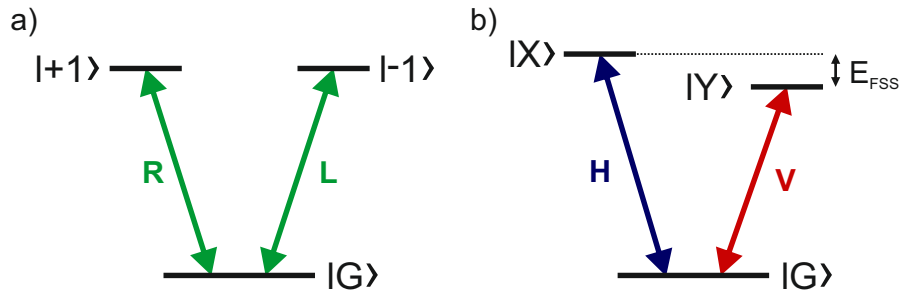

Figure 2.3: Fine-structure of the exciton state a) Level scheme for the exciton state in rotational symmetric confinement potential. The two states $|+1\rangle$ and $|-1\rangle$ are degenerate and couple to the ground state $|G\rangle$ via circularly polarized light (R and L) b) Level scheme for a non rotational symmetric confinement potential. The states $|X\rangle$ and $|Y\rangle$ show a fine-structure splitting of E_{FSS} and couple to linearly polarized light

2.2.3 The Biexciton State

The biexciton state $|B\rangle$ consists of two electron-hole pairs in the s-shell of a QD. Due to Pauli-blocking the two electrons and the two holes must have opposite spins. The $|B\rangle$-state therefore has a total angular momentum of $J_B = 0$. Coulomb interaction between the involved carriers causes the total energy of the biexciton to deviate from two times the exciton energy E_X by the biexciton binding energy ΔE_B.

$$E_B = 2E_X - \Delta E_B \tag{2.3}$$

The binding energy is dependent on the microscopic structure of the QD. Both binding and anti-binding biexcitons have been reported in literature[109]. The InGaAs-QDs used in this work have a typical binding energy of $2 - 3$ meV.

The biexciton decays optically via the biexciton cascade, sending out two photons (see figure 2.4). The first photon recombines with an emission energy of $E_{XX} = E_X - \Delta E_B$, referred to as biexcion line or XX,followed by a decay of the remaining exciton with a transition energy of E_X, referred to as X. Please note that in this work, the biexciton state is labeled B, while the biexciton line is labeled XX, in order to achieve a clear distinction between the two.

This feature can be exploited to generate high quality single photons. By tuning a laser to $E_B/2$, the biexciton can be excited via a two-photon process. Since both $|G\rangle$ and $|B\rangle$ have $j_z = 0$ the laser field must be linearly polarized. The resulting cascade is then detuned from the laser, which facilitates straylight-suppression and decreases the propability for a reexcitation[111]. These two effects strongly improve the achievable g^2-values in comparison to the X-transiton.

In an ideal QD without FSS the exciton state is two-fold degenerate, consisting of the two states $|R\rangle$ and $|L\rangle$ associated with an angular momentum of +1 and -1. The biexciton, being a $j_z = 0$ state, randomly decays into one of these two states, emitting either

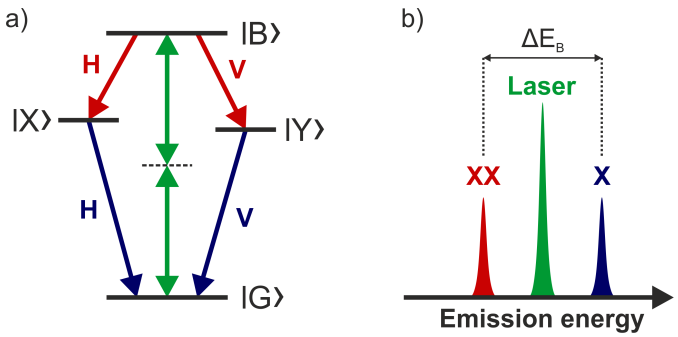

Figure 2.4: Biexciton cascade a) The biexciton state can be excited via a two-photon by tuning a laser (green) to $E_B/2$. The decay from the biexciton state $|B\rangle$ to the exciton state ($|X\rangle$ or $|Y\rangle$) and then the ground state $|G\rangle$ causes a cascaded emission of two photons (red and blue) of equal linear polarization. b) The resulting emission spectrum shows the X- and XX-line separated by the biexciton binding energy ΔE_B. The laser is located in the center of both emissions.

right or left-hand circularly polarized light of equal energy. Since the ground state also has an angular momentum of $J_{|G\rangle} = 0$, the second photon therefore must have the opposite circular polarization. Real QDs however usually show a FSS, where the two exciton states are transformed into $|X\rangle$ and $|Y\rangle$, which are both a superposition of the states $|R\rangle$ and $|L\rangle$ (see chapter 2.2.2). In this case the XX-emission consists of two orthogonally polarized lines, which are spectrally separated by the FSS. Correspondingly, the second photon emitted from either $|X\rangle$ or $|Y\rangle$ has the same linear polarization as the first one (see figure 2.4). In both cases, the biexciton cascade can be used as a source of entangled photon pairs[118, 93].

2.2.4 The Trion state

The two excitonic states discussed so far ($|X\rangle$ and $|B\rangle$), both consist of an equal number of electrons and holes, making them electrically neutral. If the quantum dot contains an unequal number of electrons and holes, this changes and these states are then called charged excitons. Naturally, they can be divided into positively and negatively charged excitons depending on which carrier type is more numerous. Though they differ in certain aspects, they do also show similar properties in many regards. For this reason, they shall be discussed together in the following.

The simplest of these states are the single charged excitons $|X^+\rangle$ and $|X^-\rangle$ with one excess hole or electron respectively (see figure 2.5).
In both cases, two different spin configurations can be identified, which are determined by the single carrier. The resulting optical emission does not show a fine-structure splitting between both configurations, but the two transitions have opposite circular polarization for both $|X^+\rangle$ and $|X^-\rangle$. The different charge configuration does however affect the binding energy of the two states, causing them to emit at different energies. Their spectral position relative to the X- or XX-line depends on the type of QD, growth parameters and the statistical deviations between individual dots. In the InGaAs QDs investigated

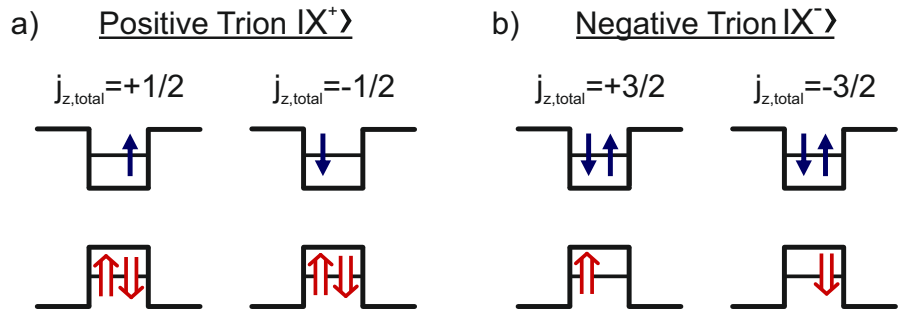

Figure 2.5: Spin configuration of charged excitons a) Positive trion b) Negative trion | The paired carrier type is restricted to anti-parallel spin constellation while the single carrier type is not restricted. It's spin determines the polarization of the resulting optical transition.

here, the X^--line usually appears about 2-3 meV below the XX-line[77, 130] The X^+-line shows a stronger variation between individual dots but usually appears within ± 2 meV relative to the X-line.

Charged excitons can be generated by different mechanisms. During the growth a δ-doping layer can be incorporated into the sample structure very close to the QD. The carriers provided by the doping atoms then tunnel into the QD, creating a charged ground state ($|h^+\rangle$ or $|e^-\rangle$)[35]. This might also happen in an uncontrolled manner through impurities in the host material.

A similar process can occur, when the QDs are embedded in a diode structure. If a suitable bias voltage is supplied to the diode, the first electron level in the QD can be below the quasi Fermi-level of the electrons in the n-doped region. Hence electrons can tunnel into the QD and charge it. Due to Coulomb interaction, the energy level for the second electron is higher up than for the first one, allowing selective charging, given a suitable voltage and a rather thin tunneling barrier to the electron reservoir. The same mechanism occurs for holes from the p-doped region if their quasi Fermi-level is below the hole energy levels of the QD (see figure 2.6). Both types of carriers are strongly influenced by the positioning of the QD layer within the diode structure. If the QDs are close to the n-doped region the tunneling of electrons is dominant and vice versa. This behavior can be used to distinguish the emission lines of charged and neutral excitons in a voltage dependent photoluminescence experiment (see chapter 5.1).

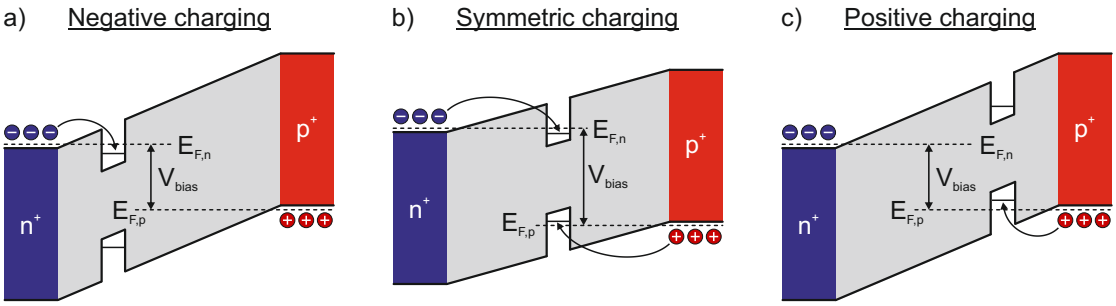

Figure 2.6: Charging of a quantum dot a) Negative charging is dominant, if the QDs are placed closer to the n-doped region. b) If the QDs are placed in the center of the pin-structure, charging with both types of carriers occurs with similar probability. c) Placing the QDs close to the p-doped region favors positive charging.

Furthermore, under strong above-band excitation the QD is statistically populated by different charge configurations including all kinds of charged excitons. This includes multiply charged excitons like $|X^{2+}\rangle$ or $|X^{2-}\rangle$ and charged biexcitons $|B^{+}\rangle$. A more detailed discussion of these states can be found for example in[50].

2.3 Rabi oscillations

When a QD is resonantly excited by short laser pulses, it can retain it's coherence during this process, enabling the observation of coherent features like Rabi oscillations[119, 137] or Ramsey interference[120]. In the scope of this work, Rabi oscillations play a role in the deterministic state preparation[53], which is why this feature shall be discussed in the following. The mathematical description presented here, is based on [130], which also provides a more extensive summary of the subject.

The easiest system to describe coherent processes in, is an isolated two-level system (TLS) consisting of the ground state $|0\rangle$ and the excited state $|1\rangle$. In a QD, such a system could be provided for example by the neutral exciton. In order to take the coherence of the system into account, the TLS is described by a density matrix.

$$\hat{\rho}_{\mathrm{TLS}} = \begin{pmatrix} \rho_{00} & \rho_{01} \\ \rho_{10} & \rho_{11} \end{pmatrix} \tag{2.4}$$

Here, ρ_{00} and ρ_{11} describe the population in the two states, while ρ_{01} and ρ_{11} describe the coherence of the system. The time evolution of this density matrix can be described by a set of differential equations, the optical Bloch equations. Here, it is beneficial to work in the rotating frame of the driving laser field to cancel out fast oscillations ($\rho_{01}(t) = e^{-i\omega_L t}\tilde{\rho}_{01}(t)$).

$$\frac{d}{dt}\rho_{00} = i\frac{\Omega_0}{2}(\tilde{\rho}_{10} - \tilde{\rho}_{01}) + \gamma_1\rho_{11} \tag{2.5}$$

$$\frac{d}{dt}\rho_{11} = i\frac{\Omega_0}{2}(\tilde{\rho}_{01} - \tilde{\rho}_{10}) - \gamma_1\rho_{11} \tag{2.6}$$

$$\frac{d}{dt}\tilde{\rho}_{01} = i\frac{\Omega_0}{2}(\rho_{11} - \rho_{00}) - (\gamma_2 + i\delta)\tilde{\rho}_{01} \tag{2.7}$$

$$\frac{d}{dt}\tilde{\rho}_{10} = i\frac{\Omega_0}{2}(\rho_{00} - \rho 11) - (\gamma_2 + i\delta)\tilde{\rho}_{10} \tag{2.8}$$

In these equations the interaction with the optical field is described by the Rabi frequency

$$\Omega_0(t) = \frac{E_0(t)\mu_{01}}{\hbar} \tag{2.9}$$

with the amplitude of the electrical field E_0 and the dipole moment of the transition under study μ_{01}. The decay of the population is expressed by the rate γ_1 and the decay of the coherence by γ_2. These two coefficients are coupled by

$$\gamma_2 = \frac{\gamma_1}{2} + \gamma_2^* \tag{2.10}$$

The pure dephasing processes described by γ_2^* are weak for a QD cooled to 4.2 K and can therefore be neglected here.

This set of equations can be solved numerically to gain insight into the behavior of the system. For continuous driving the population in the system oscillates between the two states with the Rabi frequency Ω_0 (see figure 2.7). The dephasing rate γ_2 causes the amplitude of this oscillation to decay exponentially until a stable population of $\rho_{11} = \rho_{00} = 0.5$ is reached. This corresponds to the equilibrium population in the incoherent limit.

In the context of Rabi oscillations usually the pulse area A_{pulse} is used to characterize the optical excitation.

$$A_{\text{pulse}} = \int \Omega_0(t)\ dt \tag{2.11}$$

The Rabi oscillations show extremata for pulse areas that equal multiples of π. Maxima occur for uneven multiples (1π, 3π, 5π, ...), while minima occur for even multiples (2π, 4π, 6π, ...)(see figure 2.7).

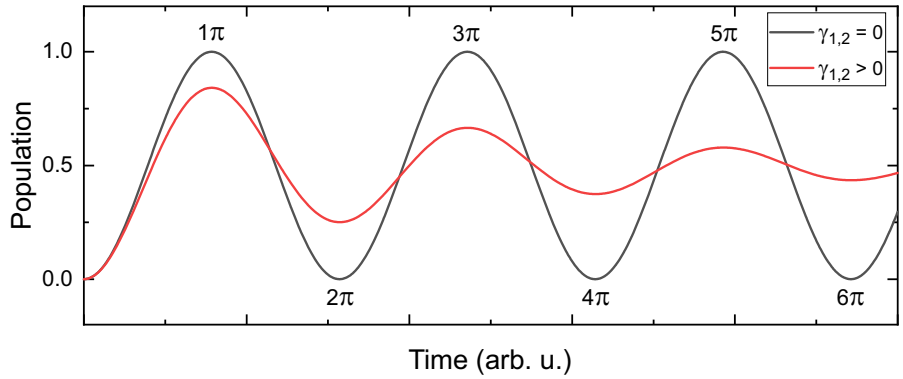

Figure 2.7: Rabi Oscillations Time-dependent population of the excited state under resonant driving. When neglecting dephasing terms (black) the population oscillates between the two states with the Rabi frequency Ω_0. Including the dephasing terms (red) causes a decay of the amplitude of this oscillation.

During an experiment the pulse area of the excitation needs to be varied to observe Rabi oscillations. Since it is experimentally challenging to realize this by varying the pulse duration, usually the laser power is varied instead. This changes the Rabi frequency Ω_0 during the pulse, which according to equation 2.11 also changes the pulse area and is much easier to realize experimentally. Figure 2.8 shows two examples for the time evolution resulting from a pulse with a pulse area of 5π in constructive interference and a 6π pulse resulting in destructive interference. Since Gaussian pulses where used in this calculation, one can observe a time dependence of Ω_0 during the pulse. The experimentally accessible parameter by observing the resonance fluorescence or photocurrent signal is proportional to the time integral over the population in the excited state

$$I_{\text{exp}} \sim \gamma_1 \int \rho_{11}(t) dt \tag{2.12}$$

A series of measurements with different laser power also shows an oscillatory behavior (see figure 2.8c). In such an experiment the pulse area is proportional to $A_{\text{pulse}} \sim \sqrt{P}$. In order to distinguish this kind of measurement from the time dependent behavior like in figure 2.7, these oscillations are sometimes called Rabi rotations [105, 49]. This is especially relevant since the mechanism for the decay of the amplitude shows a small but decisive difference. Since the pulse duration is constant, the amount of dephasing accumulated during the pulse should also be constant when assuming a constant γ_2. This dephasing however, is caused by coupling to acoustic phonons, which is dependent on the Rabi frequency, leading to faster dephasing for higher pulse area [67, 105]. Theoretical work suggests a decreasing dephasing rate for very high Rabi frequencies[127, 128, 107].

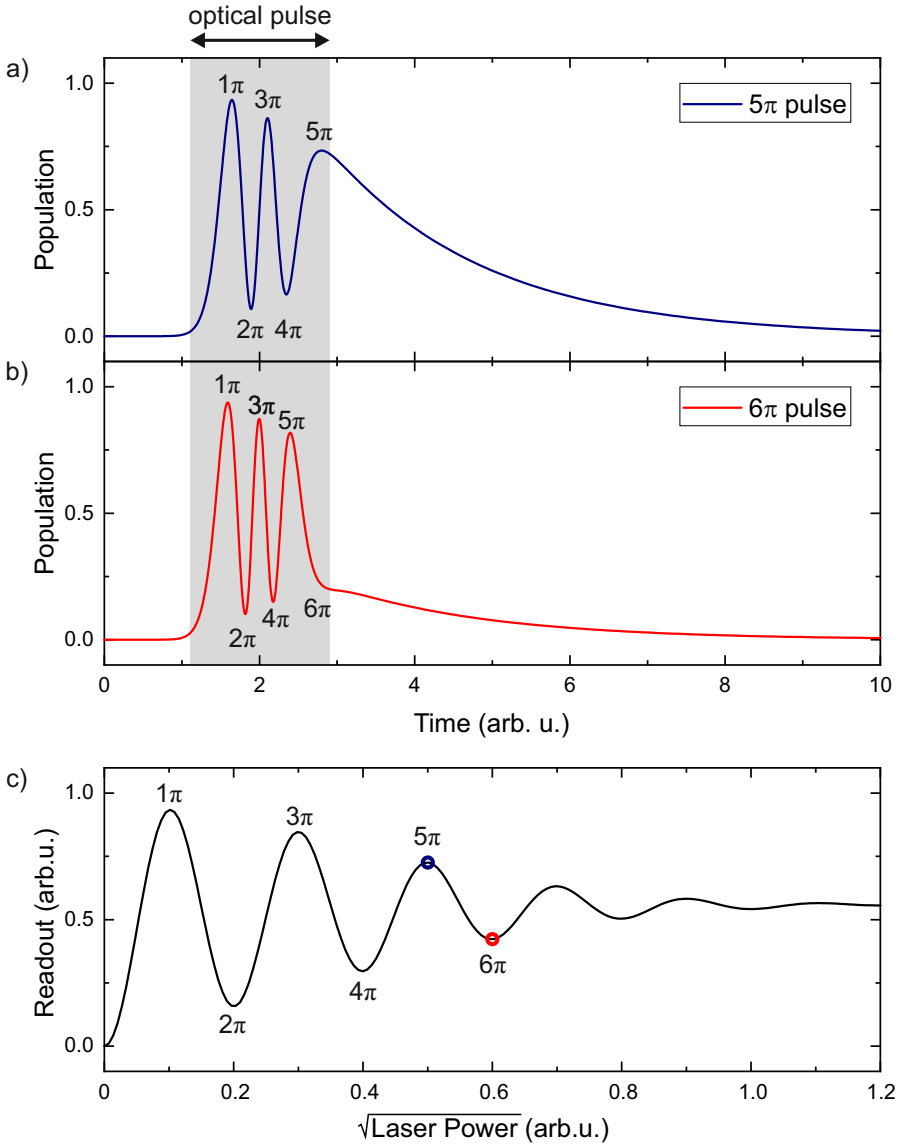

Figure 2.8: Rabi Rotations Time evolution of the population in the excited state during excitation with a 5π (a) and a 6π pulse (b). During the pulse the population oscillates. The population present at the end of the pulse then decays exponentially with the rate γ_1. c) Varying the laser power while reading out the population via the decay rate reveals the Rabi rotations, which are proportional to $\sqrt{P}$. Diagrams a) and b) each represent one data point of such a measurement (blue and red circles).

2.4 Dressed states

When an optical transition in a QD is (near-)resonantly driven by a laser field, a splitting of the emission into several lines can be observed [125, 92, 62]. This effect, known in literature as Autler-Townes effect or AC-Stark effect, was first described by S.H. Autler and C.H. Townes in 1955, for RF transitions in molecules [7].

This effect can be described quantum mechanically in a dressed state picture. In the following, this concept shall be briefly summarized based on the discussion in [82].

The atom-field interaction is treated completely quantum mechanically, which is in contrast to semi-classical models that describe the light field as a classical wave (see chapter 2.3). The simplest model system is a two-level system (with the ground state $|0\rangle$ and the excited state $|1\rangle$) coupled to a single quantized mode field $|n\rangle$. Such a system can be described by the following Hamiltonian.

$$H = H_{\mathrm{TLS}} + H_{\mathrm{Light}} + H_{\mathrm{Interaction}} \tag{2.13}$$

$$= \frac{1}{2}\hbar\omega_{\mathrm{TLS}}\sigma_z + \hbar\omega_L a^+ a + \hbar(a + a^+)(g\sigma_+ + g^*\sigma_-) \tag{2.14}$$

Here, ω_{TLS} is the resonance frequency of the TLS and ω_L the frequency of the light field, while a^+ and a are the creation and annihilation operators for the light field

$$a^+ |n\rangle = \sqrt{n+1}\,|n+1\rangle \tag{2.15}$$

$$a\,|n\rangle = \sqrt{n}\,|n-1\rangle \tag{2.16}$$

Accordingly, $a\sigma_+$ describes the excitation from the lower into the upper state under absorption of a photon from the light field, while $a^+\sigma_-$ describes the deexcitation from the upper to the lower state under emission of a photon. Expressions containing $a\sigma_-$ and $a^+\sigma_+$ are dropped when performing the rotating wave approximation. This simplifies the Hamiltonian to

$$H = \frac{1}{2}\hbar\omega_{\mathrm{TLS}}\sigma_z + \hbar\omega_L a^+ a + \hbar g(a\sigma_+ a^+\sigma_-) \tag{2.17}$$

When neglecting the interaction term the system is described by a superposition of the states $|0,n\rangle$ and $|1,n\rangle$. Adding the interaction term then couples the states $|1,n\rangle$, where the TLS is in the excited state, and $|0,n+1\rangle$, where the TLS is in the ground state but the light field contains an additional photon. Considering only a given field characterized by the photon number n, the system can be described by the matrix

$$H_n = \hbar(n+\frac{1}{2})\omega_L \begin{bmatrix} 1 & 0 \\ 0 & 1 \end{bmatrix} + \frac{\hbar}{2}\begin{bmatrix} \delta & 2g\sqrt{n+1} \\ 2g\sqrt{n+1} & -\delta \end{bmatrix} \tag{2.18}$$

where $\delta = \omega_{\mathrm{TLS}} - \omega_L$. One can furthermore introduce a generalized Rabi frequency

$$\Omega_n = \sqrt{\delta^2 + \Omega_{0,n}^2} = \sqrt{\delta^2 + 4g^2(n+1)^2} \tag{2.19}$$

With these expressions the following eigenvalues can be retrieved from the Hamiltonian

$$E_{a,n} = \hbar\omega_L(n+\frac{1}{2}) - \frac{1}{2}\hbar\Omega_n \tag{2.20}$$

$$E_{b,n} = \hbar\omega_L(n+\frac{1}{2}) + \frac{1}{2}\hbar\Omega_n \tag{2.21}$$

The corresponding eigenvectors read

$$|a,n\rangle = \cos\theta_n\,|1,n\rangle - \sin\theta_n\,|0,n+1\rangle \tag{2.22}$$

$$|b,n\rangle = \sin\theta_n\,|1,n\rangle + \cos\theta_n\,|0,n+1\rangle \tag{2.23}$$

with

$$\cos\theta_n = \frac{\Omega_n + \delta}{\sqrt{(\Omega_n - \delta)^2 + 4g^2(n+1)}} \tag{2.24}$$

$$\sin\theta_n = \frac{2g\sqrt{n+1}}{\sqrt{(\Omega_n - \delta)^2 + 4g^2(n+1)^2}} \tag{2.25}$$

In resonance these reduce to

$$|a,n\rangle = \frac{1}{\sqrt{2}}(|1,n\rangle - |0,n+1\rangle) \tag{2.26}$$

$$|b,n\rangle = \frac{1}{\sqrt{2}}(|1,n\rangle + |0,n+1\rangle) \tag{2.27}$$

These represent two different superpositons of the excited and the ground state and are referred to as dressed states.

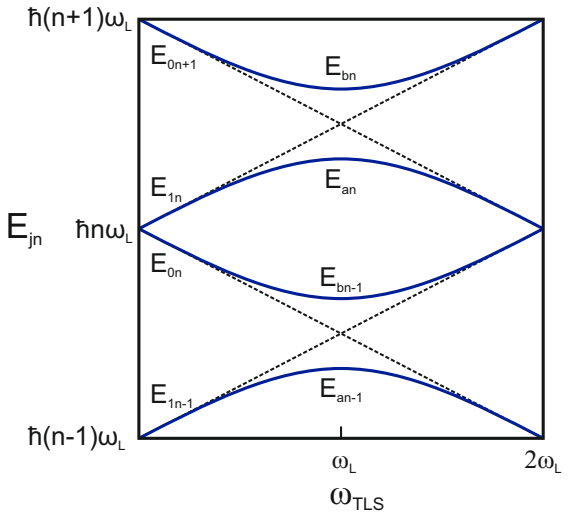

Figure 2.9: Eigenvalues of a dressed TLS In the resonant case the states $|j, n-1\rangle$ and $|j-1, n\rangle$ show an anti-crossing, with the minimal separation beeing the Rabi energy $\hbar\Omega_{0,n}$. (Figure adapted from [82])

Figure 2.9 shows a plot of the eigenvalues (solid lines) compared to the case where the interaction between TLS and light field is neglected (dashed lines). While in the unperturbed case the two states $|1,n\rangle$ and $|0,n+1\rangle$ cross each other for $\omega_L = \omega_{\mathrm{TLS}}$ the dressed states $|a,n\rangle$ and $|b,n\rangle$ repel each other. This phenomena is called anti-crossing. The minimum separation between the two is given by the Rabi energy $\hbar\Omega_{0,n} = 2g\hbar(n+1)$. In this case a total of four transitions of equal intensity can occur between two rungs (e.g. n and $n-1$). The transitions $E_{a,n} \leftrightarrow E_{a,n-1}$ and $E_{b,n} \leftrightarrow E_{b,n-1}$ are degenerate with a transition energy of $\hbar\omega_L$. Since it contains two transitions it has twice the intensity of the other two lines which are $E_{a,n} \leftrightarrow E_{b,n-1}$ with a transition energy of $\hbar\omega_L - \hbar\Omega_{0,n}$ and $E_{b,n} \leftrightarrow E_{a,n-1}$ at $\hbar\omega_L + \hbar\Omega_{0,n}$. In combination these lines are known as the Mollow triplet[125, 97] (see figure 2.10b).

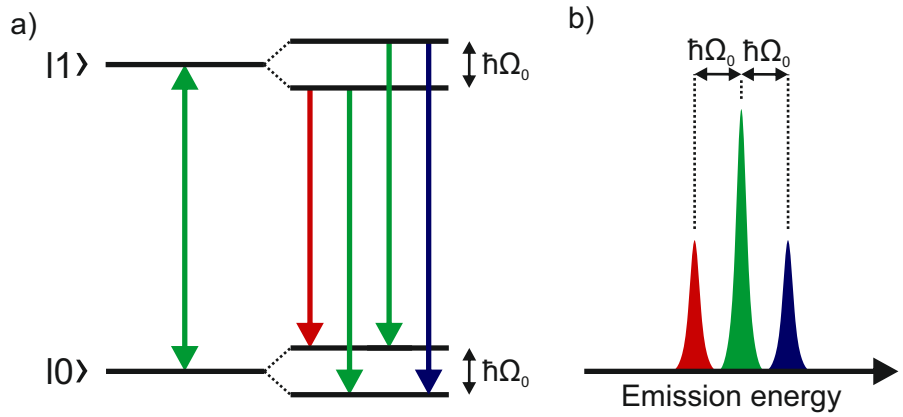

Figure 2.10: Mollow triplet a) Resonant driving of a TLS induces a splitting of both energy levels by the Rabi energy $\hbar\Omega_0$, resulting in four possible transitions. b) The resulting emission spectrum shows three lines, called the Mollow triplet, since two transitions (green) are energetically degenerate.

This behavior is often explained in a more intuitive picture[92, 45]. When in resonance, the driving laser introduces a splitting of the two states $|0\rangle$ and $|1\rangle$ by the Rabi energy $\hbar\Omega_0$ (see figure 2.10a). This configuration gives rise to the same four transitions as discussed above resulting in the appearance of the Mollow triplet.

2.5 Quantum confined Stark effect

When an electric field is applied to a QD, the optical transitions experience an energy shift. This effect was first observed in quantum well structures[81] and called "Quantum Confined Stark Effect" (QCSE)[85]. Later this term was extended to quantum dots. Today, this effect is usually induced by embedding the QD in a diode structure. By controlling the bias voltage, the internal electric field of the diode can be manipulated, which in turn offers a tuning knob for the QDs. This effect however is not restricted to the growth direction but does also work in lateral direction[114] even though this geometry is used less often.

The energy shift experienced by an excitonic state can be described by a parabolic function[79].

$$E(F) = E(F=0) + \mu_{\mathrm{QD}} \cdot F + \alpha_{\mathrm{QCSE}} \cdot F^2 \tag{2.28}$$

Here, the electric field is labeled F. The energy shift relative tho the undisturbed transition energy $E(F=0)$ consists of two contributions. The linear term is determined by the static dipole moment of the QD μ_{QD}. It appears since the wave functions of e^- and h^+ are usually sightly shifted with respect to each other. Usually the hole is located closer to the tip of the dot while the electron is located closer to the base[42, 10]. The quadratic term is proportional to the induced dipole moment α_{QCSE} caused by the electric field. In general these parameters are different for the various excitonic states. Aside from the energy shift, the electric field also causes a shift of the wave functions of electrons and holes in opposite directions decreasing the dipole matrix element of optical transitions[101].

The QCSE is often used to tune a QD during spectroscopic experiments[98, 72], which also works on ultra-fast time scales[132, 91, 131]. The achievable tuning is limited by tunneling[43] and charging effects[35, 33], which also are dependent on the applied electric field ($\sim 1-2$ meV). This range can be extended by introducing additional tunneling barriers around the QD[14].

2.6 Single photon emission

Single photons are an important resource for quantum technologies, especially with regard to applications in communications[47]. Obtaining high quality single photons with a good repetition rate is however not a trivial task. Alongside other sytems (e.g. spontaneous parametric down-conversion[90, 60], trapped ions[57, 51], 2D materials[26, 36], ...) quantum dots are of great interest in this respect[113, 3]. For this reason a few fundamental aspects of single photon emission, that are relevant in the scope of this work, shall be discussed here. The following statements are mainly based on [40], which can be consulted for further details.

An important quantity for demonstrating and characterizing single photon emission is the second order correlation function

$$g^{(2)}(\tau) = \frac{\langle I(t)I(t+\tau)\rangle}{\langle I(t)\rangle \langle I(t+\tau)\rangle} \tag{2.29}$$

Single photons show anti-bunching and the function takes a value $g^{(2)}(\tau = 0) < 1$. Perfect single photons will result in $g^{(2)}(\tau = 0) = 0$, while a value of < 0.5 can still be considered as quantum light. A laser field (coherent state) features a random photon distribution, resulting in $g^{(2)}(\tau = 0) = 1$. Incoherent light (e.g. thermal emission) shows photon bunching leading to $g^{(2)}(\tau = 0) > 1$. Figure 2.11 shows examples of $g^{(2)}$-functions for all three cases.

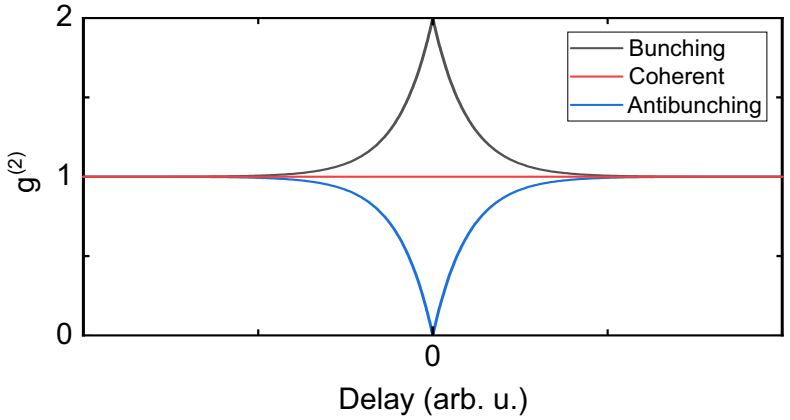

Figure 2.11: Second-order correlation function $g^{(2)}$ A classical incoherent light source with a Lorentzian line shape shows bunching around $\tau = 0$ (black curve). Coherent light (e.g. laser) features a constant $g^{(2)}$-value (red curve). Single photons show anti-bunching around $\tau = 0$ (blue curve).

Both the bunching and the anti-bunching behavior around $\tau = 0$ can be described using exponential functions.

$$g^{(2)}_{\text{bunch}}(\tau) = 1 + g^{(2)}_0 \exp\left(\frac{|\tau|}{t_{\text{bunch}}}\right) \qquad \text{Bunching (Lorentzian)} \qquad (2.30)$$

$$g^{(2)}_{\text{bunch}}(\tau) = 1 + g^{(2)}_0 \exp\left(\frac{-\tau^2}{2c^2}\right) \qquad \text{Bunching (Thermal)} \qquad (2.31)$$

$$g^{(2)}_{\text{anti}}(\tau) = 1 - g^{(2)}_0 \exp\left(\frac{-|\tau|}{t_{\text{anti}}}\right) \qquad \text{Anti-bunching} \qquad (2.32)$$

For the anti-bunching the width of the dip t_{anti} is determined by the lifetime of the optical transition . Sometimes a combination of bunching on long timescales and anti-bunching on short timescales is observed giving the $g^{(2)}$-function a "volcano-like" shape (see figure 2.12). This behavior is usually associated with blinking of the emission under study[125]. Mathematically this can be described by

$$g^{(2)}_{\text{volcano}}(\tau) = 1 - g^{(2)}_{\text{anti}} \exp\left(\frac{-|\tau|}{t_{\text{anti}}}\right) + g^{(2)}_{\text{bunch}} \exp\left(\frac{|\tau|}{t_{\text{bunch}}}\right) \qquad (2.33)$$

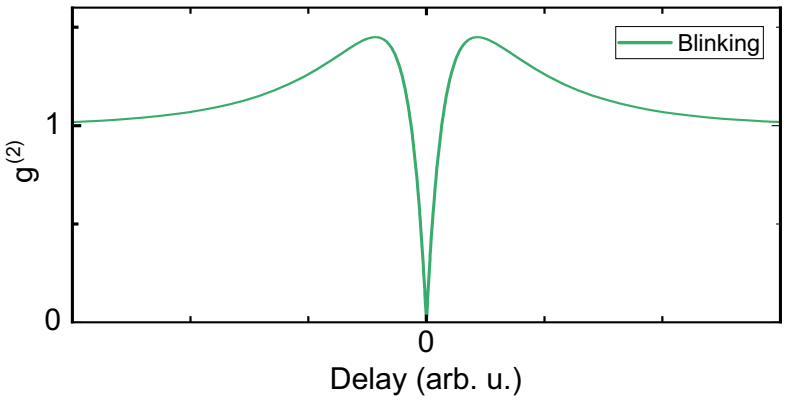

Figure 2.12: $g^{(2)}$-function of a blinking single photon source The $g^{(2)}$-function features a combination of anti-bunching on short timescales and bunching on a larger timescale, giving the function a "volcano-like" appearance.

The $g^{(2)}$-function of a light field can be experimentally determined using a Hanbury-Brown and Twiss (HBT) setup[24] (see figure 2.13). A 50:50 beamsplitter randomly sends photons onto two single photon detectors. The readout electronics measure the time difference between individual clicks of both detectors. In case of single photons emitted by a single quantum emitter the two detectors cannot click at the same time, leading to a dip at $\tau = 0$.

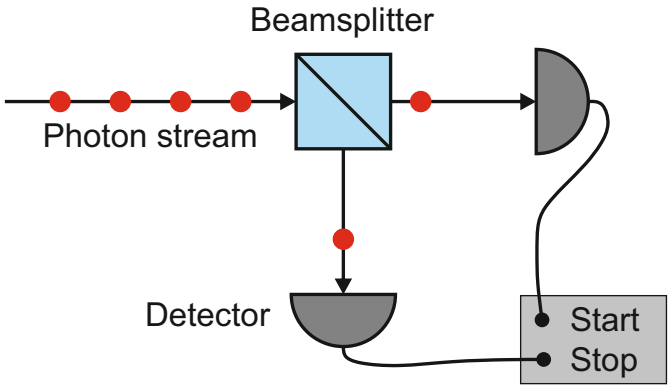

Figure 2.13: Concept of a Hanbury-Brown Twiss experiment A stream of photons is sent onto a 50:50-beamsplitter, which directs them randomly onto two single photon detectors. The readout electronics measure the time differences between the detector clicks.

The experimentally recorded histogram is always a convolution of the true $g^{(2)}$-function with the temporal response of the detection setup. It is therefore desirable to use detectors with a timing jitter well below the lifetime of the studied transition. This can be circumvented in some cases by employing a pulsed excitation scheme, resulting in an ideal histogram like it is displayed in figure 2.14.

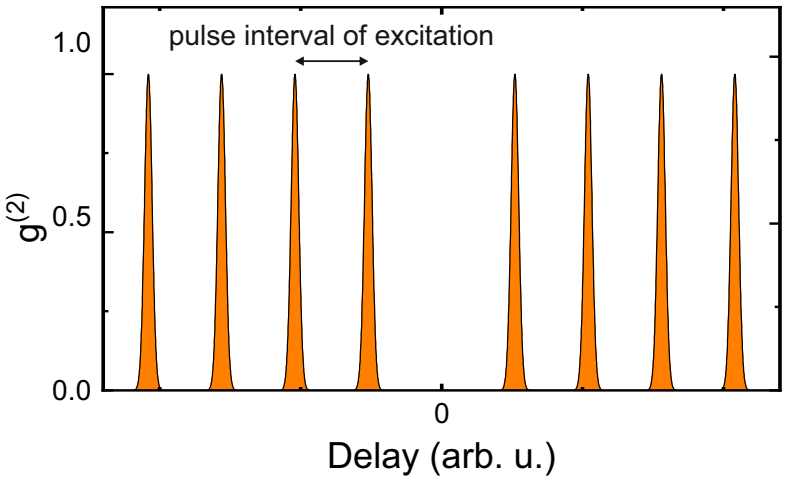

Figure 2.14: $g^{(2)}$ under pulsed excitation The pulsed excitation defines time slots where emission can occur. The resulting peaks are separated by the repetition rate of the excitation and their width is determined by a convolution between the lifetime of the signal and the timing resolution fo the detector.

2.7 Polarized light

The following chapter provides a brief overview of the mathematical description of polarized light which is based on[30].

2.7.1 The polarization ellipse

An electro-magnetic wave propagation in z-direction is composed of two transversal components.

$$E_x(z,t) = E_{0x} \cdot \cos(\tau + \delta_x) \tag{2.34}$$
$$E_y(z,t) = E_{0y} \cdot \cos(\tau + \delta_y) \tag{2.35}$$

Here $\tau = \omega t - \kappa z$ is the propagator. The polarization of this wave is defined by the amplitudes of the two components E_{0x} and E_{0y}, as well as the phase difference between the two waves $\delta = \delta_x - \delta_y$. The resulting general time trajectory takes the form of an ellipse (see Fig. 2.15 a)

$$\frac{E_x^2}{E_{0x}^2} + \frac{E_y^2}{E_{0y}^2} - 2\frac{E_x E_y}{E_{0x} E_{0y}} \cos\delta = \sin^2\delta \tag{2.36}$$

For a phase difference of $\delta = \pm n \cdot \pi$ the polarization becomes linear. The ratio between the components E_{0x} and E_{0y} then determines the direction of the polarization. Another significant case occurs for $\delta = (n + \frac{1}{2}) \cdot \pi$ where the polarization is circular. We obtain right hand circular polarization for even values of n and left hand polarization for uneven values of n.

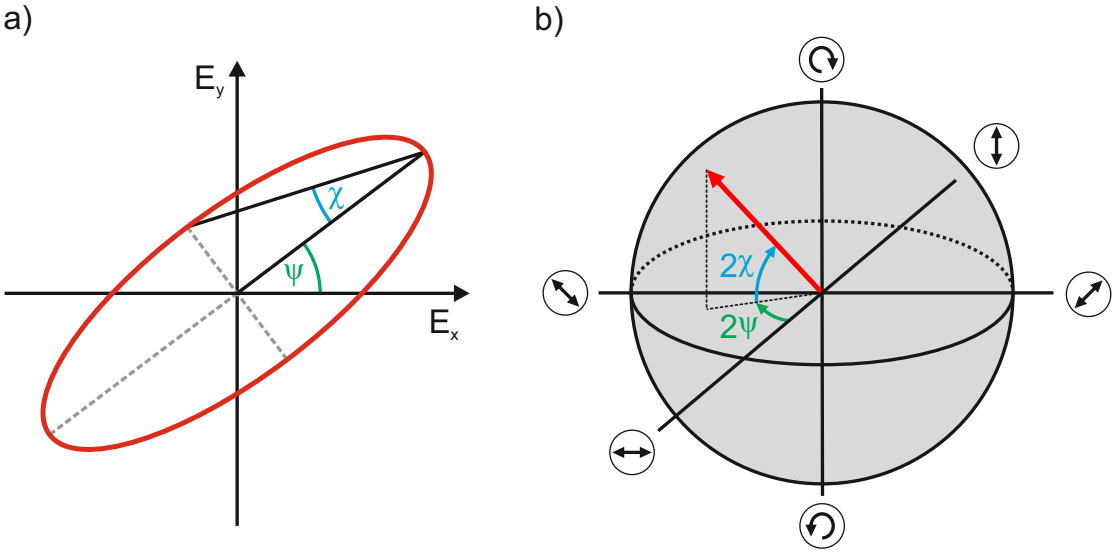

Figure 2.15: Visualization of polarization a) Polarization ellipse b) Pointcaré sphere In both cases the polarization is defined by the azimuth Ψ and the ellipticity χ.

A more intuitive way to describe the form of the polarization ellipse are the azimuth Ψ and the ellipticity χ of the ellipse (see 2.15a).

$$\Psi = \frac{1}{2}\arctan\left(\frac{2E_{0x}E_{0y}\cos\delta}{E_{0x}^2 - E_{0y}^2}\right) \qquad 0 \leq \Psi \leq \pi \tag{2.37}$$

$$\chi = \frac{1}{2}\arcsin\left(\frac{2E_{0x}E_{0y}\sin\delta}{E_{0x}^2 + E_{0y}^2}\right) \qquad -\frac{\pi}{4} \leq \chi \leq \frac{\pi}{4} \tag{2.38}$$

2.7.2 Stokes vectors and Müller matrices

The previous description is a very intuitive way to visualize a given polarization. For calculating the effect of optical elements however, it is more convenient to use the Stokes vector formalism. It allows the description of a system of optical elements with a series of matrices, the so called Müller matrices.

In this formalism a given polarization is represented by a 4-dimensional Stokes vector $\mathbf{S}$ with the elements:

$$s_0 = E_{0x}^2 + E_{0y}^2 \tag{2.39}$$

$$s_1 = E_{0x}^2 - E_{0y}^2 = s_0\cos(2\Psi)\cos(2\chi) \tag{2.40}$$

$$s_2 = 2E_{0x}E_{0y}\cos\delta = s_0\sin(2\Psi)\cos(2\chi) \tag{2.41}$$

$$s_3 = 2E_{0x}E_{0y}\sin\delta = s_0\sin(2\chi) \tag{2.42}$$

An overview of a few common polarizations and their respective Stokes vectors is given in Tab. 2.1.

Polarization	$\mathbf{S}$	Azimuth Ψ	Ellipticity χ
Horizontal (H/X)	(1, 1, 0, 0)	0	0
Vertical (V/Y)	(1,−1, 0, 0)	± 90°	0
Diagonal (D)	(1, 0, 1, 0)	+ 45°	0
Anti-diagonal (A)	(1, 0,−1, 0)	− 45°	0
Right hand circular(R)	(1, 0, 0, 1)	0	+ 45°
Left hand circular (L)	(1, 0, 0,−1)	0	− 45°

Table 2.1: List of Stokes vectors For these fundamental polarization states the Stokes parameters take values of ±1 and 0.

A common way to visualize these vectors is the Pointcaré sphere. For perfectly polarized light, every Stokes vector corresponds to a point on the surface of this sphere. Linear polarizations are found on the equator of the sphere, while the circular polarizations are located on its poles. (see Fig. 2.15 b)

In order to describe the effect of optical elements on these Stokes vectors, we can make use of the so-called Müller matrices. Here the influence of any system of optics is described by a series of 4×4-matrices M_i. The resulting Stokes vector is calculated by

$$\mathbf{S}_{out} = M_n M_{n-1} \ ... \ M_2 M_1 \cdot \mathbf{S}_{in} \tag{2.43}$$

where $\mathbf{S}_{in}$ in the initial Stokes vector, while M_1 represents the optical element that is passed first and M_n is the optical element that is passed last. Table 2.2 gives an overview of common Müller matrices that will be relevant in the scope of this work.

Horizontal polarizer	$M_{HPol} = \begin{pmatrix} 0.5 & 0.5 & 0 & 0 \\ 0.5 & 0.5 & 0 & 0 \\ 0 & 0 & 0 & 0 \\ 0 & 0 & 0 & 0 \end{pmatrix}$
Half-wave plate	$M_{\lambda/2} = \begin{pmatrix} 1 & 0 & 0 & 0 \\ 0 & \cos^2(2\theta) - \sin^2(2\theta) & -2\cos(2\theta)\sin(2\theta) & 0 \\ 0 & -2\cos(2\theta)\sin(2\theta) & \sin^2(2\theta) - \cos^2(2\theta) & 0 \\ 0 & 0 & 0 & -1 \end{pmatrix}$
Quarter-wave plate	$M_{\lambda/4} = \begin{pmatrix} 1 & 0 & 0 & 0 \\ 0 & \cos^2(2\theta) & -\cos(2\theta)\sin(2\theta) & -\sin(2\theta) \\ 0 & -\cos(2\theta)\sin(2\theta) & \sin^2(2\theta) & -\cos(2\theta) \\ 0 & \sin(2\theta) & \cos(2\theta) & 0 \end{pmatrix}$

Table 2.2: Relevant Müller matrices The table summarizes the Müller matrices needed to describe the optical elements that are relevant in the scope of this work. The angle θ describes the rotation of the wave plates relative to the H-V basis.

With the help of these Matrices one can visualize the effect of the wave plates. Figure 2.16 shows the path of the Stokes vector on the Pointcaré sphere upon rotation of the wave plates.

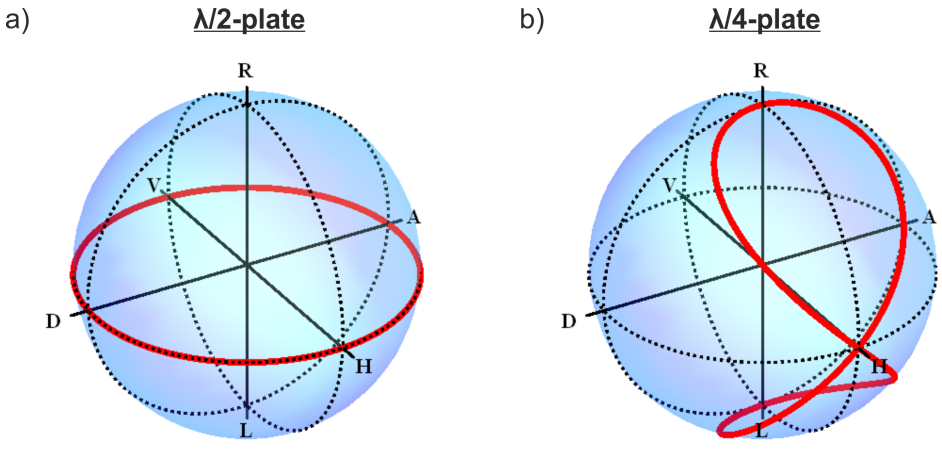

Figure 2.16: Visualization of the effect of wave plates on horizontally polarized light a) The half wave plate gives access to arbitrary linear polarization. b) The quarter wave plate moves the Stokes vector on a eight-shaped path to both poles of the sphere.

We see that a $\lambda/2$-plate rotates a linear horizontal input on the equator of the sphere and hence can be used to generate any linear polarization. This calculation however assumes an indeal wave plate with a retardation of π. In reality, wave plates often suffer from slight deviations in the retardance due to chromatic dispersion or non-perfect incidence angles. In this case, the output polarization becomes slightly elliptical. For the $\lambda/4$-plate the output polarization moves across the sphere in an 8-shaped, reaching both poles. Therefore these plates can be used to create circularly polarized light. If we assume an imperfect plate the size of the two loops changes and the polarization does not become perfectly circular.

3 Experimental setup and methods

This chapter deals with the experimental setups used to aquire the data for this work. First it will provide a brief overview of the entire system, followed by a more detailed description of the individual units and important devices. This is followed by a brief discussion of the standard techniques used to characterize quantum dots.

3.1 Overview of the setup

Measurements on single quantum dots require low temperatures around 5 K to reduce the influence of dephasing and noise. Therefore the central element of the setup is the low temperature microscope. It contains the sample and is submerged into a thermally isolated vessel filled with liquid helium. The microscope furthermore directs the laser excitation onto the sample and collects the emitted optical signal in a confocal geometry.

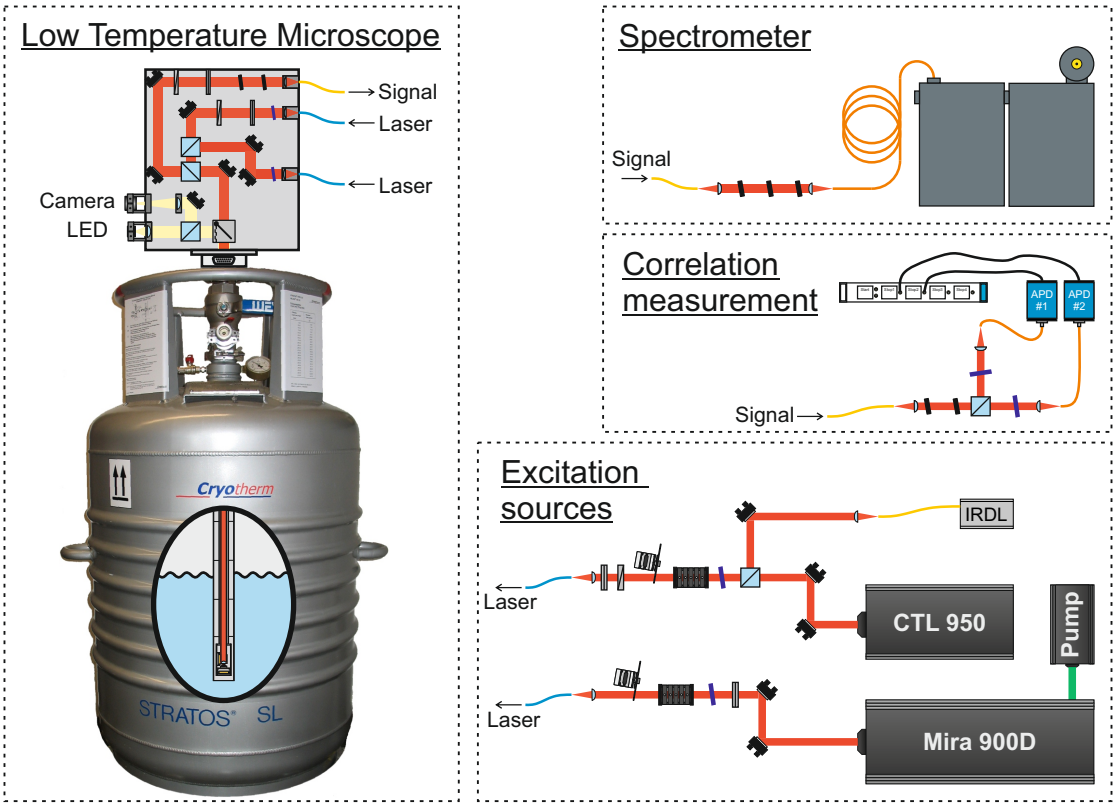

Figure 3.1: Overview of the spectroscopic setup The spectroscopic setup is divided into several units that are connected to the low temperature microscope by optical fibers. All units are discussed in detail in the corresponding sections.

Due to the limited space at the microscope head, the laser sources, the spectrometer and all other optical elements that do not necessarily have to be installed on the microscope head are located on an optical bench next to the cryostat with the microscope. Both the excitation sources and the detection equipment are connected to the microscope by optical fibers. Figure 3.1 provides an overview of the entire setup. The following chapters will take a closer look at the individual units.

3.2 Excitation Sources

For the experiments performed in the scope of this work, a number of laser sources with different properties are used. All these lasers are placed on the optical bench next to the cryostat and connected to the microscope via polarization maintaining fibers. Before being coupled into the fiber, the polarization of all lasers is aligned with the polarization maintaining axis of the fibers and a combination of a filter wheel and neutral density filters is used to adjust the laser power.

3.2.1 Above-band excitation

An above-band exciation is necessary to perform photoluminescence (PL) measurements (see 3.6). The QDs investigated in this work are embedded into a GaAs matrix with a band gap of 1.519 eV (at 4 K)[18]. This defines the lower limit for the emission energy of the PL-laser. In order to minimize the wavelength difference between the resonant lasers and the PL-laser, a fibercoupled diode laser with a wavelength of 808 nm (1.534 eV) and a maximal outpout power of 30 mW was chosen.

3.2.2 Resonant exciation

For the resonant exciation of the QDs, two tunable lasers are used. The first one is an external cavity diode laser, providing cw-excitation and the second one is a Ti:Sapphire laser, which can be operated both in cw- and pulsed mode.

External Cavity Diode Laser

The *„CTL 950“* from *„Toptica“* is an external cavity diode laser in Littrow geometry. It provides a tuning range of 915-985 nm, a narrow linewidth below 100 kHz and a maximal output power of 80 mW. Due to its mode-hope free tuning and the hands-off operation, this laser was used for the majority of experiments under cw excitation.
The laser does however have two peculiarities, which need to be taken into account when working with it. When coupling this laser into a single mode fiber, it is necessary to use a fiber with angled end-facets (APC). Otherwise Fabry-Pérot resonances between the end facets of the fiber will cause fluctuations of the output. This problem occurs specifically with this laser due to its narrow linewidth.
Furthermore this laser suffers from background emission over the entire emission range of the used diode. Even though this emission is many orders of magnitude weaker than the laser line, it becomes relevant, if the laser is spectrally suppressed, as is displayed in figure 3.2.

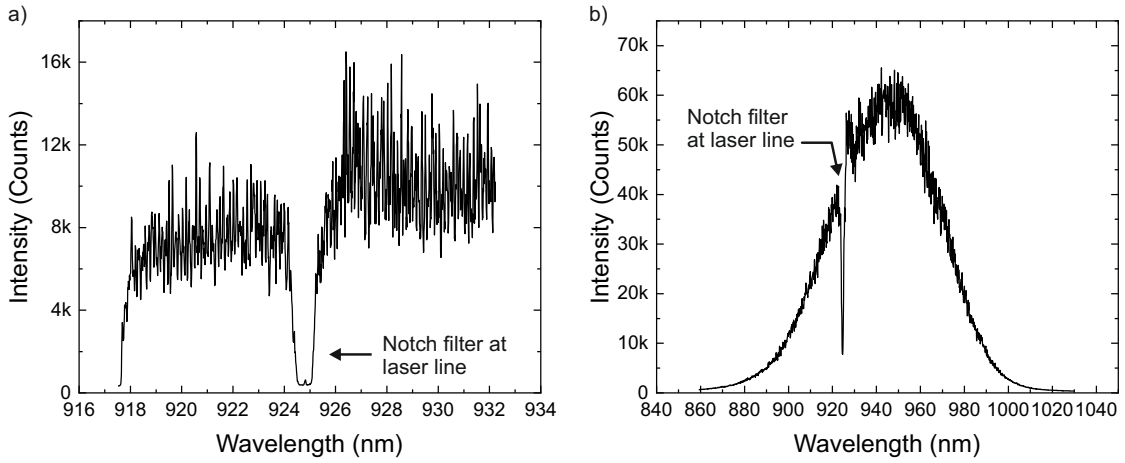

Figure 3.2: Background emission of the tunable diode laser a) High resolution spectrum of the background emission of the tunable diode laser. b) Corresponding wide range spectrum with lower resolution. In both cases the main laser line was attenuated by several orders of magnitude using a narrow band tunable notch filter. The laser features a strong background emission over its entire tuning range.

During the experiments, this background is filtered out using ultra-narrow tunable band pass filters. These filters are designed for a transmission wavelength of 935 nm with a FWHM of 0.45 nm. The transmission window can be blue-shifted by tilting the filter relative to the inciding laser beam. By doing so, the spectral properties slowly degrade, limiting the filter to a effective tuning range of roughly 920-935 nm (see figure 3.3). Depending on the experiment, specifically the spectral difference between signal and laser, 2-3 bandpass filters are used to clean the spectrum of this laser.

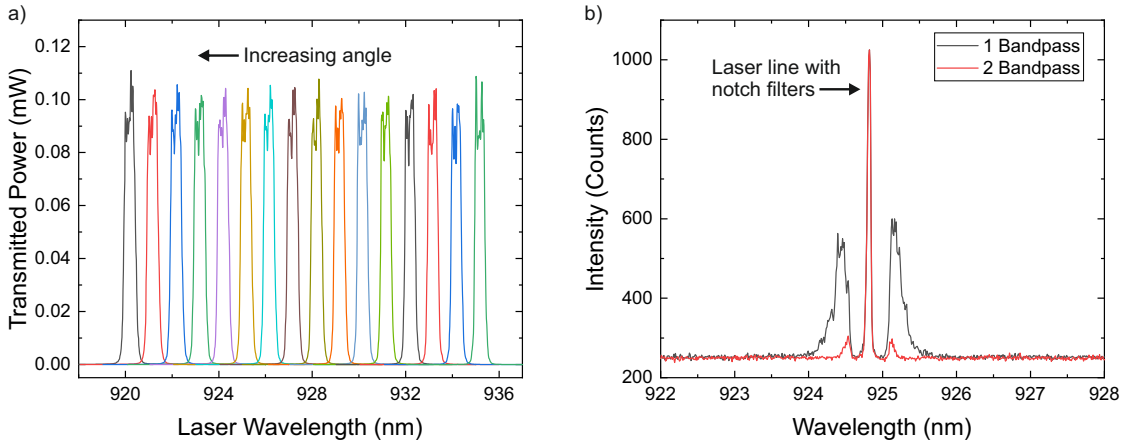

Figure 3.3: Spectral properties of ultra-narrow bandpass filters a) Series of transmission spectra of the ultra-narrow bandpass filters for different angles with respect to the optical axis. b) Spectra of the background emission of the tunable diode laser when filtered with one (black) and two (red) bandpass filters. The main laser line was suppressed using a notch filter.

Titanium Sapphire Laser

The *„Mira 900 D“* from *„Coherent“* is a Titanium Saphire laser (Ti:Sa) with an effective tuning range of 700-1000 nm and a maximum output power of 1.6 W. It can be operated both in cw or pulsed mode and is pumped by diode laser (*„Verdi G12“*) emitting at 532 nm with a maximum power of 12 W.

The laser is mainly used in conjuction with the *„CTL 950“*, when two cw lasers are needed for an experiment. In contrast to the *„CTL 950“* the *„Mira 900 D“* has a much lower background emission. (see Fig. 3.4) As a consequence, one single bandpass filter is sufficient to clean the spectrum.

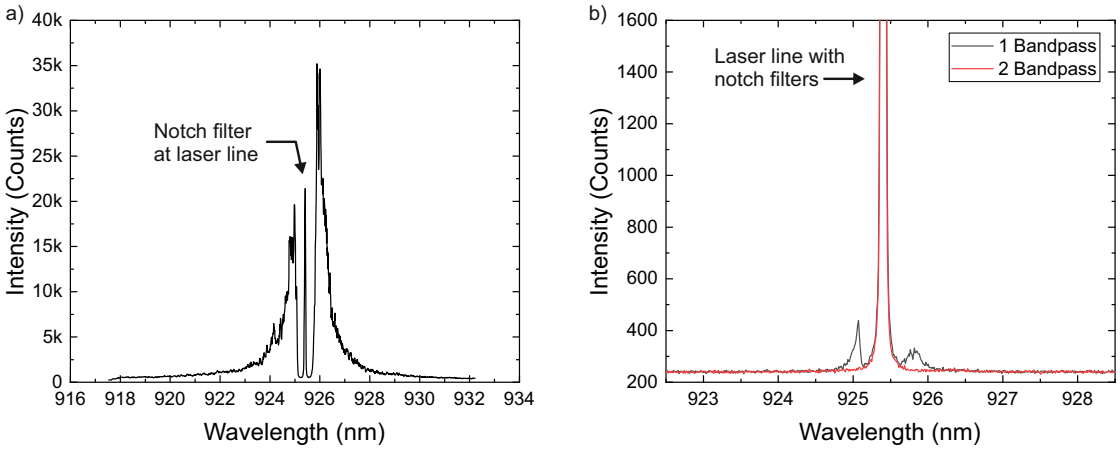

Figure 3.4: Background emission of Ti:Sapphire laser a) Spectrum of the Ti:Sa with a the main laser line strongly attenuated by a notch filter. The background emission is clearly visible on both sides of the main laser line. b) Equivalent spectra with the laser emission being filtered by one (black) and two (red) bandpass filters. While one bandpass filter strongly reduces the background, it is not detectable anymore, when two filters are used.

This laser can furthermore be operated in mode-locked mode, leading to the emission of optical pulses with a duration of 3-6 ps. On these timescales the QDs can retain their phase during the excitation, allowing the study of coherent effects such as Rabi rotations. Since these pulses are spectrally much broader than the cw emission of the laser, this poses a greater challenge for straylight suppression. For this reason, a bandpass filter is used to decrease the spectral width of the pulses by $\sim 40\%$ (see figure 3.5).

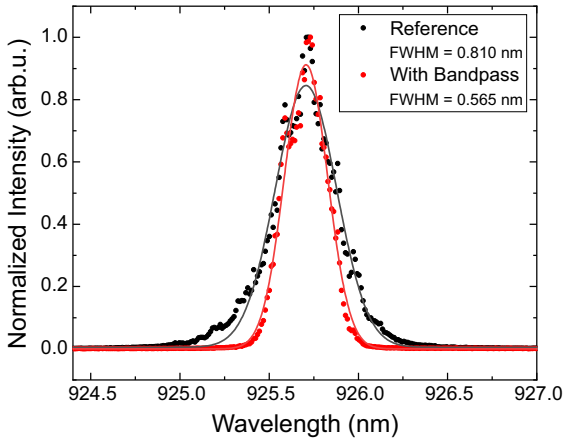

Figure 3.5: Pulse shaping with bandpass filter Spectra of the ps pulses as emitted by the Ti:Sa-laser (black) and filtered by a bandpass filter (red). The filter reduces the FWHM of the pulses by $\sim 40\%$

3.3 Low Temperature Microscope

The low temperature microscope contains the sample during the experiment and can be considered as the central unit of the experimental setup. The microscope can be divided into two major units, the lower part, which is submerged into the cryostat and the upper part, which is at room temperature. The sample is located at the lower end of the microscope and cooled close to 4 K. The microscope is evacuated to prevent condensation and freezing and then filled with a small amount of Helium, which acts as an exchange gas for better thermal conductivity.

During the experiments it is necessary to address individual QDs. To achieve this the sample is mounted on top of a set of nanopositioners that allow positioning of the sample in all three spatial dimensions with a resolution of 20 nm. The range of motion of these positioners is about 2 mm in all directions. Directly above the sample either an objective or an aspheric lens can be installed to focus the laser excitation onto a single dot and collect is emitted light. For the experiments in this work, an aspheric lens with a numerical aperture of NA $= 0.68$ ($f = 3.1$ mm) was used.

The top of the microscope is located outside of the cryostat at room temperature (see figure 3.1). It contains the necessary electrical connectors and optics to interact with the sample. The microscope is equipped with 2 shielded and 7 unshielded electric lines that can be used to apply voltages to and measure currents on the sample. An optical window in the top of the vacuum chamber provides optical access to the objective/lens and the sample. The optics necessary to direct the laser excitation from the optical fibers to the sample and the signal to the detection unit are mounted on an aluminum plate placed vertically on top of the vacuum chamber. These optics are discussed in detail in the following chapters 3.4.1 and 3.4.2. The top of the microscope furthermore contains an imaging unit that provides an image of the sample surface for orientation on the sample and easier setup alignment.

3.4 Optical Setup on the microscope head

The microscope head contains all the optics necessary to direct the laser excitation form the endfacet of the fiber to the QD sample and to collect the resulting emission. As a result of the confocal detection geometry, an important aspect is the suppression of the back-scattered laser light. Due to the high refractive index of the sample ($n_{GaAs} \approx 3.5$), the surface of the sample reflects roughly 30% of the laser excitation. In case of above-band excitation, used for photoluminescence measurements, it is sufficient to place a suitable long-pass filter in front to the spectrometer to achieve this. For resonant or near-resonant excitation, the QD-emission and the laser light are spectrally very close, creating the need for more sophisticated suppression schemes. During the experiments presented in this work two different techniques are used: cross-polarized detection and spectral filtering. The setup was subject to constant improvements. As a result two different setups will be discussed in this chapter, which were used in the course of this work. The first setup uses a combination of cross-polarized detection and spectral filtering, while the second one completely relies on spectral filtering.

Both setups share the need of superimposing two lasers and the detection path. This requires in general two beamsplitters. Both setups are fibercoupled to achieve good mechanical stability of the optical alignement. The fibercoupling is realized by achromatic lenses ($f = 20$ mm, $d = 9$ mm, NIR coating) mounted on a manual z-stage in combination with a manual x-y-stage holding the fiber. The single mode fibers have a numerical aperture of $NA_{Fiber} = 0.13$ resulting in a beam diameter of $d_{Beam} = 5.2\ mm$.

3.4.1 Setup using cross-polarized detection

This setup uses a combination of cross-polarized detection to suppress the two-photon excitation (TPE) laser and spectral filtering for the Control laser. Figure 3.6 shows a sketch of the optical setup. The principle behind cross-polarized detection is exciting the sample with a defined polarization (here s-polarization) and using a polarizer in the detection path to only detect light with perpendicular polarization (here p-polarization). A key requirement for this scheme is that the signal that is to be detected must have a polarization component perpendicular to the laser. In order to achieve a good suppression ratio, a few aspects need to be considered. Therefore, the used setup will be discussed in detail. It is based on the setup presented by Kuhlmann et al. [68].

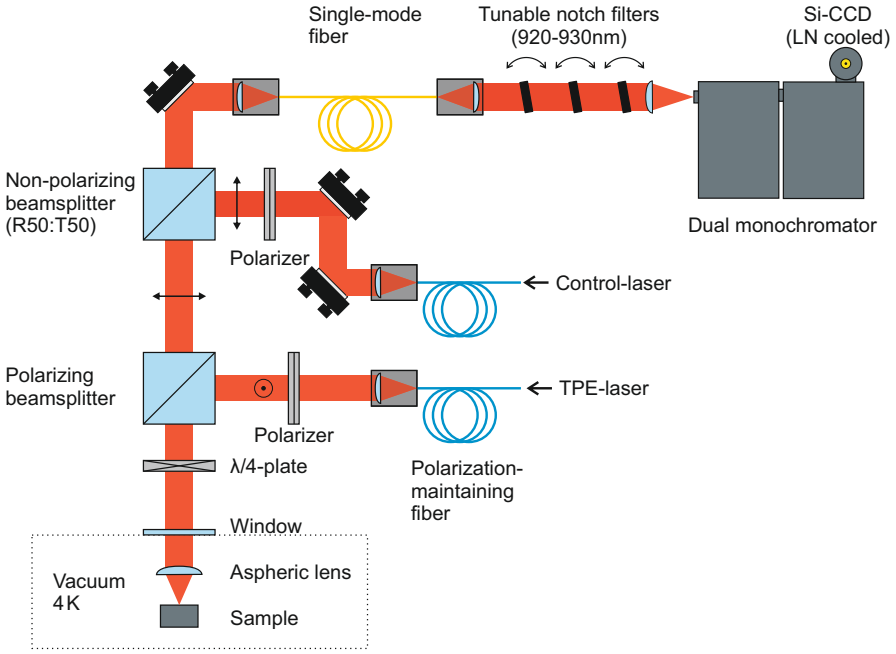

Figure 3.6: Optical setup for cross-polarized detection The TPE- and Control-lasers are superimposed. The PBS ensures suppression of backscattered light from the TPE-laser by reflecting it into the excitation path. This restricts both lasers in their polarization. Backscattered light from the Control-laser is suppressed by spectral filtering using tunable notchfilters.

The central element of the polarization suppression setup is the polarizing beamsplitter (PBS). It reflects s-polarized light (Laser) while transmitting p-polarized light (Signal), with a nominal extinction ratio of $T_p/T_s > 10^4 : 1$. For cleaning the laser polarization after it leaves the optical fiber and aligning it with the PBS a rotatable polarizer is placed in front of it. The rotatability is important for the fine-adjustment of the suppression. A $\lambda/4$-plate between the PBS and the vacuum window of the microscope is used to compensate for deviations introduced to the polarization of the backscattered light by the optics or the sample further down the microscope arm. For aligning the setup, the wave plate is rotated to an angle of 45° between the laser and the fast axis, so that backscattered light from the sample is transmitted through the PBS and sent to the detection path (see figure 3.7). For suppressing the laser, either the slow or the fast axis of the waveplate are aligned to the laser polarization. For optimizing the suppression, the $\lambda/4$-plate and the input polarizer are then slightly rotated in an iterative process.

To achieve a sufficiently high suppression it is essential to include a spatial filtering of the detection. Upon strong focusing of polarized light, there always occur components of perpendicular polarization in the focal plane. These have a clover-leaf shaped intensity distribution[96] and limit the achievable suppression ratio to $10^2 - 10^3 : 1$. If the detection is spatially restricted to the central region of the laser focus (eg. by a SM-fiber or pinhole) these polarization components are effectively suppressed, enabling suppression ratios of $10^4 - 10^5 : 1$. Here, this is realized by using a single-mode fiber with a core diameter of 5 μm for signal collection.

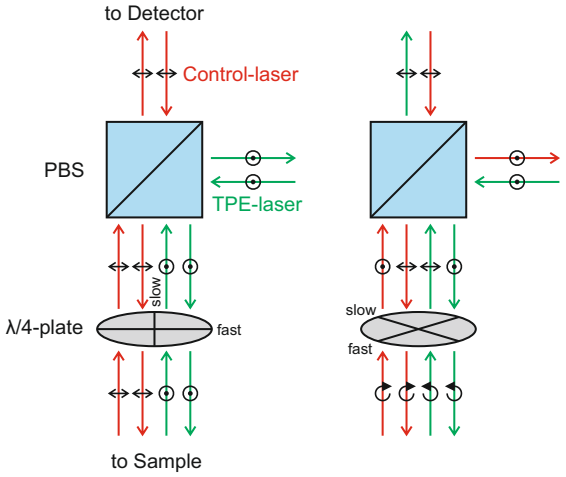

Figure 3.7: Effect of the $\lambda/4$-plate a) If the fast and slow axes are perfectly aligned with the polarization basis of the PBS, the waveplate has no effect of on both lasers. Hence, the backscattered light takes the same path it came from. b) If the wave plate is rotated by 45° it converts between linear and circular polarization. As a result the backscattered light takes the path it did not come from.

For the experiments presented in chapter 7 a second laser is needed. This laser has the same linear polarization as the expected signal and cannot be suppressed by cross-polarized detection. It is superimposed with the first laser and the detection path by a non-polarizing 50:50 beam splitter. Since it has to pass trough the PBS, it is restricted to p-polarization. This laser must be suppressed using spectral filtering. The challenge in this regard is that the laser is spectrally very close to the expected signal, in the range of 2 nm. This requires optical filters with an extremely sharp-edged blocking region. Furthermore, the transition energy of individual QDs shows some variation due to the statistical nature of QD growth.

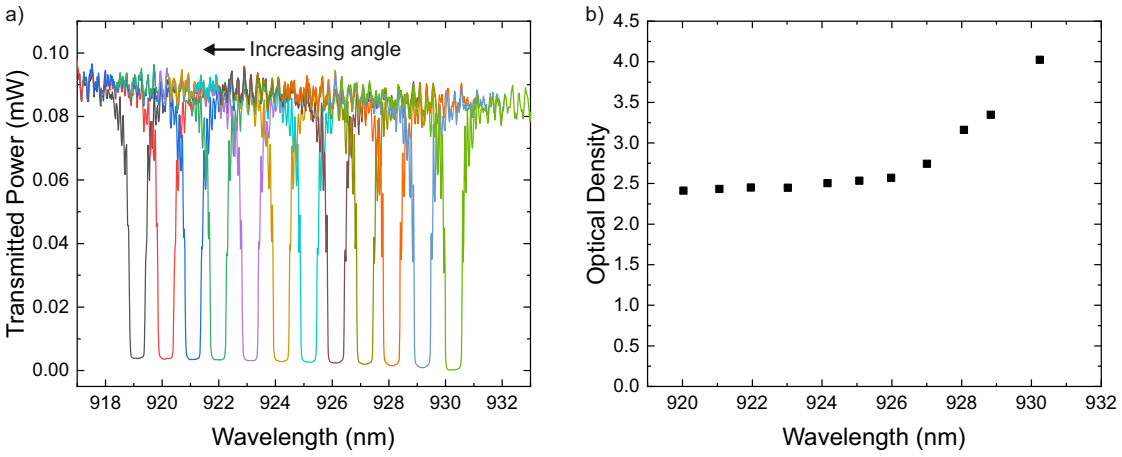

Figure 3.8: Characteristics of tunable Notchfilters a) Transmission spectra of a tunable notchfilter for a series of incidence angles measured by sweeping the emission wavelength of a tunable laser (CTL950). b) Corresponding optical density measured by tuning the blocking range of the filter onto the emission of a fixed laser (Mira 900 D).

The optical filter therefore needs to be tunable to some extend. In order to meet these requirements, narrow linewidth notch filters, containing a reflective volume Bragg grating[89, 76], were chosen. These filters are designed to have a central wavelength of $\lambda_{Center} = 930$ nm, a blocking range of FWHM $= 0.7$ nm and a nominal suppression of $> 10^4 : 1$. By tilting these filters with respect to the optical axis they can be blueshifted down to a central wavelength of 920 nm (see figure 3.8a), but this degrades the achievable suppression (see figure 3.8b). It is therefore advisable to work with QDs close to but below 930 nm. This degradation of the optical density can however be compenstated by using a larger number of filters. This is feasible due to the nearly perfect transmission outside the blocking range. It was found that two notchfilters are usually sufficient to suppress the laser during the experiments. An additional filter was used to support the cross-polarized suppression of the other laser.

3.4.2 Setup with adjustable polarization

For performing the polarization dependent measurements presented in chapter 7.5, it is necessary to modify the setup discussed above, since it restricts both lasers in their polarization. A sketch of the resulting setup is displayed in figure 3.9. The main modification is removing the polarizing beamsplitter and replacing it with a non-polarizing one. A motorized wave plate (Control) in the excitation path of the Control laser allows to manipulate the polarization of this laser.

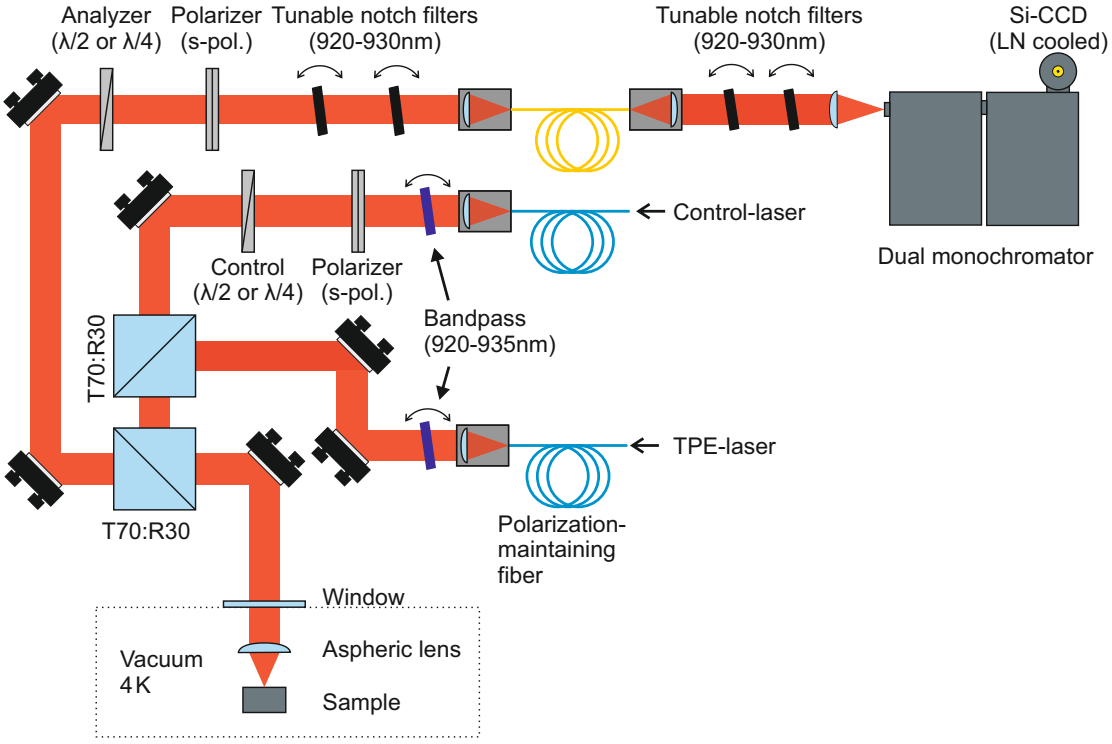

Figure 3.9: Optical setup with adjustable polarization Overview of the optical setup used for polarization dependent measurements. The suppression of backscattered light relies completely on spectral filtering, allowing the manipulation of the Control laser polarization using a wave plate

Either a half-wave or quarter-wave plate is used here, depending on whether linear or circular polarization is required. Placing a linear polarizer for s-polarization in front of the wave plate ensures a clean input polarization. Since a well-defined and known polarization is crucial in this setup, the light sent down towards the sample was characterized using a polarimeter (see figure 3.10). This data shows that the retardance of the wave-plates has only minor deviations from the ideal case and the beamsplitters installed in the setup do not degrade the polarization.

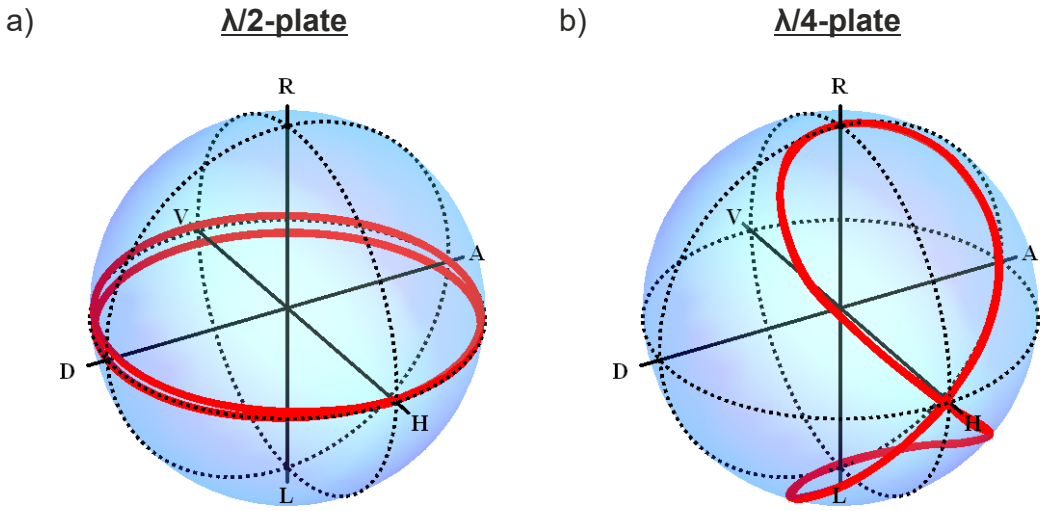

Figure 3.10: Polarization of Control laser Polarization of the Control laser as sent towards the sample upon rotation of a) a half-wave plate and b) a quarter-wave plate, measured by a polarimeter placed in front of the vacuum window.

For analyzing the polarization of the light emitted by the sample, another motorized wave plate (Analyzer) of equal type as the Control wave plate is placed in the detection path. An s-polarizer behind the waveplate provides the polarization sensitivity to the detection.

During the measurements with the first setup, it turned out that the fibers are generating a side band emission around the laser line (see figure 3.11). This appears as a weak background emission, if the laser is not suppressed before being coupled into the detection fiber. In case of cross-polarized detection this is not an issue since the PBS and the spatial filtering effectively prevent the laser from entering the fiber. This effect is therfore a greater issue in case of spectral filtering. In the modified setup this problem was solved by placing one notch filter per laser in the detection path on the microscope head. This way, most of the backscattered laser light does not enter the fiber. The remaining two notch filters are still placed on the optical bench due to space restrictions on the microscope head. Furthermore, a bandpass filter was placed in the excitation path of each laser to filter out the side band emission generated by the excitation fibers.

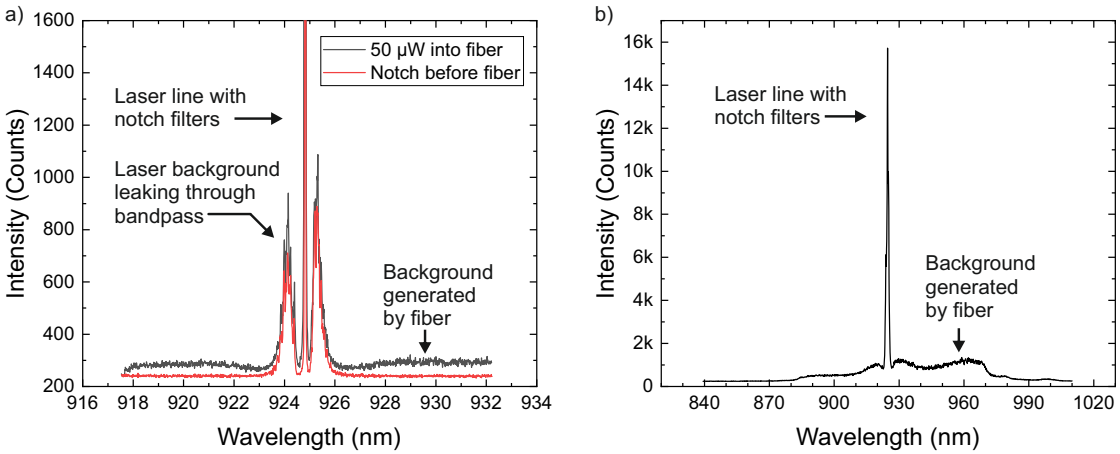

Figure 3.11: Background caused by fiber a) Sending a laser through the optical fiber created a background. This becomes apparent by comparing spectra of the laser attenuated by a notch filter, which is placed either behind (black) or in front of the fiber (red). b) Broadband spectrum of the background generated by the fiber.

3.5 Spectrometer

The spectrometer used in this work consists of two grating monochromators operated in additive mode and a Si-CCD camera. Both monochromators (*„Spectra Pro SP2500i“* from *„Princeton Instruments“*) have a Czerny-Turner geometry with a focal length of 500 mm. They are equipped with a rotating turret, which can hold up to three gratings. Rotating this turret allows adjusting the central wavelength and switching between gratings.

Auxilliary		**Main**	
Grooves/mm	Blaze Wavelength	Grooves/mm	Blaze Wavelength
1200	750 nm	1200	850 nm
300	750 nm	300	760 nm
Mirror		-	

Table 3.1: Gratings of the double monochromator Each monochromator is equipped with two gratings in a rotatable turret. The auxiliary monochromator contains a mirror in the turret which allows to operate the system like a single monochromator.

The mirror installed in the auxilliary monochromator allows using the dual monochromator like a single monochromator and thus increasing the spectral range on the CCD for the cost of decreased spectral resolution. A motorized slit is installed in between the two monochromators, allowing to filter the light that reaches the CCD.

The CCD camera (*„Pylon“* from *„Princeton Instruments“*) has a sensor array of 1340×400 pixels with a size of 20×20 μm, resulting in a sensor area of 26.8×8 mm. The sensor is cooled with liquid nitrogen to temperatures from -70°C to -120°C and has a quantum efficiency of 60% at 950 nm.

According to specification, the system has a maximum resolution of 0.03 nm (FWHM) which corresponds to 43 μeV at 925 nm. It is therefore possible to resolve the different excitonic states of a QD but a typical finestructure splitting of 10 μeV or slightly higher cannot be resolved.

3.6 Photoluminescence Measurement

The photoluminescence (PL) measurement is the method of choice for a first characterization of a QD sample. The sample is excited with light that carries a photon energy larger than the band gap of the host material. The QDs investigated within this work are embedded in GaAs which has a band gap of $E_G(T = 4\ \mathrm{K}) = 1.519$ eV[18] ($\lambda_G = 816$ nm). This excitation generates free carriers (e^- and h^+) in the sample which relax non-radiatively into states of lower energy like the band edge, the wetting layer and the QDs. From there they recombine radiatively and analyzing the emitted light with a spectrometer reveals the energetic properties of the sample (see figure 3.12). If the excitation and detection are spread out over a sufficiently large area of the sample (several 10 μm^2) this is called an ensemble PL measurement and provides information about the inhomogeneous broadening or the central wavelength of the QD ensemble. When the exciation or detection are restricted to a small area ($\sim 1\ \mu$m^2) and the areal density of QDs is low enough ($\sim 1\ QD/\mu$m^2), it is possible to address single QDs and gain information about their specific excitonic properties. Such a measurement, often called μPL, is usually used to find single QDs for further experiments.

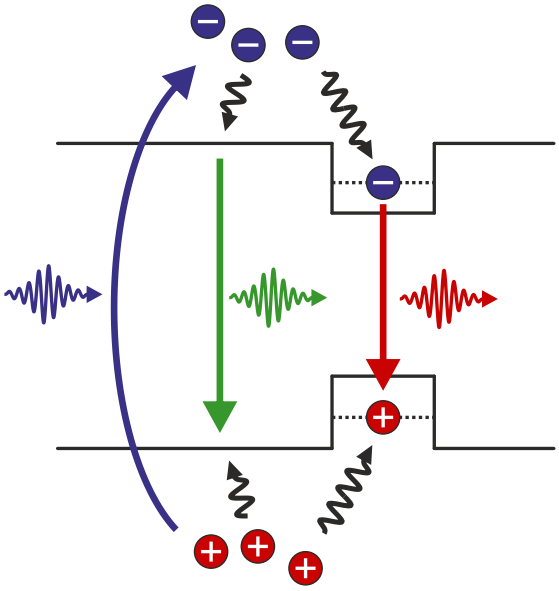

Figure 3.12: Above-band excitation A laser with a photon energy larger than the band gap (blue) creates free carriers in the host material. These relax to the band edge (green) and into the QD (red) where they recombine optically.

If the QDs are embedded in a diode structure, bias-voltage dependent PL measurements can be conducted. These are referred to as PLV and provide information on the Stark-effect and help with assigning emission lines to different charge configurations in the QD.

3.7 Photocurrent Measurement

Photocurrent (PC) measurements are a useful tool for a deeper analysis of the spectral features of a single QD. The key requirement for this techniques is that the QD must be embedded in a diode structure. During the measurement, an excitonic state in the QD is excited resonantly. If the internal electric field of the diode is high enough, a portion of these carriers can tunnel out of the QD and recombine electrically instead of optically (see figure 3.13). This creates a current that is proportional to the absorption in the QD [12, 39]. In the regime of high electric fields, the detection efficiency can reach nearly 100%, providing a quantitative readout of the population for coherent spectroscopy [137]. Under the influence low electric fields, the tunneling probability becomes very small. This prolongs the lifetime of the excitons and therefore makes the resonance narrower. Using a sensitive current measurement, this allows to study the natural linewidth or fine-structure splitting of the QD [37].

During these experiments, either the laser energy or the transition energy of the QD (via the Stark-effect) must be detuned. In principle both options are possible, but tuning the QD by sweeping the voltage applied to the diode usually results in a better resolution and lower noise. The resulting photocurrent is typically in the pA-range, but can get arbitrarly low when working in the regime of low tunneling and/or with low excitation power. For measuring these currents a device based on a transimpedance amplifier is used.

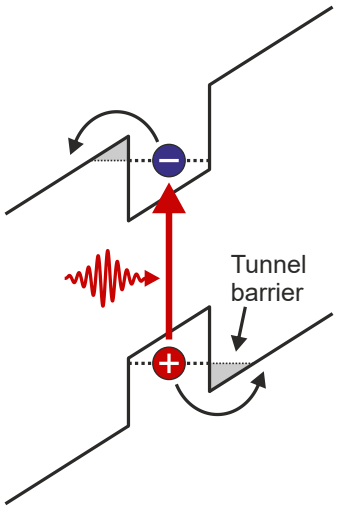

Figure 3.13: Photocurrent A resonant laser creates excitons inside the QD. The electrics field causes these carriers to tunnel out of the confinement potential. The tunneling rate is determined by the area of the tunneling barrier (marked in grey).

3.8 Correlation Setup

In the scope of this work two different setups are used to perform time correlated measurements. The first setup uses two silicon avalanche photo diodes (APD) as detectors and is used to perform the cross-correlation measurements of the biexciton decay. The second setup uses superconducting single photon detectors (SSPDs). These have a better time resolution and a lower dark count rate than the APDs, but only became available towards the end of this work. They are used for the auto-correlation measurements of the SDC process. Table 3.2 summarizes the specifications of both detector types.

	APDs	**SSPDs**
Manufacturer:	Laser Components	Single Quantum
Model:	COUNT-20B-FC	Eos
Efficiency:	20−30% @925nm	75 % @ 786nm
Dark counts:	< 20 Counts/s	< 1 Counts/s
Timing Resolution:	1000 ps	20 ps

Table 3.2: Specifications of single photon detectors The SSPDs are superior to the APDs in every regard but only became available in a late stage of the experiments.

In both cases, the same time tagger is used (*quTAG* from *qutools*). It provides 5 input channels (1 start, 4 stop) with a timing jitter of < 25 ps. This means that especially in case of the APDs the timing resolution of the detectors is the limiting factor. The two setups will be discussed individually in the following sections.

3.8.1 Cross-correlation setup using APDs

This setup uses the two Si-APDs as detectors. Since it is intended for cross-correlation measurements between different lines, a 50:50 beamsplitter cube was used to split the signal. This allows placing a tunable bandpass filter in each arm and therefore enables independent spectral filtering for both detectors. The signal is then coupled into multimode fibers to achieve a maximal coupling efficiency and sent to the detectors. The two notch filters placed in front of the beamsplitter are part of the regular straylight suppression. Figure 3.14 shows a sketch of this setup.

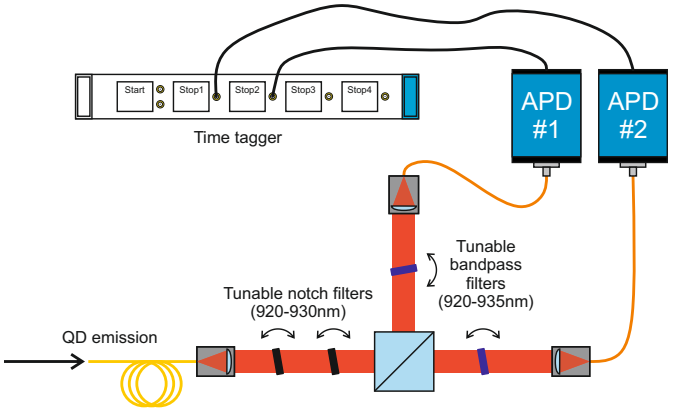

Figure 3.14: HBT setup used in combination with the APD detectors Using a beamsplitter cube allows placing tunable bandpass filters in each detection arm to perform cross-correlation measurements between different emission lines.

3.8.2 Auto-correlation setup using SSPDs

This setup makes use of the superconducting detectors that became available in at a late stage of this work. These detectors are superior to the APD, especially in the timing resolution and the dark count rate. The setup is used only for auto-correlation measurements. The spectral filtering can therefore be done before the beamsplitter, which is replaced by a fiber beamsplitter. The open arm is terminated by a fiber beam dump to minimize cross-talk between the detectors. Here, single-mode fibers are used to transmit the signal, since the cryostat containing the detectors is designed for this kind of fiber. Figure 3.15 shows a sketch of this setup.

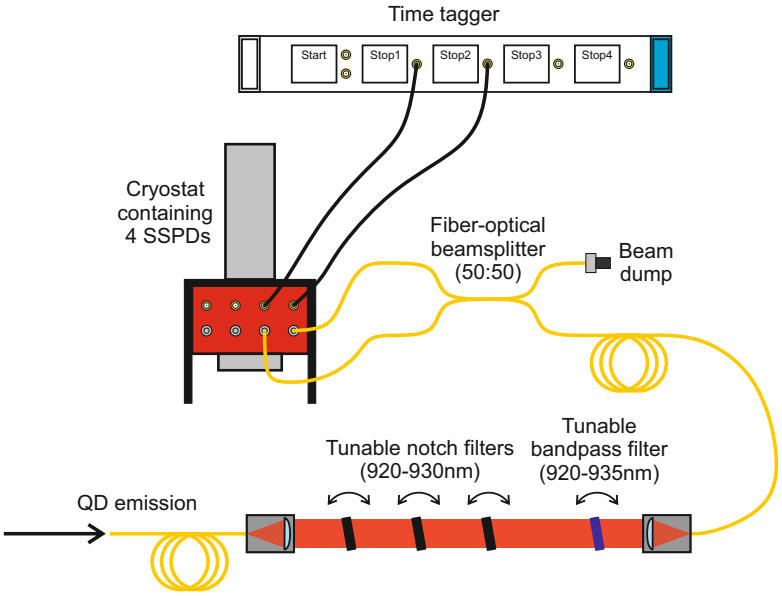

Figure 3.15: HBT setup used in combination with the SSPDs This setup contains a fiber beamsplitter, restricting the setup to auto-correlation measurement of the QD emission.

4 Signal collection enhancement with solid immersion lenses

A general challenge when working with epitaxial QDs is the collection of the optical signal. Since these QDs are embedded in a host material with a relatively high refractive index ($n_{GaAs} = 3.5$), total internal reflection occurs already at relatively small angles. Furthermore, the light that is emitted downward is also lost. If no additional measures are taken, these two effects limit the collection efficiency to a few percent[11]. There are however numerous strategies to improve this ratio. A rather intuitive method is placing a mirror underneath the QDs[13]. This way the light emitted downwards into the substrate is also collected. Cavity approaches are used to enhance the light-matter interaction and direct the emitted light. Many different cavity geometries have been employed (e.g. planar Bragg-cavities[13, 15], Micropillars [108, 116], Bullseye cavities[133, 1],...).

In the scope of this work solid immersion lenses (SIL) were used to increase the QD signal. These aim at decreasing the refractive index step at the sample surface to avoid total internal reflection (see figure 4.1). The achievable outcoupling efficiency with this method is not as high as with specialized cavity structures, but it places much lower demands on the processing of the sample.

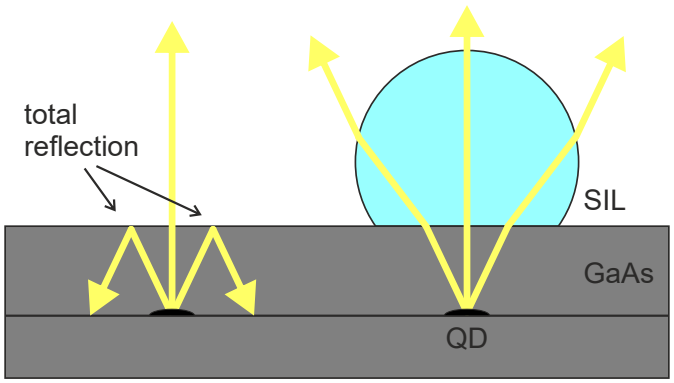

Figure 4.1: Concept of solid immersion lenses The solid immersion lens reduces the refractive index step at the surface of the sample and therefore allows to collect light, that would otherwise experience total reflection.

This chapter provides an overview of the theoretical basics of SILs. Then the sample material and how it is processed to incorporate the SILs is discussed. Finally, the resulting sample and the signal enhancement that was achieved with the help of the SILs is presented.

4.1 Theoretical description of solid immersion lenses

The problem, which the usage of SILs is intended to solve or at least decrease, is the total internal reflection at the sample surface. Due to the high refractive index of the host material ($n_{GaAs} = 3.5$), the critical angle for total reflection is relatively small:

$$\vartheta_{Crit} = \arcsin \frac{n_{Air}}{n_{GaAs}} = 16.6° \tag{4.1}$$

The idea behind the SIL is placing a material with a high refractive index on the sample surface, which decreases this critical angle. The shape of the lens ensures that the light reaches the surface of the lens at a small angles at which it can leave the lens material.

4.1.1 Types of SILs

The simplest shape is the hemispherical lens. Assuming the diameter of the lens is much larger than the distance between the emitter and the sample surface (here 500 μm vs. 0.27 μm) all rays that exit the sample material, reach the air-SIL interface with nearly normal incidence. Hence, no diffraction occurs at this surface and the SIL does not collimate the emission of the QD (see figure 4.2).

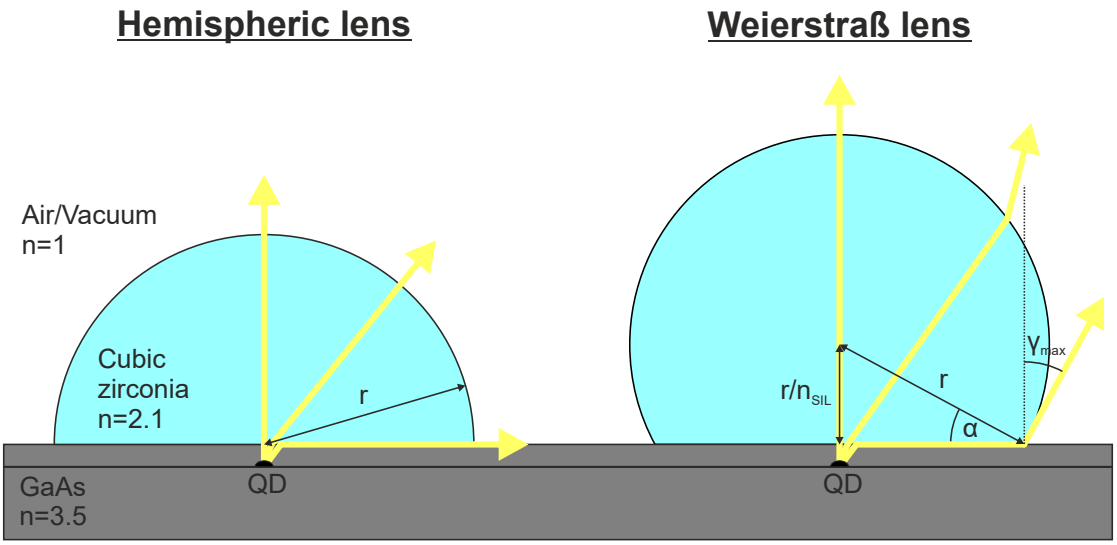

Figure 4.2: Types of solid immersion lenses The hemispheric lens increases the critical angle for total reflection at the sample surface but does not collimate the emission. The lens in Weierstraß geometry also collimates the emitted light into the angle $\gamma_{\max}$.

A shape that does achieve a collimation of the emission is a hyper-hemispherical lens in Weierstraß geometry (see figure 4.2b). Here, the truncated sphere has a height of

$$h_{\mathrm{SIL}} = r_{\mathrm{SIL}} \left(1 + \frac{1}{n_{SIL}}\right) \tag{4.2}$$

The reason for this specific value is the following. A ray that is emitted by the QD at the critical angle of the total reflection, runs parallel to the sample surface inside the

SIL. If the SIL has Weierstraß geometry the angle of incidence of this ray at the SIL surface is

$$\sin\alpha = \frac{\frac{r}{n_{SIL}}}{r} = \frac{1}{n_{SIL}} \qquad \Leftrightarrow \qquad \alpha = \arcsin\frac{1}{n_{SIL}} \tag{4.3}$$

This corresponds to the critical angle at the SIL-Air interface. The refracted ray is therefore tangential to the surface of the SIL in this point. Based on geometrical considerations it can be concluded, that $\alpha = \gamma_{max}$. This in turn, provides a value for the numerical aperture of the light emitted from the SIL.

$$NA_{max} = \sin(\gamma_{max}) \cdot n_{Air} = \frac{1}{n_{SIL}} \tag{4.4}$$

The SILs used in this work consist of cubic circonia with a refractive index of n=2.13, resulting in a numerical aperture of $NA_{max} = 0.47$. This means that an objective lens should at least have this NA to collect a maximal amount of light from the sample. The aspheric lens that is used during this work has a numerical aperture of NA=0.68 and therefore meets this criterion.

4.1.2 Calculating the extraction efficiency

A theoretical estimate for the achievable signal enhancement with SILs can be obtained by employing the theoretical model presented by Barnes et al.[11]. For the sake of completeness, this model will be briefly presented here and be applied to the material system used in this work.

The emission of the QD is modeled as a dipole oscillating along the x-axis, parallel to the sample surface. It is assumed that the emitter is located close to the surface and that this distance is negligibly small in comparison to the dimensions of the SIL.

$$I(\vartheta_{GaAs}, \varphi) = \frac{3}{8\pi}\left(1 - \sin^2(\vartheta_{GaAs})\cos^2(\varphi)\right) \tag{4.5}$$

Here, φ is the azimuth and ϑ_{GaAs} is the emission angle inside the GaAs host material. The function $I(\vartheta_{GaAs}, \varphi)$ ist normalized, so that an integration over the entire space delivers a value of 1. The collection efficiency is therefore given by integrating over all emission directions that are collected by the objective lens.

$$\eta = \int_0^{2\pi}\int_0^{\vartheta_{GaAs,max}} T(\vartheta_{GaAs}) I(\vartheta_{GaAs}, \varphi)\sin\vartheta_{GaAs} d\vartheta_{GaAs} d\varphi \tag{4.6}$$

The limiting effects of refraction and total reflection are included via the integration limit $\vartheta_{GaAs,max}$. Hence, this value changes with the geometry and refractive index of the applied SIL and the numerical aperture of the collection optics. The transmittance T also needs to be adjusted to the individual case.

In the following, the three cases of a bare surface, a hemispherical SIL and a Weierstraß SIL will be discussed. For the sake of simplicity, it is assumed that the sample and SIL are surrounded by air/vacuum with a refractive index of $n_{Air/Vac} = 1$.

Bare Surface

Here, only the refraction at the sample surface and the numerical aperture of the collection optics must be considered to determine the integration limit.

$$\vartheta_{GaAs,max} = \arcsin\left(\frac{\mathrm{NA}}{n_{GaAs}}\right) \tag{4.7}$$

For T only the GaAs/Air interface needs to be considered. Barnes et al. neglect the angle dependence of the transmission and approximate it with the value for normal incidence.

$$T_{\text{Bare Surface}} = \left[1 - \left(\frac{n_{GaAs} - n_{Air}}{n_{GaAs} + n_{Air}}\right)^2\right] \tag{4.8}$$

For a more accurate description, the angle dependence can be included. From the Fresnel equations for s-polarized light, the following equation can be derived.

$$T(\vartheta_{GaAs}) = \left[1 - \left(\frac{n_{GaAs}\cos\vartheta_{GaAs} - n_{Air}\cos\vartheta_{Air}}{n_{GaAs}\cos\vartheta_{GaAs} + n_{Air}\cos\vartheta_{Air}}\right)^2\right] \tag{4.9}$$

The case of s-polarization was chosen here, since the transmittance is lower than for p-polarization and therefore provides a more conservative estimate. The angle ϑ_{Air} directly follows from the refraction at the sample surface.

$$\vartheta_{Air} = \arcsin\left(\frac{n_{GaAs}}{n_{Air}}\sin\vartheta_{GaAs}\right) \tag{4.10}$$

Hemispherical SIL

With a hemispherical SIL at the surface, the refractive index step is reduced. Hence, the refraction and total reflection occurring at this interface are less severe. The shape of the lens leads to the fact that all rays emitted by the QD reach the SIL surface vertically and that no refraction occurs here. The integration limit is therefore

$$\vartheta_{GaAs,max} = \arcsin\left(\frac{n_{SIL}\mathrm{NA}}{n_{GaAs}}\right) \tag{4.11}$$

For T two interfaces need to be considered

$$T = \left[1 - \left(\frac{n_{GaAs} - n_{SIL}}{n_{GaAs} + n_{SIL}}\right)^2\right]\left[1 - \left(\frac{n_{SIL} - n_{Air}}{n_{SIL} + n_{Air}}\right)^2\right] \tag{4.12}$$

If the angle dependence is to be included, this is only necessary for the GaAs/SIL interface. At the SIL/Air interface it can be neglected due to the normal incidence.

$$T(\vartheta_{GaAs}) = \left[1 - \left(\frac{n_{GaAs}\cos\vartheta_{GaAs} - n_{SIL}\cos\vartheta_{SIL}}{n_{GaAs}\cos\vartheta_{GaAs} + n_{SIL}\cos\vartheta_{SIL}}\right)^2\right]\left[1 - \left(\frac{n_{SIL} - n_{Air}}{n_{SIL} + n_{Air}}\right)^2\right] \tag{4.13}$$

with

$$\vartheta_{SIL} = \arcsin\left(\frac{n_{GaAs}}{n_{SIL}}\sin\vartheta_{GaAs}\right) \tag{4.14}$$

Weierstraß SIL

This is the most complex case, but it promises the best outcoupling efficiency. Here the integration limit is

$$\vartheta_{GaAs,max} = \arcsin\left(\frac{n_{SIL}^2}{n_{GaAs}}\mathrm{NA}\right) \tag{4.15}$$

It is important to take into account, that all the emission is emitted into a numerical aperture of $\mathrm{NA}_{max}/n_{SIL}$. Therefore the integration must be stopped at this value to avoid unphysical solutions.

If the angle dependence of T is neglected, it is equal to the case of the hemispherical lens. If it is to be included, the two interfaces need to be considered individually. The GaAs/SIL interface is equal to the hemispherical case, but the SIL/Air interface requires a few geometrical considerations, which can be found in the appendix. The result is

$$\begin{aligned} T(\vartheta_{GaAs}) = &\left[1 - \left(\frac{n_{GaAs}\cos\vartheta_{GaAs} - n_{SIL}\cos\vartheta_{SIL}}{n_{GaAs}\cos\vartheta_{GaAs} + n_{SIL}\cos\vartheta_{SIL}}\right)^2\right] \\ &\cdot\left[1 - \left(\frac{n_{SIL}\cos\beta - n_{Air}\cos\vartheta_{Air}}{n_{SIL}\cos\beta + n_{Air}\cos\vartheta_{Air}}\right)^2\right] \end{aligned} \tag{4.16}$$

with the angles

$$\beta = \arcsin\left(\frac{n_{GaAs}}{n_{SIL}^2}\sin\vartheta_{GaAs}\right) \tag{4.17}$$

$$\vartheta_{Air} = \arcsin\left(\frac{n_{GaAs}}{n_{Air}n_{SIL}}\right) \tag{4.18}$$

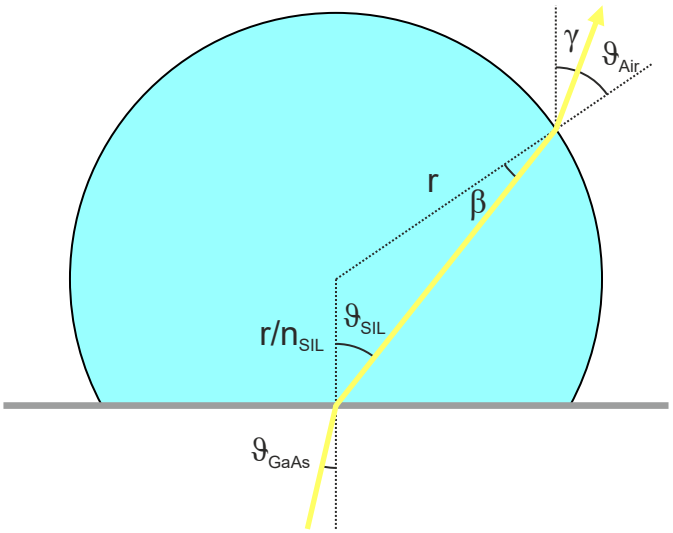

Figure 4.3: Beam path inside a Weistraß SIL The light emitted by a QD experiences in general features non-normal incidence at both the sample and the SIL surface. Therefore, it experiences refraction at both interfaces.

The results of these calculations for $n_{GaAs} = 3.5$, $n_{SIL} = 2.1$ and $n_{Air} = 1$ are summarized in figure 4.4. The dashed lines are obtained by neglecting the angle dependence of T as presented by Barnes et al., while the solid lines include the angle dependence and are therefore a more realistic scenario.

Without a SIL the collection efficiency is limited to $< 2\,\%$. This shows, that there is much to gain by implementing strategies to improve this value. A comparison between the dashed and solid lines shows, that the angle dependence of the transmittance only plays a significant role for high numerical apertures $NA > 0.8$. Therefore the approximation performed by Barnes et al. is justified for most applications.

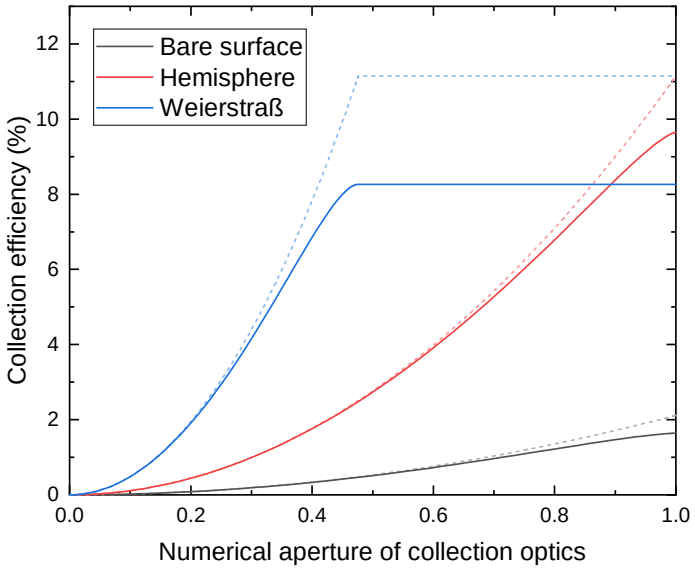

Figure 4.4: Theoretical collection efficiency Calculated collection efficiency for a bare GaAs surface (n=3.5) and with a SIL (n=2.1) of hemispheric shape and Weierstraß geometry. The dashed lines neglect the angle dependent transmission at the interfaces, while the solid ones include it.

Using a hemispheric SIL with a refractive index of $n_{SIL} = 2.1$ (e.g. cubic Zirconia), greatly increases the efficiency. For a numerical aperture of NA = 0.68, like in the setup used in this work, a collection efficiency of $\sim 5\,\%$ can be achieved. This corresponds to an improvement of > 5. To harvest the full potential of this lens, it is however necessary to use collection optics with a high numerical aperture, since the hemispherical shape does not collimate the QD emission in any way.

This is different for the Weierstraß lens. Here the outcoupling efficiency increases more rapidly with the numerical aperture of the collection optics until reaching a maximum at $\mathrm{NA}_{max} = 1/n_{SIL}$. Since here again a refractive index of $n_{SIL} = 2.1$ was assumed, this is the case at $\mathrm{NA}_{max} = 0.476$ The great advantage of this geometry is therefore, that it makes using an objective lens with a moderate numerical aperture more efficient.

Here, the difference between the dashed and solid line is more pronounced than with the hemisphere. This reduction of ~ 25 % is a result of the rather large angles under which the light reaches the SIL/Air interface. When using a very high numerical aperture NA > 0.9, this means that the hemisphere can perform slightly better than the Weierstraß lens. For NA $= 0.68$, the Weierstraß SIL clearly outperforms the hemisphere with an extraction efficiency of ~ 8.3 % and an increase by a factor of ~ 9.

SIL type	Collection efficiency NA=0.68	Enhancement factor
Bare Sample	0.92 %	-
Hemisphere	4.99 %	5.42
Weierstraß	8.27 %	8.99

Table 4.1: Comparison of collection efficiencies For a given numerical aperture of $NA = 0.68$, the Weierstraß SIL is expected to perform better than the hemispheric SIL, but both show a large improvement over the bare sample surface.

These calculations assume ideal conditions with a direct contact between SIL and the sample. This is somewhat unrealistic, as the surface roughness, not perfectly plane surfaces or small dirt particles under the SIL will introduce a narrow gap. Additional reflections caused by this gap will deteriorate the achievable efficiency[86]. These calculations should therefore be understood as an upper limit to what can be achieved by optimizing the experimental realization.

4.2 Layer sequence of the sample

For further measurements it is desirable to use QDs embedded in a diode structure. This allows tuning the transition energies via the Stark-effect and offers the possibility of performing photocurrent measurements on the sample. Since it is intended to apply SILs to the sample, a p-i-n-structure is superior to a Schottky structure. In this way there is no absorbing metal layer on top of the sample surface and the SIL can be applied to an epitaxially smooth surface.

Based on these considerations the sample *A0895* was chosen for further experiments. Here the QDs are embedded in the intrinsic region of a p-i-n-structure. The sample was grown at Paderborn University in the group of Prof. Dr. Dirk Reuter using molecular beam epitaxy. Figure 4.5 shows a cross section of this sample.

The sample is grown on a GaAs wafer in [100]-orientation. First a 100 nm thick layer of GaAs and a 120 nm thick superlattice consisting of 2 nm thick alternating layers of AlAs and GaAs are grown. These are intended to obtain a smooth surface for the further growth. Then a 110 nm thick layer of Si:GaAs with a doping concentration of $2 \cdot 10^{18}$ cm^{-3} is deposited. This layer serves as the n-region for the diode. This is followed by a 160 nm thick layer of intrinsic GaAs. On this layer the InGaAs-QDs are grown with a nominal composition of $In_{28.6}Ga_{71.4}As$. During this step the rotation of the wafer is stopped, leading to a gradient in the number of QDs per area across the wafer. This ensures that a part of the wafer has the desired QD density of ~ 1 QD/μm^2.

The QDs are then overgrown with another layer of intrinsic GaAs with a thickness of 160 nm. This is followed by a 95 nm thick layer of C:GaAs with a doping concentration of $4 \cdot 10^8$ cm^{-3} acting as the main p-region of the diode and as the final step a 15 nm thick layer of highly doped C:GaAs with a concentration of $2 \cdot 10^9$ cm^{-3}. The high doping concentration in this layer helps with contacting the p-region.

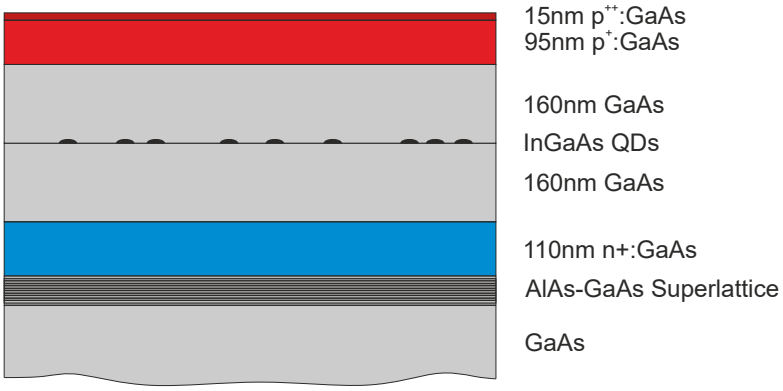

Figure 4.5: Layer sequence of the sample A0895 The sample features a pin-structure with InGaAs in the center of the intrinsic region.

4.3 Design of the pin-diodes

The SILs used in this work have a diameter of 500 μm. This means that the diodes, that these lenses are going to be placed on, must be at least equally large. Considering the traveling range of the piezo positioners ($\sim$2 mm) this creates the need for a space efficient diode design, that incorporates multiple large diodes into a sample piece.

Figure 4.6 shows the top view of the diode layout that was chosen. One sample piece has a size of 2450 $\times$ 1845 μm. In the center of such a piece there are four large mesas (D2, 3, 6, 7) for placing the SILs. Each of these has a size of 550 $\times$ 700 μm and contains a 500 $\times$ 100 μm p-contact pad. They are designed large enough to allow several attempts for the wire bonding process. The sample layout furthermore features four smaller mesas (D1,4,5,8) with a size of 150 $\times$ 300 μm. These are too small to host a SIL and are used mainly as references for the performance of the large diodes. All diodes are separated by the mesa trenches. In this area the p-region is etched away, forming electrically isolated p-i-n-diodes. This etching process is stopped in the intrinsic region above the QD-layer. In this way the PL signal of the QDs and the wettinglayer in the trenches can be used for adjustment purposes. Outside these mesa trenches there are 12 additional p-contact pads, which are intended for tests during the wire bonding. All diodes on the sample share a common n-region, which is contacted via the n-contact areas on both sides of the sample. Here the sample is etched until the n-doped layer and then metal is deposited to form the contact.

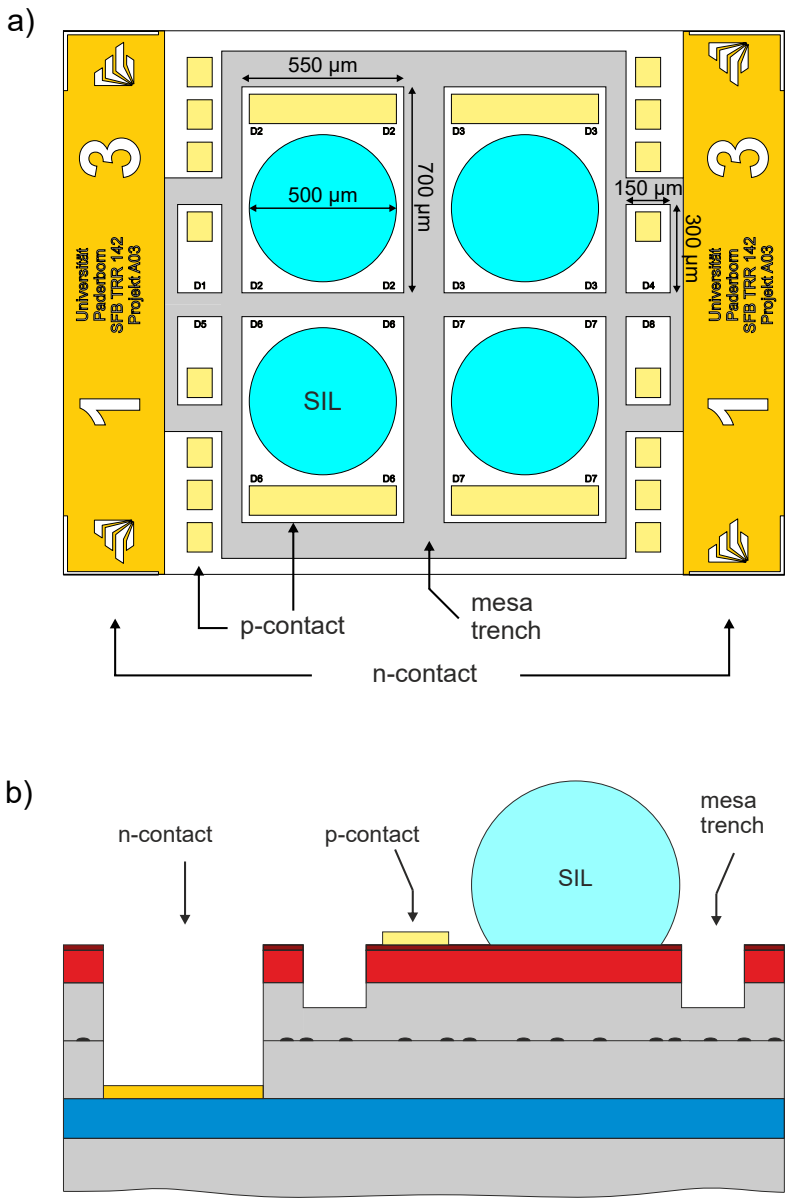

Figure 4.6: Diode design for incorporating SILs a) Top view of a sample piece: The sample contains four diodes that are large enough that a SIL can be placed on them. b) Vertical cut of a p-i-n-diode: The n-layer is contacted by etching through the overlying layers before depositing the metal. The mesa trenches electrically separate individual diodes. Please note that a) is to scale while b) is not.

4.4 Wafermapping

Before the fabrication of the diode structures can begin, it is necessary to perform a wafermapping. As discussed above, the QDs are grown using a gradient approach. This means, that the number of QDs per area varies strongly across the wafer. The wafermapping helps to identify a region on the wafer with a suitable QD density.

This measurement is basically spatially resolved ensemble PL measurement. For this, a special module for the low temperature microscope is used that allows mounting a stripe that was cleaved out of the wafer. This wafer stripe can then be moved to perform a line scan. The maximal length of the stripe that can be mounted in the module is 40 mm.

An important aspect that needs to be considered here is the internal electric field of the diode structure. If it is too high, no PL signal from the QDs or the wetting layer will be observable during the measurements. Assuming a bandgap of $E_{G,GaAs} = 1.519$ eV and high doping of the n- and p-regions, which brings the Fermi-energy very close the the band edges in these areas, the build-in voltage of the p-i-n-structure can be approximated to

$$E_{int} = \frac{1.519 \text{ eV}}{320 \text{ nm}} \approx 47.5 \frac{\text{kV}}{\text{cm}} \tag{4.19}$$

This electric field is too high to expect a PL-signal from the QDs under above-band excitation[43]. Therefore, further measures have to be taken before being able to carry out the measurement.

One method that proved to be reliable, is etching away the p-doped region in a narrow stripe along the edge of the wafer stripe and perform the wafermapping there. On the one hand, this reduces the internal electric field, since the surface states usually pin the Fermi-level approximately to the center of the band-gap. On the other hand, the surface of the sample does no longer consist of a continuous conductive layer. Carriers that are generated by the laser excitation can therefore be accumulated on the sample surface and compensate the internal electric field.

This method does however damage a part of the sample material and requires some processing of the sample. For this reason a different technique was applied here. For samples with a rather thin p-doped region located directly at the surface of the sample, it turned out to be sufficient to cover the sample with photoresist. The mechanism behind this is not completely clear, but a possible explanation might be that the photoresist creates surface states that can trap carriers during the measurement and compensate the internal electric field.

Figure 4.7 shows a wafermapping of the sample A0895 covered with a photoresist, performed at 4 K. The signal around 1.5 eV can be attributed to the emission from the GaAs bandgap. The wettinglayer (WL) is observable slightly above 1.4 eV. Due to the gradient in the deposited material it experiences a slight redshift with an increasing position value. This is a result of the increasing thickness. If the critical thickness of the wettinglayer is reached, the InGaAs forms QDs. These are visible around 1.3 eV.

The horizontal stripes in the signal are a result of cracks in the photoresist, which occur during the cooldown process.

Based on experience, a region where barely any QD signal is visible, is ideal for single QD spectroscopy. In this particular case even the region at the bottom showed a too high QD density after a first fabrication run. Therefore, the neighboring part of the wafer was cleaved and selected for further processing.

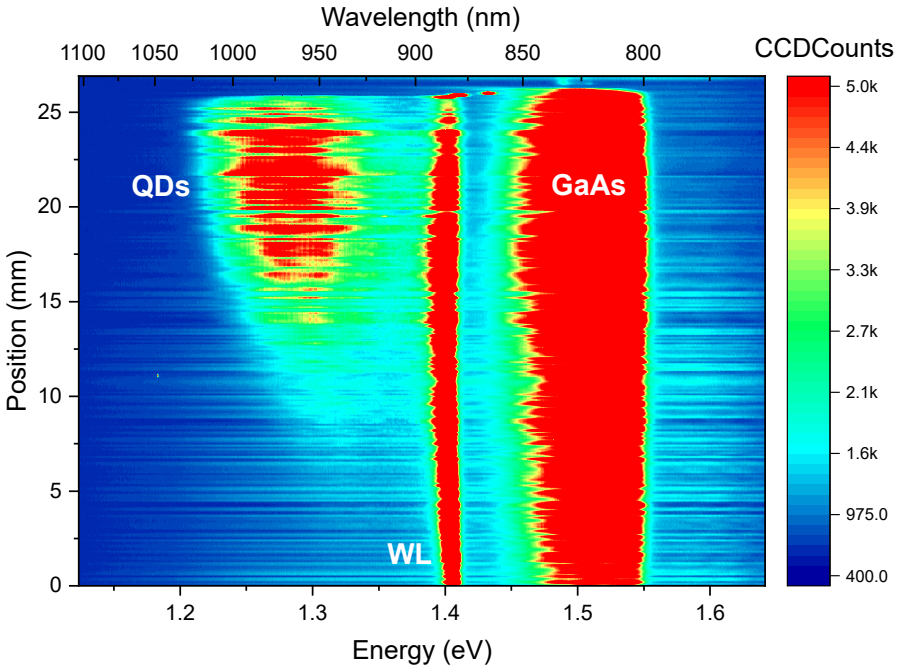

Figure 4.7: Wafermapping of A0895 The PL emission of the GaAs substrate, the wettinglayer (WL) and the QDs are clearly identifiable. The ideal density of QDs can be found in a region where hardly any QD signal can be observed.

4.5 Fabrication of the diodes

The fabrication of the presented sample material into functional p-i-n diodes requires three lithography steps for contacting the n-doped region, depositing the p-contact pads and etching the mesa trenches. All three steps were carried out using optical lithography. The fabrication was done on a 11×10 mm large wafer piece, offering space for a total of 20 samples arranged in a 5×4 matrix (see figure 4.8).

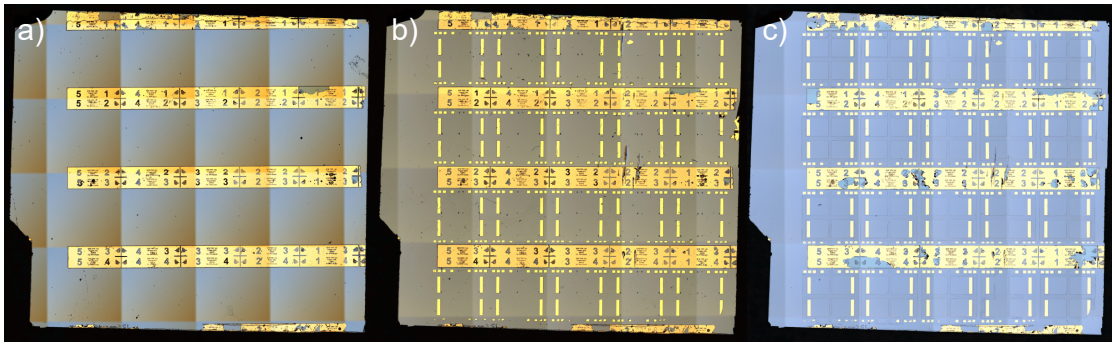

Figure 4.8: Fabrications steps Microscopic images of the sample A0895_k after a) deposition of the n-contacts, b) deposition of the p-contacts and c) etching of the mesa trenches.

Contacting the n-region:
The first step is the fabrication of the n-contact pads. Since the n-doped region is buried, an etching step is necessary before the metal for the contacts can be deposited. The etching mask is defined by optical lithography . Then a solution of phosphoric acid, hydrogen peroxide and water (6 ml H_3PO_4 : 3 ml H_2O_2 : 150 ml H_2O) is used to etch through the p-doped and the intrinsic layer into the n-doped region. The etching mask is then also used for the deposition and the liftoff process of the metal pads. These consist of the following layers (bottom to top): 30 nm Germanium, 20 nm Gold, 30 nm Chromium-Nickel, 400 nm Gold. The metal is deposited by thermal evaporation under vacuum conditions. After a liftoff-process, the n-contact pads are annealed under vacuum conditions with a temperature of 400 °C for 80 s.

Depositing the p-contact pads:
The p-contacts consist of 200 nm Gold, deposited directly on the surface of the sample. After the liftoff process the sample is annealed again to increase the adhesion between the Gold and the GaAs surface. This is important for the wirebonding process. It was found that 330 °C for 20 s sufficiently increases the adhesion without compromising the functionality of the diodes.

Etching the mesa trenches:
The etching of the mesa trenches is done with the same H_3PO_4 : H_2O_2-solution that was used for the etching of the n-contacts. The aim is to etch through the p-layer to isolate the individual diodes, but conserve the QDs.

4.6 Preparation for measurements

Before the sample can be used for spectroscopic experiments, a few more steps are necessary. The sample is glued to a chip carrier, which is equipped with the necessary electrical connections to incorporate the sample into the low temperature microscope. The electrical connections between sample and chip carrier are created by wire bonding. Finally, the SILs need to be placed on the sample. This is done under a microscope with a pair of tweezers. The SILs used here are made of cubic Zirconia with a refractive index of $n = 2.13$. They have a diameter of 500 μm and are designed in Weierstraß

geometry. In order to increase the adhesion between the SIL and the surface, a small drop of vacuum grease is applied to the diodes before placing the SIL. In case of the sample that was used for the further measurements presented in this work (A0895_k_32), one SIL (D2) was applied without the grease to provide a reference, while the other two (D6 and D7) were applied with the grease. Figure 4.9 shows a photograph of this sample with bonding wires and SILs.

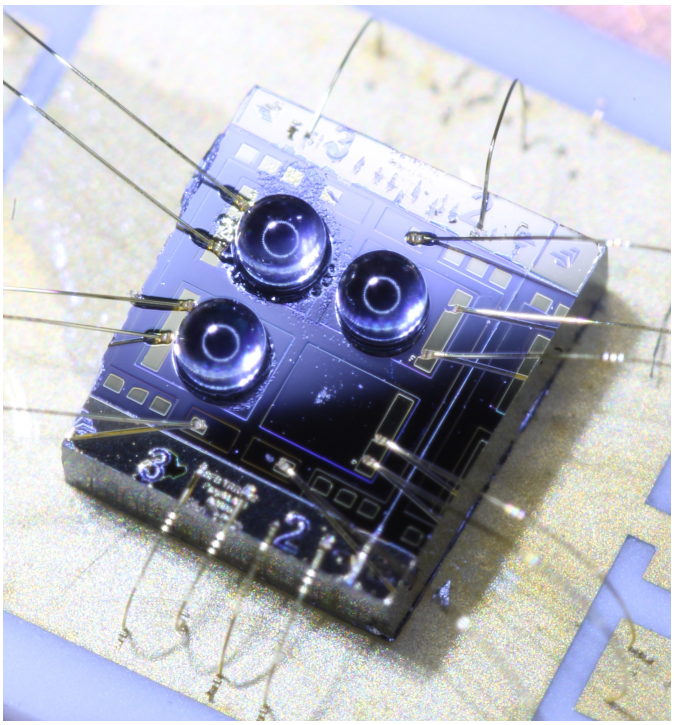

Figure 4.9: Image of completed sample A0895_k_9 The sample is glued on a chip carrier and electrically contacted by wire bonding. SILs are placed on three of the large diodes.

4.7 Electrical propterties of the large diodes

For the electrical characterization of the fabricated diodes, a measurement of the IV-characteristics is usually the first step. Figure 4.10 shows such a measurement, performed on the sample A0895_k_32 at 4 K. The sample contains six working diodes, two small ones (D1 and D4) and four large ones (D2, D3, D6 and D7).

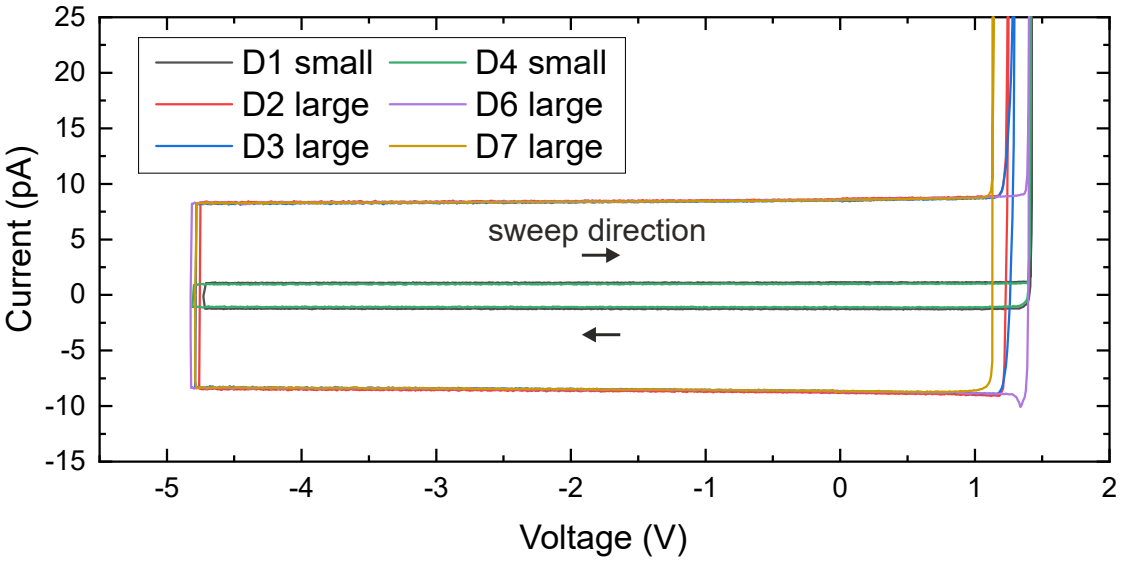

Figure 4.10: IV-characteristics of A0895_k_9 All diodes show a good blocking behavior under reverse bias. The onset voltage in forward direction varies between individual diodes. As expected the large diodes show a larger displacement current due to their larger capacitance (Sweep rate: $dV/dt = 0.1$ V/s)

Under reverse bias all diodes show a very good blocking behavior even at large negative voltage. Under forward bias the diodes show significant differences. Three diodes (D1, D4 and D6) have a very similar onset voltage of ~ 1.4 V. The other three diodes (D2, D3 and D7) vary in this regard but all show a significantly smaller onset voltage. This might be caused by imperfections and usually occurs with a portion of the fabricated diodes. From this point of view, it makes sense that the large diodes are the ones with the lower onset voltage. As a consequence of their much larger area ($385,000$ μm^2 vs. $45,000$ μm^2) they are more likely to encorporate such defects. It should be noted that the total number of diodes investigated here is very low. This conclusion should therefore be taken with a grain of salt.

An obvious difference between both types of diodes is the size of the displacement current I_{Disp} observed in the measurement. This results from the difference in capacitance C_{Diode}, which is proportional to the displacement current.

$$I_{Disp} = C_{Diode} \cdot \frac{dV}{dt} \tag{4.20}$$

The current measurement device used here, has the inherent property of measuring only a fixed portion of the displacement current. A calibration measurement performed on a capacitor of known capacitance revealed this portion to be 64.0 %. This factor needs to be taken into account, when determining the capacitance from the experimental data. A theoretical estimate for the capacitance can be obtained by describing the diode as a plate capacitor.

$$C_{Theo} = \frac{\varepsilon_0 \varepsilon_r A}{d} \tag{4.21}$$

The dielectric constant of GaAs is $\varepsilon_r = 12.46$ at 5 K[88]. For this sample the thickness of the intrinsic region is $d = 320$ nm and the diode areas are $A_{Large} = 385,000$ μm^2

and $A_{Small} = 45,000\ \mu m^2$. Table 4.2 summarizes the capacitance values determined from the IV-characteristics displayed in figure 4.10 and the theoretical estimates. The data shows a good match between the experimental and theoretical values. The slight deviations might be the result of small errors in the actual dimensions of the diodes.

Small diodes		**Large Diodes**	
Diode	Capacitance (pF)	Diode	Capacitance (pF)
		D2	136.1 ± 0.2
D1	18.7 ± 0.2	D3	134.0 ± 0.2
D4	16.2 ± 0.3	D6	134.7 ± 0.3
		D7	134.6 ± 0.3
Theory	15.5	Theory	132.7

Table 4.2: Capacitance of the diodes Both the small and the large diodes show good agreement between the theoretical and experimental values.

Overall it can be concluded, that the large diodes show good electric properties, even if they seem to be more susceptible to imperfections. Nevertheless, they are well suited for the further experiments.

4.8 Optical characterization of SILs

The main idea behind using a SIL is increasing the detection efficiency of the light emitted by QDs. This subject will be investigated in this section along with some other optical characteristics, that are of practical use.

When working with a SIL in Weierstraß geometry, it is important to consider that the SIL strongly influences the focussing behavior of the objective lens (see figure 4.11). As a result, the distance between the sample and the objective lens needs to be significantly changed, when switching from QDs under the bare sample surface to QDs located under the SIL. After a few geometrical considerations (see appendix) one can find the following relation for the focal shift Δf induced by the SIL.

$$\Delta f = \frac{r_{\mathrm{SIL}} \sqrt{1 - \frac{1}{n_{\mathrm{SIL}}^2}}}{\tan\left(\arcsin\left(\frac{1}{n_{\mathrm{SIL}}}\right)\right)} \tag{4.22}$$

For the SILs used in this work ($d_{\mathrm{SIL}=500\ \mu\mathrm{m}}$, $n_{\mathrm{SIL}} = 2.13$) this equation calculates to

$$\Delta f\,(r_{\mathrm{SIL}} = 250\ \mu\mathrm{m}, n_{\mathrm{SIL}} = 2.13) \approx 415\ \mu\mathrm{m} \tag{4.23}$$

Considering the the piezo positioner's range of motion of ~ 2 mm, this is a significant shift and is an important aspect, that needs to be kept in mind when practically working with these SILs, since the necessary adjustment of the sample's z-position is much larger than intuitively expected. A proven strategy for adjusting the sample's z-position is optimizing the photoluminescence signal of the wettinglayer in the center of the SIL, since it can be observed even under strongly defocused conditions. As the z-position

approaches good focusing, first the intensity of the wettinglayer increases and then it changes from a smooth broadened signal into an assembly of numerous discrete lines. This is a result of the spatially restricted excitation and detection under well-focused conditions. If this state is achieved, a PL signal of QDs should be observable.

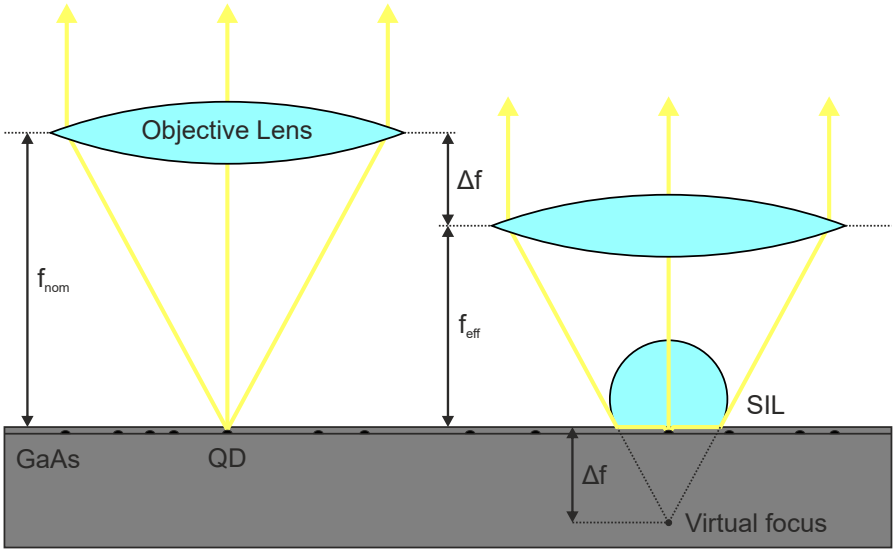

Figure 4.11: Focus shift induced by the SIL Due to its shape a SIL in Weierstraß geometry precollimates the light emitted by the QDs. As a result the effective focal length f_{eff} of the objective is significantly reduced compared to its nominal value f_{nom}.

For an assessment of the signal enhancement of the SILs it is necessary to perform PL measurements on a series of QDs, both with and without SIL, under standardized excitation conditions. Since the SIL strongly influences the focusing of the excitation laser, it is not feasible to simply use a fixed externally measured laser power for this purpose. Instead an inherent property of the QDs can be used. Figure 4.12 shows the powerdependent intensity of the brightest line in the PL spectrum of a single QD. For the QDs on this specific sample it is usually the positive trion X^+ (see chapter 5.1). The signal first grows with increasing power but reaches a maximum around 50 μW before decreasing again. This behavior is a consequence of the statistical nature of the population of the QD during above-band excitation. The number of excitons found in the QD obeys the Poissonian statistics[50] and with increasing excitation power it becomes more likely that the QD is populated by multiple excitons. Therefore, the intensity of states with a lower number of particles decreases. This behavior is generally described by

$$A\left(P,n\right) = \frac{P^n}{n!}e^{-P} \tag{4.24}$$

$$\Rightarrow \quad A(P,n=1) = P \cdot e^{-P} \tag{4.25}$$

Here $A(P,n)$ is the probability that the QD is populated by n particles, given a mean particle number of P. The mean particle number can be viewed as a normalized excitation power. The experimental data shows very good agreement with a fit function that assumes $n = 1$.

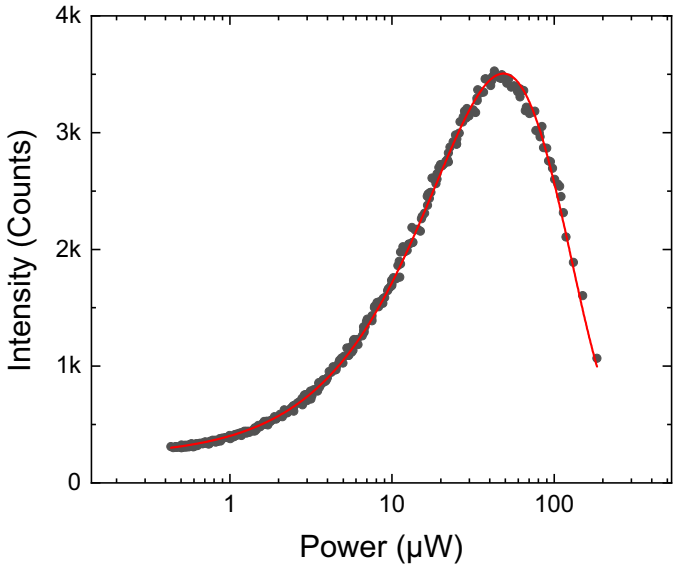

Figure 4.12: Powerdependence of the X^+ line in a PL experiment For low excitation power the X^+ intensity grows linearly with the excitation power (Please note the log-scale). At higher power it reaches a maximum before decreasing in favor of multi particle states. Fit function: $I(P) = a \cdot P \cdot e^{b \cdot P} + I_0$

In order to achieve standardized excitation conditions for a measurement of the signal enhancement the laser is set to a power that maximizes the emission of the QD. Figure 4.13 shows Pl spectra without a) and with b) a SIL that were recorded in this manner. It is directly apparent that the signal is significantly increased by the SIL. For a quantitative analysis the intensities of the strongest emission lines from each spectrum were averaged (see table 4.3)

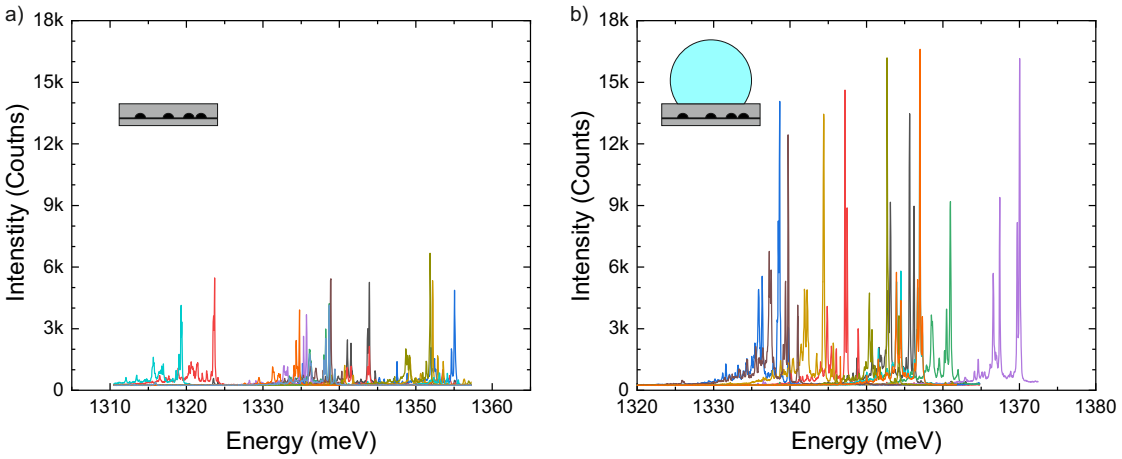

Figure 4.13: Enhancement of PL-signal by SIL PL spectra of several QDs at maximized intensity a) without and b) with a SIL. The SIL clearly increases the signal intensity.

From this data an enhancement by factor of ~ 3 can be concluded. This value is significantly lower than the calculated factor of ~ 9. As discussed above these calculations assume ideal conditions with direct contact between SIL and GaAs. In reality there are most likely always small dirt particles in between, which create a gap [86]. This can be reduced by thoroughly cleaning the sample, but in the present case the wire bonding procedure limits the amount of cleaning that can be done directly before the SILs are applied. A preliminary test on an unprocessed intrinsic sample delivered an enhancement of 4.05, which supports this interpretation (see appendix).

	Average Counts
Bare Sample	$4,829 \pm 900$
SIL	$14,215 \pm 2266$
Enhancement	2.94

Table 4.3: Experimentally achieved signal enhancement The average counts where obtained by averaging over the strongest lines from each spectrum.

A further improvement would be possible by combining the SILs with a Bragg-mirror underneath the dots[64]. This way, the half of the light that is emitted into the substrate could also be collected. Nevertheless the SILs as they are used here do increase the QD signal and therefore help with the further experiments.

5 General properties of the investigated quantum dots

This chapter will take a closer look on the basic properties of the quantum dots investigated in the scope of this work. The majority of the QDs on the sample (A895_k_32) behave very similar with slight differences in properties like transition energies or linewidth. For the sake of coherence, the data in this chapter is from *QD2* on diode *D2*, which was used for most of the experiments. Only the polarization dependent photocurrent measurements are from *QD8* on the same diode, since this QD is later on used for polarization dependent measurements. The characterization begins with an analysis of the photoluminescence (PL), allowing an identification of the different emission lines of the QD. This is followed by a photocurrent analysis, providing a deeper insight into the properties of the neutral exciton like linewidth, fine-structure splitting and tunneling effects. Finally, the chapter ends with a summary.

5.1 Photoluminescence

We will now take a closer look at the photoluminescence properties of the QD. Figure 5.1 shows emission spectra of *QD2* and *QD8*, both taken at a diode voltage of $V_{\text{bias}} = 0.7$ V. Both QDs where used for further experiments due to their spectral position in the tuning range of the notch filters ($E_{\text{Notch}} = 1333 - 1348$ meV). Furthermore, it was important to choose QDs where the X- and X^+- lines are spectrally clearly separated. This ensures that they stay separated during further voltage dependent measurements. Since both dots show a very similar behavior, the following characterization will be done on *QD2*, which was used for the majority of the experiments, while results for *QD8* can be found in the appendix.

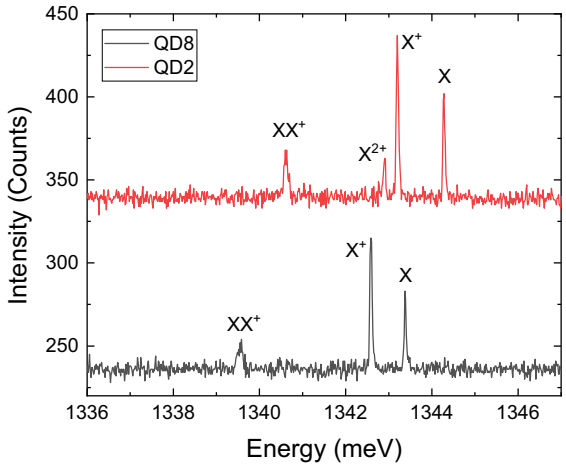

Figure 5.1: Photoluminescence spectra of single QDs The two QDs that were used for the bulk of the following experiments show a similar emission spectrum with the X^+ beeing the strongest line ($V_{\text{bias}} = 0.7$ V)

The first step of the charakterization is typically a voltage dependent PL measurement (see figure 5.2). This shows the Stark-tuning behavior of the QD emission and provides insight into the charging behavior of the QD. Therefore, this measurement allows to identify the charged and neutral excitons.

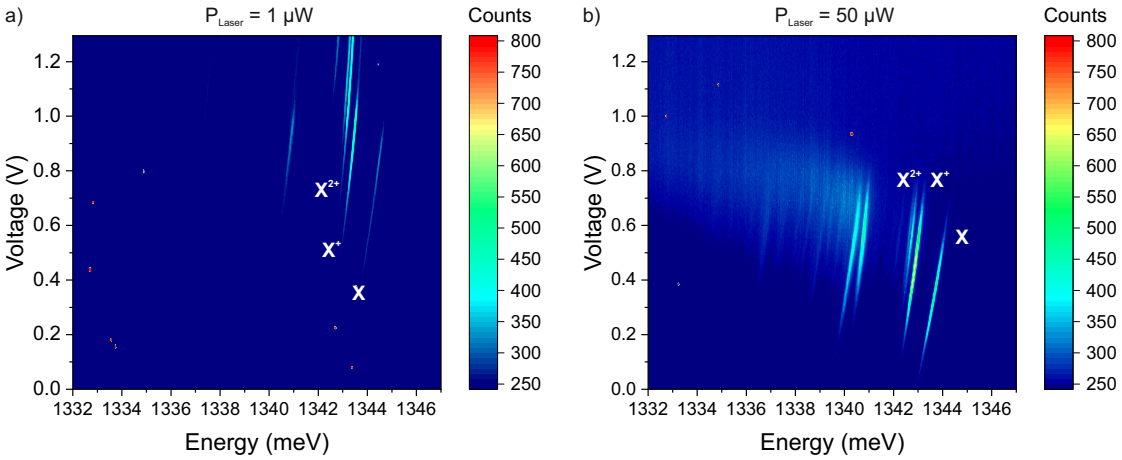

Figure 5.2: Voltage-dependent photoluminescence measurements a) At low excitation power relatively few lines are observable. They all experience an energy shift caused by the Stark-effect ($P_{\text{Laser}} = 1$ μW). b) At high excitation power the emission is shifted towards lower bias voltages and many weak lines associated with multi particle states appear ($P_{\text{Laser}} = 50$ μW).

The measurement shows multiple emission lines, which vary in intensity with the applied voltage and experience a Stark-shift. At low bias-voltages, the internal electric field of the pin-structure is high. This causes tunneling of carriers out of the confining potential of the QD and therefore prevents PL-emission. In figure 5.2a, this is the case for voltages of below $V_{\text{bias}} = -0.3$ V. When a forward voltage is applied to the diode, the internal

electric field is compensated, which increases the PL-intensity. With increasing forward voltage charge carriers from the doped regions of the diodes can tunnel into the QD. In case of a pin-diode, this is possible for both electrons and holes, but the thickness of the tunneling barriers between the QD and the doped regions determines the probability for both types of carriers. If the QD is located closer to the n-doped region it is charged with electrons and if it is closer to the p-doped region it is charged with holes[35]. In this sample, the QDs are located in the center of the intrinsic region, resulting in similar charging probabilities for both types of carriers. The tunneling barriers on both sides of the QDs have a thickness of 160 nm. This results in a very smeared out transition between different charge configurations, making the identification of the different types of excitons more challenging than in other samples with thinner tunneling barriers. Nevertheless, it is still possible to identify the most important lines.

The neutral exciton line (X) disappears at bias voltages above $V_{\text{bias}} = 1.0$ V. It can be identified with certainty by a photocurrent measurement which shows the fine-structure splitting that distinguishes it from other lines. (see chapter 5.2)
Energetically next to the exciton line, a group of lines, which can be associated with positively charged excitons, can be found. They typically appear rather close to the neutral exciton, but their exact emission energy depends strongly on the individual QD and can appear energetically on either side of the exciton emission. The line appearing at the lowest voltage is the single positively charged exciton or positive trion (X^+), which decreases in intensity for higher voltages when charging with more holes becomes possible. The resulting twice positively charged exciton (X^{2+}) is split into multiple lines. This is a result of different spin configurations[34]. Overall the X^+ shows a higher intensity than the X, which is general tendency on this sample.
The relatively weak emission at $\sim$ 1340.5 meV might be associated to the positively charged biexciton (XX^+). It is spectrally close to the expected energy of the neutral biexciton (2-3 meV below X), but it is detuned from the XX-emission observed under resonant two-photon excitation (see chapter 6). The neutral biexciton (XX) itself is not visible in this measurement, which is typical for this sample.

Comparing figures 5.2a and b shows another important feature. With high excitation power the PL-regime shifts towards lower voltages and can result in PL-emission in the photocurrent regime. This behavior is most likely a result of flooding the diode structure with carriers, but does not influence the Stark-shift of the emission.

5.1.1 Single photon emission

The single photon character of the photoluminescence, can be revealed by measuring the second order correlation function ($g^{(2)}(\tau)$) of a single emission line. To perform such an experiment, first the selected emission line needs to be spectrally isolated. This can for example be achieved using a bandpass filter (see figure 5.3a). Here, the X-line is isolated and sent into the HBT setup (see chapter 3.8.1). The resulting $g^{(2)}$-measurement is displayed in figure 5.3b. The data shows a clear anti-bunching around $\tau = 0$, indicating single photon emission. The depth of the dip however, reaches only a value of $g^{(2)}(\tau = 0) = 0.51 \pm 0.02$, which technically does not fulfill the criterion for quantum light ($g^{(2)}_{\text{quantum}}(\tau = 0) < 0.5$) [40]. This a result of the limited time resolution

of the APD-detectors used for this measurement ($t_{\mathrm{res,APD}} = 1$ ns). The time resolution is comparable to typical lifetimes of the QD-emission, which determines the width of the dip. The detector response function therefore masks the true $g^{(2)}$-value.

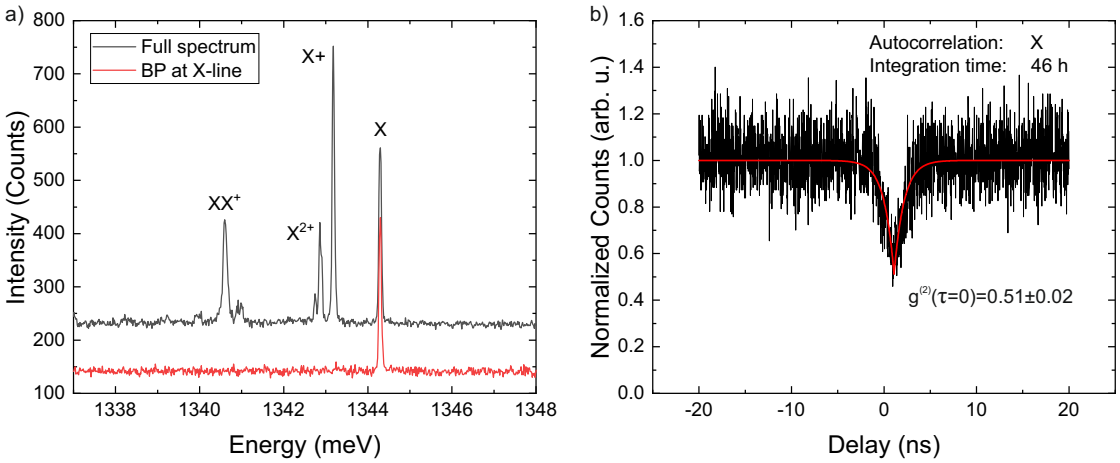

Figure 5.3: Single photon emission of PL a) The emission spectrum of the QD is filtered using a bandpass filter effectively isolating the X-emission b) Auto-correlation measurement of the X-line, showing anti-bunching for $\tau = 0$.

5.2 Photocurrent spectroscopy

The QD shall now be further characterized using photocurrent (PC) spectroscopy. This provides insight into tunneling in the sample and reveals more details of the spectral shape of the exciton line. In figure 5.4, a series of PC resonances of the exciton transition excited with a cw-laser with varied emission energy is displayed. These resonances appear whenever the QD transition is tuned into resonance with the laser by the Stark-effect. If this condition is fulfilled, the laser creates electron-hole pairs in the QD. Depending on the applied voltage, a portion of these charge carriers tunnels out of the QD, generating a current, which can be measured. Since the linewidth of the laser (nominally < 0.4 neV) is several orders of magnitude smaller than the linewidth of a typical QD (a few µeV), the PC resonances have a Lorentzian shape (see figure 5.6), as it is expected for a two-level system (TLS)[56] .

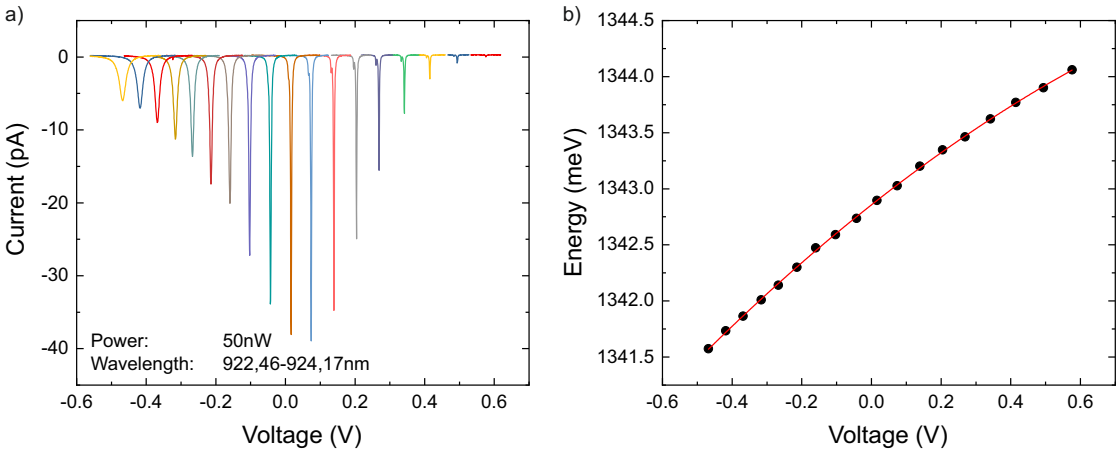

Figure 5.4: Photocurrent measurement a) Series of bias voltage dependent photocurrent resonances of the X-transition for varied laser wavelength/energy. b) Plotting the laser energy against the resonance voltage allows determining the parameters of the QCSE by fitting the data with a parabolic function.

We see that the PC signal becomes weaker towards towards positive bias voltages. Here, the internal electric field of the diode is decreased, resulting in longer tunneling times for the excitons. Therefore, it becomes more likely for the excitons to recombine optically instead of tunneling out ouf the QD. This results in an increased lifetime of the excitons an therefore a narrower linewidth of the resonance. The minimal achievable linewidth is however limited by the lifetime for the optical recombination. As a consequence of the decreased linewidth, we can resolve the fine-structure splitting (FSS) of the exciton state in this regime. In the measurement displayed here, the laser polarization was roughly aligned with one FSS-axis of the QD. Therefore, mainly one of the two possible transitions is excited. Nevertheless the other transition is weakly visible next to the main peak.
Towards negative voltages the internal electric field is increased resulting in faster tunneling and consequently lower lifetimes and increased linewidths (see figure 5.5a). The faster tunneling also increases the photocurrent signal up to the point where all excitons separated by the electric field. For large fields, the peak amplitude decreases but it's area saturates and remains constant. Here, this is the case for $V_{\text{bias}} < -0.2$ V (see figure 5.5b)

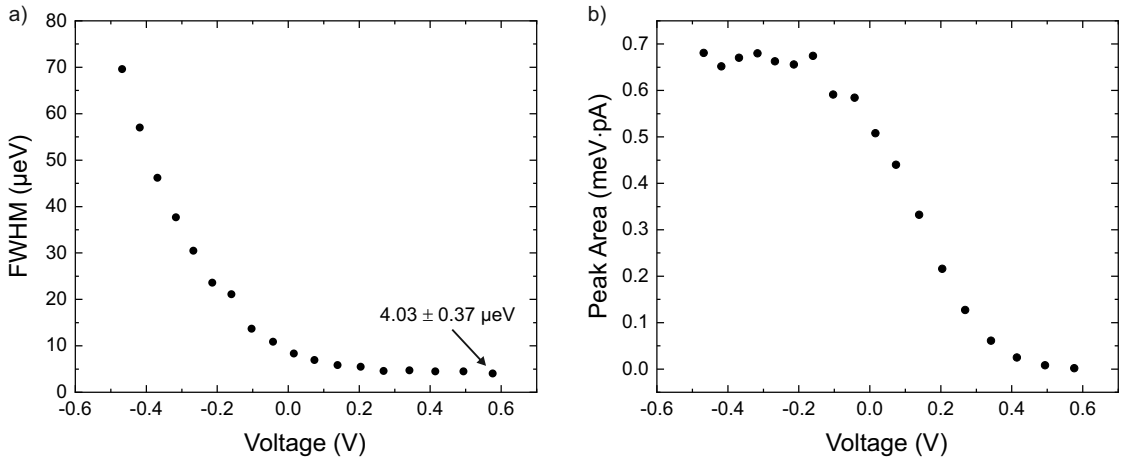

Figure 5.5: Linewidth and peak area of the photocurrent data a) Towards reverse bias the linewidth of the photocurrent resonances increases due to faster tunneling rates. As a consequence the lowest linewidths are measured in the weak tunneling regime towards moderate forward voltages b) The higher tunneling rate towards reverse bias voltage increases the peak area of the resonances, since a larger portion of the created carriers tunnels out of the QD. The peak area reaches a plateau, when all carriers tunnel instead of recombining optically.

For a further analysis, the Stark effect needs to be exctracted from the photocurrent data. The resonances are fitted with Lorentzian functions and the resulting resonance voltages are plotted against the used laser energy (see figure 5.4b). Comparing the resonance energy in the low tunneling regime around $V_{\mathrm{bias}} = 0.6$ V to the PLV data in figure 5.2 supports the previously conducted identification of the exciton emission. The resulting data points are then fitted with a parabolic function which delivers:

$$E(V) = 1342.85677 \text{ meV} + 2.4528\frac{\text{meV}}{\text{V}} \cdot V - 0.63603\frac{\text{meV}}{\text{V}^2} \cdot V^2 \tag{5.1}$$

This equation can be used to transform the voltage scale of the raw measurement data into an energy scale and determine the linewidth and FSS of the QD. Figure 5.6a shows the resonance recorded with an excitation energy of 1342.91 meV resulting in a resonance in the low tunneling regime at 0.49 V. The data was fitted with a dual Lorentzian function, delivering a linewidth of 4.5±0.2 µeV for the main peak and 3.9±1.1 µeV for the smaller one. The FSS is 17.9±0.7 µeV. This measurement still suffers from power-broadening and some tunneling broadening. To decrease this, one can go to even lower excitation power and lower electric fields, which also decreases the signal strength (see figure 5.6b). In this way, a linewidth of 3.3±0.3 µeV could be measured. This is a typical value [122] and there distinguishes this QD as a promising candidate for further experiments.

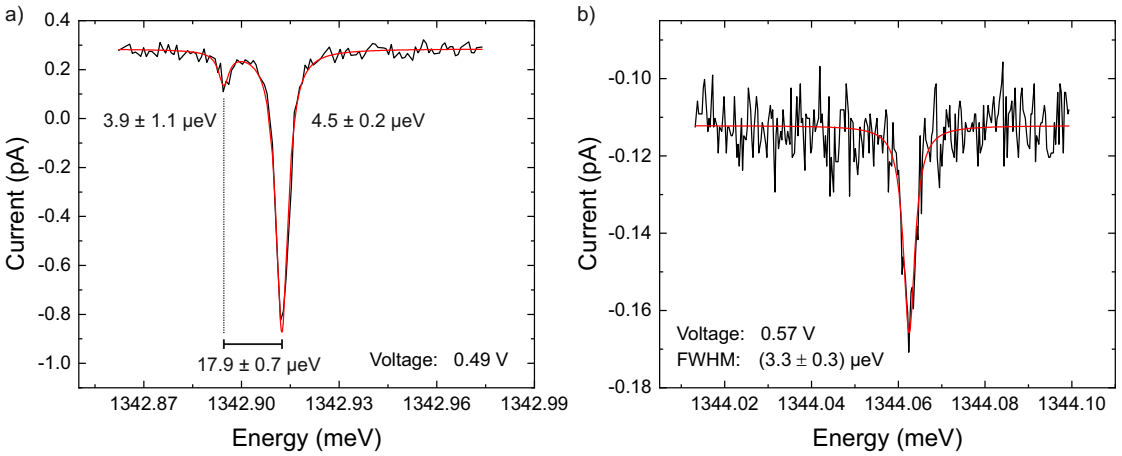

Figure 5.6: Linewidth of QD2 High resolution photocurrent measurement of QD2 in the low tunneling regime with minimal excitation power. This measurement shows the lowest achievable linewidth with this QD.

The previous measurements were carried out using a setup with a fixed laser polarization. The FSS-axis of the investigated dot was by chance roughly aligned to the laser polarization, resulting in the excitation of mainly one of the two transitions. This is however not the case for all QDs on the sample. Figure 5.7a shows the PC-resonance of *QD8*. Here a half-wave plate was used to rotate the laser polarization to an angle of 45° in relation to the QD axis, resulting in an equal amplitude of both transitions. This QD, which was used for the polarization dependent measurements in chapter 7.5, shows a slightly larger linewidth of 6.4±0.8 µeV, but it is still suitable for further experiments and shows a FSS of 17.1±0.6 µeV.

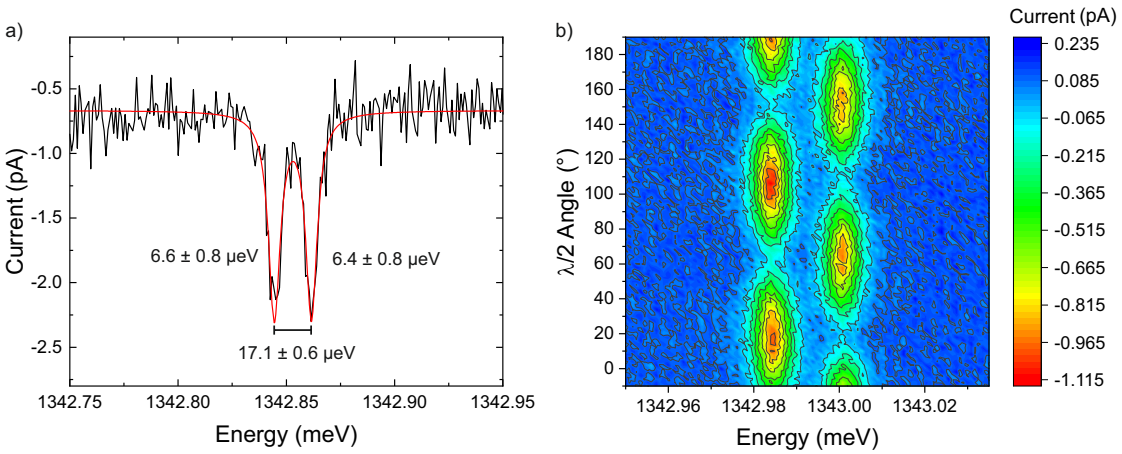

Figure 5.7: Linewidth and fine-structure splitting of QD8 a) The photocurrent resonance of QD8 reveals the linewidth and fine-structure splitting (FSS) of the QD b) Rotating the linear polarization of the laser excitation using a half wave plate shows the polarization dependence of the two transitions of the FSS.

Figure 5.7b shows a polarization dependent PC measurement of this QD. Here, the polarization was rotated using a half-wave plate. The measurement shows the expected sinosoidal modulation of both lines, with a phase shift of π between them, showing that the two transitions have perpendicular polarization. An angle of 0° corresponds to s-polarization, the same configuration as in the previous measurements performed on *QD2*. In this configuration both peaks have an approximatley equal amplitude. We can therefore conclude that the FSS axis of *QD8* is rotated by $\sim 45°$ in relation to *QD2*.

5.3 Conclusion

In this chapter a general characterization of the QDs on the sample A895_k_32 was conducted. Based on voltage-dependent photoluminescence measurements the most important emission lines could be assigned to the corresponding excitonic charge configurations in the QD. This revealed the tendency of the QDs to be positively charged, which manifests itself in a stronger intensity of emission lines associated with positively charged excitons compared to their neutral counterparts. This behavior will also be observable in experiments presented in the following chapters, but does not pose a significant problem.

Photocurrent spectroscopy of the neutral exciton state confirmed the identification of this line and the good linewidth observed in these measurements supports the assessment that the positive charging of the QDs does not pose major obstacle for the following experiments. Furthermore, the fine-structure splitting of *QD8*, which is later on being used for polarization dependent measurements was characterized.

Overall, this chapter can be concluded by stating that the sample provides suitable QDs for the further experiments.

6 Two-photon excitation of the biexciton state

The biexciton state $|B\rangle$ is an important asset for QD based quantum technolgies as it provides a formidable source of single photons [111] and entangled photon pairs [73]. In the scope of this work, it acts as the initial state for the down-conversion experiments, discussed in chapter 7. Therefore, this chapter contains an experimental characterization of its preparation via resonant and non-resonant two-photon excitation (TPE).

6.1 Resonant two-photon absorption

This section will take a closer look at the resonant excitation of the biexciton using a cw laser. To perform such an experiment, the backscattered light of the laser must be attenuated by several orders of magnitude before reaching the spectrometer, in order to be able to detect the QD emission. This straylight suppression was realized with a combination of cross-polarized detection and spectral filtering, as described in chapter 3.4.1. The laser is tuned to $E_B/2$ in the center of the X- and XX-emission, to meet the resonance condition for the two-photon absorption. The approximate spectral position can be estimated from PL measurements, but for finding the resonance, it is necessary to finetune either the laser excitation or the QD transition. Tuning the laser strongly will deteriorates the straylight suppression, since both the polarization and spectral filtering are highly susceptible to wavelenght changes. It is therefore more feasible to make use of the Stark-effect for this finetuning.
Figure 6.1a shows a spectrum of such an experiment performed on *QD2*. Here the laser was tuned to $E_{Laser} = 1342.14$ meV and set to a power of 0.1 mW, resulting in a TPE-resonance at a voltage of $V_{\text{bias}} = 0.230$ V. The spectrum clearly shows the expected biexciton cascade, consisting of the lines X and XX, with residual laser light in the center. The measurement shows a biexciton binding energy of $\Delta E_B = 3.15$ meV.

If the laser is tuned to a lower energy the resonance condition is met at a lower diode voltage. An exemplary measurement is displayed in figure 6.1b. Here the laser was tuned to $E_{Laser} = 1341.54$ meV resulting in a resonance at $V_{\text{bias}} = 0.086$ V. This spectrum shows two significant changes compared to the spectrum taken at $V_{\text{bias}} = 0.230$ V. The most striking difference is the appearance of an additional line at $E_{X^+} = 1342.20$ meV. By comparison with voltage dependent PL-data, this line can be attributed to the positive trion (X^+). The appearance of this line under resonant excitation has also been reported in literature[95]. Furthermore, the amplitude of the X-emission is now weaker than the XX-emission, suggesting that not the entire biexciton population decays via the biexciton cascade. This is supported by the visibility of the X^+-emission. The TPE-process will be investigated more closely in the following chapters.

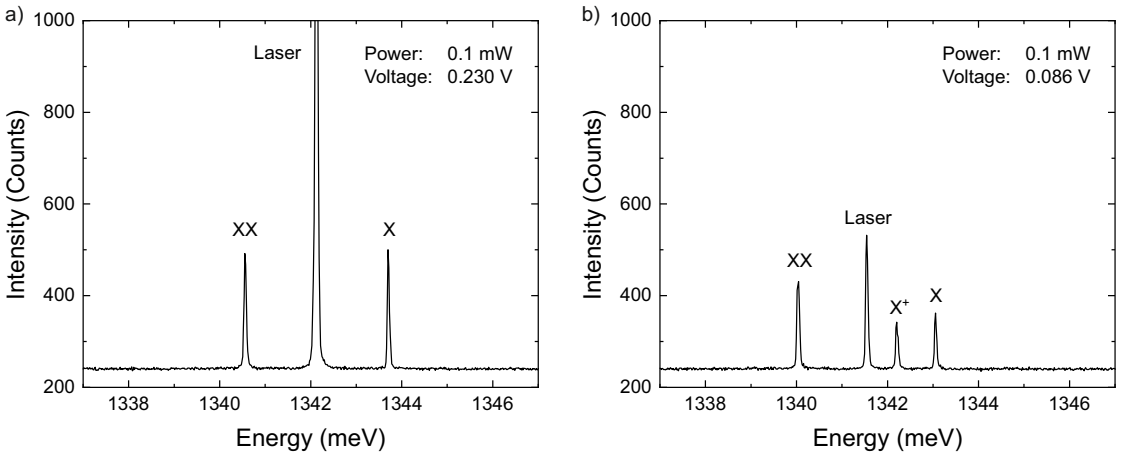

Figure 6.1: Resonant two-photon excitation of the biexciton a) When the laser is tuned to $E_B/2$ the biexciton state is excited via a two-photon absorption process. The system then decays in a cascaded process via the exciton state, resulting in the two emission lines X and XX. ($V_{\text{bias}} = 0.230$ V) b) When this experiment is performed under a lower bias voltage the two emissions show different intensity and additionally the X^+-line appears. ($V_{\text{bias}} = 0.086$ V)

6.1.1 Linewidth of the two-photon resonance

In this chapter, the linewidth of the two-photon absorption will be investigated. The linewidth can be determined, following a strategy similar to the one employed for the exciton in chapter 5.2. The Stark-effect is used to detune the QD in relation to the laser. While doing so the emission of the X and XX is used to monitor the absorption. Such a measurement is displayed in figure 6.2.

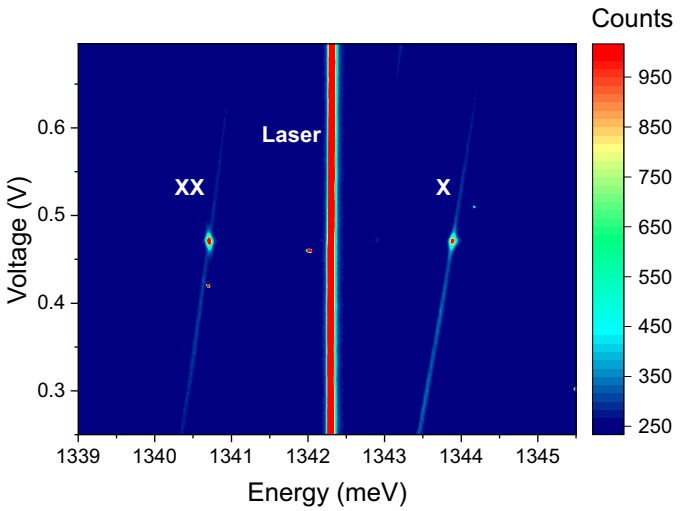

Figure 6.2: Voltage induced detuning during TPE experiment The diode voltage is used to sweep the two-photon resonance through the laser energy. In this way the line shape of the resonance can be obtained.

The data shows the TPE resonance at $V_{\text{bias}} \approx 0.47$ V, with the X emitting at $E_X = 1344.0$ meV and the XX at $E_{XX} = 1340.5$ meV. From this data the voltage-dependent intensity of X and XX, as well as the parameters for the Stark-effect can be extracted. Since this measurement is performed with a moderate excitation power of 0.5 mW, it shows a weak off-resonant excitation of the QD. This reveals the Stark-effect of both emission lines. This off-resonant excitation is caused by a phonon-assisted process, which is discussed in more detail in chapter 6.2.

For a further analysis of the data, the spectral position and size of the emission peaks need to be extracted. This was realized using a script that searches each spectrum for peaks above an adjustable threshold and returns the wavelength with the highest intensity. Figure 6.3a shows the emission energy of X and XX in dependence of the voltage applied to the diode. Both data sets are fitted with a parabolic function resulting in:

$$E_X(V_{bias}) = 1342.899 \text{ meV} + 2.303 \frac{\text{meV}}{\text{V}} \cdot V_{bias} - 0.436 \frac{\text{meV}}{\text{V}^2} \cdot V_{bias}^2 \tag{6.1}$$

$$E_{XX}(V_{bias}) = 1339.903 \text{ meV} + 1.876 \frac{\text{meV}}{\text{V}} \cdot V_{bias} - 0.345 \frac{\text{meV}}{\text{V}^2} \cdot V_{bias}^2 \tag{6.2}$$

From these functions, the Stark-shift of the $|B\rangle$-state can be obtained by

$$E_B(V_{bias}) = E_X(V_{bias}) + E_{XX}(V_{bias}) \tag{6.3}$$

The biexciton energy therefore experiences a Stark-shift roughly twice as large as the exciton or biexciton lines (see figure 6.3).

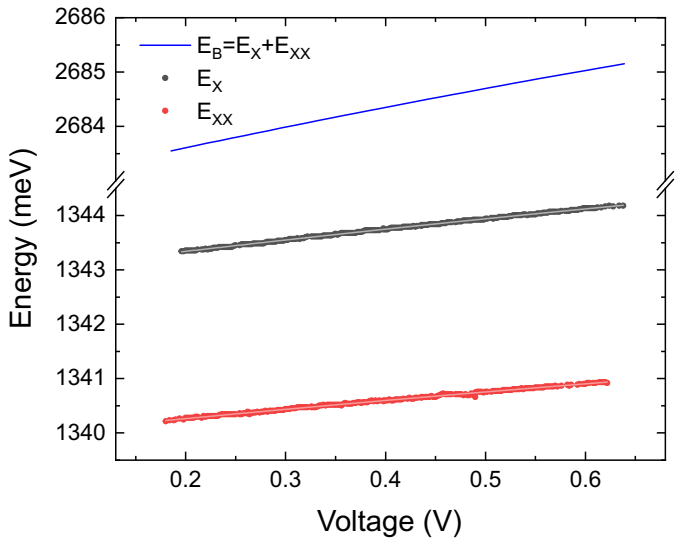

Figure 6.3: Stark-shift of exciton and biexciton emission Both emission lines (E_X and E_{XX}) show a parabolic Stark-shift of comparable magnitude. The Stark-shift of E_B is given by the sum of both emission lines and is hence roughly twice as strong.

The obtained relation can now be used to transform the applied diode voltage into the corresponding biexciton energy to determine the linewidth of the two-photon absorption (see figure 6.4a). Both emissions show a distinct peak at 2684.6 meV, which

corresponds to two times the laser energy. The X-emission is roughly 30% weaker than the XX-emission. This might be connected to the weak emission from the X^+, which is visible in the raw data (see figure 6.2). Both peaks are very well described by a Lorentzian function, delivering linewidth of $\mathrm{FWHM}_X = 24.8 \pm 0.5$ μeV from the X-line and $\mathrm{FWHM}_{XX} = 23.3 \pm 0.4$ μeV from the XX-line. Since both lines show the absorption linewidth of the TPE and not the linewidth of the corresponding emission line, the two obtained values can be averaged. This delivers a linewidth of $\mathrm{FWHM} = 24.1 \pm 0.5$ μeV for an excitation power of 0.5 mW and a diode voltage of $V_{\mathrm{bias}} = 0.47$ V. Both the laser power and the diode voltage will however influence the measured linewidth and hence motivate a more detailed analysis.

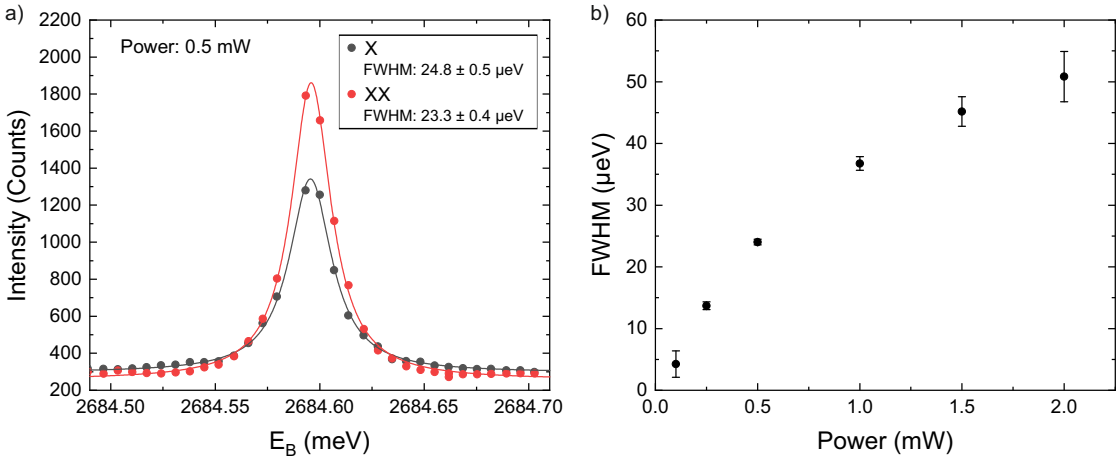

Figure 6.4: Linewidth of the two-photon absorption a) After calibration of the energy scale using the obtained Stark-shift parameters, the linewidth of the two-photon absorption can be determined. The resonances appearing in both emission lines are well described by Lorentzian fit functions. b) The linewidth of the two-photon absorption for varied excitation power at $V_{\mathrm{bias}} = 0.47$ V. The data clearly shows the powerbroadening of the absorption.

Figure 6.4b shows the linewidth of the two-photon absorption for a series of excitation powers. This data clearly shows the powerbroadening of the transition, which is well known from atomic physics[29] and the linear absorption of the exciton[122]. This effect is caused by a saturation of the absorption in the center of the resonance, where the dipole-matrix element is the strongest, while the sides of the resonance still benefit from increased excitation power[2]. The lowest linewidth observed in the low power limit is $\mathrm{FWHM} = 4.2 \pm 2.1$ μeV.

6.1.2 Powerdependence of the two-photon absorption

This chapter will now take a closer look at the powerdependent behavior of the two-photon process. The dynamics in the system can be described by rate equations for the involved transitions. In case of the resonant TPE experiment, the QD can be described by a three-level system, consisting of the ground state $|G\rangle$, the exciton $|X\rangle$ and the biexciton $|B\rangle$ (see figure 6.5)

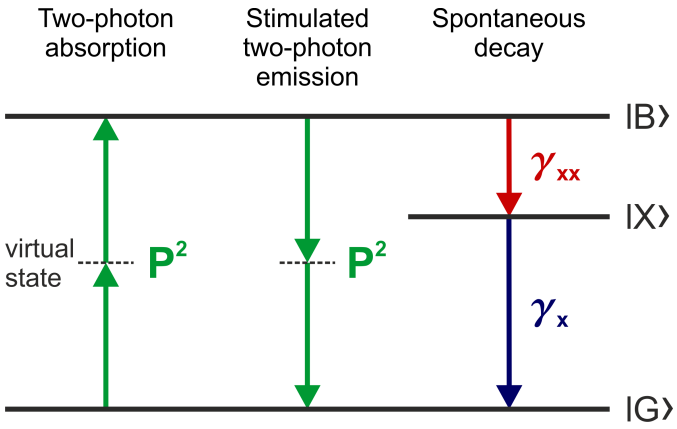

Figure 6.5: Optical transitons in a three-level system under two-photon driving The transition rate of the laser induced processes of two-photon absorption and two-photon emission scale quadratically with the excitation power P^2 , while the spontaneous decay is characterized by the constant decay rates γ_{xx} and γ_x.

In order to describe the dynamics of this system, four transitions must be taken into account. On the one hand, there are the laser driven processes of (stimulated) absorption and stimulated emission. Since the Einstein-coefficients of both processes are equal and both of them are two-photon transitions, they scale quadractically with the normalized excitation power $\tilde{P}$[56]. On the other hand, there are the two spontaneous emission processes from $|B\rangle$ to $|X\rangle$ with the transition rate γ_{xx} and from $|X\rangle$ to $|G\rangle$ with the transition rate γ_x.

Based on these contemplations, the rate equations for the populations of the three states $N_{|B\rangle}$, $N_{|X\rangle}$ and $N_{|G\rangle}$ are given by

$$\frac{dN_{|B\rangle}}{dt} = N_{|G\rangle} \cdot \tilde{P}^2 - N_{|B\rangle} \cdot \tilde{P}^2 - N_{|B\rangle} \cdot \gamma_{xx} \stackrel{!}{=} 0 \tag{6.4}$$

$$\frac{dN_{|X\rangle}}{dt} = N_{|B\rangle} \cdot \gamma_{XX} - N_{|X\rangle} \cdot \gamma_X \stackrel{!}{=} 0 \tag{6.5}$$

$$\frac{dN_{|G\rangle}}{dt} = -N_{|G\rangle} \cdot \tilde{P}^2 + N_{|B\rangle} \cdot \tilde{P}^2 + N_{|x\rangle} \cdot \gamma_x \stackrel{!}{=} 0 \tag{6.6}$$

Since the system is continuously driven, it will converge into a steady state. Under this condition, all three equations must be equal to zero. Together with the condition that the entire population must add up to one.

$$N_{|G\rangle} + N_{|X\rangle} + N_{|B\rangle} = 1 \tag{6.7}$$

the system of equations can be solved, delivering the following equations:

$$N_{|B\rangle} = \frac{\tilde{P}^2}{\tilde{P}^2 \left(2 + \frac{\gamma_{xx}}{\gamma_x}\right) + \gamma_{xx}} \tag{6.8}$$

$$N_{|X\rangle} = N_{|B\rangle} \frac{\gamma_{xx}}{\gamma_x} \tag{6.9}$$

$$N_{|G\rangle} = 1 - N_{|B\rangle} - N_{|x\rangle} \tag{6.10}$$

In the limit of weak excitation the population shows a parabolic powerdependence:

$$\tilde{P}^2\left(2+\frac{\gamma_{xx}}{\gamma_x}\right) \ll \gamma_{xx} \qquad \Rightarrow \qquad N_{|B\rangle} \approx \frac{\tilde{P}^2}{\gamma_{xx}} \tag{6.11}$$

For large excition power, on the other hand, the equations shows a saturation:

$$\tilde{P}^2\left(2+\frac{\gamma_{xx}}{\gamma_x}\right) \gg \gamma_{xx} \qquad \Rightarrow \qquad N_{|B\rangle} \approx \frac{1}{2+\frac{\gamma_{xx}}{\gamma_x}} \underbrace{=}_{\gamma_{xx}=2\gamma_x} \frac{1}{4} \tag{6.12}$$

Figure 6.6a shows plots of the powerdependent populations. Both the parabolic powerdependence at low powers and the saturation are clearly visible. It also reveals the different saturated populations of $|B\rangle$ and $|X\rangle$. This results from the different decay rates of both states. The slower decay of $|X\rangle$ creates a bottleneck, effectively accumulating population in this state. This difference in population however, is not observable in the emission intensities of both transistions I_{XX} and I_X, again due to the different transition rates.

$$I_{XX} = N_{|B\rangle} \cdot \gamma_{xx} \qquad\qquad I_X = N_{|X\rangle} \cdot \gamma_x \tag{6.13}$$

This is visible in the plot shown in figure 6.6b.

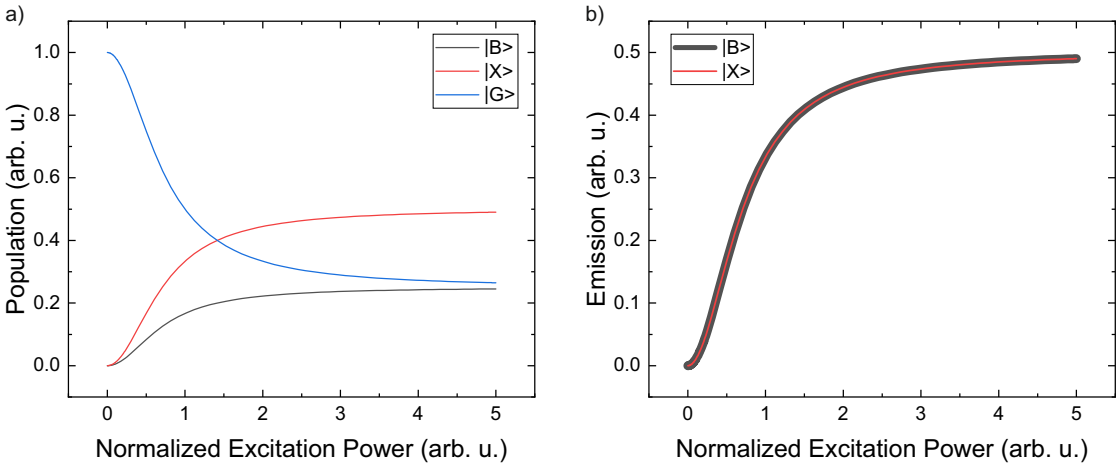

Figure 6.6: Powerdependence of resonant TPE - Theory a) Population in the three states $|G\rangle$, $|X\rangle$ and $|B\rangle$ for $\gamma_{XX}/\gamma_X = 2$. b) Optical emission of the X- and XX-line resulting from these populations. Even though the populations of $|X\rangle$ and $|B\rangle$ are not equal, the two emissions have the same intensity due to their different decay rates.

In order to test the theoretically predicted behavior, a powerdependent TPE experiment is conducted. The excitation power is varied using a filterwheel and an emission spectrum is recorded for each power setting. The result is displayed in figure 6.7a.

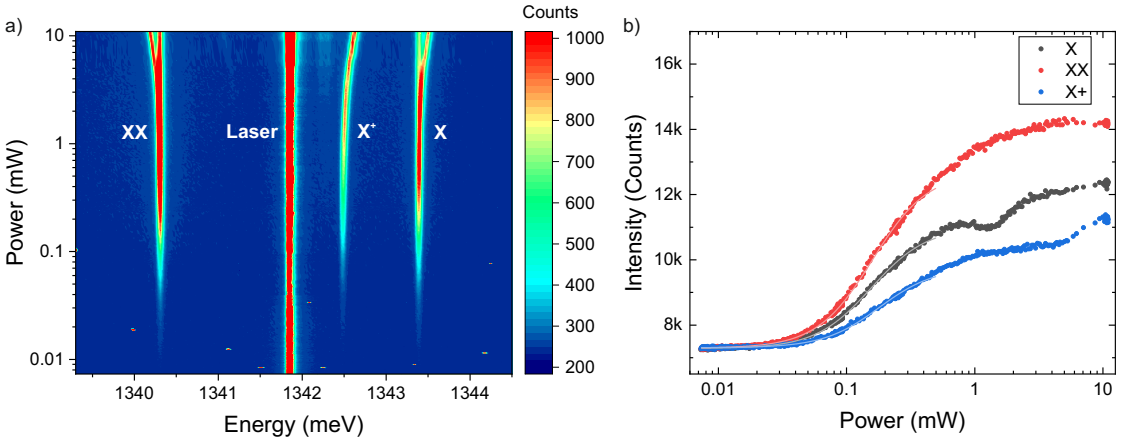

Figure 6.7: Powerdependence of resonant TPE - Experiment a) Powerdependent emission spectrum of a QD under resonant TPE ($V_{\text{bias}} = 0.22$ V) b) Intensities of the three emission lines, extracted by binning of 30 camera pixels.
(Fit: $I(P) = \frac{A \cdot p^2}{B \cdot P^2 + 1} + I_{\text{offset}}$)

Apart from the powerdependence of the TPE, this plot reveals two additional distinct features. Under strong excitation in the range above 5 mW. The X^+-line experiences a shift away from the laser emission towards higher energy. This can be explained by an off-resonant driving of the trion transition by the TPE-laser. This results in an asymmetric rabi-splitting of the of the $|h^+\rangle$- and $|X^+\rangle$-state (see figure 6.8).

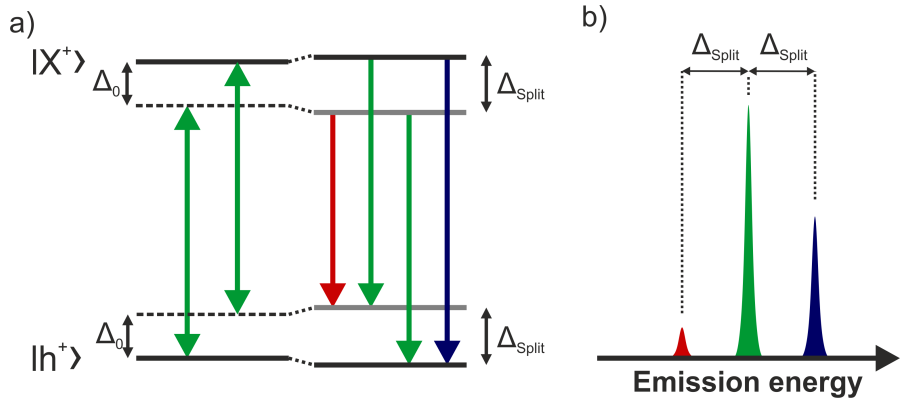

Figure 6.8: Non-resonant driving of the positive trion transition a) The detuned driving by the laser field induces an asymmetric dressing of $|h^+\rangle$ and $|X^+\rangle$. b) The emission resulting from the dressed system contains three lines each separates by Δ_{Split}.

This effect is expected to result in a Mollow-triplet (see 2.4). It consists of the central line, which is in this case not observable, since it has the same energy as the TPE-laser, and the two side bands. The trion emission corresponds in the present case to the sideband on the high energy side and is the stronger one, due to the negative detuning of the driving laser. The sideband on the low energy side is therefore expected symmetrically on the other side of the laser. At that position there is indeed a very weak signal observable, which supports this interpretation (see figure 6.9). The shift of the trion-line

with increasing power can be explained with an increase of the Rabi-frequency, since the splitting between the Rayleigh-line and the side bands obeys

$$\Delta_{\text{Split}} = \sqrt{\Omega_0^2 + \Delta^2}. \tag{6.14}$$

A related effect is observable in the X- and XX-emission. At high excitation power both lines experience a splitting, which is a result of the resonant driving of the $|G\rangle$-$|B\rangle$-transition[20] (see figure 6.9). This effect will be discussed in more detail in chapter 6.3.

As a result of the two effects mentioned above, it is necessary to perform a binning of several camera pixels when extracting the intensity profiles of the emission lines. This compensates minor shifts in the spectral position and the splitting of the X- and XX-lines. In the present case, a binning of 30 pixels was found to be sufficient. The obtained data is displayed in figure 6.7b. All three emission lines show a clear saturation behavior. The intensity of X and XX is however not equal, a behavior already discussed above and probably a result of tunneling effects, since this measurement was performed at a diode voltage of $V_{\text{bias}} = 0.22$ V. The X emission furthermore shows a slight reduction in intensity in the range of 1-2 mW, which is most likely related to some kind of drift in experimental setup. In the regime of weak and moderate excitation the data is very well described by a fitting function based on equation 6.9. For fitting the data, the theoretically derived equation needs to be modified to avoid an overparametrization, resulting in

$$I_{X,XX}(P) = A\frac{P^2}{B \cdot P^2 + 1} + I_0. \tag{6.15}$$

If the data from the regime of strong excitation above 1 mW is included into the fit, this results in larger deviations to the resulting fitting function. This might be the result of a minor laser-induced detuning of the QD, modifying the spectral overlap between the laser and the TPE resonance.

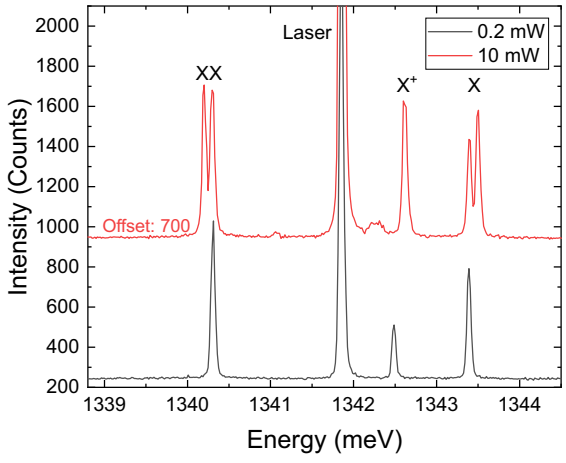

Figure 6.9: Resonant TPE under strong driving Under strong driving both X and XX show a splitting due to a dressing of the system. This also happens at lower excitation power but cannot be resolved by the spectrometer.

6.2 Phonon-assisted two-photon excitation

The resonant two-photon excitation has shown to be an efficient way to prepare the biexciton state. It is however susceptible to slight shifts of the resonance conditions, which can be caused by either an instability of the laser emission energy or fluctuations of the QD transition energy, caused for example by charging in the diode. For experiments on down-conversion processes (see chapter 7), which require the biexciton as initial state, it is desirable to use a more robust process. During the experiments on the linewidth of the resonant TPE, a weak off-resonant excitation of the biexciton was observed. This process can be identified as a phonon-assisted transition, which has been reported in literature [48, 5, 19] and used to perform a robust preparation of the biexciton state for further experiments[106]. The phonon-assisted TPE will therefore be characterized in this chapter.

The phonon-assisted TPE occurs, if the QD is excited by a strong laser field, which is detuned from $E_B/2$. In case of positive detuning ($E_{Laser} > E_B/2$) the excess energy can be absorbed by emitting a phonon. Respectively in the case of negative detuning ($E_{Laser} < E_B/2$), the missing energy can be provided by the absorption of a phonon (see figure 6.10).

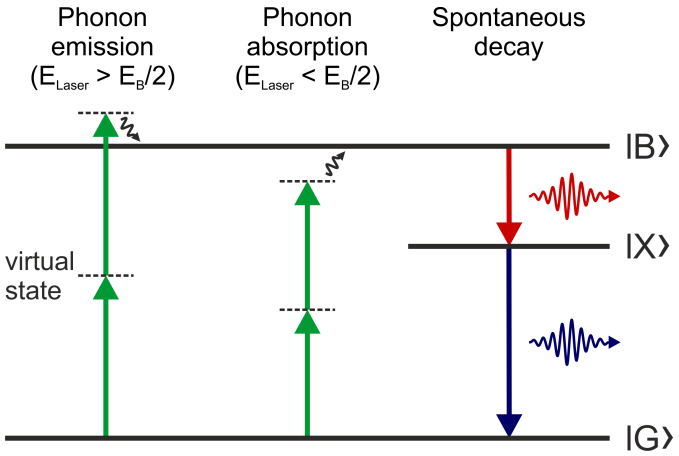

Figure 6.10: Phonon-assisted two-photon absorption - Scheme Under sufficiently strong driving the biexciton state can be excited non-resonantly by a phonon-assisted process. The energy gap between the laser and the biexciton is overcome by emission or absorption of a phonon.

This process only becomes significant under strong excitation. This can be observed in figure 6.11, which shows voltage-dependent emission spectra for moderate a) and strong b) excitation. Under moderate excitation, the resonant process is substantially stronger than the phonon-assisted absorption. This changes under strong excitation. Here, both processes result in a comparable emission intensity, since the resonant excitation is saturated. In the following, this chapter will provide a closer look at the powerdependence of this process.

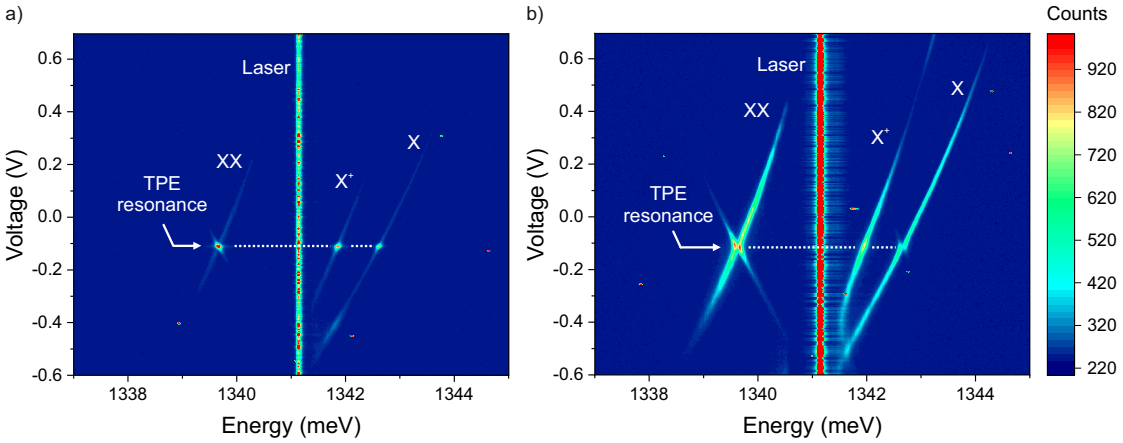

Figure 6.11: Phonon-assisted two-photon absorption a) TPE experiment with low excitation power($P = 0.5$ mW). The QD is only excited when the laser is in resonance with $E_B/2$. b) TPE experiment with high excitation power ($P = 10.0$ mW). Excitation of the biexciton state can be observed up to a detuning of $\Delta E \approx \pm 1$ meV.

6.2.1 Powerdependence

The powerdependence of the phonon-assisted TPE can be described in a similar fashion as the resonant case. The starting point is again an overview of the occurring processes, as illustrated in figure 6.12.

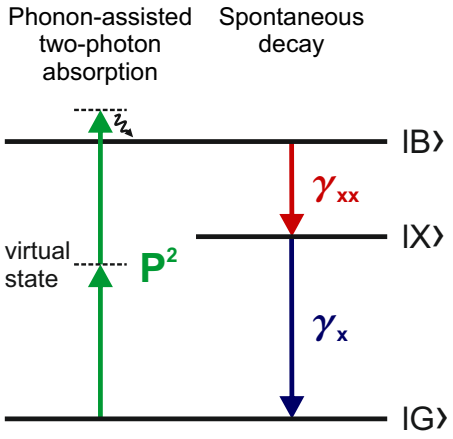

Figure 6.12: Optical transitons in a three-level system under phonon-assisted two-photon driving Like in the resonant case the optically driven excitation scales quadratically with the laser power.

Since the optical absorption is again a two-photon process, it is justified to assume a quadratic power dependence for it. Assuming an inverse process of a phonon-assisted stimulated emission would deliver the same result as the resonant case. For now, such a

process shall be neglected. The rate equations for the system therefore result to:

$$\frac{dN_{|B\rangle}}{dt} = N_{|G\rangle} \cdot \tilde{P}^2 - N_{|B\rangle} \cdot \gamma_{XX} \stackrel{!}{=} 0 \tag{6.16}$$

$$\frac{dN_{|X\rangle}}{dt} = N_{|B\rangle} \cdot \gamma_{XX} - N_{|X\rangle} \cdot \gamma_X \stackrel{!}{=} 0 \tag{6.17}$$

$$\frac{dN_{|G\rangle}}{dt} = -N_{|G\rangle} \cdot \tilde{P}^2 + N_{|X\rangle} \cdot \gamma_X \stackrel{!}{=} 0 \tag{6.18}$$

$$\tag{6.19}$$

In the steady state, all these rates need to be equal to zero and the total population must add up to one.

$$N_{|G\rangle} + N_{|X\rangle} + N_{|B\rangle} = 1 \tag{6.20}$$

Solving this system of equations results in

$$N_{|B\rangle} = \frac{\tilde{P}^2}{\tilde{P}^2 \left(1 + \frac{\gamma_{xx}}{\gamma_x}\right) + \gamma_{xx}} \tag{6.21}$$

$$N_{|X\rangle} = N_{|B\rangle} \frac{\gamma_{xx}}{\gamma_x} \tag{6.22}$$

$$N_{|G\rangle} = 1 - N_{|B\rangle} - N_{|x\rangle} \tag{6.23}$$

The equation for the biexciton population $N_{|B\rangle}$ takes a very similar form as in the resonant case. The only difference is found in the denominator where the "2" in the resonant case was exchanged for a "1". This results from the lack of a stimulated emission process. In the limit of strong excitation, this results in a complete depletion of the ground state (see figure 6.13a).

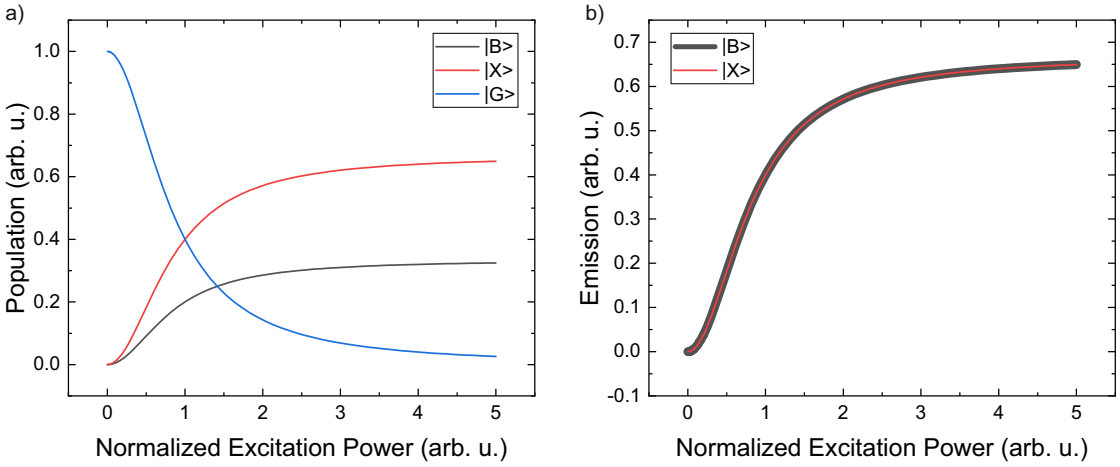

Figure 6.13: Powerdependence of phonon-assisted TPE - Theory a) Population of the three states $|G\rangle$, $|X\rangle$ and $|B\rangle$ for $\gamma_{XX}/\gamma_X = 2$. b) Optical emission of X- and XX-line resulting from these populations. The system qualitatively shows the same saturation as for the resonant case. The absolute values of the saturation however deviate due to the neglect of the stimulated emission process.

Assuming a ratio of $\gamma_{xx}/\gamma_x = 2$ delivers a saturated biexciton population of $N_{|B\rangle} = 1/3$ and an exciton population of $N_{|X\rangle} = 2/3$, resulting in a 33 % increase of the maximum

achievable emission in comparison to the resonant excitation (see figure 6.13). This is however based on the assumption that no stimulated emission occurs.

The theoretical contemplation is tested by a power dependent measurement (see figure 6.14a). At high power the data shows a small shift in energy for all three observable emission lines. This can be associated to an off-resonant driving of the QD, similar to the shift of the trion line in the resonant measurement (see 6.7a).

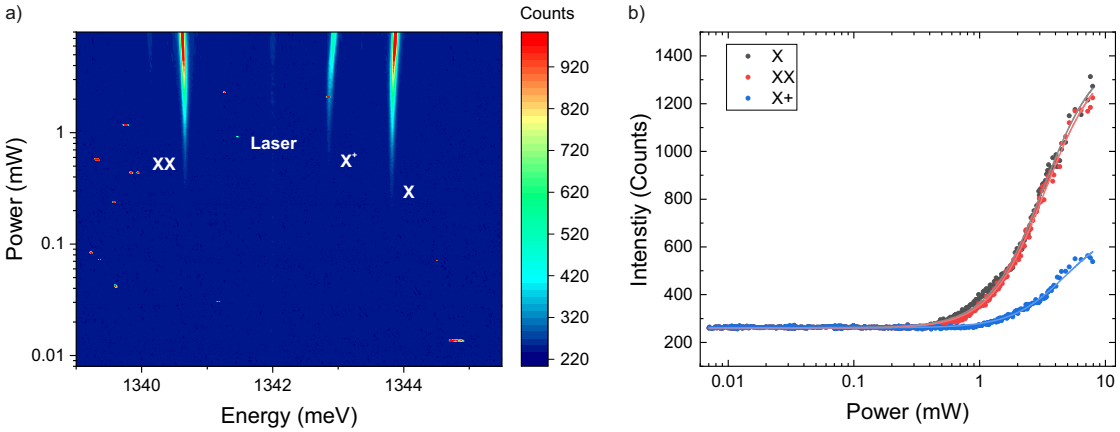

Figure 6.14: Powerdependence of phonon-assisted TPE - Experiment Powerdependent spectrum of a QD under phonon-assisted TPE b) Extracted intensities of the three emission lines. The process needs approximately one order of magnitude more power than the resonant process. (Fit: $I(P) = \frac{A \cdot p^2}{B \cdot P^2 + 1} + I_{\text{offset}}$)

Figure 6.14b shows the intensity profiles of the three observable emissions. They were extracted by selecting the CCD-pixel with the highest counts for each peak. The data clearly shows that the phonon-assisted process requires about an order of magnitude more power than the resonant process to generate a significant biexciton population in the QD (compare to figure 6.7b). In order to use the theoretically derived equation 6.21 as a fitting function, it needs to be modified to account for the experimental conditions and avoid an overparametrization. This results in the same fit function as for the case of the resonant TPE (equation 6.15). The fit therefore offers no information, if a stimulated emission process occurs or not. The resulting fits are in very good agreement with the data, supporting the assumption of a quadratic dependence on the laser power for the phonon-assisted TPE. The required excitation power for this process however turned out to be to high to completely saturate the system with the given setup.

6.3 Dressed states

In the scope of the previous chapters on the resonant and phonon-assisted excitation of the biexciton state, some measurements were presented that revealed a splitting of the X- and XX-line under strong excitation (see figures 6.7a and 6.11b). This splitting is a result of the AC-Stark effect (also known as Autler-Townes effect) and has been observed and studied to some extent in literature[4, 52, 20]. Here, the resonant or near-resonant driving of an optical transition by an oscillating light-field (typically a laser) leads to a

coupling between the electronic states of the QD and the light field and result in new eigenstates for the system, the so-called "dressed states" (see chapter 2.4).

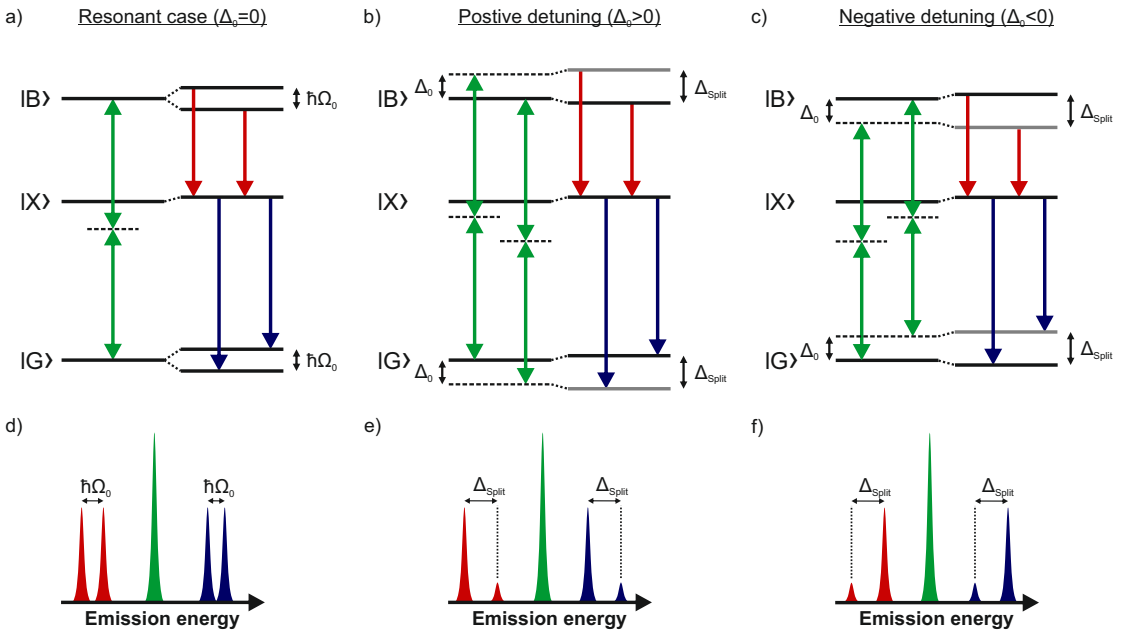

Figure 6.15: Two-photon dressing of the biexciton system a)-c) Energy levels for resonant and detuned laser. d)-f) Corresponding emission spectra. The laser induces a splitting of $|B\rangle$ and $|G\rangle$ and a minor shift of $|X\rangle$. Consequently the X- and XX-lines are also split. The observed splitting Δ_{Split} depends on the Rabi frequency Ω_0 and the detuning Δ_0

In the specific case of the two-photon excitation of the biexciton, the driven transition takes place between the ground state $|G\rangle$ and the biexciton state $|B\rangle$. Hence, these two states are split by the Rabi energy $\hbar\Omega_0$ that drives the transition (see figure 6.15a). This results in a splitting of the XX- an X-line into two lines each, separated also by $\hbar\Omega_0$ (see figure 6.15d).Figure 6.16 shows a two-photon excitation experiment that shows this effect. At a voltage of $V_{\mathrm{bias}} = 0.47$ V the laser is in resonance with $E_B/2$. Hence, the $|G\rangle - |B\rangle$-transition is resonantly driven, leading to an Autler-Townes splitting of the XX- and X-lines. When the laser is detuned from the resonance, the observed splitting increases and the system evolves into a regime where the two lines can be reasonably described as the undisturbed X- (or XX-)line, which is the stronger emission and the emission from (or into) a laser induced virtual state. Figure 6.15b and c show sketches of the energy levels for the detuned cases.

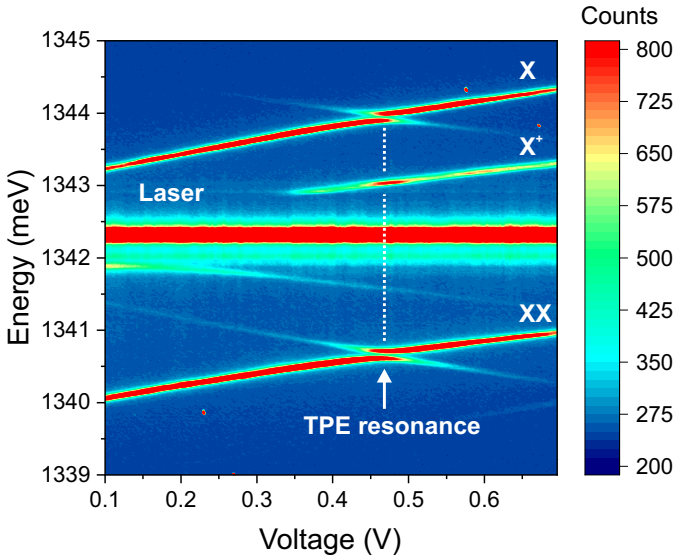

Figure 6.16: Experimental observation of biexciton dressing In resonance a splitting of X and XX is observable. When the system is detuned by changing the bias voltage of the diode, an anti-crossing can be observed in both lines. ($P = 10$ mW)

Based on literature[82] the following relation between the detuning Δ_0 and the observed splitting Δ_{Split} is expected here.

$$\Delta_{Split} = \sqrt{\Omega_0^2 + \Delta_0^2} \tag{6.24}$$

This behavior can be tested by rescaling the x-axis into the detuning relative to the two photon transition ($\Delta_0 = 2E_{Laser} - E_B$) and the y-axis into the energy relative to the undisturbed X- (figure 6.17a) and XX-line (figure 6.17b). Both rescalings are carried out using the Stark-shift from the undisturbed X- and XX-lines. Far away from the resonance, the emission can be clearly identified as the X (or XX) and its dressed counterpart. This classification is however not possible in a regime close to the resonance. This regime is dominated by the coupling between the excitonic states of the QD and the photonic states of the light field, which leads to new eigenstates in the system. In order to account for this, the low enegy branch will be labeled A and the high energy branch will be labeled B during this section.

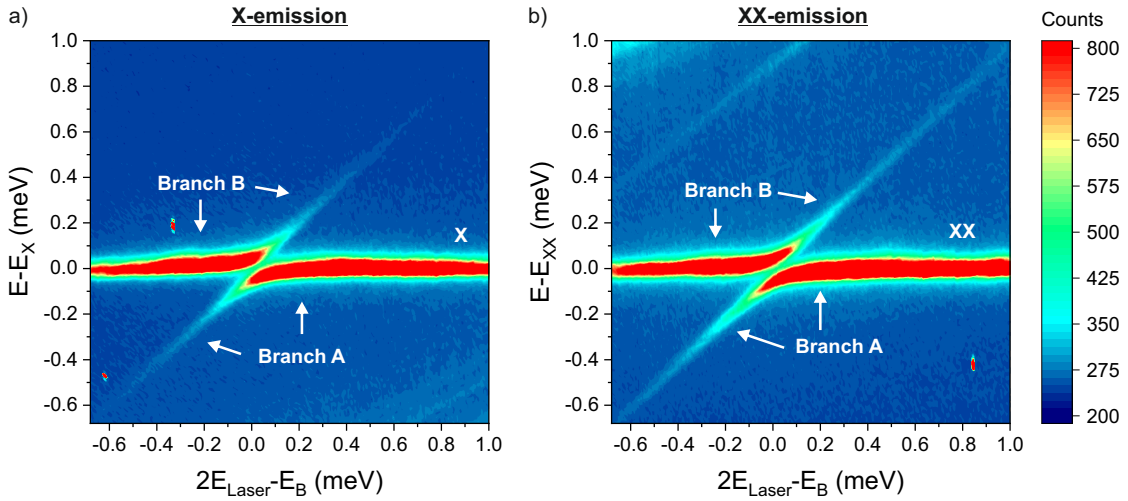

Figure 6.17: Anti-crossing of X and XX with calibrated energy scale Close up of the anti-crossings observed at the X (a) and XX line (b). The energy scale is calibrated using the Stark effect parameters for X and XX obtained from the raw data.

In the plots in figure 6.17 one can already observe that in a regime reasonably far away from the anti-crossing the splitting between the dressed and the unperturbed emission is at least roughly equal to the detuning of the two-photon excitation. This behavior can be intuitively explained by sketching the energy levels in the system, like it is shown in figure 6.15b and c. Furthermore it follows from equation 6.24 for the limit of large detuning:

$$\Delta_0 \gg \Omega_0 \qquad \Rightarrow \qquad \Delta_{Split} \approx \Delta_0 \tag{6.25}$$

For a deeper analyis of this behavior, a subsample of the spectra shown in figure 6.17 was fitted with Lorentzian functions to obtain the exact position of each peak. This allows for a precise determination of the splitting. The results of this analysis are shown in figure 6.18 for the X-line (a) and the XX-line (b). In both cases the splitting shows a minimum for a detuning of zero and an approximately linear behavior far off the resonance. The data is very well descibed by a fitting function based on equation 6.24. The fit therefore delivers a reliable value for the Rabi energy: $\hbar\Omega_0 = 99.0 \pm 2.7$ µeV from the X-line and $\hbar\Omega_0 = 98.6 \pm 1.6$ µeV from the XX-line. These two values are equal within the error range. It can therefore be concluded that the $|G\rangle$ and $|B\rangle$ experience the same Rabi-splitting.

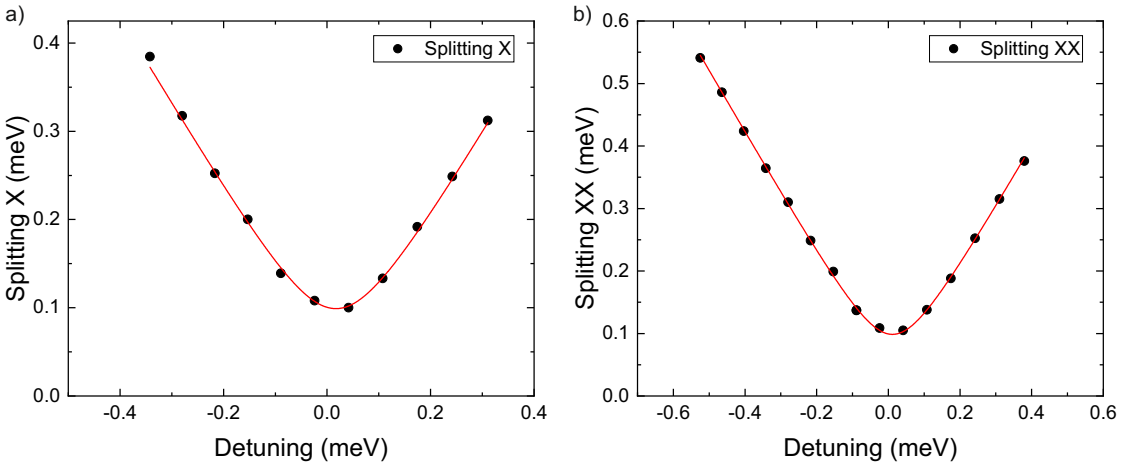

Figure 6.18: Energy splitting in the anti-crossing Energy difference between the two branches of the anti-crossing plotted over the laser detuning for a) the X-emission and b) the XX-emission. (Fit: $\Delta_{\mathrm{Split}} = \sqrt{(\Delta_{\mathrm{Laser}} - \Delta_{\mathrm{offset}})^2 + (\hbar\Omega_0)^2}$)

Another interesting aspect in this regard is the intensity of the dressed emission in relation to its detuning from the undisturbed QD emission. To investigate this the peak amplitude of both branches of the emission (A and B) are plotted against the detuning relative to the undisturbed emission. These values are determined from the fits already performed previously. In order to account for general changes of the intensity induced by sweeping the diode voltage during the measurement, the peak amplitudes are normalized to the sum of both branches. The result of this analysis is displayed in figure 6.19 for both emission lines. The emission clearly decreases as the absolute value of the detuning increases. This behavior is very well-described by independent Lorentzian functions for each branch. The profile is symmetric around a detuning of zero for X and XX. This is supported by the equal width of the Lorentzian functions resulting from the fits of both branches: $\mathrm{FWHM}_{X,A} = 92.6 \pm 4.2$ µeV and $\mathrm{FWHM}_{X,B} = 96.6 \pm 6.7$ µeV for the X-line and $\mathrm{FWHM}_{XX,A} = 142.4 \pm 6.8$ µeV and $\mathrm{FWHM}_{XX,B} = 140.4 \pm 14.4$ µeV for the XX-line. Around the XX-line the dressed emission is observable for larger detuning. This is already visible in the raw data (see figure 6.17) and now supported by the larger width of the Lorentzian functions. This might be connected to the overall larger intensity of the biexciton emission.

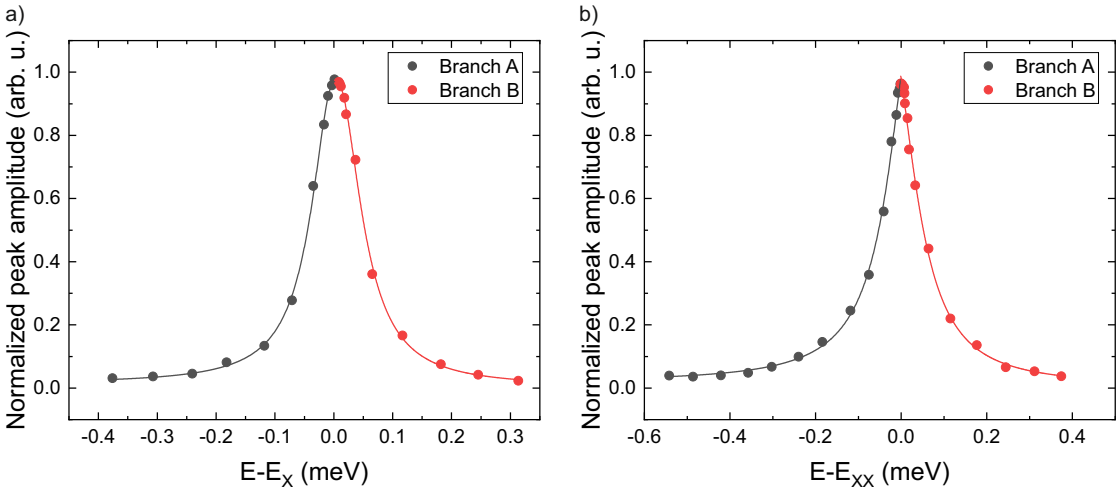

Figure 6.19: Intensity of the two branches of the anti-crossing The intensity of both branches of the anti-crossing is plotted against the detuning relative to the unperturbed emission of a) the X and b) the XX-line. Each branch is well described by one side of a Lorentzian function.

6.4 Origin of the trion emission

During the previous experiments dealing with two-photon excitation of the biexciton, under certain conditions the positive trion line (X^+) is observable. This raises the question for the mechanism that leads to this emission, since the trion is not a regular part of the biexciton cascade. In order to learn more about the processes at work here, a set of voltage dependent measurements and a set of correlation measurements were conducted and will be presented in the following.

6.4.1 Voltagedependence of biexciton decay

The main difference between the two measurements in figure 6.1, one showing trion emission, while the other one does not, is the applied diode voltage at the resonance condition. This qualifies tunneling processes as a potential candidate for the mechanism behind the trion emission and motivates an investigation of the influence of the diode voltage on the biexciton cascade.

For this purpose a series of measurements is performed. The TPE laser is systematically varied in emission energy and thus changing the diode voltage, where the two-photon resonance occurs. The voltage is then set to this value, by maximizing the QD emission and the resulting spectrum is recorded. The resulting peak amplitudes of X, XX and X^+ are then plotted against the diode voltage. Figure 6.20a shows a measurement performed using low excitation power of 0.1 mW. The diagram can be divided into three major regimes.

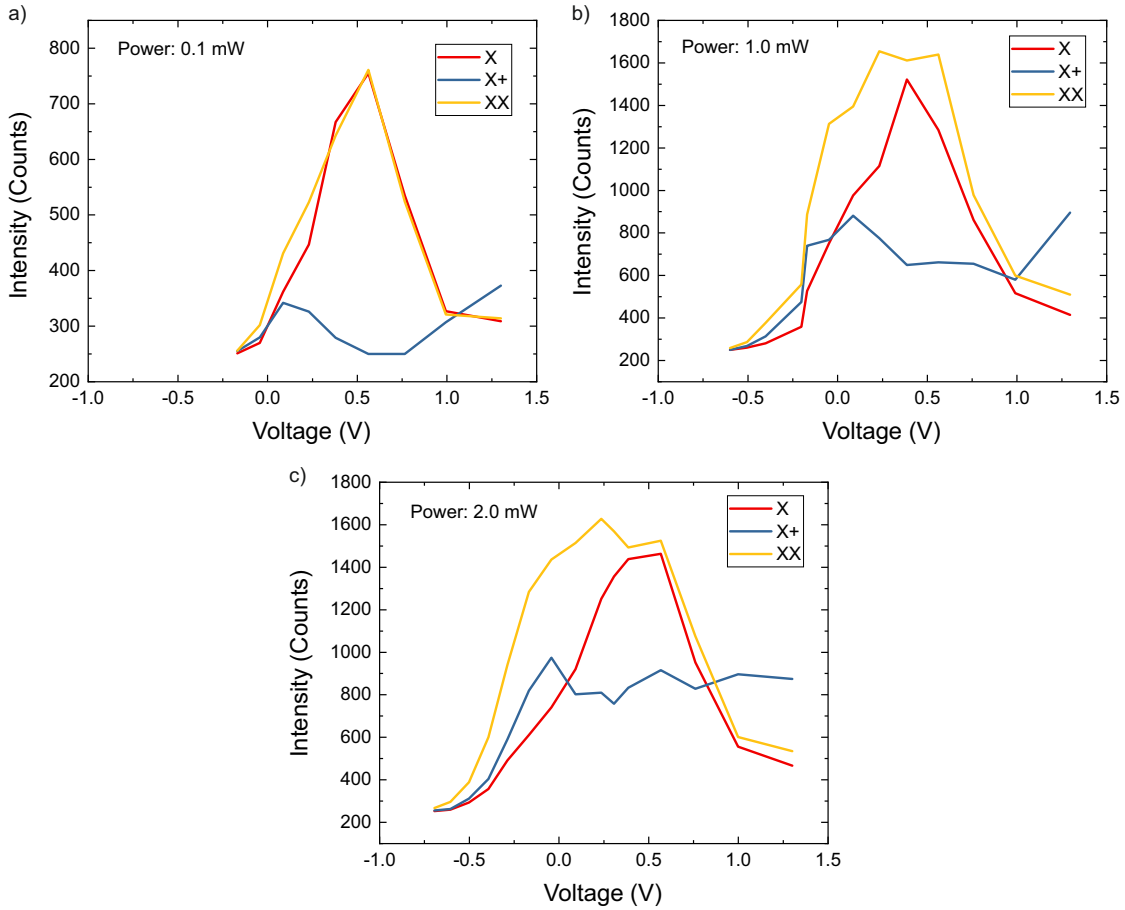

Figure 6.20: Voltage dependence of biexciton decay Intensity of the three emission lines X, X^+ and XX under resonant excitation of the biexciton state for a series of bias voltages at a) low, b) moderate and c) increased excitation power. The ratio of the emission from the positive trion shows a dependence of the applied bias voltage and generally increases with the laser power.

Towards high forward voltages the intensity of both X and XX strongly decreases, while the X^+ appears at about $V_{\text{bias}} = 0.75$ V and then grows in intensity. This behavior can be explained by charging of the QD with carriers from the doped regions. Since in this sample the QDs are located exactly in the center of a pin-structure, in principle both types of carriers can tunnel into the QD. In this specific sample, charging with holes from the p-doped region seems to be more likely than charging with electrons from the n-doped region, as can be concluded from the PL characterization (see chapter 5.1). The QD, being charged with a hole, can then not be excited into the biexciton state and thus decreases the emission of both X and XX. The contribution of the X^+ emission might be a result of a off-resonant excitation of the trion state, a process that was already observed in chapter 6.1.2.

At moderate forward voltages only emission of X and XX is observable. Both are of equal intensity and reach their maximum in this regime. Here the forward voltage is too low to induce charging of the QD with holes from the p-region. The laser can therefore

very efficiently excite biexcitons in the QD. Since the diode voltage is still high enough to prevent carriers from tunneling out of the QD, as can be concluded from the photocurrent characterization (see chapter 5.2), the entire population recombines optically leading to a strong emission.

This changes in the regime of low forward or negative voltages applied to the diode. Here, the overall intensity decreases and a trion emission becomes observable. The system is clearly entering the photocurrent regime, causing an increasing portion of the population to recombine electrically and thus decreasing the overall optical emission from the QD. Since the biexciton generally has a smaller optical lifetime compared to the exciton[126, 94], it is less affected by the tunneling, explaining the slight difference in intensity between X and XX. The tunneling processes can also explain the visibility of X^+ emission in this regime. In a QD, the electron usually has a shorter tunneling time than the hole[44]. This leaves the QD in a positively charged state for a limited amount of time. Since cw excitation was used in this experiment, an off-resonant excitation of the trion can occur during this time, leading to a corresponding emission.

This measurement shows that in case of low excitation power, the emission of the biexciton cascade is strongly determined by tunneling effects. This may however change to a certain degree, if increased excitation power is used. Therefore, the experiment is repeated using an increased excitation power of 1 mW and 2 mW (see figure 6.20b and c). As expected under these conditions, an overall increase of the signal, compared to the low power case, is observable. The emission of X and XX shows indication for a saturation between the measurements performed with 1 mW and 2 mW. This is investigated in more detail in chapter 6.1.2. In these two cases the X^+ is observable over the entire voltage range where optical recombination is dominant and becomes stronger with increasing laser power. In the 1 mW case an increased X^+ emission is observable in the regimes of high and low voltages, similar to the low power case, but vanishes in case of the 2 mW measurement. This behavior indicates that, in addition to tunneling effects, there is another laser induced effect generating positively charged trions that becomes more dominant at high exciation power. A possible candidate is the generation of free carriers in the sample, possibly via two-photon processes [99] or excitation in the wettinglayer tail [70] that are then captured by the QD. Furthermore a laser induced loss of an electron from the neutral exciton state via the internal photoeffect[74] might lead to a charging of the dot.

6.4.2 Correlation measurements

Further insight into this matter can be provided by correlation measurements. They provide information on which emissions occur simultaneously and which exclude each other. Therefore a series of such measurements was carried out.

During these measurements, the biexciton state is excited via phonon-assisted TPE, to achieve a stable excitation, which is insensitive towards minor drifts of the laser or the QD resonances. This is of particular importance during these measurements due to the long integration times of several hours. Figure 6.21a shows a spectrum of the QD under

phonon-assisted TPE at a diode voltage of $V_{\text{bias}} = 0.4$ V. These conditions are used for the following correlation measurements. For the actual measurements the individual lines are isolated (see figure 6.21b) using tunable bandpass filters and sent towards the APDs.

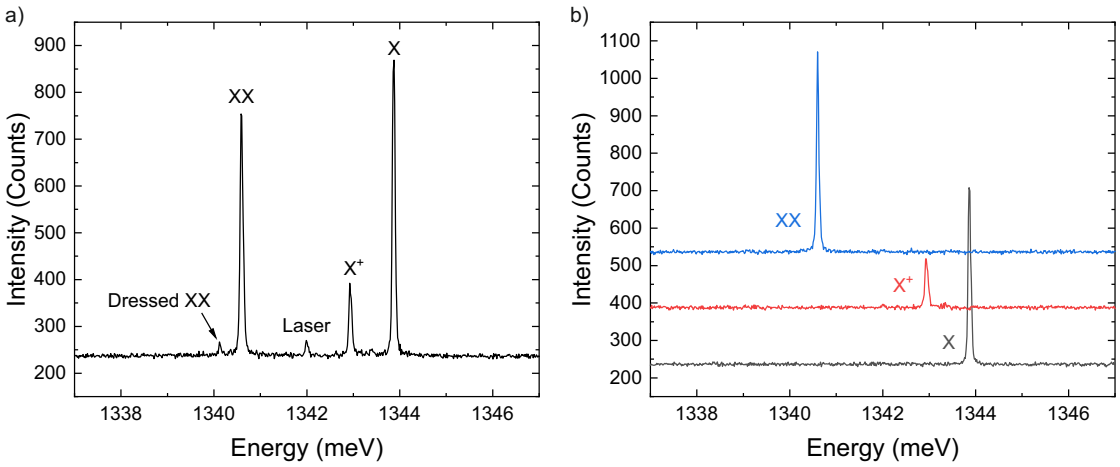

Figure 6.21: Spectral filtering for correlation measurements a) Spectrum of a QD under phonon-assisted TPE b) The same spectrum filtered by tunable bandpass filters, spectrally isolating individual emission lines. ($V_{\text{bias}} = 0.4$ V)

Figure 6.22a and b show autocorrelation measurements of the X- and XX-emission. Both lines show a bunching on long time-scales and an anti-bunching on short time scales. This behavior can be described by a combination of two exponential functions as discussed in chapter 2.6. The anti-bunching indicates single photon emission from both the exciton and biexciton line. The width of these dips is $t_{X,anti} = 1.34 \pm 0.31$ ns for X and $t_{XX,anti} = 1.26 \pm 0.27$ ns for the XX. Due to the limited time resolution of the APDs of 1 ns, these dips cannot be fully resolved and the observed width is mainly determined by the detectors. However, the biexciton cascade is generally associated with high-quality single photon emission[93, 111]. The bunching on the other hand, is well resolvable with these detectors as it has longer time constants of $t_{X,bunch} = 5.29 \pm 0.95$ ns and $t_{XX,bunch} = 4.72 \pm 0.83$ ns. A behavior like this, anti-bunching on short and bunching on long timescales, is typically associated with blinking of the selected line[125], meaning that the conditions in the QD are randomly changing between two states, where only one allows the emission of the biexciton cascade.

An autocorrelation measurement of the positive trion (X^+) shows a similar behavior (see 6.22c). Due to the lower countrate of this emission, a longer integration time was necessary. Here, the anti-bunching is even narrower ($t_{X^+,anti} = 0.56 \pm 0.15$ ns) and barely resolvable due to the limited time resolution. The bunching behavior however is resolvable and delivers a time constant of $t_{X^+,bunch} = 5.23 \pm 0.32$ ns. Within the error range this value is equal to the bunching observed for the X- and XX-emission.

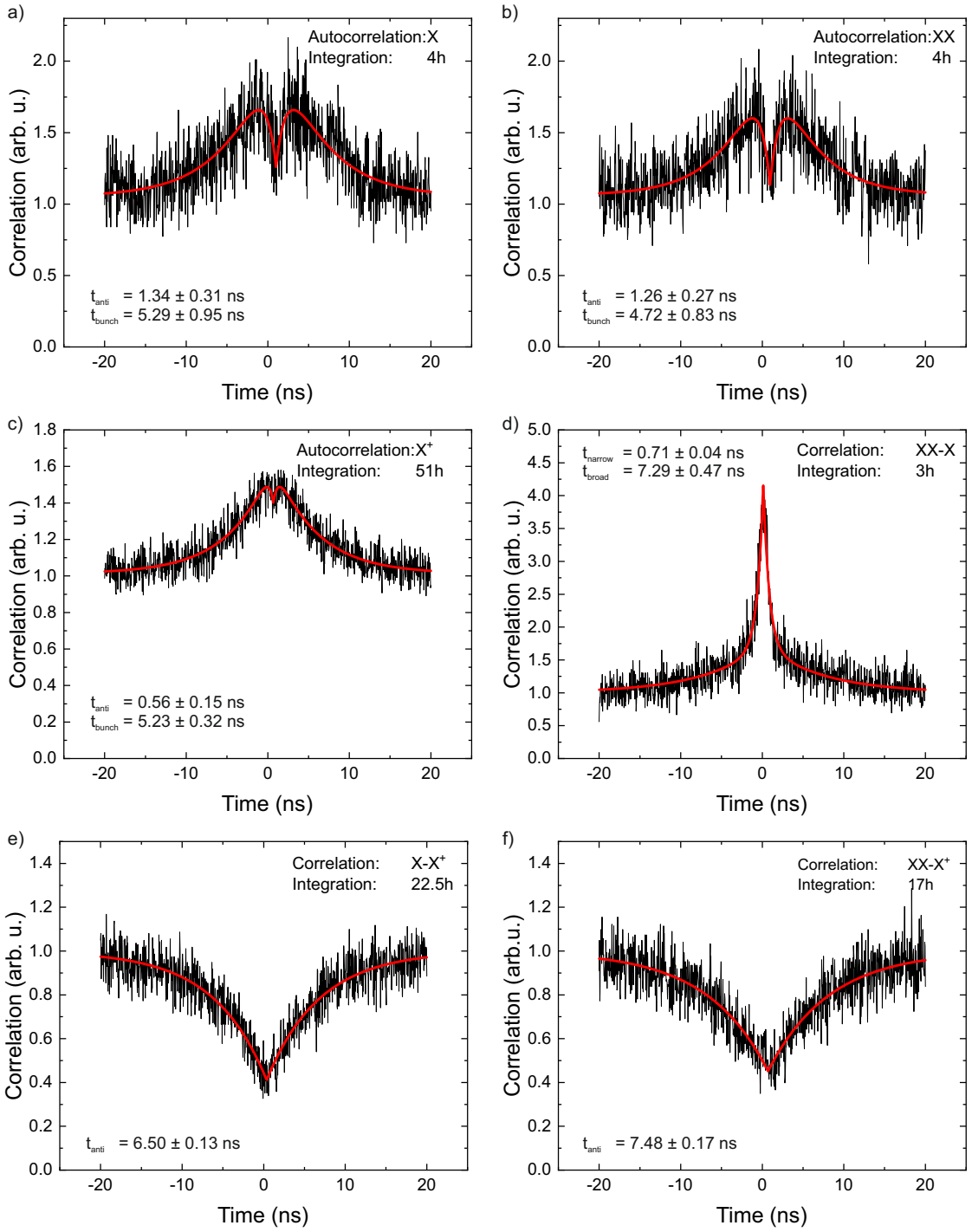

Figure 6.22: Correlation measurements of emission lines occurring during biexciton decay a) Auto-correlation of X b) Auto-correlation of XX c) Auto-correlation X^+ d) Cross-correlation of XX and X e) Cross-correlation of X and X^+ f) Cross-correlation of XX and X^+. During these experiments, the biexciton state is excited by phonon-assisted TPE. Please note that due to the limited time resolution of the detectors the anti-bunching in a)-c) as well as the expected asymmetry of the bunching in d) cannot be fully resolved.

Based on these measurements alone, it is not yet possible to determine, if the QD is switching between the X^+-emission and the XX-X-cascade or if both occur simultaneously. In order to resolve this question, a series of cross-correlation measurements were carried out. Figure 6.22d shows a cross correlation of X and XX. Here, a strong and narrow bunching and a weak broad bunching are observable. The narrow bunching ($t_{narrow} = 0.71 \pm 0.04$ ns) results from the basic nature of the cascade, which first emits an XX-photon, followed by an X-photon. This should result in an asymmetric peak with bunching on the one side and anti-bunching on the other[66]. This is however not resolvable with the used detectors. The broad and weak bunching ($t_{broad} = 7.29 \pm 0.47$ ns) is again associated with the fast switching.

The most insightful measurements, are the cross-correlations between the trion emission and the X-line (see figure 6.22e) and the XX-line (6.22f). Both measurements show a broad anti-bunching with $t_{X-X^+,anti} = 6.50 \pm 0.13$ ns and $t_{XX-X^+,anti} = 7.48 \pm 0.17$ ns. This means that neither of the two emissions of the biexciton cascade occur together with the trion emission. It can therefore be concluded that the QD experiences a switching between the biexciton cascade and the trion emission.

6.4.3 Discussion

By combining the results from the voltage dependent measurements with correlation measurements, one can get a basic understanding of the mechanism behind the trion emission during the two-photon excitation experiments. The correlation measurements show that the QD is switching between a neutral and a charged configuration, on a timescale of several nanoseconds. While the QD is in the neutral configuration, the biexciton cascade is resonantly driven by the laser, but when the QD switches into the charged configuration, this is no longer possible. Instead, the positive trion is then off-resonantly excited, leading to the X^+ emission (see figure 6.23). The effect of off-resonant driving of the X^+ was already observed in the resonant TPE experiment under strong driving (see figure 6.7).

The remaining open question is the one for the exact process that causes the fast switching between these two configurations. It is reasonable to assume that the QD must exchange carriers (e^- or h^+) with the surrounding host material. Figure 6.23 illustrates four possible transition channels that could in principle contribute to the switching, although with different transition rates. These rates will of course be subject to change when experimental parameters such as the diode voltage and the laser power are varied.

The voltage dependent measurements show that under the influence of large electric fields within the diode (reverse bias), tunneling of carriers out of the QD becomes more likely. Typically the electron has a shorter tunneling time [44], which will lead to a loss of an e^- from the $|B\rangle$- or $|X\rangle$-state and result in a transition to the charged configuration. Since the lifetime of $|B\rangle$ is typically shorter than that of $|X\rangle$, it is more likely for the exciton to loose an electron. If the QD is in the positively charged configuration, tunneling of a hole from either of the two states $|h^+\rangle$ or $|X^+\rangle$ will bring the QD back into the neutral configuration.

Since the sample used for these measurements contains a pin-structure, charging with both types of carriers is possible under forward bias conditions, which is especially relevant here, since the QDs are located in the exact center of the intrinsic region. This charging can be a cause for a transition between the two configurations. These contemplations are in good aggreement with the experimental observations in figure 6.20a.

Further experiments, with increased power suggest that there is also a laser induced mechanism for the exchange of carriers. Possible candidates are the internal photoeffect [74] or the generation of free carriers by the laser, e.g. through two-photon excitation in the host material[99] or absorption in tail states[70].

In summary, the experiments presented here, shine some light into the mechanism behind the trion emission. A fast switching between a neutral and a charged configuration combined with an off-resonant driving of the $|h^+\rangle - |X^+\rangle$-transition was identified. The mechanism behind the switching however remains uncertain to some degree but must involve an exchange of carriers with the host material. In order to investigate this in more detail, more experiments would be required.

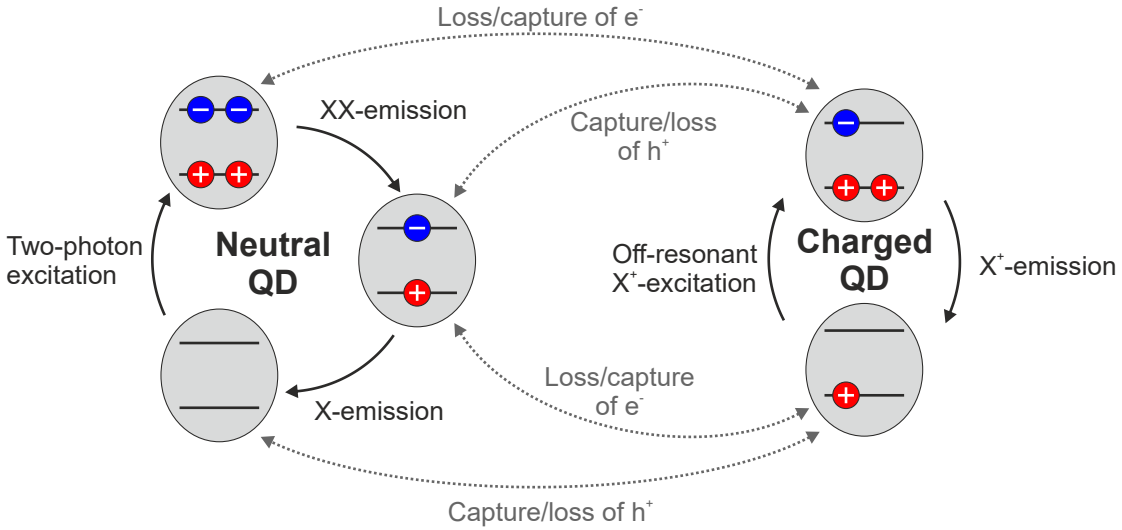

Figure 6.23: Proposed mechanism behind the occurrence of the positive trion emission The QD is either found in a neutral configuration, where two-photon excitation drives the emission of the biexcitons cascade or a charged configuration, where off-resonant excitation of the trion state drives the corresponding emission. The system can switch between the two configurations via several channels, which all involve the loss or capture of single electrons or holes.

6.5 Two-photon Rabi rotations

The previously discussed methods for the biexciton preparation used cw excitation leading to a statistical population that saturates clearly below $N_{|B\rangle} < 1$. By switching to an excitation with ps optical pulses the coherent properties of the quantum system can be exploited to achieve near perfect population inversion for both one-photon (eg. exciton)[137] and two-photon transitions (eg. biexciton)[121]. This technique is widely used to generate on-demand single photons[53, 93, 124].

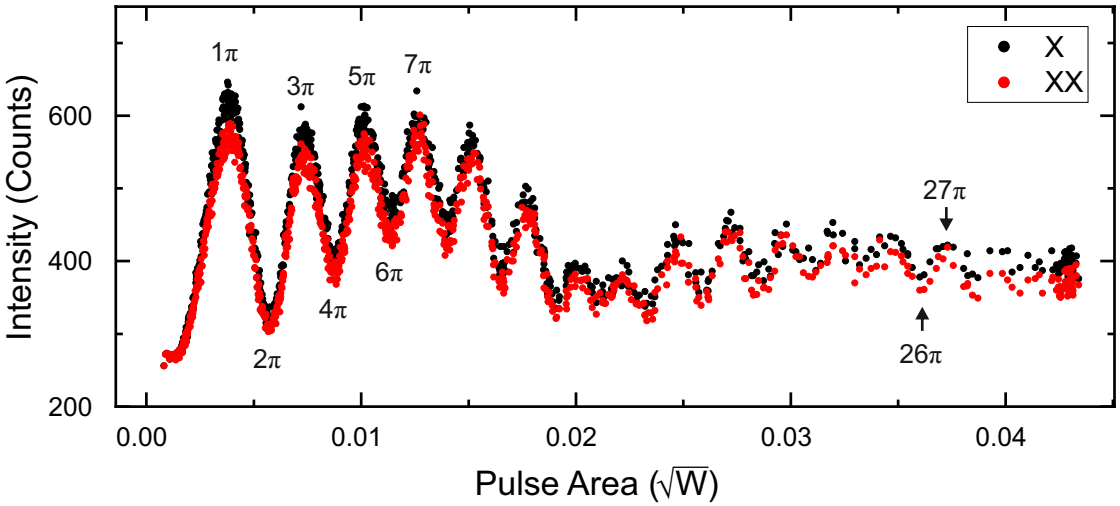

Figure 6.24: Biexciton Rabi rotations The system shows synchronous Rabi rotations of X and XX up to a pulse area of up to 27π.

To perform such an experiment the Ti:Sa laser is operated in ps-mode. The laser spectrum is filtered by a bandpass filter to suppress unwanted background emission and to decrease the spectral width of the pulses (see chapter 3.2.2). Both help with the suppression of unwanted back-scattered light. The laser is tuned to $E_B/2$ to be in resonance with the two-photon transition from $|G\rangle$ to $|B\rangle$. In order to observe Rabi rotations the laser power is varied during the experiment. Figure 6.24 shows the result of such an experiment performed at a diode voltage of $V_{\text{bias}} = 0.3$ V. Here, the intensity of both the X- and XX-line is plotted over the square root of the laser power, which is proportional to the pulse area. Both lines show the clear signature of Rabi rotations. The amplitude of the oscillations decreases towards high pulse area and oscillations are observable up to a pulse area of 27π. The data is furthermore superimposed with an additional slow oscillation, the origin of which cannot be uncovered based on the available data.

In order to use this technique for state preparation the laser is set to a power that corresponds to a pulse area of 1π.

6.6 Conclusion

In this chapter, a thorough study of the two-photon excitation of the biexciton state was conducted. It was found that the resonant process using a cw laser provides an efficient way of excitation but is very susceptible to drifts of the laser emission energy or the bias voltage applied to the diode, due to the narrow linewidth of the transition.

As an alternative a phonon-assisted two-photon process was studied. It requires a higher excitation power of roughly a factor of 10, but leads to a more robust preparation of the biexciton state. A tuning range of 2 meV could be realized using this method, making it a valuable tool for further experiments that require a population of the biexciton state.

The high laser power however, causes the appearance of two additional effects: a splitting of the exciton and biexciton line due to a dressing of the system and a strong emission from the positive trion. Both effects were subjected to a detailed investigation as they will be observable if the phonon-assisted process is used in further experiments.

Additionally, the resonant excitation of the biexciton using short optical pulses was briefly investigated. During this experiment Rabi rotations could be observed up to a pulse area of 27π.

In summary, this chapter provides valuable knowledge on the state preparation necessary for the experiments on nonlinear downconversion, which will be the subject of the following chapter.

7 Nonlinear down-conversion in a single quantum dot

The following chapter presents the experiments on nonlinear down-conversion in a single quantum dot, which form the main results of this work. The process is a two-transition from the biexciton state into the ground state. Hence, the biexciton state $|B\rangle$ needs to be populated, which can be achieved in a very efficient manner by resonant two-photon excitation[4] and, in case of pulsed excitation, also on-demand[93]. Furthermore phonon-assisted two-photon excitation provides robustness against detuning for the price of higher required excitation power[5, 19, 106]. These processes have been thoroughly studied in the previous chapter. For stimulating the down-conversion process a control-laser is used, which off-resonantly drives the system (see 7.1). This laser induces a virtual state and thus opens a new decay path, which is detuned from the biexciton-cascade. During this process, two photons are emitted simultaneously. The first of which inherits the properties of the control-laser field, while the second photon, the stimulated down-conversion (SDC) photon, must have complementary properties to ensure the conservation of energy and angular momentum in the system. This means that the process can be used to tailor the single photon emission of the quantum dot. As was already shown by theoretical studies, it is possible to control the emitted photons in energy, polarization, spectral shape and emission time[55, 22, 23].

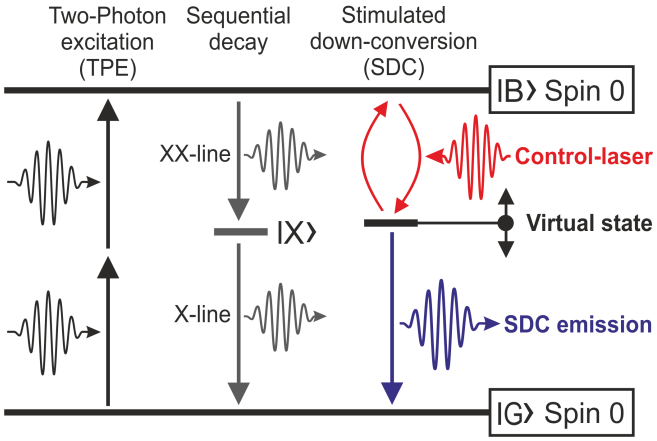

Figure 7.1: Nonlinear down-conversion scheme After preparation of the biexcitons state $|B\rangle$, a virtual state is defined by the non-resonant control-laser, opening an alternative decay channel in addition to the biexciton cascade.[61]

Even though processes like this are known from atomic physics[134, 21], it has not yet been realized in single quantum dots. There are however studies conducted on Λ-systems in charged quantum dot molecules that investigate a similar process. They use

their so-called Raman-process to perform energy tuning[123] and pulse shaping[103]. As pointed out by *Breddermann et al.* this Raman-process in a Λ-system is mathematically equivalent to the nonlinear down-conversion in the exciton-biexciton ladder system [23].

7.1 Experimental demonstration

As discussed above, the starting point for the nonlinear down-conversion is the preparation of the biexciton state. For the following experiments phonon-assisted TPE with a cw laser was chosen. This process reliably excites biexcitons, even under considerable detuning in the range of meV. Furthermore, the cw excitation makes timing considerations between the TPE- and control-laser unnecessary. Figure 7.2 shows experimental data of phonon-assisted TPE for varied bias-voltage. The laser was tuned to 1341.17 meV and set to a power of 12 mW to achieve saturated excitation conditions. For the experiments in this chapter, the setup with polarization suppression was used. Therefore, the backscattered laser light is suppressed by a combination of polarization filtering and two notch filters.

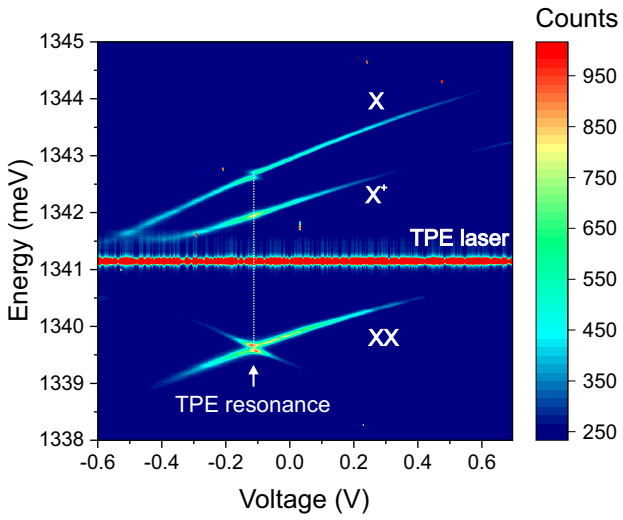

Figure 7.2: Robust preparation of the biexciton state The biexciton state is excited non-resonantly via phonon-assisted TPE under saturated conditions ($P_{TPE} = 12$ mW). This results in a population of the biexciton state, which is robust against detuning and forms the basis for studying the down-conversion process.[61]

The measurement shows robust preparation of the biexciton state over a tuning range of roughly 2 meV, centered around the TPE resonance at $V_{bias} = -0.12$ V. As already discussed in chapter 6.4, the positive trion X^+ is also observed in this measurement, but does not hinder the further experiments and interpretations.

This robust preparation of the biexciton forms an ideal foundation for the down-conversion experiment, since it allows the identification of the SDC-emission based on its distinct Stark-shift fingerprint. In figure 7.2 we can observe that the X- and XX-line experience an approximately equal Stark-shift. From this we can conclude that the biexciton state $|B\rangle$ experiences a Stark-shift approximately twice as large as the exciton state $|X\rangle$. This tuning behavior is sketched in Figure 7.3.

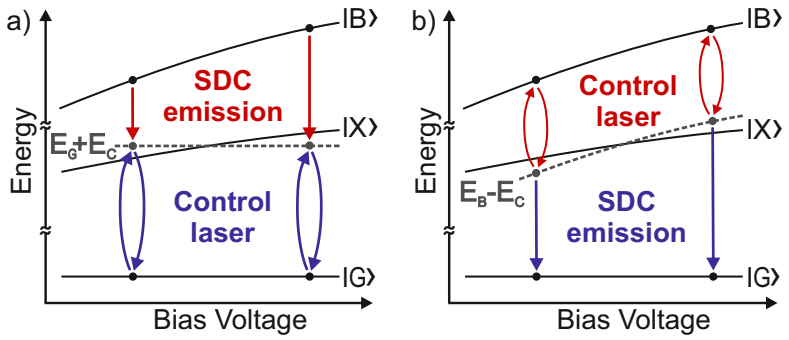

Figure 7.3: Stark-shift of SDC emission Two equivalent cases can be identified: a) Control-laser close to X transition b) Control-laser close to XX transition. In both cases the SDC emission inherits the Stark-shift of $|B\rangle$, which is roughly twice as strong as the shift of X or XX.[61]

If a control-laser with an energy of E_C is introduced, one can differentiate two scenarios for the formation of a virtual state. Figure 7.3a shows a scenario where the virtual state is defined relative to the ground state at $E = E_G + E_C$. This scenario becomes relevant when the control-laser is tuned close to the X-line, since the strongest SDC signal is expected if the virtual state is energetically close to the exciton state. In this case the virtual state can be considered as the final state of the SDC transition. The second scenario is depicted in figure 7.3b. Here, the virtual state is defined relative to the biexciton state at $E = E_B - E_C$. This means that the laser should be tuned close to the XX-line to achieve a good signal. In this case, the virtual state forms the initial state of the SDC transition. For both cases we can conclude that the SDC-emission inherits the Stark-shift from the biexciton state and can therefore be identified in a voltage dependent measurement.

This strategy can now be employed to analyze the data displayed in figure 7.4. Here, the biexciton was excited via phonon-assisted TPE under comparable conditions like in figure 7.2, but now a control-laser was introduced and focused on the QD. Due to the selection rules for the SDC process the laser and SDC are expected to have the same linear polarization. Therefore, this laser cannot be suppressed by polarization filtering. For this reason the straylight suppression must rely on spectral filtering, which is in this case realized by two notch filters. As a result of this, the QD emission close to the control-laser cannot be observed in the experimental data.

In figure 7.4a the control-laser was tuned to an energy close to the X-emission. We can observe the SDC emission close to the XX-line with the expected Stark-shift signature (sum of the slopes of X- and XX-line). At a bias-voltage of about $V_{bias} = 0.2$ V the SDC emission shows an avoided crossing with the XX-line. This coincides with the voltage where the control-laser is in resonance with the X-transition. Under this condition, the exciton and ground state are split due to the AC-Stark effect (dressed) resulting in the appearance of a Mollow-triplet (see figure 7.5a). Due to the spectral filtering, this is not observable in the experimental data. It is however clearly visible in the corresponding simulation (see figure 7.4c). The dressing of the exciton state therefore explains the avoided crossing of the SDC emission.

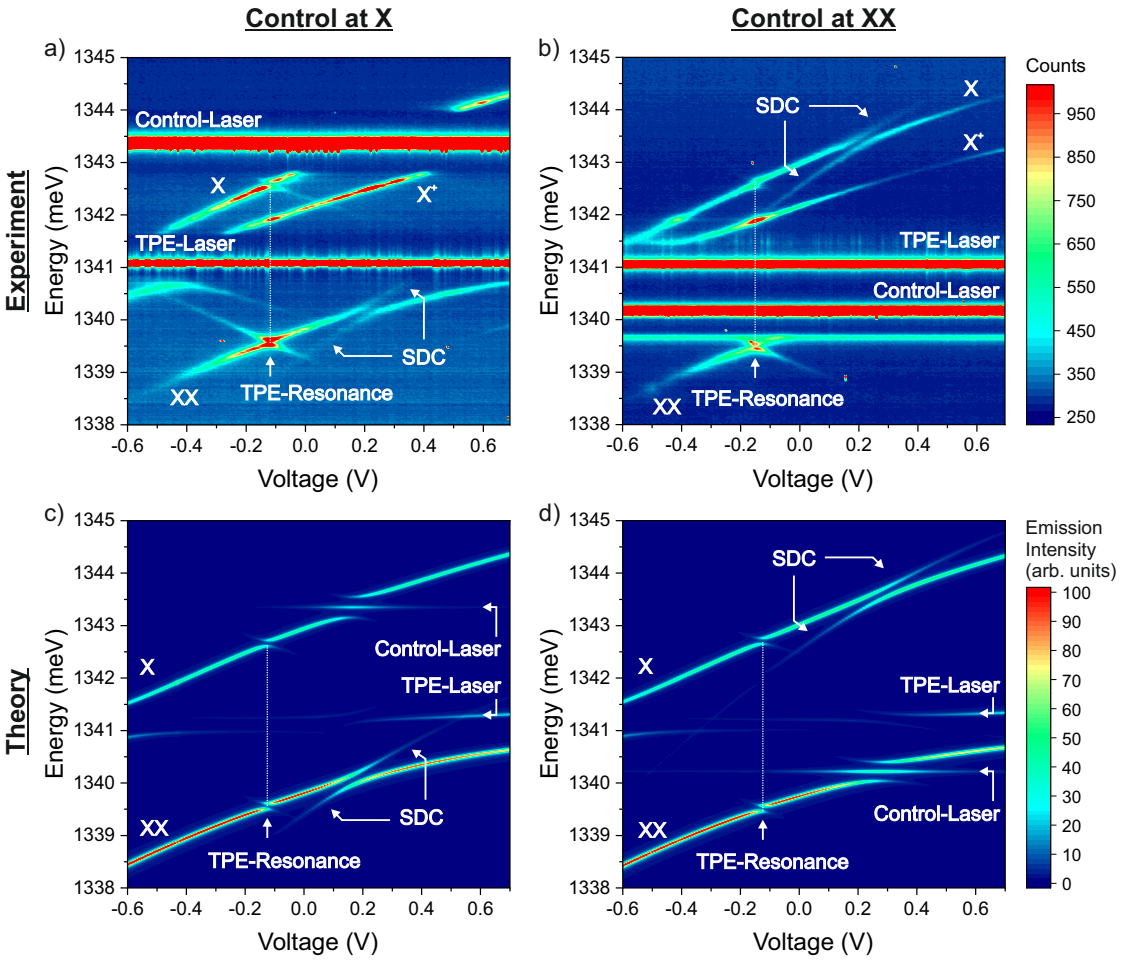

Figure 7.4: Identification of SDC emission Experimental data with the control-laser tuned close to a) the X emission and b) the XX emission. (P_{TPE} = 10 mW, P_{Control} = 1.5 mW) c) Corresponding theoretical data for case (a) ($\hbar\Omega_0 = 0.198$ meV) d) Corresponding theoretical data for case (b) ($\hbar\Omega_0 = 0.189$ meV) The SDC emission is identified based on it's Stark shift fingerprint.[61]

Figure 7.4b shows an equivalent measurement with the control-laser tuned close to the XX-transition energy. Here one can observe the SDC emission with the expected Stark-shift around the X-emission. Again, an avoided crossing can be observed at $V_{bias} = 0.2$ V, this time with the X-line, when the laser is in resonance with the XX-line. The theoretical data again reveals the Mollow-triplet.

The simulations shown in figure 7.4c and d were kindly provided by Dr. Dirk Heinze from the group of Prof. Stefan Schumacher. The calculations are based on a density matrix description of the electronic states ($|G\rangle$, $|X_{H,V}\rangle$ and $|B\rangle$) and a classical light field. The off-resonant phonon-assisted excitation is implemented using an incoherent pump term. The time evolution of the system is calculated using the von-Neumann equation, including pure dephasing and radiative losses. A more detailed discussion of the theoretical model can be found in the methods section of [61]. The Stark-shift

applied in the simulation was obtained from the experimental data in figure 7.2.

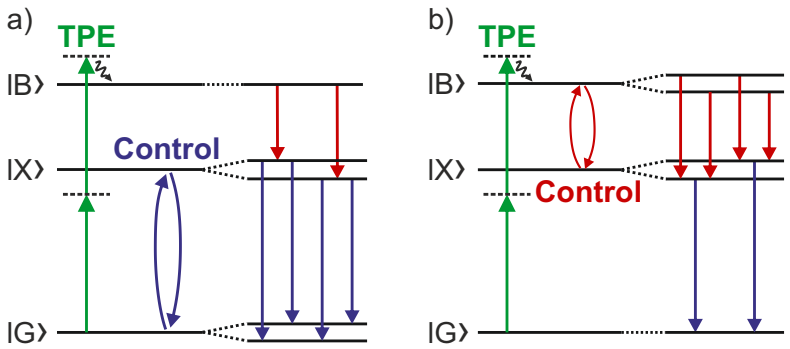

Figure 7.5: Autler-Townes splitting for resonant control laser a) When the control-laser is in resonance with X-line it dresses this transition forming a Mollow triplet while the XX-line is split into the Autler-Townes douplet. b) When the control-laser is in resonance with the XX-line the same effects occur on the other lines respectively.[61]

Based on the available data the desired down-conversion process can be clearly identified due to it's unique Stark-shift behavior, while the good agreement between experiment and theory supports the interpretation of the experimental data. Based on these findings a more detailed study of the nonlinear down-conversion can be conducted with a focus on several aspects, which will be presented in the following sections.

7.2 Analysis of the anti-crossing

The anti-crossing observed in the data shown in figure 7.4, is an unexpected feature, when considering the SDC as a nonlinear process involving a virtual state that acts as the intermediate level. On the other hand, this behavior can be intuitively explained in a dressed state picture. It is therefore interesting to perform a more detailed analysis of this feature to gain more insight into the relation between these two models. To this end the data is analyzed in the same fashion as discussed in chapter 6.3, when analyzing the anti-crossing occurring at the TPE-resonance. Accordingly, a sub-sample of the recorded spectra was fitted with Lorentzian functions to obtain information on the amplitude and spectral position of the emission.

Figure 7.6 shows the splitting Δ_{Split} between the SDC emission and the a) XX-line b) X-line plotted against the detuning $\Delta_{\text{L-X/XX}}$ between the control-laser and the a) X-line b) XX-line respectively. $\Delta_{\text{L-X/XX}}$ is determined by considering the Stark-shift parameters of X and XX obtained from the data presented in figure 7.2.

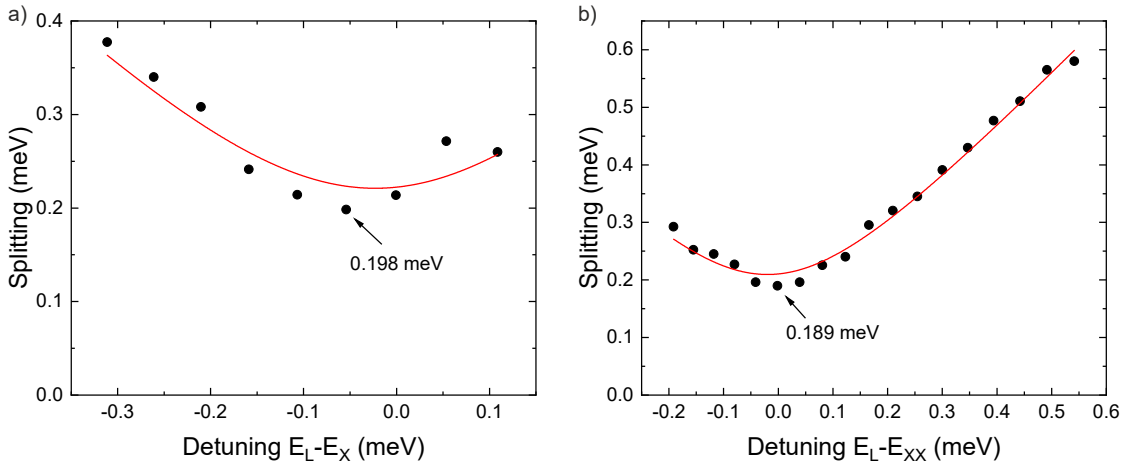

Figure 7.6: Anti-crossing of SDC-emission Energy difference between the SDC and a) the XX-line b) the X-line plotted over the laser detuning (Fit: $\Delta_{\text{Split}} = \sqrt{(\Delta_{\text{L-X/XX}} - \Delta_{\text{offset}})^2 + (\hbar\Omega_0)^2}$)[61]

For large detuning the data is reasonably well-described by a fitting function based on $\Delta_{Split} = \sqrt{\Delta^2_{\text{L-X/XX}} + \hbar^2\Omega_0^2}$. Close to the resonance however, it shows a non-neglectable deviation, which influences the obtained Rabi energy $\hbar\Omega_0$ and leads to an overestimation. For this reason the data point with the lowest splitting was chosen as input parameter for the simulations presented in figure 7.4c and d. Using this value leads to a much better agreement between theory and experiment than the value obtained from the fit. Table 7.1 summarizes the obtained Rabi energies.

	Rabi energy $\hbar\Omega_0$	
	Control at X	Control at XX
Fit	0.221 ± 0.01 meV	0.210 ± 0.005 meV
Data Point	0.198 meV	0.189 meV

Table 7.1: Rabi energy of the control-laser The Rabi energy obtained from the fit function is in both cases slightly higher than the value taken from the single data point of the minimal splitting.

The experimental data shown in figure 7.4 shows a difference in the SDC intensity depending on whether it occurs close to the X- or the XX-line. Especially the case of negative detuning relative to the X-line shows a stronger signal than the other cases. This behavior shall now be investigated in more detail. Figure 7.7 shows the intensity of the SDC emission in dependence of it's detuning from the undisturbed X/XX-emission. Diagrams a) and b) show experimental data extracted from the spectra shown in figure 7.4, while c) and d) show corresponding theoretical data. The intensities were determined by fitting the experimental and theoretical spectra with Lorentzian functions. Since the overall brightness of the QD varies over the tuning range, the obtained intensity values were normalized to the sum of SDC and X/XX $\left(I_{\text{SDC,norm}} = \frac{I_{\text{SDC}}}{I_{\text{SDC}}+I_{\text{X/XX}}}\right)$.

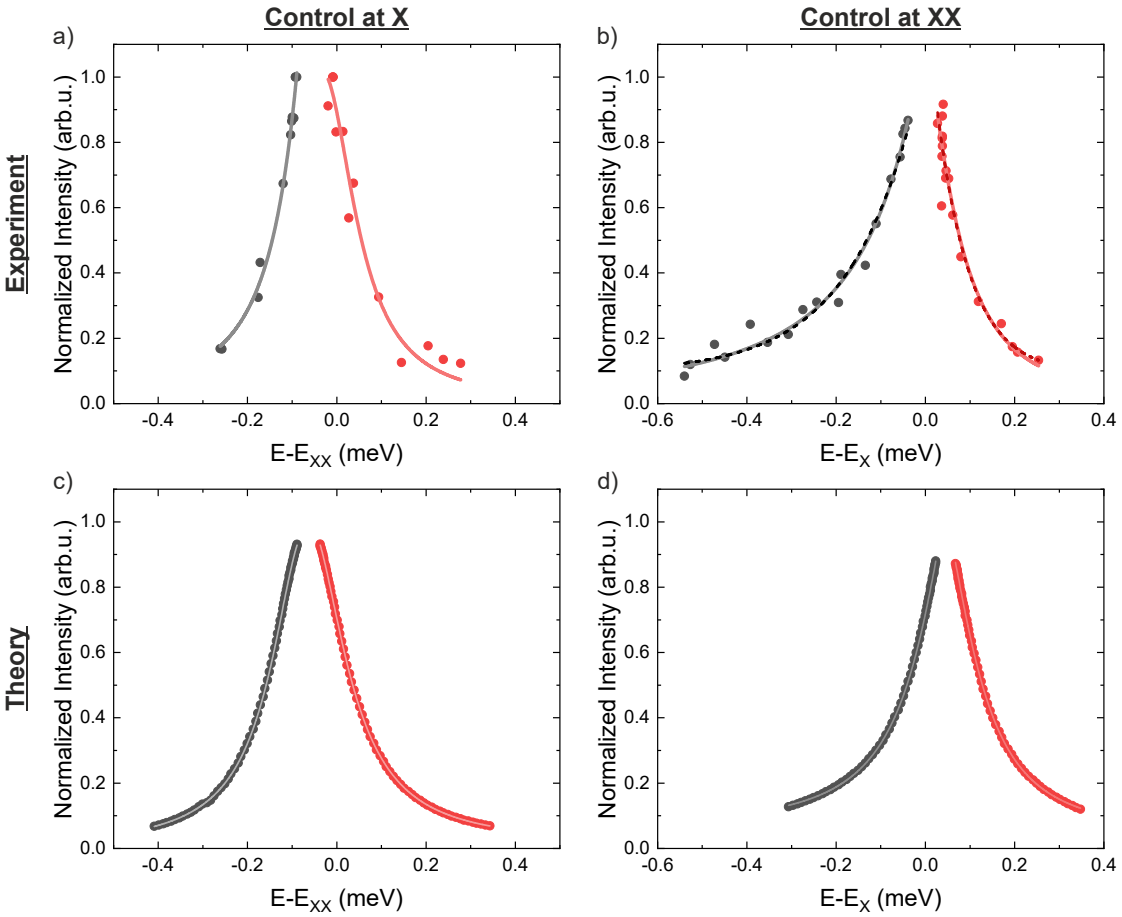

Figure 7.7: Tuning range of the SDC emission Intensity of the SDC emssion plotted over the detuning relative to the undisturbed host line. The intensity is normalized to the sum of SDC and X/XX. Solid lines: Fit with Lorentzian functions. Dashed lines in b): Fit with exponential function[61]

The resulting diagrams show a decreasing intensity with increasing detuning. This behavior is well described by independent Lorentzian functions for positive and negative detuning, which is especially true for the theoretical results, while the experimental data suffers to some extend from the low overall signal intensity and the resulting low signal-to-noise ratio. The same behavior was observed during the analysis of the anti-crossing at the TPE resonance (see chapter 6.3). The FWHM values resulting from the Lorentzian fits are summarized in table 7.2.

	Control at X		Control at XX	
	Experiment	Theory	Experiment	Theory
High energy side	0.135 ± 0.06	0.198 ± 0.001	0.175 ± 0.03	0.194 ± 0.002
Low energy side	0.172 ± 0.07	0.185 ± 0.001	(0.006 ± 17.9)	0.204 ± 0.002
	All values in meV.			

Table 7.2: FWHM of the SDC tuning range The experimental value for the low energy side with the control-laser at XX is not reliable since the Lorentzian fit does not converge properly in this case.

The theoretical results are approximately symmetrical leading to very similar FWHM values. For the experimental data the low signal-to-noise ratio limits the evidential value of the fit parameters. They do however coincide with the theoretical values within the margin of error. The branch with negative detuning to the X-line in figure 7.7b is an exception in this regard and in general the most interesting case. Here, the experimental signal extends to larger detunings than the corresponding simulation. Unfortunately, the Lorentzian fit does not deliver a reasonable value for the FWHM for this dataset. For this reason, the data in figure 7.7b was fitted with exponential functions, which describe the data reasonably well (see dashed lines). The resulting decay constants are $\tau_- = 0.152 \pm 0.001$ meV for the side of negative detuning and $\tau_+ = 0.074 \pm 0.002$ meV for the side of positive detuning. This clearly shows the asymmetry of the SDC emission around the X-line. The mechanism behind this is not clear. Since the simulations do not include phonon processes, this might be a good starting point for further investigations. In this branch of the SDC the control-laser generates a virtual state slightly below the $|X\rangle$. A part of the population could therefore be transferred into the virtual state by emitting a phonon. At this point, this is however merely a hypothesis that needs to be investigated.

In summary, the anti-crossing between the SDC and the X/XX-line of the quantum dots shows the same characteristics as observed for the dressed states induced by the TPE laser (see chapter 6.3). Based on these observations, it can be concluded that the driving mechanism behind the nonlinear down-conversion is in fact a dressing of the system induced by the control-laser. Following this interpretation, the postulated virtual state would then be a superposition of the exciton state and the light field. Such an interpretation would surely be more complete and powerful but also much more complex. Especially, in cases with a large detuning between the laser and the X/XX-lines the simple model with a virtual state still provides a good description of the system.

7.3 Powerdependence

An aspect of great interest, especially with regard to potential applications, is how the SDC process scales with the intensity of the control-field, since this greatly influences the amount of light that can be generated by this process. For this reason an analysis of the powerdependence was conducted.

In order to derive a fit function the same method as in chapters 6.1.2 and 6.2 can be applied. Figure 7.8 shows an overview of all states and transitions that need to be taken into account. The biexciton preparation via phonon-assisted TPE is described by a constant pump term γ_{pump} from the ground state $|G\rangle$ to the biexciton state $|B\rangle$. The spontaneous decay via the excitons state $|X\rangle$ is described by the transition rates γ_{xx} and γ_x. Within this model the virtual state $|V\rangle$ is treated as a regular state with the population $N_{|V\rangle}$. The control-laser drives transitions between $|B\rangle$ and $|V\rangle$. Based on the theoretical findings of [23] this transition rate is assumed to scale linearly with the laser power. The SDC emission is described as a spontaneous decay from $|V\rangle$ to $|G\rangle$ with the transition rate γ_{SDC}.

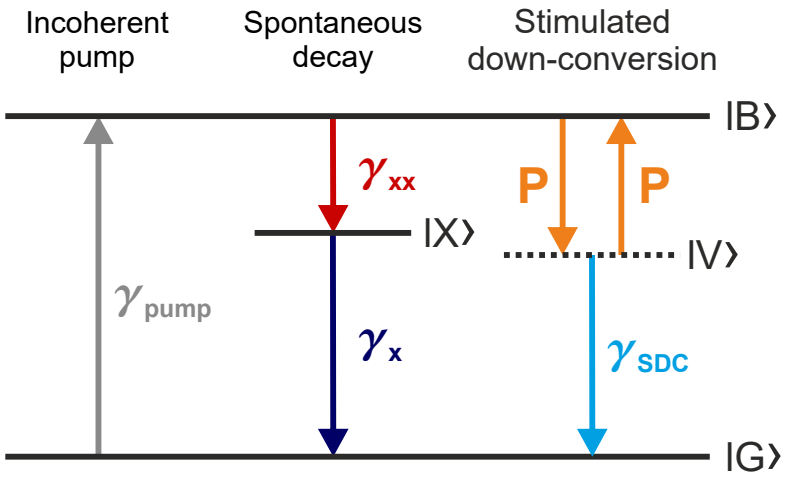

Figure 7.8: Levels and optical transitions during SDC experiment The virtual state $|V\rangle$ created by the control-laser is treated as a regular state that is coupled to $|B\rangle$ by stimulated emission and absorption scaling linear to the control power. The SDC emission is modeled as a spontaneous decay from $|V\rangle$ to $|G\rangle$ with the transition rate γ_{SDC}.

Considering these states and transitions, the following rate equations can be set up, which all need to be equal to zero in the steady state.

$$\frac{dN_{|B\rangle}}{dt} = N_{|G\rangle}\gamma_{\text{pump}} - N_{|B\rangle}\gamma_{\text{xx}} - N_{|B\rangle}\tilde{P} + N_{|V\rangle}\tilde{P} \stackrel{!}{=} 0 \tag{7.1}$$

$$\frac{dN_{|X\rangle}}{dt} = N_{|B\rangle}\gamma_{\text{xx}} - N_{|X\rangle}\gamma_{\text{x}} \stackrel{!}{=} 0 \tag{7.2}$$

$$\frac{dN_{|V\rangle}}{dt} = N_{|B\rangle}\tilde{P} - N_{|V\rangle}\tilde{P} - N_{|V\rangle}\gamma_{\text{SDC}} \stackrel{!}{=} 0 \tag{7.3}$$

$$\frac{dN_{|G\rangle}}{dt} = N_{|X\rangle}\gamma_{\text{x}} + N_{|V\rangle}\gamma_{\text{SDC}} - N_{|G\rangle}\gamma_{\text{pump}} \stackrel{!}{=} 0 \tag{7.4}$$

Furthermore, the population in all states needs to add up to one.

$$1 = N_{|B\rangle} + N_{|X\rangle} + N_{|V\rangle} + N_{|G\rangle} \tag{7.5}$$

By solving this system of equations the following relation is obtained:

$$N_{|V\rangle} = \frac{\tilde{P}}{\tilde{P}\left(2 + \frac{\gamma_{\text{SDC}}}{\gamma_{\text{pump}}}\right) + \gamma_{\text{SDC}}\left(1 + \frac{\gamma_{\text{xx}}}{\gamma_{\text{x}}} + \frac{\gamma_{\text{x}}}{\gamma_{\text{pump}}}\right)} \tag{7.6}$$

The intensity of the SDC emission is directly proportional to the population of $|V\rangle$ ($I_{SDC}(\tilde{P}) = N_{|V\rangle}\gamma_{\text{SDC}}$). Figure 7.9 displays a plot of this function. One can observe a linear behavior at low power, while the emission saturates at high powers.

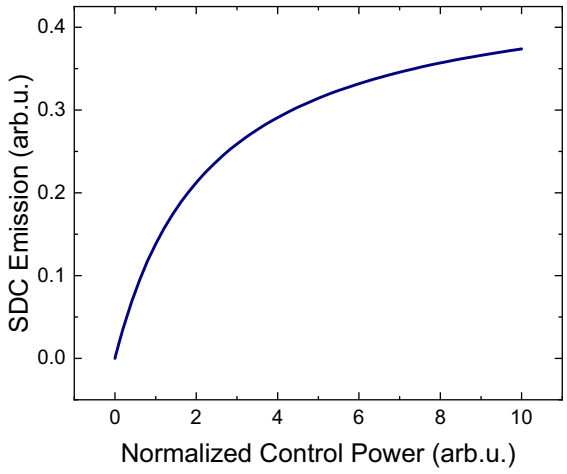

Figure 7.9: Powerdependence of SDC - Theory At low power the SDC emission scales linearly with the control power, while showing saturation towards high power.

In order to use this function for fitting experimental data, several parameters need to be summarized to avoid overparametrization and possible background needs to be taken in to account. These operations deliver the following fit function.

$$I_{SDC}(P) = I_{\text{sat}}\frac{P_{\text{norm}}}{P_{\text{norm}} + 1} + I_{\text{offset}} \tag{7.7}$$

Here, the strength of the optical driving is expressed in terms of a normalized power, which is proportional to the measured laser power $P_{\text{norm}} = a \cdot P$ and to the square of the Rabi energy $P_{\text{norm}} = b \cdot (\hbar\Omega_0)^2$.

For testing this theoretical prediction the following experiment was conducted. The QD is excited by phonon-assisted TPE, with the laser set to a fixed power that saturates the biexciton population. The control-laser is tuned to an energy above but close to the XX-line resulting in SDC emission slightly below the X emission energy. This regime was selected since it shows the strongest SDC emission (see chapter 7.1). Figure 7.10 shows the QD emission under these conditions for varied control power. As expected the SDC signal increases with the control power. Furthermore all three lines (X^+, SDC, X) experience a shift towards higher energy. This effect might be caused by off-resonant driving through the control-laser. Due to the restrictions of the experimental setup the available control power is limited to 3.5 mW.

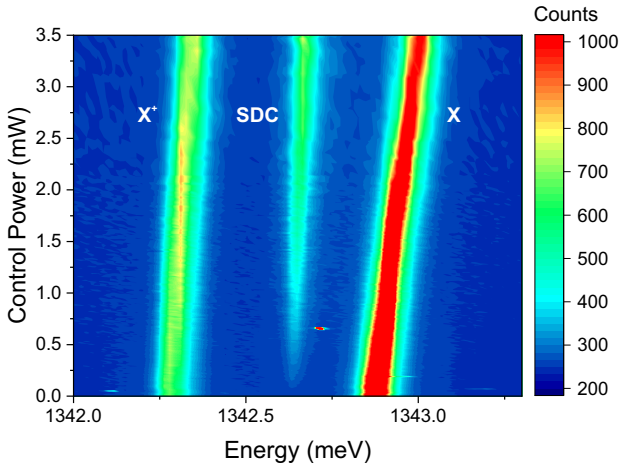

Figure 7.10: Powerdependent spectra of the SDC emission Besides increasing the intensity of the SDC signal, the control-laser induces a shift of all observable emission lines. The power of the control-laser was limited by the experimental setup to a maximum of 3.5 mW.[61]

From this data set the SDC intensity can be extracted and plotted vs. the normalized excitation power (see figure 7.11a). In the regime of low power the data shows a linear behavior, with very slight indication for a saturation at high power. Figure 7.11b shows a corresponding simulation covering a much larger parameter range. Here, the saturation is clearly visible.

Both data sets are in very good agreement with the fitting function derived above. It can therefore be concluded that the assumption of a linear power dependence of the SDC is correct, further confirming the analytical relation found by *Breddermann et al.*[23]. The SDC intensity in the experiment was limited by the available excitation power. By looking at the experimental and theoretical data, both plotted against the normalized power, it can be estimated that the SDC intensity can be increased by at least a factor of three by increasing the available laser power or enhancing the coupling strength between laser and QD (eg. by cavity structures).

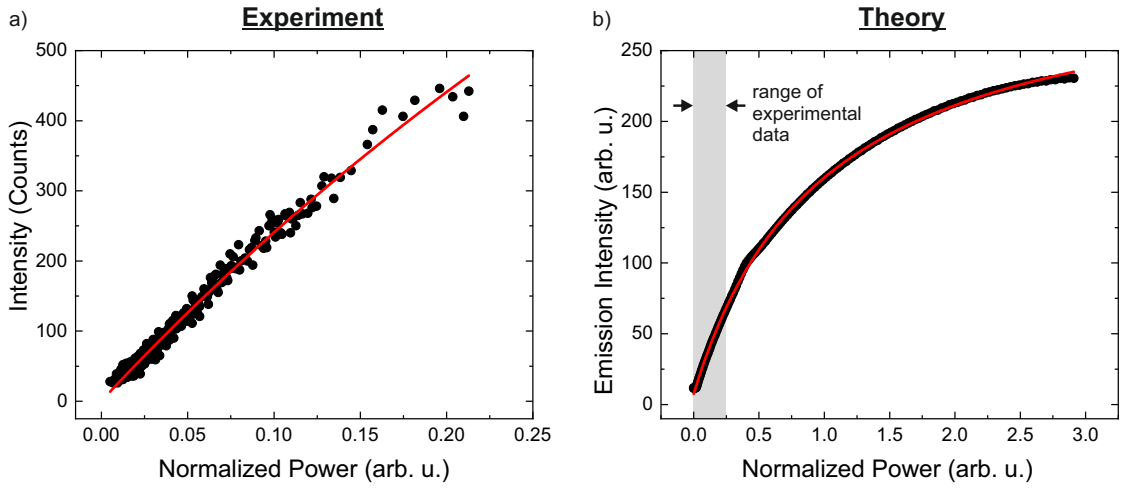

Figure 7.11: Powerdependence of SDC a) Experimental intensity of SDC emission plotted over normalized power b) Corresponding theoretical data with range of experimental data marked in gray. In both cases, equation 7.7 was used as fit function.[61]

7.4 Single-photon emission

With regard to applications in quantum technologies, especially in quantum communication, single photon emission is a key feature of quantum dots[47, 100]. The proof of single photon emission by the SDC process is therefore of great importance. The logical step to investigate this is an auto-correlation measurement of the SDC emission. The low count rates obtained in the previous experiments, provide a major challenge in this regard, since the rate of coincidences scales quadratically with the overall signal intensity. In order to reduce the impact of this issue, a preparation of the biexciton via resonant TPE with ps optical pulses was chosen in combination with a cw control-laser. The pulsed TPE creates a pulsed population in the biexciton state and hence a pulsed SDC emission. Under these conditions it is generally easier to identify anti-bunching, which is especially helpful in case of low countrates. The cw control-laser ensures that the SDC emission is still spectrally sharp, helping to isolate the signal. Furthermore, superconducting single photon detectors became available for this experiment. They feature very low dark count rates and are suited for measurements with very weak signals (see chapter 3.8.2).

For the experiment, the Ti:Sapphire laser is operated in ps mode and tuned to $E_B/2$. The emission is filtered using a bandpass filter (see chapter 3.2.2) to help with spectrally filtering the laser. This is of particular importance as this experiment was conducted using a setup that is not optimized for cross-polarized detection (see chapter 3.4.2). The $\lambda/2$-plates in the setup are however adjusted accordingly to suppress the backscattered light of this laser. The laser is set to a power that corresponds to a pulse area of π resulting in an inversion of the QD into the biexciton state $|B\rangle$ (see chapter 6.5). Figure 7.12 shows the resulting spectrum of the biexciton cascade.

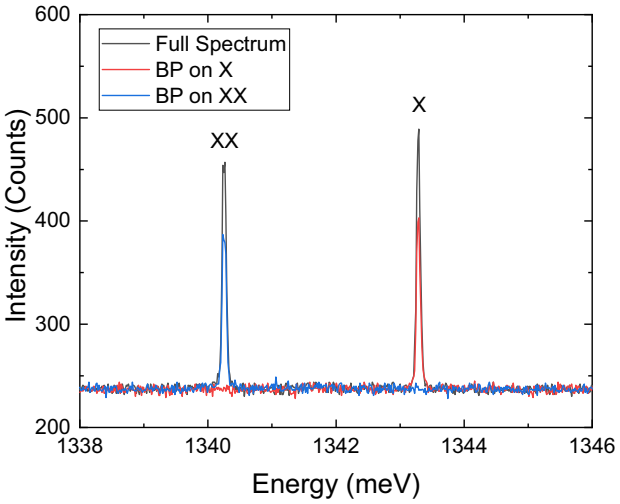

Figure 7.12: Pulsed preparation of biexciton state Two-photon excitation of the QD with ps optical pulses with a pulse area of 1π. For the correlation measurements bandpass filters are used to isolate X and XX. ($V_{\text{bias}} = 0.58$ V)

For testing the capabilities of the detectors and the entire setup, auto-correlation measurements of both emission lines, X and XX, were conducted. Therefore, the corresponding emission line was isolated with a tunable bandpass filter in the detection path (red and blue curves in figure 7.12). The resulting histograms are displayed in figure 7.13. Both measurements show a very clear anti-bunching behavior, proving the expected single photon emission from the biexciton cascade[111]. In case of the X-emission, not a single count was recorded in the center. Based on this $g^{(2)}(t = 0) < (7.75 \pm 0.23)10^{-4}$ can be estimated. In case of the XX-emission a few coincidences were detected in the center peak, delivering $g^{(2)}(t = 0) = (5.75 \pm 0.12) \cdot 10^{-3}$. In this case most likely some laser light leaked into the detection fiber.

These results clearly show the single photon character of both lines. Even though better values were reported in literature[93], these values are still reasonably good, especially considering that no background correction had to be applied. This demonstrates the capabilities of the SSPDs, making them the ideal tool to measure the weak signal from the SDC emission.

The good time resolution of the detectors allows determining the lifetimes of both emission lines from this data set. Figure 7.14 shows a close up of one of the peaks from the data displayed in figure 7.13. The lifetime can be determined by fitting the peak with a symmetric exponential decay.

$$I(t) = I_0 \exp\left(-\frac{|t - t_0|}{t_{decay}}\right) \tag{7.8}$$

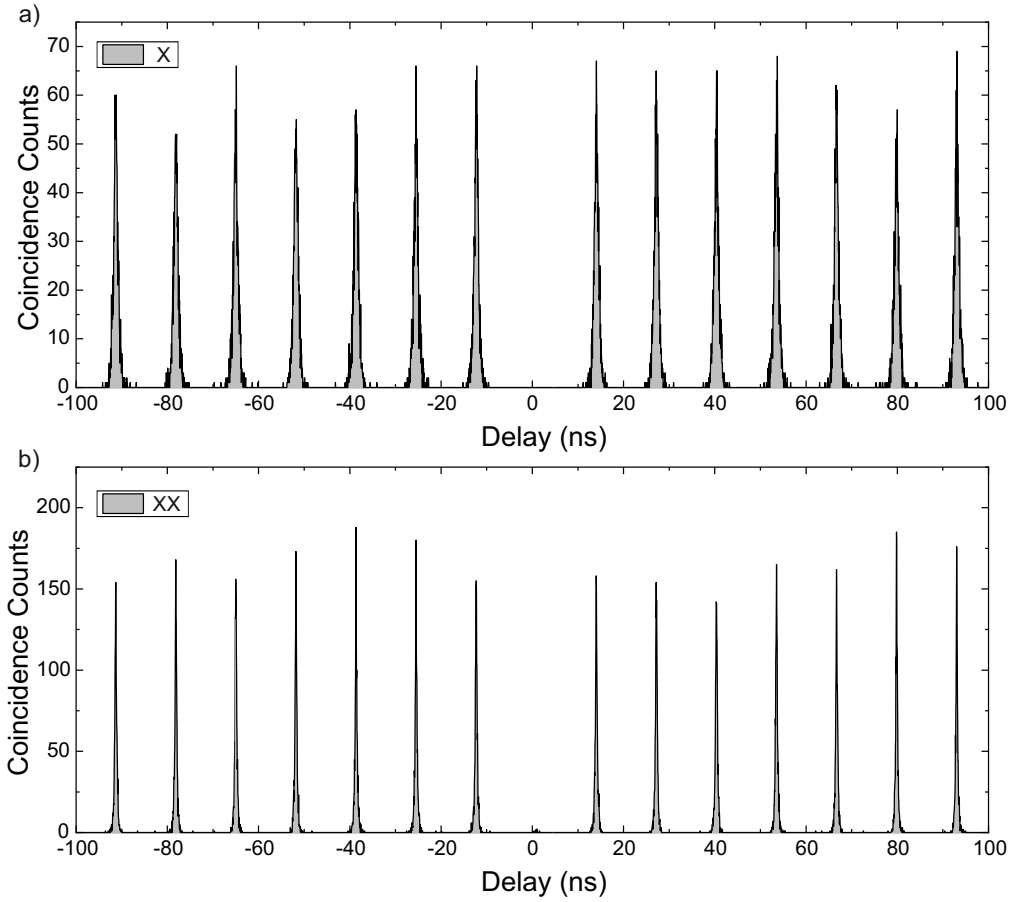

Figure 7.13: Auto-correlation measurements of biexciton cascade under pulsed excitation a) Auto-correlation of X b) Auto-correlation of XX. For these measurements SSPD detectors were used, which offer better time resolution and lower dark count rates compared to the previously used APDs. ($\tau_{\text{bin}} = 0.05\ ns$)

This function describes the experimental data very well and delivers lifetimes of $t_X = 0.489 \pm 0.011$ ns and $t_{XX} = 0.223 \pm 0.003$ ns. These values show the typical ratio of $t_X/t_{XX} \approx 2$. The reason for the shorter lifetime of the XX-line is that the $|B\rangle$-state has two possible decay channels into the two fine-structure states of $|X\rangle$. The lifetimes can be translated into a corresponding linewidth using

$$\text{FWHM} = h \cdot \frac{1}{t_{dec}} \tag{7.9}$$

This delivers $\text{FWHM}_X = 8.45 \pm 0.19\ \mu$eV and $\text{FWHM}_{XX} = 18.14 \pm 0.24\ \mu$eV. The value for X is higher than the linewidth determined from photocurrent measurements performed on the same QD ($\text{FWHM}_{X,PC} = 6.6 \pm 0.8\ \mu$eV, see figure 5.7a). The correlation measurement was performed at approximately $V_{bias} = 0.6$ V while the photocurrent value was measured at $V_{bias} = 0.4$ V. The difference therefore cannot be explained by an increased tunneling rate. It is more likely an result of charging effects. The voltage dependent photoluminescence measurement of this QD shows a significant signal from the positive trion (X^+) at $V_{bias} = 0.6$ V, leading to the conclusion that the QD is most likely charged with a hole.

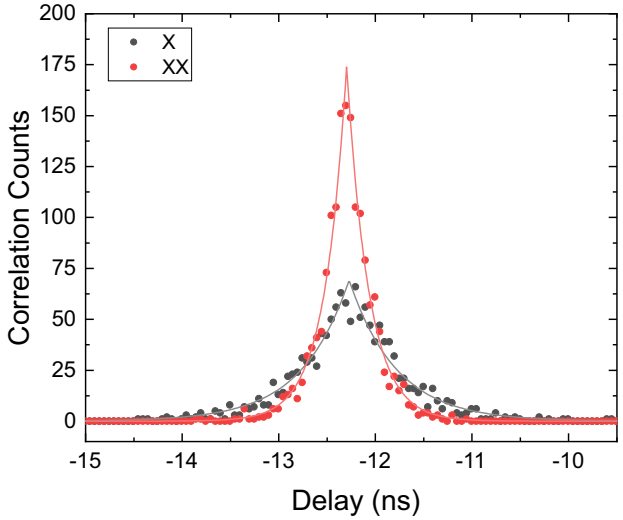

Figure 7.14: Lifetime of X and XX The lifetime of X and XX was determined by fitting one of the coincidence peaks from figure 7.13 with exponential functions, resulting in $t_X = 0.489 \pm 0.011$ ns and $t_{XX} = 0.228 \pm 0.003$ ns.

After this successful test, the control-laser is activated. Based on the results presented in chapter 7.2, the best SDC signal can be expected close to the X-line, specifically at negative detuning. This would however cause a greater challenge with regard to the straylight suppression of the TPE laser, which is now spectrally broad due to it being operated in ps-mode. To avoid this the control-laser was tuned to an energy slightly below the XX-line ($\Delta_{\text{Control-XX}} = E_{\text{Control}} - E_{\text{XX}} = -0.255$ meV). The resulting emission spectrum including X and SDC is displayed in figure 7.15. The detuning between X and SDC is $\Delta_{\text{SDC-X}} = E_{\text{SDC}} - E_{\text{X}} = 0.469$ meV. Based on $\Delta^2_{\text{SDC-X}} = \Delta^2_{\text{Control-XX}} + \hbar^2\Omega_0^2$ a Rabi energy of $\hbar\Omega_0 = 0.393$ meV can be concluded. Under these conditions the small peak can be clearly classified as SDC. Filtering the emission with a combination of a bandpass filter and a notch filter allows isolating this peak (see red curve in figure 7.15). The intensity is however very weak and only observable with the spectrometer due to an increased integration time of 5 s.

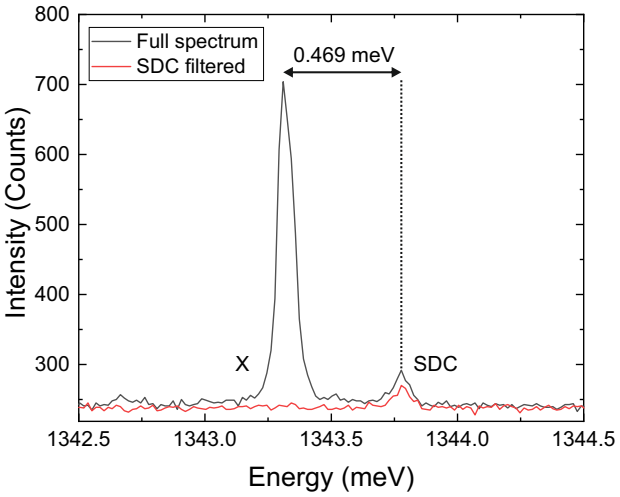

Figure 7.15: SDC emission under pulsed biexciton preparation The detuning of the control-laser was chosen in order to achieve a reasonably large detuning between SDC and X to help with the spectral selection of the SDC-line. ($T_{int} = 5$ s)

Figure 7.16 shows an auto-correlation measurement of this signal. Due to the low count rate both the size of the time bins and the integration time had to be increased in comparison to the previous measurements on the X- and XX-emission. The measurement shows the expected pulsed SDC emission caused by the pulsed biexciton preparation. The center peak at a time delay of zero is missing, indicating single photon emission from this process. Aside from the weak general background which is a result of the extremely long integration time, there is no signal observable at zero time delay. Since the average peak size of the peaks is 10.5 and assuming that the number of counts in the center peak is < 1, one can estimate $g^{(2)}(t = 0) < 0.1$. This is however a very conservative estimate and could be greatly improved by an increased count rate.

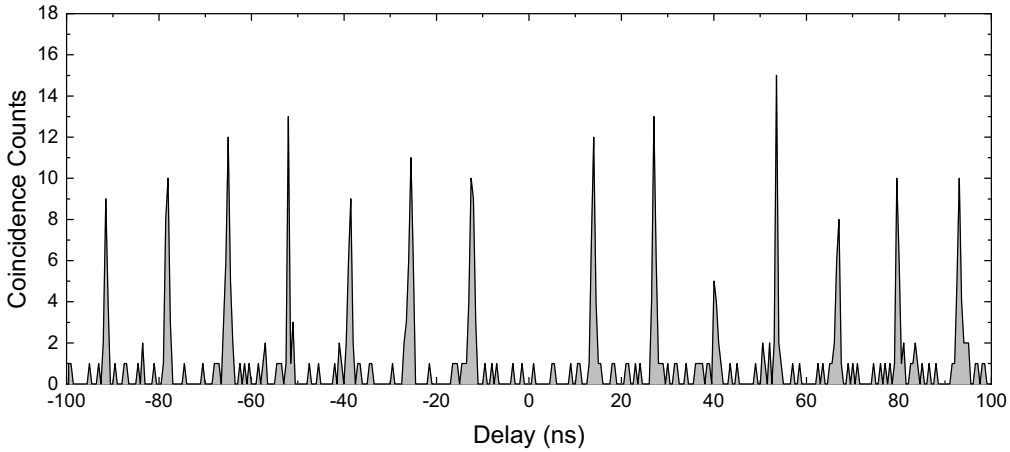

Figure 7.16: Auto-correlation measurement of the SDC emission The histogram shows clear anti-bunching. The counts present at $\tau = 0$ can be attributed to dark counts of the detectors. $\tau_{\text{bin}} = 0.5\ ns$, $t_{\text{int}} = 118$ h[61]

7.5 Polarization control

As briefly discussed above, the nonlinear down-conversion provides a mechanism to tailor the polarization of the emitted SDC-photons by manipulating the polarization of the control-laser. This method is based on the selection rules for two-photon processes. Since both $|B\rangle$ and $|G\rangle$ have a total angular momentum of of $J_{|B\rangle} = J_{|G\rangle} = 0$, the spin carried by the two photons involved in the process needs to add up to zero. This condition is a direct result of the conservation of angular momentum and must be fulfilled by all three processes depicted in figure 7.17. While the polarization of the sequential decay

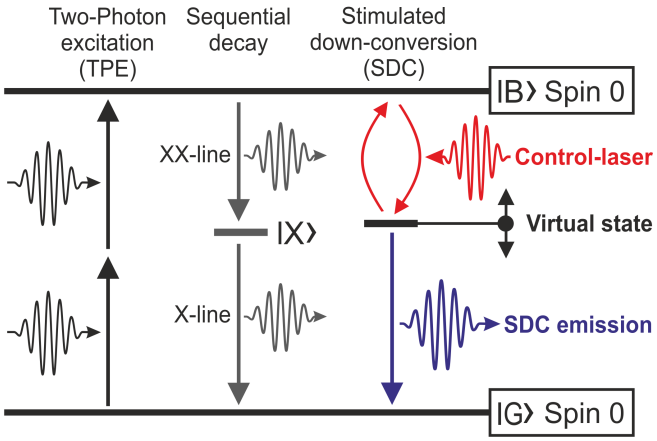

Figure 7.17: Scheme for polarization control Since both $|B\rangle$ and $|G\rangle$ have a total angular momentum of $j_{z,|B\rangle} = j_{z,|G\rangle} = 0$ the polarization of the SDC photon can be fully defined by the polarization of the control-laser.[61]

is determined by the nature of the intermediate state, here $|X\rangle$, the polarization of the two-photon absorption can be chosen more freely, as long as the conservation of angular momentum is ensured. This means that the polarization of one photon determines the necessary polarization of the other one. This behavior occurs in a completely analogous manner during SDC emission. Here, the control-laser stimulates the emission of a photon with equal polarization, which in turn defines the polarization of the SDC-emission.

Circularly polarized photons are associated with a spin of ± 1:

$$j_{z,|R\rangle} = +1 \qquad\qquad j_{z,|L\rangle} = -1 \tag{7.10}$$

This means that for a right hand circular polarized control-laser the SDC emission must be left hand circular polarized to ensure the conservation of angular momentum and vice versa. Linear polarization can be expressed as a superposition of two circular components, while the phase between these two components determines the orientation.

$$|H\rangle = \frac{1}{\sqrt{2}}\left(|R\rangle + |L\rangle\right) \qquad\qquad |V\rangle = \frac{1}{\sqrt{2}}\left(|R\rangle - |L\rangle\right) \tag{7.11}$$

In case of perpendicular polarization, e.g. $|H\rangle$ and $|V\rangle$, one circular component would be canceled out due to this phase shift. Therefore, the conservation of angular momentum cannot be fulfilled. This means that in case of a linearly polarized control-laser, the

SDC-emission has the same linear polarization. Table 7.3 summarizes these rules.

Circular		Linear	
Control	SDC	Control	SDC
		$\|H\rangle$	$\|H\rangle$
$\|R\rangle$	$\|L\rangle$	$\|V\rangle$	$\|V\rangle$
$\|L\rangle$	$\|R\rangle$	$\|D\rangle$	$\|D\rangle$
		$\|A\rangle$	$\|A\rangle$

Table 7.3: Optical selection rules for SDC emission A circularly polarized control-laser creates an opposite circular polarization of the SDC. A linearly polarized control-laser creates SDC photons of equal linear polarization.

The concept can be generalized to arbitrary elliptical polarization. When visualizing the special cases of linear and circular polarization as Stokes vectors on the Poincaré-sphere, it is apparent that the vector of the control-laser must be mirrored on the equatorial plane to obtain the Stokes-vector of the SDC emission. This operation can be extended to arbitrary elliptical polarization. An example is visualized in figure 7.18 .

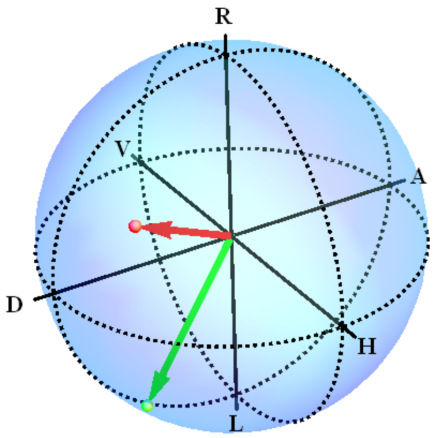

Figure 7.18: Visulalization of the SDC selection rules The selection rules of the SDC emission can be visualized on the Poincaré sphere for arbitrary polarization by mirroring the Stokes vector of the control-laser (red) on the equatorial plane of the sphere. This operation gives the Stokes vector of the SDC photons (green).

Mathematically this operation can be expressed by inverting the sign of the ellipticity χ, while the azimuth Ψ stays constant.

$$\Psi_{SDC} = \Psi_{Control} \qquad \chi_{SDC} = -\chi_{Control} \tag{7.12}$$

In terms of Stokes-vectors, this means that the sign of the s_3 parameter is inverted, while all other parameters are not affected.

$$s_{0,SDC} = s_{0,Control} \tag{7.13}$$
$$s_{1,SDC} = s_{1,Control} \tag{7.14}$$
$$s_{2,SDC} = s_{2,Control} \tag{7.15}$$
$$s_{3,SDC} = -s_{3,Control} \tag{7.16}$$

This operation can furthermore be expressed by a Müller matrix.

$$\mathbf{M}_{SDC} = \begin{pmatrix} 1 & 0 & 0 & 0 \\ 0 & 1 & 0 & 0 \\ 0 & 0 & 1 & 0 \\ 0 & 0 & 0 & -1 \end{pmatrix} \tag{7.17}$$

For testing the validity of these rules a series of measurements with systematic variation of the control polarization and polarization sensitive detection was conducted. For these experiments, the setup used for the previous experiments needed to be modified. This was necessary, since the polarization suppression restricts both lasers to a fixed polarization. The modified setup is discussed in detail in chapter 3.4.2.

After the control-laser is coupled out of the polarization maintaining fiber it is roughly s-polarized (horizontal). After cleaning the polarization with a polarizer, this forms the basis for the following experiment. The control polarization is then manipulated by a waveplate (Control). In case of a $\lambda/2$-plate, all linear polarizations, which are located on the equator of the Poincaré-sphere, are accessible (see figure 2.16a). Half a rotation of $\lambda/2$-plate leads to a full rotation of the polarization. It is therefore sufficient to scan a range of 180° to realize a full sweep over all possible linear polarizations. In the other case, the $\lambda/4$-plate, the achievable polarizations are located on an eight-shaped trajectory, centered around the input polarization, which is in this case horizontal (see figure 2.16b). For anlges of 45° and 135° the $\lambda/4$-plate generates circular polarization. Again, a rotation of 180° is sufficient to scan all points of this trajectory. With these two cases it is therefore possible to test a significant sub sample of the Pointcaré-sphere with regard to the selection rules of the SDC. For analyzing the polarization of the SDC-emission and the backscattered laser light, the second waveplate (Analyzer), which is of equal type as the control waveplate, is rotated. Since it is positioned in front of another horizontal polarizer (s-pol.), this allows for a polarization sensitive detection.

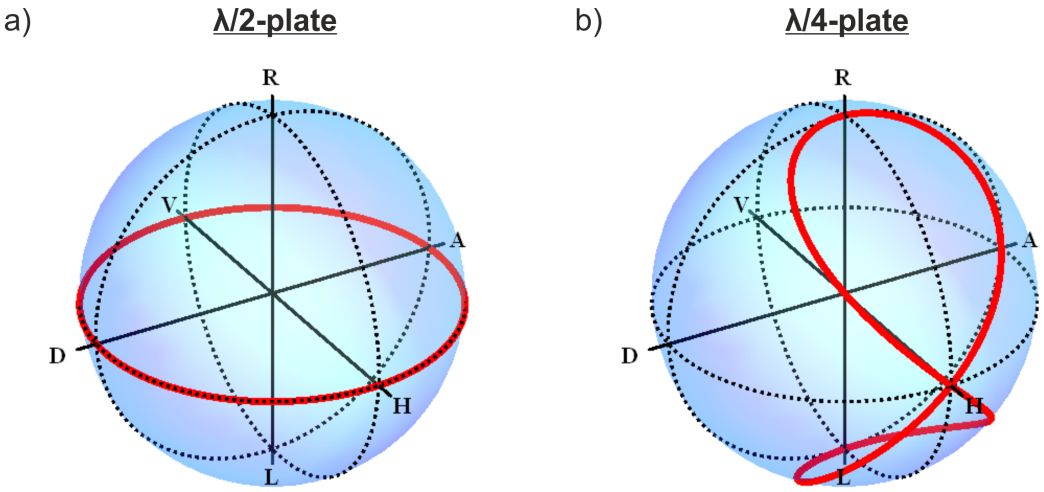

Figure 7.19: Visualization of the effect of waveplates on horizontally polarized light a) The half waveplate gives access to arbitrary linear polarization. b) The quarter waveplate moves the Stokes vector on an eight-shaped path to both poles of the sphere.

During the following experiments, performed on *QD8*, the control-laser was tuned to an energy slightly above the undisturbed XX-line, resulting in an SDC emission 0.386 meV below the X-emission (see figure 7.20). As discussed above this is the regime with the highest efficiency of the SDC-process.

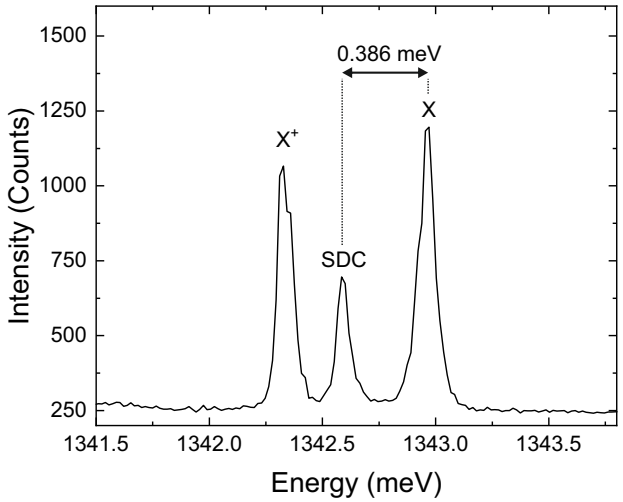

Figure 7.20: Emission spectrum for polarization control For the experiments on polarization control, the energy of the control-laser was selected accordingly to achieve an SDC emission between the X- and X^+-lines. This is the regime with the strongest SDC-emission and allows a clear distinction between the three emission lines of X, X^+ and SDC.

Figure 7.21a shows the intensity of the SDC-emission in dependence of the angles of the two $\lambda/2$-plates acting as Control and Analyzer. Figure 7.21b shows a corresponding measurement for the intensity of the backscattered laser light. Please note that for the backscattered laser it is important to record the intensity of an unfocused laser beam. Here, a mirror was placed in front of the vacuum window of the low temperature microscope to ensure this. This is necessary, since strong focusing will lead to cross-polarized components in the focal plane, which are in turn also backscattered and detected. The resulting measurement would therefore be distorted. This does however not affect the results for the SDC, since the cross-polarized components have a clover leaf shaped intensity distribution with no intensity in the center. The QD which is much smaller (several 10 nm) than the laser focus (~ 1 μm) sees the pure laser polarization, since the adjustment of the whole setup ensures that the QD is positioned in the center of the focus.

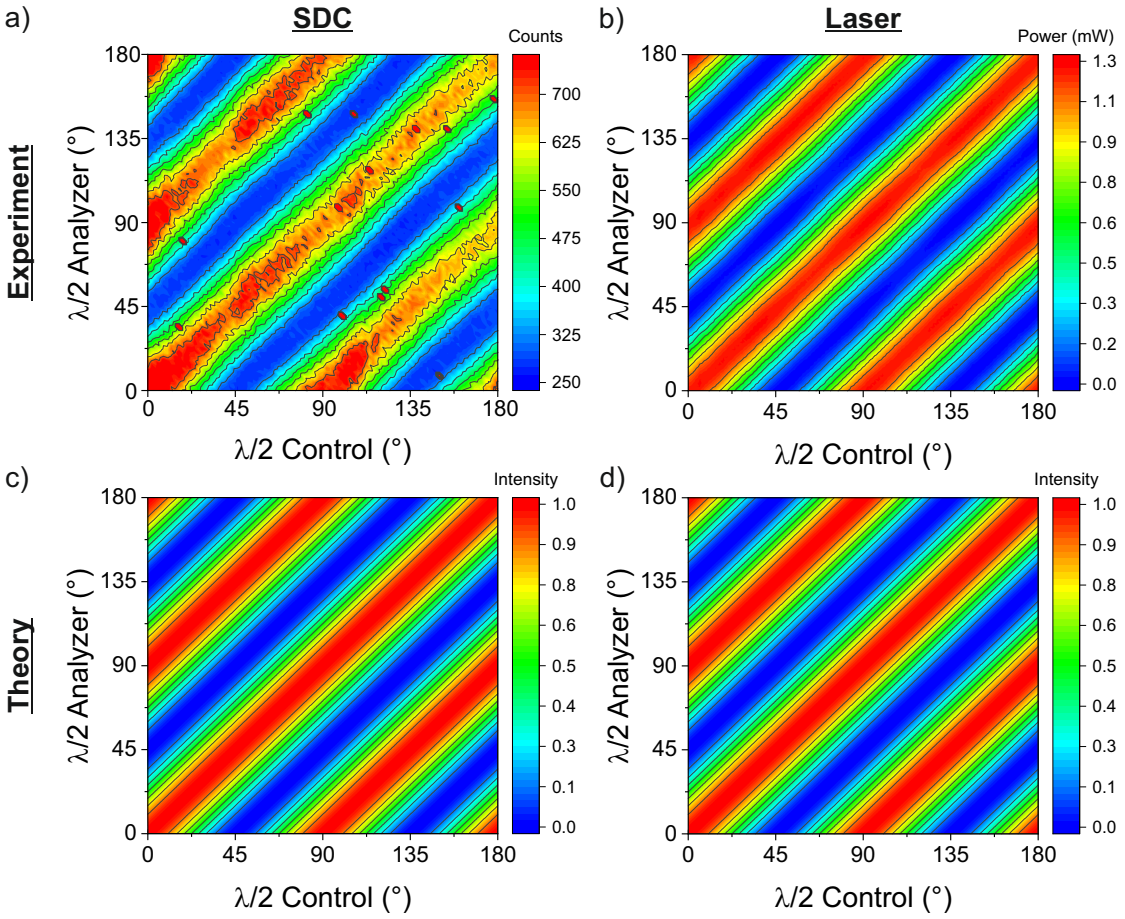

Figure 7.21: Polarization control for linear polarization Experimental data for a) intensity of SDC line and b) reflected laser power and corresponding calculations (c) and (d) for rotation of both half waveplates. The experimental data shows good agreement with the theoretically predicted pattern of diagonal stripes.[61]

Both measurements show a pattern featuring diagonal stripes. Especially for the backscattered laser, this pattern can be intuitively explained. If both waveplates are at an angle of 0° both of them do not change the horizontal input polarization, since it is aligned to the fast axis of both waveplates. The light can therefore pass through the horizontal polarizer in the detection path. When the control waveplate is rotated by a certain angle, the Analyzer waveplate needs to be rotated by the same angle in order to align the the laser with the polarizer. Hence, the diagonal stripes emerge. The fact that the SDC emission shows exactly the same pattern as the control-laser demonstrates that the polarization of the SDC emission nicely follows the polarization of the control-field. The SDC emission furthermore shows no indication for an influence of the fine-structure splitting on the emitted polarization. (A polarization dependent photocurrent measurement of the X-transition in this QD is displayed in figure 5.7.) The data does however show a certain drop of the overall intensity visible towards higher control angles. This can be attributed to a drift in the optomechanical system, most likely the piezo positioners, during the measuring time of 11 h.

These experimental results can be supplemented by a theoretical model based of the Müller calculus (see chapter 2.7.2). Here, a series of matrices representing the effect of the waveplates $\mathbf{M}_{\lambda/x}$ ($\lambda/2$ or $\lambda/4$), the polarizer in the detection path $\mathbf{M}_{HPol}$ and the SDC process $\mathbf{M}_{SDC}$ is multiplied to the stokes vector of the horizontal input polarization $\mathbf{S}_H$.

$$\mathbf{S}_{out,SDC} = \mathbf{M}_{HPol} \cdot \mathbf{M}_{\lambda/x}(\theta_2) \cdot \mathbf{M}_{SDC} \cdot \mathbf{M}_{\lambda/x}(\theta_1) \cdot \mathbf{S}_{in} \tag{7.18}$$

$$\mathbf{S}_{out,Laser} = \mathbf{M}_{HPol} \cdot \mathbf{M}_{\lambda/x}(\theta_2) \cdot \mathbf{M}_{\lambda/x}(\theta_1) \cdot \mathbf{S}_{in} \tag{7.19}$$

The intensity of both the SDC and the laser can then be obtained from the s_0 parameter of the resulting output Stokes vectors $\mathbf{S}_{out,SDC}$ and $\mathbf{S}_{out,Laser}$. The source code for the implementation of this model in *Mathematica* can be found in the appendix.

For the case of $\lambda/2$-plates as Control and Analyzer, this model delivers the same pattern of diagonal stripes as the experimental data (see figure 7.21c and d) It can therefore be concluded that the matrix derived for the SDC process $\mathbf{M}_{SDC}$ well-describes the case of linear polarization. This is however the more trivial case since the matrix only affects the parameter s_3 which is zero per definition for linear polarization. This model is however of great importance for the following measurements with $\lambda/4$-plates and circular polarization.

The previous measurements showed that the polarization control works for linear polarization. To investigate the case of circular polarization, a set of analogous measurements and calculations was conducted using $\lambda/4$-plates as Control and Analyzer (see figure 7.22). This data reveals a more complex pattern than the experiments with linear polarization. Nevertheless, it can provide an intuitive insight, when looking at the critical points of the pattern. These are located at waveplate angles, where the control waveplate generates circular polarization and the Analyzer waveplates projects circular polarization into the H-V-basis. This is the case at waveplate angles of 45° and 135°, defining four points of interest:

(45°| 45°) (45°|135°) (135°|45°) (135°|135°)

At these points both the SDC and the laser intensity show either a maximum or a minimum. These extrema are furthermore always opposing each other, leading to the conclusion that SDC and laser have opposite circular polarization in these points. This is exactly the prediction derived from the conservation of angular momentum. Again, this data set shows a very good agreement with the theoretical model.

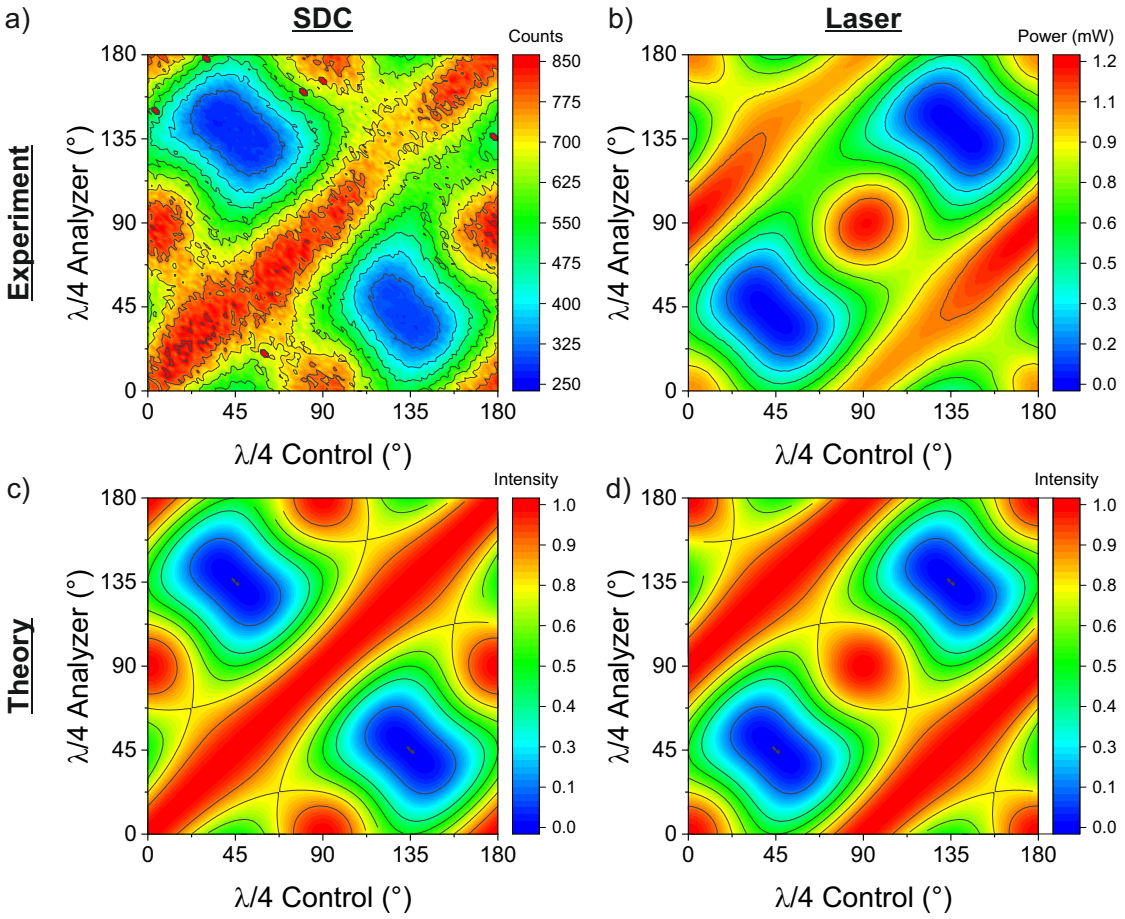

Figure 7.22: Polarization control for circular polarization Experimental data for a) intensity of SDC line and b) reflected laser power and corresponding calculations (c) and (d) for rotation of both quarter waveplates. The data shows counteracting behavior in the critical points and overall good agreement between theory and experiment.[61]

7.5.1 Polarization of the exciton

After the fundamental demonstration of polarization control, a few additional aspects can be investigated. One of these is the behavior of the X-line during these experiments (see figure 7.23). For both linear and circular polarization the intensity of the X-line is also influenced by the control laser and shows a counteracting behavior to the intensity of the SDC emission.

In case of linear polarization the same stripe pattern like for the SDC emission is observed, but it is shifted by 45°. This means that the X-line shows a maximum, whenever

the SDC emission shows a minimum and vice versa. Even though this pattern is not as pronounced as for the SDC peak it is nevertheless significant. At control angles of 45° and 135° the intensity of the X emission is significantly increased. Under this condition both lasers, Control and TPE, are parallel polarized, which might indicate a nonlinear interaction between the two laser fields. A connection with the orientation of the fine structure splitting can be excluded, since here a periodicity of 45° would be expected.

For circular polarization a further interesting feature can be observed. The maxima at 45°|135° and 135°|45° suggest that the X-line is in fact emitting circularly polarized light, which is opposite to the circular polarization of the SDC photons. This is especially remarkable as an exciton with a fine-structure splitting usually does not emit circularly polarized light.

A similar behavior was described for a fixed polarization by [62, 4], when studying dressed states. There it is claimed that the driving laser field imprints its polarization basis onto the QD.

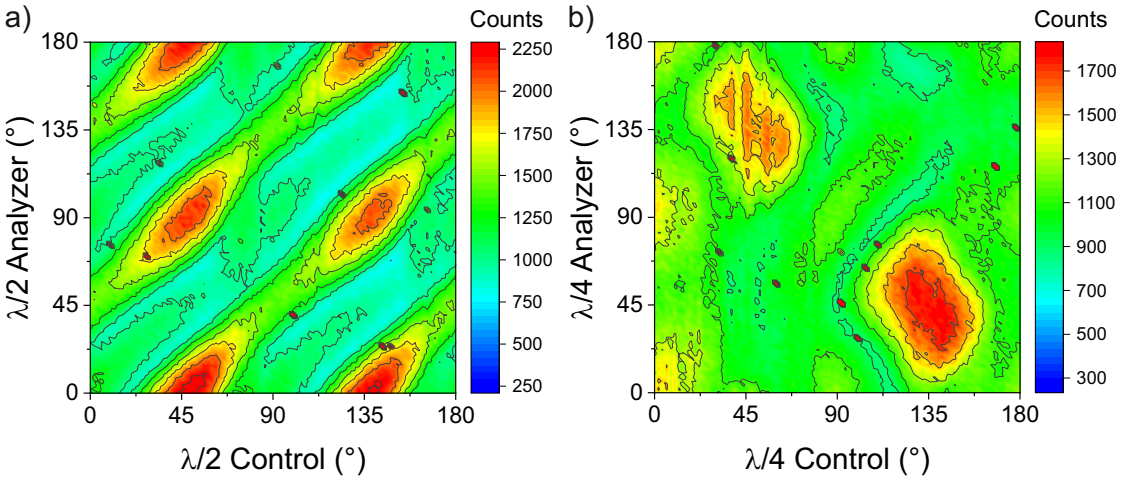

Figure 7.23: Polarization of the X-emission Intensity of the exciton line during polarization control of the SDC emission for a) linear polarization and b) circular polarization. The polarization of the exciton emission is partially influenced by the polarization of the control-laser and shows an opposite behavior as compared to the SDC emission.

7.5.2 Down-conversion in proximity of the biexciton

The results presented above were all obtained in a configuration where the SDC occurs close to the X-line. The SDC process however, does also work in proximity of the XX-line, even though this configuration has a lower efficiency (see chapter 7.1). Figure 7.24 shows the result of a polarization control experiment with the SDC occurring at $E_{SDC} - E_{XX} = 0.445$ meV. For both linear (a) and circular (b) polarization the same patterns as in the previous measurements are observed. The overall intensity of the SDC however shows a much stronger dependence on the angle of the control waveplate. In case of linear polarization a variation of the SDC intensity along the diagonals is observed. Maxima occur at control angles of approximately 45° and 135°, where the control-laser is V-polarized (p-polarization in the frame of the beamsplitters on the mi-

croscope head) and therefore parallel to the TPE-laser. For the circular polarization an increased SDC emission is observed for a waveplate angle of 45°, which corresponds to circular polarization, while there is no such enhancement observable at an angle of 135°. Furthermore, the XX-line shows the same opposite behavior as observed in the previous case, even though it is less pronounced (see figure 7.24c and d).

These measurements look in general less clean as the case, where the SDC occurs close to the X-line. Based on the available data the mechanism behind this cannot be fully uncovered. Accordingly, this might be a subject for further research.

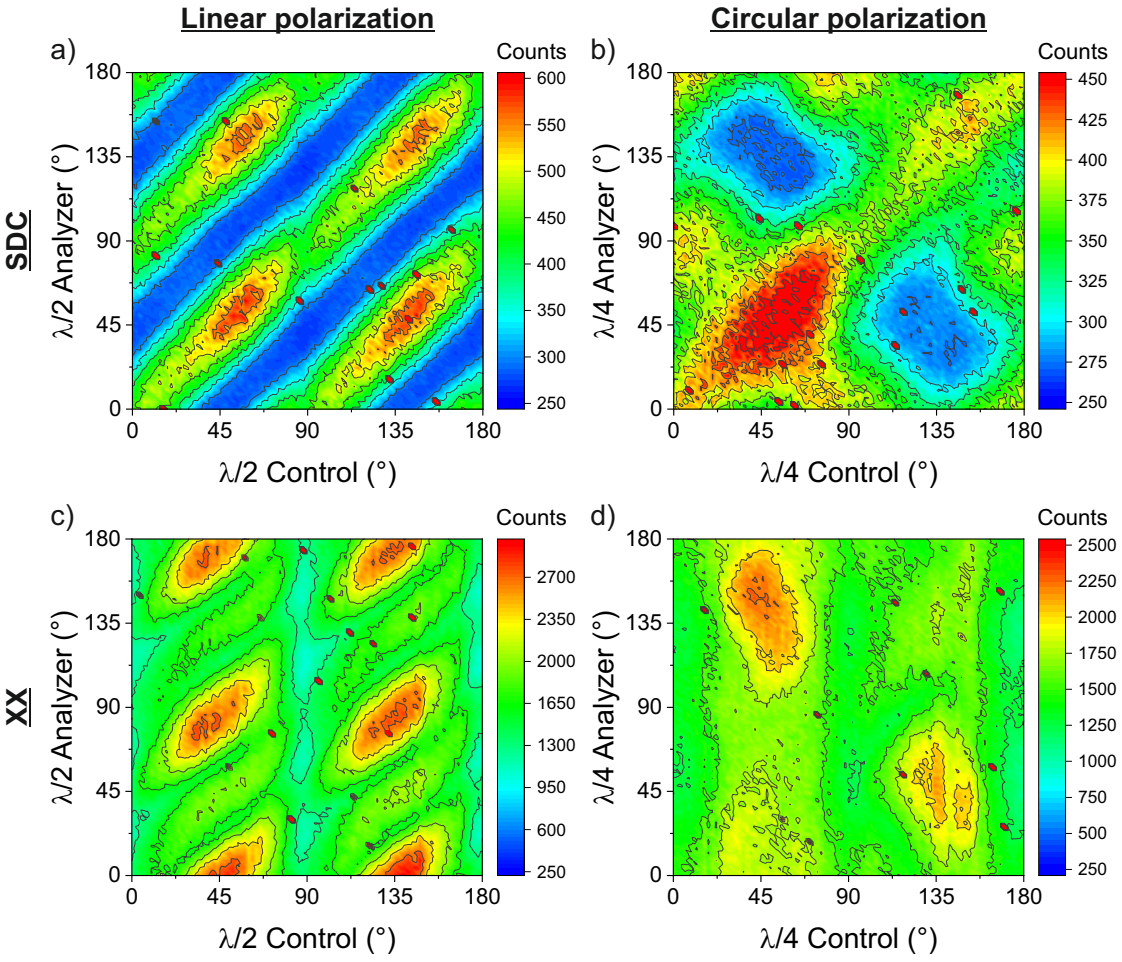

Figure 7.24: Polarization control with control-laser close to X-line Intensity of SDC for a) linear and b) circular polarization and intensity of XX for c) linear and d) circular polarization. The data generally shows the same behavior as before but the overall intensity is influenced by the polarization of the control-laser.

7.6 Single-laser down-conversion

The previous experiments on nonlinear down-conversion were always carried out with separate lasers for TPE and Control. This allowed completely independent tuning of the virtual state for the SDC emission. The TPE laser itself does also create a virtual

state that acts as an intermediate state of the two-photon absorption. This state can in turn also act as the virtual state for the down-conversion (see figure 7.25).

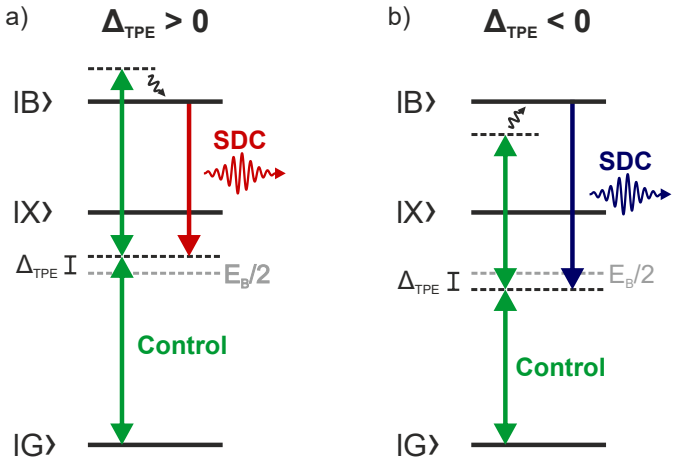

Figure 7.25: Energy levels during single laser SDC experiment The virtual level created by the two-photon process serves as the virtual level for the SDC process.

All previously presented experiments on TPE were carried out using the setup with cross-polarized detection for straylight suppression. Therefore, no SDC emission was observable during these experiments, since laser and SDC have the same linear polarization. Figure 7.26 shows two experiments carried out with the setup with variable polarization, one with cross-polarized and one with parallel detection.

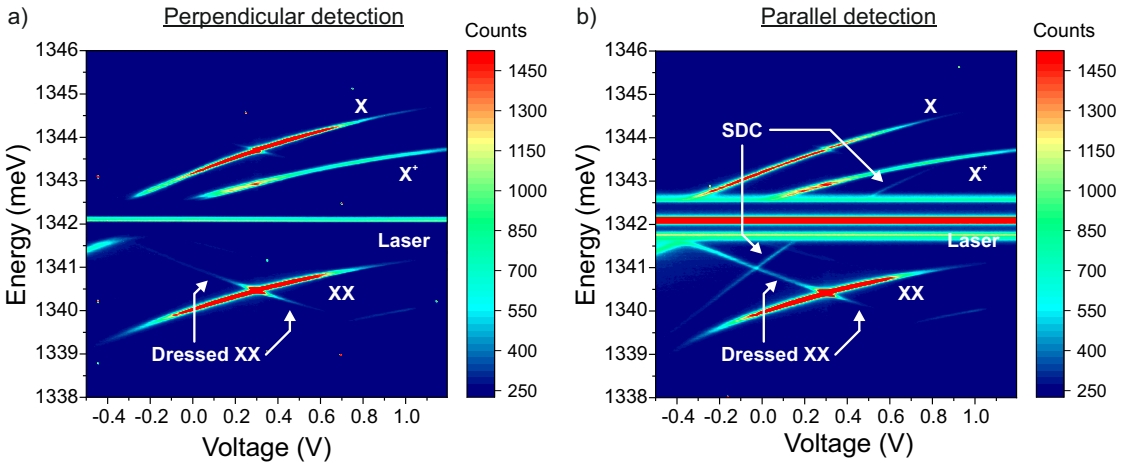

Figure 7.26: SDC emission induced by a single laser Voltage-dependent spectra of *QD5* under phonon-assisted TPE with a) cross-polarized detection and b) parallel polarized detection. The parallel detection scheme allows the observation of an additional emission that is identified as SDC

The cross-polarized measurement shows the typical features discussed in chapter 6.2. In the parallel-polarized measurement the laser is less suppressed and some background emission leaks into the spectrum. Furthermore, the emission from the dressed XX is more pronounced and visible over a larger detuning range. The most interesting differ-

ence however is the appearance of a completely new emission observable on a diagonal between X and XX. This is the SDC emission via the virtual state induced by the TPE laser. The data shows that this process works for larger detunings relative to X or XX than for the case where two lasers are used. In this measurement a detuning up to 1 meV is observable. This might be a result of the better adjustment that is achievable when working with a single laser.

If this process can be classified as SDC it must obey to the selection rules of this process. In order to test this, analogous measurements to those presented in chapter 7.5 were carried out. Figure 7.27a shows the results obtained with $\lambda/2$-plates acting as Control and Analyzer. The SDC intensity shows the same pattern of diagonal stripes that is expected from theory for this configuration (see 7.21c). Therefore, it can be concluded that the selection rules hold for linear polarization and that polarization control is possible in this case.

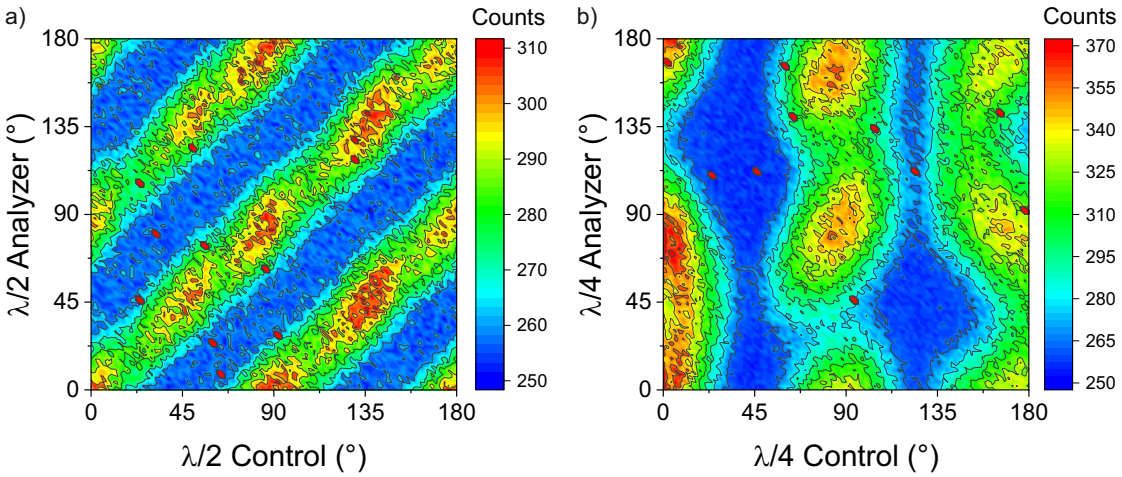

Figure 7.27: Polarization control with single laser SDC SDC intensity for a) linear (*QD8*) and b) circular polarization (*QD5*). The polarization control works well for linear polarization but an SDC emission with circular polarization is not possible as the circularly polarized laser cannot excite the biexciton state.

The overall intensity does however show a clear influence of the orientation of the laser polarization with maxima every 45° in the waveplate angle. This corresponds to the 90° period in the angle of the linear polarization. Therefore, it is intuitive to consider an influence of the fine-structure splitting of the QD. A comparison with a polarization dependent photocurrent measurement performed on this QD (see figure 5.7b) shows that the maxima in the SDC emission occur when the laser polarization is at an angle of ±45° relative to the orientation of the FSS-axes. This behavior was not observed in the experiments with separate TPE- and control-lasers and suggests that the intensity variation of the SDC is a consequence of a variation in the biexciton population and not an inherent property of th SDC process. Reasons for this might be a polarization dependence of the phonon-assisted TPE or the transmission ratios of the beamsplitters and other optics. Based on the available data this question cannon be completely resolved. Nevertheless, the linear polarization of the emitted photons can be controlled by this process.

Figure 7.27b shows an equivalent experiment performed with $\lambda/4$-plates as Control and Analyzer. The displayed data shows a significant deviation from the theoretical expectation (see figure 7.22d). At control angles of $\sim 45°$ and $\sim 130°$ there is no SDC emission observable, independent of the Analyzer position. In these two cases, the laser is circularly polarized. Since the phonon-assisted TPE obeys the same selections rules as the resonant TPE, the preparation of the biexciton state cannot happen under these conditions. When neglecting this feature, the SDC intensity does show a good match with the theoretical prediction. It can therefore be concluded that the selection rules hold for circular polarization, but since the biexciton state cannot be excited by a single circularly polarized laser this case it not suited for applications.

In conclusion the single laser SDC provides a rather simple way to realize an SDC process. As a result of the excitation scheme the emission is only possible between the X- and XX-line, but a larger detuning from these is possible, compared to a two-laser experiment. This might be a result of the inherent perfect overlap of TPE- and control-field. The maximum intensity is generally smaller then in the two-laser experiments since the virtual state cannot be brought arbitrarily close to the exciton state. Experiments on the polarization control show that the linear polarization of the SDC emission can be nicely controlled, while circular polarization suffers from a problem with the biexciton preparation.

7.7 Conclusion

The first subject in this chapter was the experimental demonstration of nonlinear down-conversion in a single quantum dot. This was achieved by employing the setup and the knowledge presented in the previous chapters. Finally, the SDC emission could be identified by means of its unique Stark-shift fingerprint and an excellent agreement with theoretical data.

In the following, the study of the process was extended to several more detailed aspects. An analysis of the anti-crossing between SDC and (bi)exciton showed the close relation of the down-conversion process to the concept of dressed states. It was experimentally confirmed that the intensity of the SDC emission scales linearly with the control power, as theoretically predicted in literature. Furthermore, single photon emission by SDC was proven.

The next important subject was the polarization control of the photons emitted by the down-conversion. This control was demonstrated for the important cases of linear and circular polarization. The good agreement of these experimental results with a theoretical model supports that the concept can be extended to arbitrary polarization.

Finally, a special case, in which the laser that is used for exciting the biexciton state, simultaneously acts as the control-laser and induces an SDC emission, was briefly investigated.

8 Summary

The aim of this work was the investigation of a nonlinear down-conversion process in single quantum dots that allows to manipulate the quantum dot emission by means of a control laser field. The quantum dot is first prepared in the biexciton state. Then the non-resonant control laser field creates a virtual state, opening up an additional decay channel for the population in the biexciton state. The properties of the photons emitted via this channel are fully defined by the nature of the control laser. This process had already been studied by theoretical methods, but experimental studies had not yet been conducted, expect from several studies on a related process in a Λ-system in quantum dot molecules.

In order to study this process from an experimental point of view, the necessary spectroscopic techniques had to be implemented. Especially an effective suppression of back-scattered laser light turned out to be crucial. First, a state of the art cross-polarized detection scheme was implemented and later complemented with high-resolution spectral filtering. For this technique especially the side-band emission of the lasers themselves, as well as the one induced by the optical fibers needed to be overcome. Finally, a setup was developed that allows experiments with arbitrary polarization.

Furthermore, the intensity of the quantum dot signal needed to be increased to be able to observe the down-conversion process. Ultimately an approach using solid immersion lenses proved successful in this regard and was used during the experiments presented in this work. To make use of the advantages provided by embedding the quantum dots in a diode structure in combination with the increased collection efficiency provided by the lens, a new design for pin-diodes with an area large enough to place a solid immersion lens was developed (Diode: 550×700 μm, SIL: 500 μm). These proved functional, even though they showed to be more susceptible to defects in the semiconductor material, which was manifested in a larger variation of the onset voltage under forward bias. The diodes were however perfectly capable of housing the lenses. With the sample used in this work, a signal enhancement by a factor of 2.9 could be achieved.

Since the desired down-conversion process requires the quantum dot to be in the biexciton state, a thorough study of it's excitation was conducted. During strong driving, which is required to achieve a saturated population with a continuous wave laser, several interesting features were observed. A phonon-assisted two-photon excitation of the biexciton was studied. This process enables a selective excitation of the biexciton state, while being robust against a detuning of the system. Therefore, this process was ultimately chosen for the state preparation during the following measurements. The strong laser fields induced strong dressing of the biexciton-exciton-system leading to splittings of the emission lines. Finally, an unexpected emission from the positive trion was observed. Through a combination of a voltage dependent study of the emission and correlation

measurements, the trion emission could be traced to back to a fast switching between a neutral and a charged configuration in the quantum dot.

With these building blocks in place the nonlinear down-conversion could finally be studied. The emission was identified by it's unique Stark-shift fingerprint and comparison with corresponding theoretical data. During these experiments, the emission of the down-conversion process showed an anti-crossing with the exciton and biexciton emission lines, which is a result of state dressing by the control-laser. Further investigation of the process supported this interpretation, as it showed the same characteristics as observed during the dressing of the system under resonant two-photon excitation. Additionally, the single photon character of the SDC emission could be demonstrated.

Following this first study, further experiments were conducted to test the expected mechanism for controlling the polarization of the emitted photons. For this experiment the spectroscopic setup had to be redesigned. To gain the freedom of using an arbitrary polarization of the control laser, the setup had to rely completely on spectral filtering for straylight suppression. Using this modified setup polarization control was successfully shown for both linear and circular polarization. The results are in very good agreement with a theoretical model, based on the generalized selection rules for the process. The experimental results therefore provide a strong evidence that the polarization control works for arbitrary polarization, even though just a sub-sample of the entire Pointcaré-sphere was tested.

Finally, experiments were conducted where the two-photon excitation laser simultaneously acts as control-laser. It was found that SDC with polarization control works well for linear polarization, while the process is not applicable for circular polarization since the two-photon excitation requires linear polarization to create a population in the biexciton state.

Outlook

The experiments conducted in the scope of this work generally show a rather low intensity of the down-conversion signal. This is on the one side an inherent property of the process itself since it competes with the regular biexciton cascade and on the other side a consequence of the limited collection efficiency of the setup. Both issues could be addressed simultaneously by embedding the quantum dot into a photonic cavity structure that provides a high Purcell factor. In order to preserve the mechanism for polarization control, a cavity design with polarization degenerate modes is necessary. A possible candidate would be micropillar cavities with a perfectly round shape. Such a system could potentially provide a strong increase of the efficiency of the process. Theoretical work suggests an efficiency of up to 80% under optimized conditions[23].

In such an optimized scenario, pulsed lasers would be used for both state preparation and control. This would further give the opportunity of shaping the emission temporally and spectrally by shaping the control pulse. Experiments like these have already been demonstrated in Λ-systems in quantum dot molecules[103]. During such an experiment the emission would become spectrally broader, posing a larger challenge on the spectral filtering. In this case, cavity structures would be helpful by allowing a larger spectral separation between the SDC emission and other lines of the QD.

9 Appendix

Voltage-dependent photoluminescence of QD8

Figure 9.1 shows a voltage dependent photoluminescence measurement performed on *QD8*. Here again, the X^+ is the strongest emission line emitting roughly 1 meV below X. The emission from X^{2+} is less pronounced than in *QD2*. Overall, this quantum dot shows very similar characteristics compared to *QD2*.

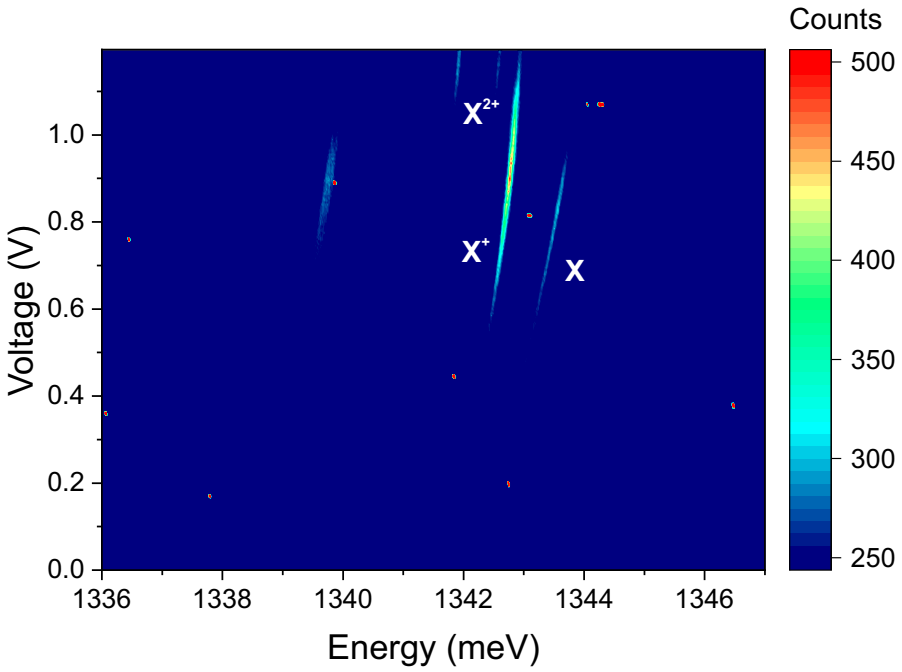

Figure 9.1: Voltage-dependent photoluminescence measurement of QD8 This quantum dot shows a very similar behavior to *QD2*. ($P_{\text{Laser}} = 1\ \mu\text{W}$)

SIL test on intrinsic sample

Before fabricating diodes large enough to house a SIL, a preliminary test was performed using an undoped sample. One SIL was placed onto a small drop of vacuum grease, in order to determine, if the grease increases the adhesion between the SIL and the GaAs surface, which it did. A second SIL was placed directly on the surface to provide a reference (see figure 9.2a). The sample was then cooled to 4 K and PL spectra were recorded for several dots on the bare surface and both SILs (see figure 9.2b-c). For each dot the power was adjusted to maximize the emission (see chapter 4.8). In both cases, the QD signal is significantly increased in comparison to the bare surface. With grease underneath the SIL an enhancement factor of $\beta_{\text{Grease}} = 3.75 \pm 1.48$ was achieved and without the grease this value is $\beta_{\text{noGrease}} = 4.05 \pm 1.39$. The two values are very similar, suggesting that the effect of the grease is at least very limited.

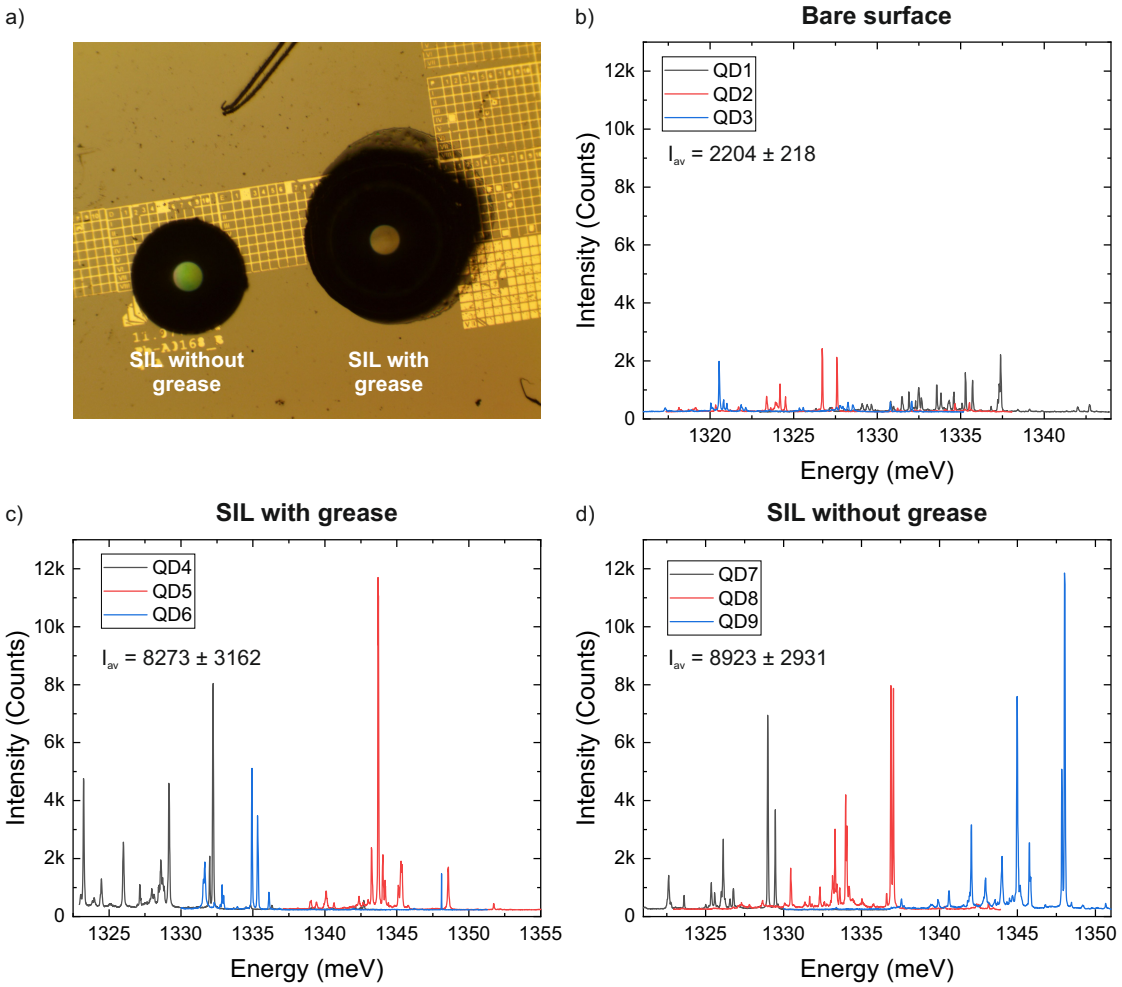

Figure 9.2: SIL test on undoped sample a) Microscopic image of the sample with two SILs applied to surface, one with and one without grease. PL spectra of QDs under b) the bare surface c) a SIL without grease and d) a SIL with grease. The SILs show a significant enhancement of the signal intensity.

Geometrical considerations with a Weiertraß-SIL

This section contains several geometrical considerations concerning solid immersion lenses in Weierstraß geometry.

Path of an arbitrary beam

Figure 9.3 shows the path of an arbitrary light beam emitted by a QD. For the calculations presented in chapter 4.1 a relation between the angles ϑ_{GaAs} and γ is needed. For deriving such an expression, the refraction at the GaAs-SIL interface and the SIL-Air interface need to be considered. Furthermore an equation connecting the angles ϑ_{SIL} and β needs to be derived.

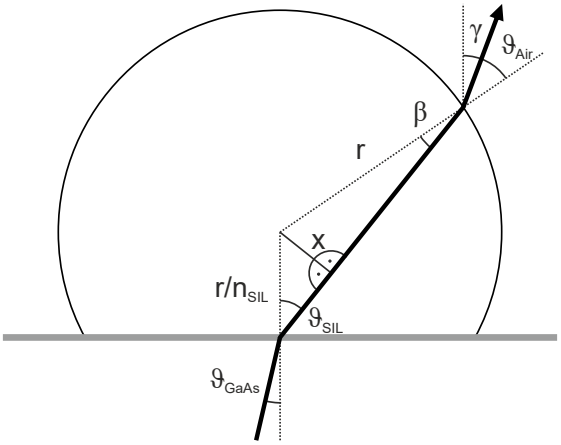

Figure 9.3: Path of an arbitrary beam through the SIL A beam emitted by a QD under the angle ϑ_{GaAs} experiences refraction at the GaAs-SIL and the SIL-Air interface. For calculating the angle β, two right-angled triangles are constructed inside the SIL.

For connecting ϑ_{SIL} and β two triangles can be constructed, which both contain the line X. These deliver the following expressions.

$$\sin\vartheta_{SIL} = \frac{x}{r/n_{SIL}} \qquad \sin\beta = \frac{x}{r} \tag{9.1}$$

Combining these equations leads to

$$\sin\beta = \frac{1}{n_{SIL}}\sin\vartheta_{SIL} \tag{9.2}$$

Considering the refraction at the GaAs-SIL interface provides the following equation.

$$n_{GaAs}\sin\vartheta_{GaAs} = n_{SIL}\sin\vartheta_{SIL} \tag{9.3}$$

$$\sin\vartheta_{SIL} = \frac{n_{GaAs}}{n_{SIL}}\sin\vartheta_{GaAs} \tag{9.4}$$

Combining equations 9.2 and 9.4 delivers

$$\sin\beta = \frac{n_{GaAs}}{n_{SIL}^2}\sin\vartheta_{GaAs} \tag{9.5}$$

Now, one can consider refraction at the surface of the SIL.

$$n_{Air} \sin \vartheta_{Air} = n_{SIL} \sin \beta \tag{9.6}$$

$$\sin \vartheta_{Air} = \frac{n_{SIL}}{n_{Air}} \sin \beta \tag{9.7}$$

Combining this expression with 9.5 finally delivers the desired relation between ϑ_{GaAs} and ϑ_{Air}.

$$\sin \vartheta_{Air} = \frac{n_{GaAs}}{n_{SIL} n_{Air}} \sin \vartheta_{GaAs} \tag{9.8}$$

$$\vartheta_{Air} = \arcsin\left(\frac{n_{GaAs}}{n_{SIL} n_{Air}} \sin \vartheta_{GaAs} \right) \tag{9.9}$$

Focal shift induced by the SIL

The focal shift induced by the lens can be determined by looking at the path of the ray that is emitted by a quantum dot located in the center of the lens under the critical angle $\vartheta_{\mathrm{Crit}}$ (see figure 9.4).

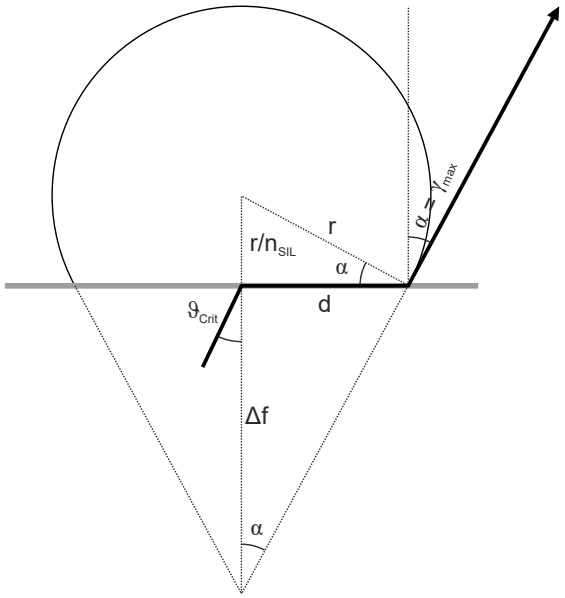

Figure 9.4: Focal shift induced by the SIL For determining the focal shift Δf, a beam leaving the SIL under the maximum emission angle γ_{max} needs to be considered.

First the length d can be determined by considering the smaller triangle constructed inside the lens.

$$r^2 = (\frac{r}{n_{SIL}})^2 + d^2 \tag{9.10}$$

$$\Leftrightarrow d = r\sqrt{1 - \frac{1}{n_{SIL}^2}} \tag{9.11}$$

Furthermore, it is necessary to determine the angle α. The height of a Weierstraß SIL is chosen in a way that a ray running parallel to the sample surface reaches the SIL-Air interface under the critical angle. As a result this ray runs tangential to the surface of the lens after being refracted at the interface. This defines the maximum emission angle of the SIL γ_{max}, which is for geometrical reasons equal to α. Hence, the angle α can be calculated from the radius r and cut-off height $\frac{r}{n_{SIL}}$ of the lens.

$$\sin\alpha = \frac{\frac{r}{n_{SIL}}}{r} = \frac{1}{n_{SIL}} \tag{9.12}$$

$$\Leftrightarrow \quad \alpha = \arcsin\frac{1}{n_{SIL}} \tag{9.13}$$

With α and d known, one can now calculate the focal shift Δf.

$$\frac{d}{\Delta f} = \tan\alpha \tag{9.14}$$

$$\Leftrightarrow \quad \Delta f = \frac{d}{\tan\alpha} = \frac{r\sqrt{1-\frac{1}{n_{SIL}^2}}}{\tan\left(\arcsin\left(\frac{1}{n_{SIL}}\right)\right)} \tag{9.15}$$

Model for Polarization control

The theoretical model for the polarization control was implemented in *„Mathematica“*. The following code contains an example for calculating the polarization map of the SDC, when quarter-wave plates are used in the setup.

Definitions;

```
(*Stokes vector of horizontal polarization*)
H = {1, 1, 0, 0};

(*Müller matrix of half-wave plate*)
L2[θ_] = {{1, 0, 0, 0},
   {0, Cos[2 θ]^2 - Sin[2 θ]^2, -2 * Cos[2 θ] * Sin[2 θ], 0},
   {0, -2 * Cos[2 θ] * Sin[2 θ], Sin[2 θ]^2 - Cos[2 θ]^2, 0},
   {0, 0, 0, -1}};

(*Müller matrix of quarter-wave plate*)
L4[θ_] = {{1, 0, 0, 0},
   {0, Cos[2 θ]^2, -Cos[2 θ] * Sin[2 θ], -Sin[2 θ]},
   {0, -Cos[2 θ] * Sin[2 θ], Sin[2 θ]^2, Cos[2 θ]},
   {0, Sin[2 θ], Cos[2 θ], 0}};

(*Müller matrix of down-conversion*)
DC = {{1, 0, 0, 0}, {0, 1, 0, 0}, {0, 0, 1, 0}, {0, 0, 0, -1}};

(*Müller matrix of horizontal polarizer*)
PolH = {{0.5, 0.5, 0, 0}, {0.5, 0.5, 0, 0}, {0, 0, 0, 0}, {0, 0, 0, 0}};
```

SDC with $\lambda/4$;

```
(*Calculating the output Stokes vector*)
SOutDualPolDC[θ1_, θ2_] = PolH.L4[θ1].DC.L4[θ2].H;

(*Plotting the s0 parameter of the output Stokes vector*)
ContourPlot[SOutDualPolDC[θ1 * Pi / 180, θ2 * Pi / 180][[1]], {θ1, 0, 180}, {θ2, 0, 180},
 AspectRatio → Automatic, ColorFunction → "Rainbow", FrameLabel → {"PolIn [rad]", "PolOut [rad]"},
 PlotRange → Full, Contours → 20]

(*Exporting the results*)
ResultsSOutDualL4PolDC = Table[{θ1, θ2, SOutDualPolDC[θ1 * Pi / 180, θ2 * Pi / 180][[1]]}, {θ1, 0, 180, 1},
   {θ2, 0, 180, 1}];
Export["ResultsSOutDualL4PolDC.txt", ResultsSOutDualL4PolDC]
```

List of Figures

List of Tables

Bibliography

[1] Abudayyeh, Hamza ; Lubotzky, Boaz ; Blake, Anastasia ; Wang, Jun ; Majumder, Somak ; Hu, Zhongjian ; Kim, Younghee ; Htoon, Han ; Bose, Riya ; Malko, Anton V. ; Hollingsworth, Jennifer A. ; Rapaport, Ronen: Single photon sources with near unity collection efficiencies by deterministic placement of quantum dots in nanoantennas. In: *APL Photonics* 6 (2021), Nr. 3, S. 036109. http://dx.doi.org/10.1063/5.0034863. – DOI 10.1063/5.0034863

[2] Allen, Leslie ; Eberly, Joseph H.: *Interscience monographs and texts in physics and astronomy*. Bd. 28: *Optical resonance and two-level atoms*. New York, NY : Wiley, 1975. – ISBN 0–471–02327–2

[3] Arakawa, Yasuhiko ; Holmes, Mark J.: Progress in quantum-dot single photon sources for quantum information technologies: A broad spectrum overview. In: *Applied Physics Reviews* 7 (2020), Nr. 2, S. 021309. http://dx.doi.org/10.1063/5.0010193. – DOI 10.1063/5.0010193

[4] Ardelt, P.-L. ; Koller, M. ; Simmet, T. ; Hanschke, L. ; Bechtold, A. ; Regler, A. ; Wierzbowski, J. ; Riedl, H. ; Finley, J. J. ; Müller, K.: Optical control of nonlinearly dressed states in an individual quantum dot. In: *Physical Review B* 93 (2016), Nr. 16. http://dx.doi.org/10.1103/PhysRevB.93.165305. – DOI 10.1103/PhysRevB.93.165305. – ISSN 1098–0121

[5] Ardelt, Per-Lennart ; Hanschke, Lukas ; Fischer, Kevin A. ; Müller, Kai ; Kleinkauf, Alexander ; Koller, Manuel ; Bechtold, Alexander ; Simmet, Tobias ; Wierzbowski, Jakob ; Riedl, Hubert ; Abstreiter, Gerhard ; Finley, Jonathan J.: Dissipative preparation of the exciton and biexciton in self-assembled quantum dots on picosecond time scales. In: *Physical Review B* 90 (2014), Nr. 24, S. 1065. http://dx.doi.org/10.1103/PhysRevB.90.241404. – DOI 10.1103/PhysRevB.90.241404. – ISSN 1098–0121

[6] Arute, Frank ; Arya, Kunal ; Babbush, Ryan ; et al.: Quantum supremacy using a programmable superconducting processor. In: *Nature* 574 (2019), Nr. 7779, S. 505–510. http://dx.doi.org/10.1038/s41586-019-1666-5. – DOI 10.1038/s41586–019–1666–5. – ISSN 0028–0836

[7] Autler, S. H. ; Townes, C. H.: Stark Effect in Rapidly Varying Fields. In: *Physical Review* 100 (1955), Nr. 2, S. 703–722. http://dx.doi.org/10.1103/PhysRev.100.703. – DOI 10.1103/PhysRev.100.703. – ISSN 0031–899X

[8] Babinec, Thomas M. ; Hausmann, Birgit J. M. ; Khan, Mughees ; Zhang, Yinan ; Maze, Jeronimo R. ; Hemmer, Philip R. ; Loncar, Marko: A diamond nanowire single-photon source. In: *Nature nanotechnology* 5 (2010), Nr. 3, S. 195–199. http://dx.doi.org/10.1038/nnano.2010.6. – DOI 10.1038/nnano.2010.6. – ISSN 1748–3395

[9] Ball, Philip: First quantum computer to pack 100 qubits enters crowded race. In: *Nature* 599 (2021), Nr. 7886, S. 542. http://dx.doi.org/10.1038/d41586-021-03476-5. – DOI 10.1038/d41586–021–03476–5. – ISSN 0028–0836

[10] Barker, J. A. ; O'Reilly, E. P.: Theoretical analysis of electron-hole alignment in InAs-GaAs quantum dots. In: *Physical Review B* 61 (2000), Nr. 20, S. 13840–13851. http://dx.doi.org/10.1103/PhysRevB.61.13840. – DOI 10.1103/PhysRevB.61.13840. – ISSN 1098–0121

[11] Barnes, W. L. ; Björk, G. ; Gérard, J. M. ; Jonsson, P. ; Wasey, J.A.E. ; Worthing, P. T. ; Zwiller, V.: Solid-state single photon sources: light collection strategies. In: *The European Physical Journal D* 18 (2002), Nr. 2, S. 197–210. http://dx.doi.org/10.1140/epjd/e20020024. – DOI 10.1140/epjd/e20020024. – ISSN 1434–6060

[12] Beham, Evelin ; Zrenner, Artur ; Stufler, Stefan ; Findeis, Frank ; Bichler, Max ; Abstreiter, Gerhard: Coherent and incoherent properties of single quantum dot photodiodes. In: *Physica E: Low-dimensional Systems and Nanostructures* 16 (2003), Nr. 1, S. 59–67. http://dx.doi.org/10.1016/S1386-9477(02)00586-6. – DOI 10.1016/S1386–9477(02)00586–6. – ISSN 1386–9477

[13] Benisty, H. ; Neve, H. de ; Weisbuch, C.: Impact of planar microcavity effects on light extraction-Part I: Basic concepts and analytical trends. In: *IEEE Journal of Quantum Electronics* 34 (1998), Nr. 9, S. 1612–1631. http://dx.doi.org/10.1109/3.709578. – DOI 10.1109/3.709578. – ISSN 0018–9197

[14] Bennett, A. J. ; Pooley, M. A. ; Stevenson, R. M. ; Ward, M. B. ; Patel, R. B. ; de la Giroday, A. Boyer ; Sköld, N. ; Farrer, I. ; Nicoll, C. A. ; Ritchie, D. A. ; Shields, A. J.: Electric-field-induced coherent coupling of the exciton states in a single quantum dot. In: *Nature Physics* 6 (2010), Nr. 12, S. 947–950. http://dx.doi.org/10.1038/nphys1780. – DOI 10.1038/nphys1780. – ISSN 1745–2473

[15] Bennett, A. J. ; Unitt, D. C. ; See, P. ; Shields, A. J. ; Atkinson, P. ; Cooper, K. ; Ritchie, D. A.: Microcavity single-photon-emitting diode. In: *Applied Physics Letters* 86 (2005), Nr. 18, S. 181102. http://dx.doi.org/10.1063/1.1921332. – DOI 10.1063/1.1921332. – ISSN 00036951

[16] Bhushan, Bharat: *Springer Handbook of Nanotechnology*. Berlin, Heidelberg : Springer Berlin Heidelberg, 2017. http://dx.doi.org/10.1007/978-3-662-54357-3. http://dx.doi.org/10.1007/978-3-662-54357-3. – ISBN 978–3–662–54355–9

[17] Bimberg, Dieter (Hrsg.): *Semiconductor nanostructures*. Berlin : Springer, 2008 (Nanoscience and technology). http://www.worldcat.org/oclc/222164259. – ISBN 3540778985

[18] Blakemore, J. S.: Semiconducting and other major properties of gallium arsenide. In: *Physical Review* 53 (1982), Nr. 10, S. R123–R181. http://dx.doi.org/10.1063/1.331665. – DOI 10.1063/1.331665. – ISSN 0031–899X

[19] Bounouar, S. ; Müller, M. ; Barth, A. M. ; Gläßl, M. ; Axt, V. M. ; Michler, P.: Phonon-assisted robust and deterministic two-photon biexciton preparation in a quantum dot. In: *Physical Review B* 91 (2015), Nr. 16, S. 1065. http://dx.doi.org/10.1103/PhysRevB.91.161302. – DOI 10.1103/PhysRevB.91.161302. – ISSN 1098–0121

[20] Bounouar, Samir ; Strauss, Max ; Carmele, Alexander ; Schnauber, Peter ; Thoma, Alexander ; Gschrey, Manuel ; Schulze, Jan-Hindrik ; Strittmatter, André ; Rodt, Sven ; Knorr, Andreas ; Reitzenstein, Stephan: Path-Controlled Time Reordering of Paired Photons in a Dressed Three-Level Cascade. In: *Physical Review Letters* 118 (2017), Nr. 23, S. 233601. http://dx.doi.org/10.1103/PhysRevLett.118.233601. – DOI 10.1103/PhysRevLett.118.233601. – ISSN 0031–9007

[21] Bräunlich, P. ; Lambropoulos, P.: Detection of Singly Stimulated Two-Photon Emission from Metastable Deuterium Atoms. In: *Physical Review Letters* 25 (1970), Nr. 3, S. 135–138. http://dx.doi.org/10.1103/PhysRevLett.25.135. – DOI 10.1103/PhysRevLett.25.135. – ISSN 0031–9007

[22] Breddermann, D. ; Heinze, D. ; Binder, R. ; Zrenner, A. ; Schumacher, S.: All-optical tailoring of single-photon spectra in a quantum-dot microcavity system. In: *Physical Review B* 94 (2016), Nr. 16. http://dx.doi.org/10.1103/PhysRevB.94.165310. – DOI 10.1103/PhysRevB.94.165310. – ISSN 1098–0121

[23] Breddermann, Dominik ; Praschan, Tom ; Heinze, Dirk ; Binder, Rolf ; Schumacher, Stefan: Microscopic theory of cavity-enhanced single-photon emission from optical two-photon Raman processes. In: *Physical Review B* 97 (2018), Nr. 12. http://dx.doi.org/10.1103/PhysRevB.97.125303. – DOI 10.1103/PhysRevB.97.125303. – ISSN 1098–0121

[24] BROWN, R. H. ; Twiss, R. Q.: Correlation between Photons in two Coherent Beams of Light. In: *Nature* 177 (1956), Nr. 4497, S. 27–29. http://dx.doi.org/10.1038/177027a0. – DOI 10.1038/177027a0. – ISSN 0028–0836

[25] Carey, Graham H. ; Abdelhady, Ahmed L. ; Ning, Zhijun ; Thon, Susanna M. ; Bakr, Osman M. ; Sargent, Edward H.: Colloidal Quantum Dot Solar Cells. In: *Chemical reviews* 115 (2015), Nr. 23, S. 12732–12763. http://dx.doi.org/10.1021/acs.chemrev.5b00063. – DOI 10.1021/acs.chemrev.5b00063

[26] Chakraborty, Chitraleema ; Vamivakas, Nick ; Englund, Dirk: Advances in quantum light emission from 2D materials. In: *Nanophotonics* 8 (2019), Nr. 11, S. 2017–2032. http://dx.doi.org/10.1515/nanoph-2019-0140. – DOI 10.1515/nanoph–2019–0140

[27] Chen, Teng-Yun ; Wang, Jian ; Liang, Hao ; Liu, Wei-Yue ; Liu, Yang ; Jiang, Xiao ; Wang, Yuan ; Wan, Xu ; Cai, Wei-Qi ; Ju, Lei ; Chen, Luo-Kan ; Wang, Liu-Jun ; Gao, Yuan ; Chen, Kai ; Peng, Cheng-Zhi ; Chen, Zeng-Bing ; Pan, Jian-Wei: Metropolitan all-pass and inter-city quantum communication network. In: *Optics Express* 18 (2010), Nr. 26, S. 27217. http://dx.doi.org/10.1364/OE.18.027217. – DOI 10.1364/OE.18.027217. – ISSN 1094–4087

[28] Chen, Yu-Ao ; Zhang, Qiang ; Chen, Teng-Yun ; Cai, Wen-Qi ; Liao, Sheng-Kai ; Zhang, Jun ; Chen, Kai ; Yin, Juan ; Ren, Ji-Gang ; Chen, Zhu ; Han, Sheng-Long ; Yu, Qing ; Liang, Ken ; Zhou, Fei ; Yuan, Xiao ; Zhao, Mei-Sheng ; Wang, Tian-Yin ; Jiang, Xiao ; Zhang, Liang ; Liu, Wei-Yue ; Li, Yang ; Shen, Qi ; Cao, Yuan ; Lu, Chao-Yang ; Shu, Rong ; Wang, Jian-Yu ; Li, Li ; Liu, Nai-Le ; Xu, Feihu ; Wang, Xiang-Bin ; Peng, Cheng-Zhi ; Pan, Jian-Wei: An integrated space-to-ground quantum communication network over 4,600 kilometres. In: *Nature* 589 (2021), Nr. 7841, S. 214–219. http://dx.doi.org/10.1038/s41586-020-03093-8. – DOI 10.1038/s41586–020–03093–8. – ISSN 0028–0836

[29] Citron, M. L. ; Gray, H. R. ; Gabel, C. W. ; Stroud, C. R.: Experimental study of power broadening in a two-level atom. In: *Physical Review A* 16 (1977), Nr. 4, S. 1507–1512. http://dx.doi.org/10.1103/PhysRevA.16.1507. – DOI 10.1103/PhysRevA.16.1507. – ISSN 1050–2947

[30] Collett, Edward: *Optical engineering*. Bd. 36: *Polarized light: Fundamentals and applications*. New York : Dekker, 1993. – ISBN 0–8247–8729–3

[31] Da Silva, Saimon Filipe C. ; Undeutsch, Gabriel ; Lehner, Barbara ; Manna, Santanu ; Krieger, Tobias M. ; Reindl, Marcus ; Schimpf, Christian ; Trotta, Rinaldo ; Rastelli, Armando: GaAs quantum dots grown by droplet etching epitaxy as quantum light sources. In: *Applied Physics Letters* 119 (2021), Nr. 12, S. 120502. http://dx.doi.org/10.1063/5.0057070. – DOI 10.1063/5.0057070. – ISSN 00036951

[32] Dähne, Mario ; Eisele, Holger ; Jacobi, Karl: The Atomic Structure of Quantum Dots. In: Bimberg, Dieter (Hrsg.): *Semiconductor nanostructures*. Berlin : Springer, 2008 (Nanoscience and technology). – ISBN 3540778985, S. 123–137

[33] Ediger, M. ; Bester, G. ; Badolato, A. ; Petroff, P. M. ; Karrai, K. ; Zunger, A. ; Warburton, R. J.: Peculiar many-body effects revealed in the spectroscopy of highly charged quantum dots. In: *Nature Physics* 3 (2007), Nr. 11, 774–779. http://dx.doi.org/10.1038/nphys748. – DOI 10.1038/nphys748. – ISSN 1745–2473

[34] Ediger, M. ; Bester, G. ; Gerardot, B. D. ; Badolato, A. ; Petroff, P. M. ; Karrai, K. ; Zunger, A. ; Warburton, R. J.: Fine Structure of Negatively and Positively Charged Excitons in Semiconductor Quantum Dots: Electron-Hole Asymmetry. In: *Physical Review Letters* 98 (2007), Nr. 3, S. 36808. http://dx.doi.org/10.1103/PhysRevLett.98.036808. – DOI 10.1103/PhysRevLett.98.036808. – ISSN 0031–9007

[35] Ediger, M. ; Dalgarno, P. A. ; Smith, J. M. ; Gerardot, B. D. ; Warburton, R. J. ; Karrai, K. ; Petroff, P. M.: Controlled generation of neutral, negatively-charged and positively-charged excitons in the same single quantum dot. In: *Applied Physics Letters* 86 (2005), Nr. 21, S. 211909–3. http://dx.doi.org/10.1063/1.1937996. – DOI 10.1063/1.1937996

[36] Errando-Herranz, Carlos ; Schöll, Eva ; Picard, Raphaël ; Laini, Micaela ; Gyger, Samuel ; Elshaari, Ali W. ; Branny, Art ; Wennberg, Ulrika ;

Barbat, Sebastien ; Renaud, Thibaut ; Sartison, Marc ; Brotons-Gisbert, Mauro ; Bonato, Cristian ; Gerardot, Brian D. ; Zwiller, Val ; Jöns, Klaus D.: Resonance Fluorescence from Waveguide-Coupled, Strain-Localized, Two-Dimensional Quantum Emitters. In: *ACS photonics* 8 (2021), Nr. 4, S. 1069–1076. http://dx.doi.org/10.1021/acsphotonics.0c01653. – DOI 10.1021/acsphotonics.0c01653. – ISSN 2330–4022

[37] Ester, P. ; Stufler, S. ; Michaelis de Vasconcellos, S. ; Bichler, Max ; Zrenner, Artur: High resolution photocurrent-spectroscopy of a single quantum dot. In: *physica status solidi (c)* 3 (2006), Nr. 11, S. 3722–3725. http://dx.doi.org/10.1002/pssc.200671572. – DOI 10.1002/pssc.200671572. – ISSN 16101634

[38] Fafard, Simon: Quantum dot structures and devices with sharp adjustable electronic shells. In: *Physica E: Low-dimensional Systems and Nanostructures* 8 (2000), Nr. 2, S. 107–116. http://dx.doi.org/10.1016/S1386-9477(00)00126-0. – DOI 10.1016/S1386–9477(00)00126–0. – ISSN 1386–9477

[39] Fasching, G. ; Schrey, F. F. ; Brezna, W. ; Smoliner, J. ; Strasser, G. ; Unterrainer, K.: Photocurrent spectroscopy of single InAs/GaAs quantum dots. In: *physica status solidi (c)* 2 (2005), Nr. 8, S. 3114–3117. http://dx.doi.org/10.1002/pssc.200460772. – DOI 10.1002/pssc.200460772. – ISSN 16101634

[40] Fox, Anthony M.: *Oxford master series in physics Atomic, optical, and laser physics*. Bd. 15: *Quantum optics: An introduction*. Repr. Oxford : Oxford Univ. Press, 2011. – ISBN 978–0–19–856672–4

[41] Fox, Mark ; Ispasoiu, Radu: Quantum Wells, Superlattices, and Band-Gap Engineering. Version: 2007. http://dx.doi.org/10.1007/978-0-387-29185-7{_}42. In: Kasap, Safa O. (Hrsg.): *Springer handbook of electronic and photonic materials ; with 168 tables*. New York : Springer, 2007. – DOI 10.1007/978–0–387–29185–7_42. – ISBN 978–0–387–26059–4, S. 1021–1040

[42] Fry, P. ; Itskevich, I. ; Mowbray, D. ; Skolnick, M. ; Finley, J. ; Barker, J. ; O'Reilly, E. ; Wilson, L. ; Larkin, I. ; Maksym, P. ; Hopkinson, M. ; Al-Khafaji, M. ; David, J. ; Cullis, A. ; Hill, G. ; Clark, J.: Inverted Electron-Hole Alignment in InAs-GaAs Self-Assembled Quantum Dots. In: *Physical Review Letters* 84 (2000), Nr. 4, S. 733–736. http://dx.doi.org/10.1103/PhysRevLett.84.733. – DOI 10.1103/PhysRevLett.84.733. – ISSN 0031–9007

[43] Fry, P. W. ; Finley, J. J. ; Wilson, L. R. ; Lema?tre, A. ; Mowbray, D. J. ; Skolnick, M. S. ; Hopkinson, M. ; Hill, G. ; Clark, J. C.: Electric-field-dependent carrier capture and escape in self-assembled InAs/GaAs quantum dots. In: *Applied Physics Letters* 77 (2000), Nr. 26, S. 4344–4346. http://dx.doi.org/10.1063/1.1334363. – DOI 10.1063/1.1334363. – ISSN 00036951

[44] Geller, M. ; Stock, E. ; Kapteyn, C. ; Sellin, R. ; Bimberg, D.: Tunneling emission from self-organized In(Ga)As/GaAs quantum dots observed via time-resolved capacitance measurements. In: *Physical Review B* 73 (2006), Nr. 20. http://dx.doi.org/10.1103/PhysRevB.73.205331. – DOI 10.1103/PhysRevB.73.205331. – ISSN 1098–0121

[45] Gerardot, B. D. ; Brunner, D. ; Dalgarno, P. A. ; Karrai, K. ; Badolato, A. ; Petroff, P. M. ; Warburton, R. J.: Dressed excitonic states and quantum interference in a three-level quantum dot ladder system. In: *New Journal of Physics* 11 (2009), Nr. 1, S. 13028. http://dx.doi.org/10.1088/1367-2630/11/1/013028. – DOI 10.1088/1367–2630/11/1/013028. – ISSN 1367–2630

[46] Gibney, Elizabeth: Quantum gold rush: the private funding pouring into quantum start-ups. In: *Nature* 574 (2019), Nr. 7776, S. 22–24. http://dx.doi.org/10.1038/d41586-019-02935-4. – DOI 10.1038/d41586–019–02935–4. – ISSN 0028–0836

[47] Gisin, Nicolas ; Thew, Rob: Quantum communication. In: *Nature Photonics* 1 (2007), Nr. 3, S. 165–171. http://dx.doi.org/10.1038/nphoton.2007.22. – DOI 10.1038/nphoton.2007.22. – ISSN 1749–4885

[48] Gläßl, M. ; Barth, A. M. ; Axt, V. M.: Proposed robust and high-fidelity preparation of excitons and biexcitons in semiconductor quantum dots making active use of phonons. In: *Physical Review Letters* 110 (2013), Nr. 14, S. 147401. http://dx.doi.org/10.1103/PhysRevLett.110.147401. – DOI 10.1103/PhysRevLett.110.147401. – ISSN 0031–9007

[49] Gordon, S. ; Yacob, M. ; Reithmaier, J. P. ; Benyoucef, M. ; Zrenner, A.: Coherent photocurrent spectroscopy of single InP-based quantum dots in the telecom band at 1.5 µm. In: *Applied Physics B* 122 (2016), Nr. 2, S. 37. http://dx.doi.org/10.1007/s00340-015-6279-6. – DOI 10.1007/s00340–015–6279–6. – ISSN 0946–2171

[50] Gordon, Simon: *Einzelne Quantenpunkte in elektrisch abstimmbaren Diodenstrukturen: Photolumineszenz und kohärente Photostromspektroskopie*, UB-PAD - Paderborn University Library, Diss., 2017. http://dx.doi.org/10.17619/UNIPB/1-258. – DOI 10.17619/UNIPB/1–258

[51] Hannegan, J. ; Saha, U. ; Siverns, J. D. ; Cassell, J. ; Waks, E. ; Quraishi, Q.: C-band single photons from a trapped ion via two-stage frequency conversion. In: *Applied Physics Letters* 119 (2021), Nr. 8, S. 084001. http://dx.doi.org/10.1063/5.0059966. – DOI 10.1063/5.0059966. – ISSN 00036951

[52] Hargart, F. ; Müller, M. ; Roy-Choudhury, K. ; Portalupi, S. L. ; Schneider, C. ; Höfling, S. ; Kamp, M. ; Hughes, S. ; Michler, P.: Cavity-enhanced simultaneous dressing of quantum dot exciton and biexciton states. In: *Physical Review B* 93 (2016), Nr. 11, S. 681. http://dx.doi.org/10.1103/PhysRevB.93.115308. – DOI 10.1103/PhysRevB.93.115308. – ISSN 1098–0121

[53] He, Yu-Ming ; He, Yu ; Wei, Yu-Jia ; Wu, Dian ; Atatüre, Mete ; Schneider, Christian ; Höfling, Sven ; Kamp, Martin ; Lu, Chao-Yang ; Pan, Jian-Wei: On-demand semiconductor single-photon source with near-unity indistinguishability. In: *Nature Nanotechnology* 8 (2013), Nr. 3, S. 213–217. http://dx.doi.org/10.1038/nnano.2012.262. – DOI 10.1038/nnano.2012.262. – ISSN 1748–3387

[54] He, Yu-Ming ; He, Yu ; Wei, Yu-Jia ; Wu, Dian ; Atatüre, Mete ; Schneider, Christian ; Höfling, Sven ; Kamp, Martin ; Lu, Chao-Yang ; Pan, Jian-Wei: On-demand semiconductor single-photon source with near-unity indistinguishability. In: *Nature nanotechnology* 8 (2013), Nr. 3, S. 213–217. http://dx.doi.org/10.1038/nnano.2012.262. – DOI 10.1038/nnano.2012.262. – ISSN 1748–3395

[55] Heinze, Dirk ; Breddermann, Dominik ; Zrenner, Artur ; Schumacher, Stefan: A quantum dot single-photon source with on-the-fly all-optical polarization control and timed emission. In: *Nature communications* 6 (2015), S. 8473. http://dx.doi.org/10.1038/ncomms9473. – DOI 10.1038/ncomms9473. – ISSN 2041–1723

[56] Hertel, Ingolf V. ; Schulz, Claus-Peter: *Atome, Moleküle und optische Physik 1.* Springer Berlin Heidelberg, 2008. – ISBN 978–3–540–30613–9

[57] Higginbottom, D. B. ; Slodička, L. ; Araneda, G. ; Lachman, L. ; Filip, R. ; Hennrich, M. ; Blatt, R.: Pure single photons from a trapped atom source. In: *New Journal of Physics* 18 (2016), Nr. 9, S. 093038. http://dx.doi.org/10.1088/1367-2630/18/9/093038. – DOI 10.1088/1367–2630/18/9/093038. – ISSN 1367–2630

[58] Jacak, Lucjan ; Hawrylak, Paweł ; Wójs, Arkadiusz: *Quantum dots.* Berlin [u.a] : Springer, 1998. – ISBN 3–540–63653–6

[59] Javadi, A. ; Söllner, I. ; Arcari, M. ; Hansen, S. L. ; Midolo, L. ; Mahmoodian, S. ; Kiršanskė, G. ; Pregnolato, T. ; Lee, E. H. ; Song, J. D. ; Stobbe, S. ; Lodahl, P.: Single-photon non-linear optics with a quantum dot in a waveguide. In: *Nature communications* 6 (2015), S. 8655. http://dx.doi.org/10.1038/ncomms9655. – DOI 10.1038/ncomms9655. – ISSN 2041–1723

[60] Jin, Boyuan ; Mishra, Dhananjay ; Argyropoulos, Christos: Efficient single-photon pair generation by spontaneous parametric down-conversion in nonlinear plasmonic metasurfaces. In: *Nanoscale* 13 (2021), Nr. 47, S. 19903–19914. http://dx.doi.org/10.1039/D1NR05379E. – DOI 10.1039/D1NR05379E

[61] Jonas, B. ; Heinze, D. ; Schöll, E. ; Kallert, P. ; Langer, T. ; Krehs, S. ; Widhalm, A. ; Jöns, K. D. ; Reuter, D. ; Schumacher, S. ; Zrenner, A.: Nonlinear down-conversion in a single quantum dot. In: *Nature communications* 13 (2022), Nr. 1, S. 1387. http://dx.doi.org/10.1038/s41467-022-28993-3. – DOI 10.1038/s41467–022–28993–3. – ISSN 2041–1723

[62] Jundt, Gregor ; Robledo, Lucio ; Högele, Alexander ; Fält, Stefan ; Imamoğlu, Atac: Observation of Dressed Excitonic States in a Single Quantum Dot. In: *Physical Review Letters* 100 (2008), Nr. 17. http://dx.doi.org/10.1103/PhysRevLett.100.177401. – DOI 10.1103/PhysRevLett.100.177401. – ISSN 0031–9007

[63] Kagan, Cherie R. ; Bassett, Lee C. ; Murray, Christopher B. ; Thompson, Sarah M.: Colloidal Quantum Dots as Platforms for Quantum Information Science.

In: *Chemical reviews* 121 (2021), Nr. 5, S. 3186–3233. http://dx.doi.org/10.1021/acs.chemrev.0c00831. – DOI 10.1021/acs.chemrev.0c00831

[64] Kaldewey, Timo ; Lüker, Sebastian ; Kuhlmann, Andreas V. ; Valentin, Sascha R. ; Ludwig, Arne ; Wieck, Andreas D. ; Reiter, Doris E. ; Kuhn, Tilmann ; Warburton, Richard J.: Coherent and robust high-fidelity generation of a biexciton in a quantum dot by rapid adiabatic passage. In: *Physical Review B* 95 (2017), Nr. 16. http://dx.doi.org/10.1103/PhysRevB.95.161302. – DOI 10.1103/PhysRevB.95.161302. – ISSN 1098–0121

[65] Kastner, Marc A.: Artificial Atoms. In: *Physics Today* 46 (1993), Nr. 1, S. 24. http://dx.doi.org/10.1063/1.881393. – DOI 10.1063/1.881393. – ISSN 00319228

[66] Kiraz, A. ; Fälth, S. ; Becher, C. ; Gayral, B. ; Schoenfeld, W. V. ; Petroff, P. M. ; Zhang, Lidong ; Hu, E. ; Imamoğlu, A.: Photon correlation spectroscopy of a single quantum dot. In: *Physical review. B, Condensed matter* 65 (2002), Nr. 16. http://dx.doi.org/10.1103/PhysRevB.65.161303. – DOI 10.1103/PhysRevB.65.161303. – ISSN 0163–1829

[67] Krügel, A. ; Axt, V. M. ; Kuhn, T. ; Machnikowski, P. ; Vagov, A.: The role of acoustic phonons for Rabi oscillations in semiconductor quantum dots. In: *Applied Physics B* 81 (2005), Nr. 7, 897–904. http://dx.doi.org/10.1007/s00340-005-1984-1. – DOI 10.1007/s00340–005–1984–1. – ISSN 0946–2171

[68] Kuhlmann, Andreas V. ; Houel, Julien ; Brunner, Daniel ; Ludwig, Arne ; Reuter, Dirk ; Wieck, Andreas D. ; Warburton, Richard J.: A dark-field microscope for background-free detection of resonance fluorescence from single semiconductor quantum dots operating in a set-and-forget mode. In: *The Review of scientific instruments* 84 (2013), Nr. 7, S. 073905. http://dx.doi.org/10.1063/1.4813879. – DOI 10.1063/1.4813879. – ISSN 0034–6748

[69] Kurtsiefer ; Mayer ; Zarda ; Weinfurter: Stable solid-state source of single photons. In: *Physical Review Letters* 85 (2000), Nr. 2, S. 290–293. http://dx.doi.org/10.1103/PhysRevLett.85.290. – DOI 10.1103/PhysRevLett.85.290. – ISSN 0031–9007

[70] Li, Tian ; Dagenais, Mario: Below-bandgap absorption in InAs/GaAs self-assembled quantum dot solar cells. In: *Progress in Photovoltaics: Research and Applications* 23 (2015), Nr. 8, S. 997–1002. http://dx.doi.org/10.1002/pip.2515. – DOI 10.1002/pip.2515. – ISSN 10627995

[71] Litvin, A. P. ; Martynenko, I. V. ; Purcell-Milton, F. ; Baranov, A. V. ; Fedorov, A. V. ; Gun'ko, Y. K.: Colloidal quantum dots for optoelectronics. In: *Journal of Materials Chemistry A* 5 (2017), Nr. 26, S. 13252–13275. http://dx.doi.org/10.1039/c7ta02076g. – DOI 10.1039/c7ta02076g. – ISSN 2050–7488

[72] Liu, Feng ; Brash, Alistair J. ; O'Hara, John ; Martins, Luis M. P. P. ; Phillips, Catherine L. ; Coles, Rikki J. ; Royall, Benjamin ; Clarke, Edmund

; Bentham, Christopher ; Prtljaga, Nikola ; Itskevich, Igor E. ; Wilson, Luke R. ; Skolnick, Maurice S. ; Fox, A. M.: High Purcell factor generation of indistinguishable on-chip single photons. In: *Nature nanotechnology* 13 (2018), Nr. 9, S. 835–840. http://dx.doi.org/10.1038/s41565-018-0188-x. – DOI 10.1038/s41565–018–0188–x. – ISSN 1748–3395

[73] Liu, Jin ; Su, Rongbin ; Wei, Yuming ; Yao, Beimeng ; Da Silva, Saimon Filipe C. ; Yu, Ying ; Iles-Smith, Jake ; Srinivasan, Kartik ; Rastelli, Armando ; Li, Juntao ; Wang, Xuehua: A solid-state source of strongly entangled photon pairs with high brightness and indistinguishability. In: *Nature nanotechnology* 14 (2019), Nr. 6, S. 586–593. http://dx.doi.org/10.1038/s41565-019-0435-9. – DOI 10.1038/s41565–019–0435–9. – ISSN 1748–3395

[74] Lochner, P. ; Kerski, J. ; Kurzmann, A. ; Wieck, A. D. ; Ludwig, A. ; Geller, M. ; Lorke, A.: Internal photoeffect from a single quantum emitter. In: *Physical Review B* 103 (2021), Nr. 7. http://dx.doi.org/10.1103/PhysRevB.103.075426. – DOI 10.1103/PhysRevB.103.075426. – ISSN 1098–0121

[75] Lodahl, Peter ; Stobbe, Søren: Solid-state quantum optics with quantum dots in photonic nanostructures. In: *Nanophotonics* 2 (2013), Nr. 1, S. 39–55. http://dx.doi.org/10.1515/nanoph-2012-0039. – DOI 10.1515/nanoph–2012–0039

[76] Lumeau, Julien ; Smirnov, Vadim ; Glebov, Alexei ; Glebov, Leonid B.: Ultra-narrow bandpass filters based on volume Bragg grating technologies. In: Kazemi, Alex A. (Hrsg.) ; Kress, Bernard C. (Hrsg.) ; Chan, Eric Y. (Hrsg.): *Photonics in the Transportation Industry: Auto to Aerospace III*, SPIE, 2010 (SPIE Proceedings), S. 76750H

[77] Mantei, Dirk: *Polarisationsabhängige Zustandskontrolle einzelner Halbleiter-Quantenpunkte*. Paderborn, Dissertation, 2014

[78] Mäntynen, Henrik ; Anttu, Nicklas ; Sun, Zhipei ; Lipsanen, Harri: Single-photon sources with quantum dots in III–V nanowires. In: *Nanophotonics* 8 (2019), Nr. 5, S. 747–769. http://dx.doi.org/10.1515/nanoph-2019-0007. – DOI 10.1515/nanoph–2019–0007

[79] Mar, J. D. ; Baumberg, J. J. ; Xu, X. L. ; Irvine, A. C. ; Williams, D. A.: Precise measurements of the dipole moment and polarizability of the neutral exciton and positive trion in a single quantum dot. In: *Physical Review B* 95 (2017), Nr. 20. http://dx.doi.org/10.1103/PhysRevB.95.201304. – DOI 10.1103/PhysRevB.95.201304. – ISSN 1098–0121

[80] Massaro, Marcello ; Meyer-Scott, Evan ; Montaut, Nicola ; Herrmann, Harald ; Silberhorn, Christine: Improving SPDC single-photon sources via extended heralding and feed-forward control. In: *New Journal of Physics* 21 (2019), Nr. 5, S. 053038. http://dx.doi.org/10.1088/1367-2630/ab1ec3. – DOI 10.1088/1367–2630/ab1ec3. – ISSN 1367–2630

[81] Mendez, E. E. ; Bastard, G. ; Chang, L. L. ; Esaki, L. ; Morkoc, H. ; Fischer, R.: Effect of an electric field on the luminescence of GaAs quantum wells.

In: *Physical Review B* 26 (1982), Nr. 12, S. 7101–7104. http://dx.doi.org/10.1103/PhysRevB.26.7101. – DOI 10.1103/PhysRevB.26.7101. – ISSN 1098–0121

[82] Meystre, Pierre ; Sargent, Murray: *Elements of Quantum Optics*. 4. Berlin, Heidelberg : Springer Berlin Heidelberg, 2007. http://dx.doi.org/10.1007/978-3-540-74211-1. http://dx.doi.org/10.1007/978-3-540-74211-1. – ISBN 978–3–540–74209–8

[83] Michler, P. ; Kiraz, A. ; Becher, C. ; Schoenfeld, W. V. ; Petroff, P. M. ; Lidong Zhang ; Hu, E. ; Imamoglu, A.: A Quantum Dot Single-Photon Turnstile Device. In: *Science* 290 (2000), Nr. 5500, S. 2282–2285. http://dx.doi.org/10.1126/science.290.5500.2282. – DOI 10.1126/science.290.5500.2282

[84] Michler, Peter: *Single Semiconductor Quantum Dots*. Berlin, Heidelberg : Springer-Verlag Berlin Heidelberg, 2009 (Nanoscience and technology). http://dx.doi.org/10.1007/978-3-540-87446-1. http://dx.doi.org/10.1007/978-3-540-87446-1. – ISBN 3540874461

[85] Miller, D. A. B. ; Chemla, D. ; Damen, T. ; Gossard, A. ; Wiegmann, W. ; Wood, T. ; Burrus, C.: Band-Edge Electroabsorption in Quantum Well Structures: The Quantum-Confined Stark Effect. In: *Physical Review Letters* 53 (1984), Nr. 22, S. 2173–2176. http://dx.doi.org/10.1103/PhysRevLett.53.2173. – DOI 10.1103/PhysRevLett.53.2173. – ISSN 0031–9007

[86] Moehl, S. ; Zhao, Hui ; Don, B. D. ; Wachter, S. ; Kalt, H.: Solid immersion lens-enhanced nano-photoluminescence: Principle and applications. In: *Physical review. B, Condensed matter* 93 (2003), Nr. 10, S. 6265–6272. http://dx.doi.org/10.1063/1.1567035. – DOI 10.1063/1.1567035. – ISSN 0163–1829

[87] Mohan, A. ; Felici, M. ; Gallo, P. ; Dwir, B. ; Rudra, A. ; Faist, J. ; Kapon, E.: Polarization-entangled photons produced with high-symmetry site-controlled quantum dots. In: *Nature Photonics* 4 (2010), Nr. 5, S. 302–306. http://dx.doi.org/10.1038/nphoton.2010.2. – DOI 10.1038/nphoton.2010.2. – ISSN 1749–4885

[88] Moore, W. J. ; Holm, R. T.: Infrared dielectric constant of gallium arsenide. In: *Journal of Applied Physics* 80 (1996), Nr. 12, S. 6939–6942. http://dx.doi.org/10.1063/1.363818. – DOI 10.1063/1.363818

[89] Moser, C. ; Havermeyer, F.: Ultra-narrow-band tunable laserline notch filter. In: *Applied Physics B* 95 (2009), Nr. 3, S. 597–601. http://dx.doi.org/10.1007/s00340-009-3447-6. – DOI 10.1007/s00340–009–3447–6. – ISSN 0946–2171

[90] Mosley, Peter J. ; Lundeen, Jeff S. ; Smith, Brian J. ; Wasylczyk, Piotr ; U'Ren, Alfred B. ; Silberhorn, Christine ; Walmsley, Ian A.: Heralded generation of ultrafast single photons in pure quantum States. In: *Physical Review Letters* 100 (2008), Nr. 13, S. 133601. http://dx.doi.org/10.1103/PhysRevLett.100.133601. – DOI 10.1103/PhysRevLett.100.133601. – ISSN 0031–9007

[91] Mukherjee, Amlan ; Widhalm, Alex ; Siebert, Dustin ; Krehs, Sebastian ; Sharma, Nandlal ; Thiede, Andreas ; Reuter, Dirk ; Förstner, Jens

; Zrenner, Artur: Electrically controlled rapid adiabatic passage in a single quantum dot. In: *Applied Physics Letters* 116 (2020), Nr. 25, S. 251103. http://dx.doi.org/10.1063/5.0012257. – DOI 10.1063/5.0012257. – ISSN 00036951

[92] Muller, Andreas ; Fang, Wei ; Lawall, John ; Solomon, Glenn S.: Emission spectrum of a dressed exciton-biexciton complex in a semiconductor quantum dot. In: *Physical Review Letters* 101 (2008), Nr. 2, S. 027401. http://dx.doi.org/10.1103/PhysRevLett.101.027401. – DOI 10.1103/PhysRevLett.101.027401. – ISSN 0031–9007

[93] Müller, M. ; Bounouar, S. ; Jöns, K. D. ; Gläßl, M. ; Michler, P.: On-demand generation of indistinguishable polarization-entangled photon pairs. In: *Nature Photonics* 8 (2014), Nr. 3, S. 224–228. http://dx.doi.org/10.1038/NPHOTON.2013.377. – DOI 10.1038/NPHOTON.2013.377. – ISSN 1749–4885

[94] Narvaez, Gustavo A. ; Bester, Gabriel ; Zunger, Alex: Excitons, biexcitons, and trions in self-assembled (In,Ga)As/GaAs quantum dots: Recombination energies, polarization, and radiative lifetimes versus dot height. In: *Physical Review B* 72 (2005), Nr. 24. http://dx.doi.org/10.1103/PhysRevB.72.245318. – DOI 10.1103/PhysRevB.72.245318. – ISSN 1098–0121

[95] Nawrath, C. ; Olbrich, F. ; Paul, M. ; Portalupi, S. L. ; Jetter, M. ; Michler, P.: Coherence and indistinguishability of highly pure single photons from non-resonantly and resonantly excited telecom C-band quantum dots. In: *Applied Physics Letters* 115 (2019), Nr. 2, S. 023103. http://dx.doi.org/10.1063/1.5095196. – DOI 10.1063/1.5095196. – ISSN 00036951

[96] Novotny, L. ; Grober, R. D. ; Karrai, K.: Reflected image of a strongly focused spot. In: *Optics Letters* 26 (2001), Nr. 11, S. 789–791. http://dx.doi.org/10.1364/OL.26.000789. – DOI 10.1364/OL.26.000789. – ISSN 0146–9592

[97] Ortiz-Gutiérrez, Luis ; Teixeira, Raul C. ; Eloy, Aurélien ; Da Ferreira Silva, Dilleys ; Kaiser, Robin ; Bachelard, Romain ; Fouché, Mathilde: Mollow triplet in cold atoms. In: *New Journal of Physics* 21 (2019), Nr. 9, S. 093019. http://dx.doi.org/10.1088/1367-2630/ab3ca9. – DOI 10.1088/1367–2630/ab3ca9. – ISSN 1367–2630

[98] Patel, Raj B. ; Bennett, Anthony J. ; Farrer, Ian ; Nicoll, Christine A. ; Ritchie, David A. ; Shields, Andrew J.: Two-photon interference of the emission from electrically tunable remote quantum dots. In: *Nature Photonics* 4 (2010), Nr. 9, S. 632–635. http://dx.doi.org/10.1038/nphoton.2010.161. – DOI 10.1038/nphoton.2010.161. – ISSN 1749–4885

[99] Penzkofer, A. ; Bugayev, A. A.: Two-photon absorption and emission dynamics of bulk GaAs. In: *Optical and Quantum Electronics* 21 (1989), Nr. 4, S. 283–306. http://dx.doi.org/10.1007/BF02027300. – DOI 10.1007/BF02027300. – ISSN 0306–8919

[100] Pirandola, S. ; Andersen, U. L. ; Banchi, L. ; Berta, M. ; Bunandar, D. ; Colbeck, R. ; Englund, D. ; Gehring, T. ; Lupo, C. ; Ottaviani, C.

; Pereira, J. L. ; Razavi, M. ; Shamsul Shaari, J. ; Tomamichel, M. ; Usenko, V. C. ; Vallone, G. ; Villoresi, P. ; Wallden, P.: Advances in quantum cryptography. In: *Advances in Optics and Photonics* 12 (2020), Nr. 4, S. 1012. http://dx.doi.org/10.1364/AOP.361502. – DOI 10.1364/AOP.361502

[101] Polland, H. ; Schultheis, L. ; Kuhl, J. ; Göbel, E. ; Tu, C.: Lifetime Enhancement of Two-Dimensional Excitons by the Quantum-Confined Stark Effect. In: *Physical Review Letters* 55 (1985), Nr. 23, S. 2610–2613. http://dx.doi.org/10.1103/PhysRevLett.55.2610. – DOI 10.1103/PhysRevLett.55.2610. – ISSN 0031–9007

[102] Portalupi, Simone L. ; Jetter, Michael ; Michler, Peter: InAs quantum dots grown on metamorphic buffers as non-classical light sources at telecom C-band: a review. In: *Semiconductor Science and Technology* 34 (2019), Nr. 5, S. 053001. http://dx.doi.org/10.1088/1361-6641/ab08b4. – DOI 10.1088/1361–6641/ab08b4. – ISSN 0268–1242

[103] Pursley, B. C. ; Carter, S. G. ; Yakes, M. K. ; Bracker, A. S. ; Gammon, D.: Picosecond pulse shaping of single photons using quantum dots. In: *Nature communications* 9 (2018), Nr. 1, S. 115. http://dx.doi.org/10.1038/s41467-017-02552-7. – DOI 10.1038/s41467–017–02552–7. – ISSN 2041–1723

[104] Rai, Ashish K.: *Optically pumped and electrically triggered single photon emission from a single quantum dot.* Bochum, Ruhr-Universität Bochum, Dissertation, 31.01.2013. http://www-brs.ub.ruhr-uni-bochum.de/netahtml/HSS/Diss/RaiAshishKumar/diss.pdf

[105] Ramsay, A. J. ; Gopal, Achanta V. ; Gauger, E. M. ; Nazir, A. ; Lovett, B. W. ; Fox, A. M. ; Skolnick, M. S.: Damping of Exciton Rabi Rotations by Acoustic Phonons in Optically Excited InGaAs/GaAs Quantum Dots. In: *Physical Review Letters* 104 (2010), Nr. 1. http://dx.doi.org/10.1103/PhysRevLett.104.017402. – DOI 10.1103/PhysRevLett.104.017402. – ISSN 0031–9007

[106] Reindl, Marcus ; Jöns, Klaus D. ; Huber, Daniel ; Schimpf, Christian ; Huo, Yongheng ; Zwiller, Val ; Rastelli, Armando ; Trotta, Rinaldo: Phonon-Assisted Two-Photon Interference from Remote Quantum Emitters. In: *Nano letters* 17 (2017), Nr. 7, S. 4090–4095. http://dx.doi.org/10.1021/acs.nanolett.7b00777. – DOI 10.1021/acs.nanolett.7b00777. – ISSN 1530–6984

[107] Reiter, D. E. ; Kuhn, T. ; Glässl, M. ; Axt, V. M.: The role of phonons for exciton and biexciton generation in an optically driven quantum dot. In: *Journal of physics. Condensed matter : an Institute of Physics journal* 26 (2014), Nr. 42, S. 423203. http://dx.doi.org/10.1088/0953-8984/26/42/423203. – DOI 10.1088/0953–8984/26/42/423203. – ISSN 0953–8984

[108] Reitzenstein, S. ; Forchel, A.: Quantum dot micropillars. In: *New Journal of Physics* 43 (2010), Nr. 3, S. 033001. http://dx.doi.org/10.1088/0022-3727/43/3/033001. – DOI 10.1088/0022–3727/43/3/033001. – ISSN 1367–2630

[109] Rodt, S. ; Heitz, R. ; Schliwa, A. ; Sellin, R. L. ; Guffarth, F. ; Bimberg, D.: Repulsive exciton-exciton interaction in quantum dots. In: *Physical Review B*

68 (2003), Nr. 3, S. 201302. http://dx.doi.org/10.1103/PhysRevB.68.035331. – DOI 10.1103/PhysRevB.68.035331. – ISSN 1098–0121

[110] Schwartz, I. ; Cogan, D. ; Schmidgall, E. R. ; Don, Y. ; Gantz, L. ; Kenneth, O. ; Lindner, N. H. ; Gershoni, D.: Deterministic generation of a cluster state of entangled photons. In: *Science (New York, N.Y.)* 354 (2016), Nr. 6311, S. 434–437. http://dx.doi.org/10.1126/science.aah4758. – DOI 10.1126/science.aah4758. – ISSN 1095–9203

[111] Schweickert, Lucas ; Jöns, Klaus D. ; Zeuner, Katharina D. ; Covre da Silva, Saimon F. ; Huang, Huiying ; Lettner, Thomas ; Reindl, Marcus ; Zichi, Julien ; Trotta, Rinaldo ; Rastelli, Armando ; Zwiller, Val: On-demand generation of background-free single photons from a solid-state source. In: *Applied Physics Letters* 112 (2018), Nr. 9, S. 093106. http://dx.doi.org/10.1063/1.5020038. – DOI 10.1063/1.5020038. – ISSN 00036951

[112] Seidl, Stefan ; Kroner, Martin ; Högele, Alexander ; Karrai, Khaled ; Warburton, Richard J. ; Badolato, Antonio ; Petroff, Pierre M.: Effect of uniaxial stress on excitons in a self-assembled quantum dot. In: *Applied Physics Letters* 88 (2006), Nr. 20, S. 203113. http://dx.doi.org/10.1063/1.2204843. – DOI 10.1063/1.2204843. – ISSN 00036951

[113] Senellart, Pascale ; Solomon, Glenn ; White, Andrew: High-performance semiconductor quantum-dot single-photon sources. In: *Nature nanotechnology* 12 (2017), Nr. 11, S. 1026–1039. http://dx.doi.org/10.1038/NNANO.2017.218. – DOI 10.1038/NNANO.2017.218. – ISSN 1748–3395

[114] Seufert, J. ; Obert, M. ; Scheibner, M. ; Gippius, N. A. ; Bacher, G. ; Forchel, A. ; Passow, T. ; Leonardi, K. ; Hommel, D.: Stark effect and polarizability in a single CdSe/ZnSe quantum dot. In: *Applied Physics Letters* 79 (2001), Nr. 7, S. 1033–1035. http://dx.doi.org/10.1063/1.1389504. – DOI 10.1063/1.1389504. – ISSN 00036951

[115] Sharma, Nand L.: *Molecular beam epitaxy of tailored (In,Ga)As/GaAs quantum dot heterostructures*, UB-PAD - Paderborn University Library, Diss., 2017. http://dx.doi.org/10.17619/UNIPB/1-228. – DOI 10.17619/UNIPB/1–228

[116] Somaschi, N. ; Giesz, V. ; Santis, L. de ; Loredo, J. C. ; Almeida, M. P. ; Hornecker, G. ; Portalupi, S. L. ; Grange, T. ; Antón, C. ; Demory, J. ; Gómez, C. ; Sagnes, I. ; Lanzillotti-Kimura, N. D. ; Lemaítre, A. ; Auffeves, A. ; White, A. G. ; Lanco, L. ; Senellart, P.: Near-optimal single-photon sources in the solid state. In: *Nature Photonics* 10 (2016), Nr. 5, S. 340–345. http://dx.doi.org/10.1038/nphoton.2016.23. – DOI 10.1038/nphoton.2016.23. – ISSN 1749–4885

[117] Stevenson, R. ; Young, R. ; See, P. ; Gevaux, D. ; Cooper, K. ; Atkinson, P. ; Farrer, I. ; Ritchie, D. ; Shields, A.: Magnetic-field-induced reduction of the exciton polarization splitting in InAs quantum dots. In: *Physical Review B* 73 (2006), Nr. 3. http://dx.doi.org/10.1103/PhysRevB.73.033306. – DOI 10.1103/PhysRevB.73.033306. – ISSN 1098–0121

[118] Stevenson, R. M. ; Young, R. J. ; Atkinson, P. ; Cooper, K. ; Ritchie, D. A. ; Shields, A. J.: A semiconductor source of triggered entangled photon pairs. In: *Nature* 439 (2006), Nr. 7073, S. 179–182. http://dx.doi.org/10.1038/nature04446. – DOI 10.1038/nature04446. – ISSN 0028–0836

[119] Stievater, T. H. ; Li, Xiaoqin ; Steel, D. G. ; Gammon, D. ; Katzer, D. S. ; Park, D. ; Piermarocchi, C. ; Sham, L. J.: Rabi Oscillations of Excitons in Single Quantum Dots. In: *Physical Review Letters* 87 (2001), Nr. 13. http://dx.doi.org/10.1103/PhysRevLett.87.133603. – DOI 10.1103/PhysRevLett.87.133603. – ISSN 0031–9007

[120] Stufler, S. ; Ester, P. ; Zrenner, Artur ; Bichler, M.: Ramsey Fringes in an Electric-Field-Tunable Quantum Dot System. In: *Physical Review Letters* 96 (2006), Nr. 3, S. 37402. http://dx.doi.org/10.1103/PhysRevLett.96.037402. – DOI 10.1103/PhysRevLett.96.037402. – ISSN 0031–9007

[121] Stufler, S. ; Machnikowski, P. ; Ester, P. ; Bichler, M. ; Axt, V. ; Kuhn, T. ; Zrenner, Artur: Two-photon Rabi oscillations in a single InxGa1−xAs / GaAs quantum dot. In: *Physical Review B* 73 (2006), Nr. 12. http://dx.doi.org/10.1103/PhysRevB.73.125304. – DOI 10.1103/PhysRevB.73.125304. – ISSN 1098–0121

[122] Stufler, Stefan ; Ester, Patrick ; Zrenner, Artur ; Bichler, Max: Power broadening of the exciton linewidth in a single InGaAs GaAs quantum dot. In: *Applied Physics Letters* 85 (2004), Nr. 18, S. 4202. http://dx.doi.org/10.1063/1.1815373. – DOI 10.1063/1.1815373. – ISSN 00036951

[123] Sweeney, Timothy M. ; Carter, Samuel G. ; Bracker, Allan S. ; Kim, Mijin ; Kim, Chul S. ; Yang, Lily ; Vora, Patrick M. ; Brereton, Peter G. ; Cleveland, Erin R. ; Gammon, Daniel: Cavity-stimulated Raman emission from a single quantum dot spin. In: *Nature Photonics* (2014). http://dx.doi.org/10.1038/nphoton.2014.84. – DOI 10.1038/nphoton.2014.84. – ISSN 1749–4885

[124] Tomm, Natasha ; Javadi, Alisa ; Antoniadis, Nadia O. ; Najer, Daniel ; Löbl, Matthias C. ; Korsch, Alexander R. ; Schott, Rüdiger ; Valentin, Sascha R. ; Wieck, Andreas D. ; Ludwig, Arne ; Warburton, Richard J.: A bright and fast source of coherent single photons. In: *Nature nanotechnology* 16 (2021), Nr. 4, S. 399–403. http://dx.doi.org/10.1038/s41565-020-00831-x. – DOI 10.1038/s41565–020–00831–x. – ISSN 1748–3395

[125] Ulhaq, A. ; Weiler, S. ; Ulrich, S. M. ; Rossbach, R. ; Jetter, M. ; Michler, P.: Cascaded single-photon emission from the Mollow triplet sidebands of a quantum dot. In: *Nature Photonics* (2012). http://dx.doi.org/10.1038/nphoton.2012.23. – DOI 10.1038/nphoton.2012.23. – ISSN 1749–4885

[126] Ulrich, S. M. ; Benyoucef, M. ; Michler, P. ; Baer, N. ; Gartner, P. ; Jahnke, F. ; Schwab, M. ; Kurtze, H. ; Bayer, M. ; Fafard, S. ; Wasilewski, Z. ; Forchel, A.: Correlated photon-pair emission from a charged single quantum dot. In: *Physical Review B* 71 (2005), Nr. 23. http://dx.doi.org/10.1103/PhysRevB.71.235328. – DOI 10.1103/PhysRevB.71.235328. – ISSN 1098–0121

[127] Vagov, A. ; Croitoru, M. D. ; Axt, V. M. ; Kuhn, T. ; Peeters, F. M.: High pulse area undamping of Rabi oscillations in quantum dots coupled to phonons. In: *physica status solidi (b)* 243 (2006), Nr. 10, S. 2233–2240. http://dx.doi.org/10.1002/pssb.200668029. – DOI 10.1002/pssb.200668029. – ISSN 03701972

[128] Vagov, A. ; Croitoru, M. D. ; Axt, V. M. ; Kuhn, T. ; Peeters, F. M.: Nonmonotonic field dependence of damping and reappearance of Rabi oscillations in quantum dots. In: *Physical Review Letters* 98 (2007), Nr. 22, S. 227403. http://dx.doi.org/10.1103/PhysRevLett.98.227403. – DOI 10.1103/PhysRevLett.98.227403. – ISSN 0031–9007

[129] Vora, Patrick M. ; Bracker, Allan S. ; Carter, Samuel G. ; Sweeney, Timothy M. ; Kim, Mijin ; Kim, Chul S. ; Yang, Lily ; Brereton, Peter G. ; Economou, Sophia E. ; Gammon, Daniel: Spin-cavity interactions between a quantum dot molecule and a photonic crystal cavity. In: *Nature communications* 6 (2015), S. 7665. http://dx.doi.org/10.1038/ncomms8665. – DOI 10.1038/ncomms8665. – ISSN 2041–1723

[130] Widhalm, Alex: *Ultraschnelle elektrische Kontrolle optischer Eigenschaften und Übergänge einzelner Halbleiter-Quantenpunkte*. Paderborn, Univerität Paderborn, Dissertation, 2018. http://dx.doi.org/10.17619/UNIPB/1-493. – DOI 10.17619/UNIPB/1–493

[131] Widhalm, Alex ; Krehs, Sebastian ; Siebert, Dustin ; Sharma, Nand L. ; Langer, Timo ; Jonas, Björn ; Reuter, Dirk ; Thiede, Andreas ; Förstner, Jens ; Zrenner, Artur: Optoelectronic sampling of ultrafast electric transients with single quantum dots. In: *Applied Physics Letters* 119 (2021), Nr. 18, S. 181109. http://dx.doi.org/10.1063/5.0061358. – DOI 10.1063/5.0061358. – ISSN 00036951

[132] Widhalm, Alex ; Mukherjee, Amlan ; Krehs, Sebastian ; Sharma, Nandlal ; Kölling, Peter ; Thiede, Andreas ; Reuter, Dirk ; Förstner, Jens ; Zrenner, Artur: Ultrafast electric phase control of a single exciton qubit. In: *Applied Physics Letters* 112 (2018), Nr. 11, S. 111105. http://dx.doi.org/10.1063/1.5020364. – DOI 10.1063/1.5020364

[133] Xia, Sijia ; Aoki, Tomoyuki ; Gao, Kang ; Arita, Munetaka ; Arakawa, Yasuhiko ; Holmes, Mark J.: Enhanced Single-Photon Emission from GaN Quantum Dots in Bullseye Structures. In: *ACS photonics* 8 (2021), Nr. 6, S. 1656–1661. http://dx.doi.org/10.1021/acsphotonics.1c00032. – DOI 10.1021/acsphotonics.1c00032. – ISSN 2330–4022

[134] Yatsiv, Shaul ; Rokni, M. ; Barak, S.: Enhanced Two-Proton Emission. In: *Physical Review Letters* 20 (1968), Nr. 23, S. 1282–1284. http://dx.doi.org/10.1103/PhysRevLett.20.1282. – DOI 10.1103/PhysRevLett.20.1282. – ISSN 0031–9007

[135] Zhang, Chao ; Huang, Yun-Feng ; Liu, Bi-Heng ; Li, Chuan-Feng ; Guo, Guang-Can: Spontaneous Parametric Down–Conversion Sources for Multiphoton Experiments. In: *Advanced Quantum Technologies* 4 (2021), Nr. 5, S. 2000132.

http://dx.doi.org/10.1002/qute.202000132. – DOI 10.1002/qute.202000132. – ISSN 2511–9044

[136] Zhong, Han-Sen ; Wang, Hui ; Deng, Yu-Hao ; Chen, Ming-Cheng ; Peng, Li-Chao ; Luo, Yi-Han ; Qin, Jian ; Wu, Dian ; Ding, Xing ; Hu, Yi ; Hu, Peng ; Yang, Xiao-Yan ; Zhang, Wei-Jun ; Li, Hao ; Li, Yuxuan ; Jiang, Xiao ; Gan, Lin ; Yang, Guangwen ; You, Lixing ; Wang, Zhen ; Li, Li ; Liu, Nai-Le ; Lu, Chao-Yang ; Pan, Jian-Wei: Quantum computational advantage using photons. In: *Science (New York, N.Y.)* 370 (2020), Nr. 6523, S. 1460–1463. http://dx.doi.org/10.1126/science.abe8770. – DOI 10.1126/science.abe8770. – ISSN 1095–9203

[137] Zrenner, Artur ; Beham, E. ; Stufler, S. ; Findeis, F. ; Bichler, M. ; Abstreiter, Gerhard: Coherent properties of a two-level system based on a quantum-dot photodiode. In: *Nature* 418 (2002), Nr. 6898, S. 612–614. http://dx.doi.org/10.1038/nature00912. – DOI 10.1038/nature00912. – ISSN 0028–0836

Acknowledgments

Over the years, numerous people have contributed directly or indirectly to the success of this work. I would like to thank:

- **Prof. Dr. Artur Zrenner** for giving me the opportunity to work in his group and for supervising my thesis.
- **Prof. Dr. Stefan Schumacher** for reviewing my thesis as the second supervisor and his group for providing the theoretical support for the research project. In particular, I would like to thank **Dr. Dirk Heinze**, who performed the simulations included in this work.
- **Prof. Dr. Dirk Reuter** and his group for providing the MBE material. Especially, **Timo Langer** who ended up spending a lot of time at the MBE, growing the majority of my samples.
- The colleagues from **AG Zrenner** and **AG Jöns** for creating a great working environment, lots of mutual assistance and interesting discussions. In particular, I would like to mention: **Alex** and **Sebastian**, who accompanied me during the entire PhD time and on several great trips to conferences. **Patricia**, who investigated the SILs during her master thesis and did the fabrication of the sample that ended up being THE sample for this thesis. **Eva**, who brought some valuable know-how to the lab and helped with the alignment of the setup during the first successful down-conversion experiment
- All my friends that accompanied me during the time of my PhD and my studies, making it a memorable time: **Artjom** and **Markus**, my best friends and long-term roommates with whom I spend many great nights in the bars of Paderborn. **Dennis**, **Jannick**, **Peter** and **Thomas**, who alongside me fought their way through the numerous exams during our studies, all the way to our Master's degrees and were always good company for nerdy discussions and activities. My **Rockharz crew**, who helped a lot in taking my mind off science every once in a while, by undertaking lots of fun trips to festivals and sometimes just doing stupid stuff.
- My **family** for always supporting me, even though they probably had no clue what I was actually doing.

Ich versichere, dass ich diese Dissertation selbstständig verfasst und nur die angegebenen Quellen und Hilfsmittel verwendet habe.

München, den 19. September 2022

.....
(Björn Jonas)